FACULDADE DE ENGENHARIA DA UNIVERSIDADE DO PORTO

Development of extended and advanced failure models and design criteria for aerospace composites

Giuseppe Corrado



Doctoral program in Mechanical Engineering

Supervisors:
Dr. Albertino José Castanho Arteiro
Dr. António Torres Marques

January 26, 2023

© Porto, 2023

Development of extended and advanced failure models and design criteria for aerospace composites

Giuseppe Corrado

Doctoral program in Mechanical Engineering

January 26, 2023

Abstract

In the aerospace sector, to cope with the objectives in terms of sustainability, the expected increase of air traffic should come with a new generation of aerostructures and powerplants. The former will need to be designed and built to withstand more extreme weather conditions, by using advanced materials that can adapt to different conditions, for example to enable climate-optimized routing. Furthermore, performance-based certification using virtual qualification and certification tools is expected to be widely applied. In this context, research in advanced composite materials and their failure analysis plays a crucial role.

This work is part of the European Industrial Doctorate OptiMACS, which is focussed on the development and application of new methods for optimization of multifunctional aerospace composite structures. In particular, the application of advanced failure criteria and damage models for composite structures is proposed and validated.

Firstly, this thesis presents the implementation of an advanced phenomenological failure model, based on invariant structural tensors, to perform more accurate and safer failure prediction of composite structures. With this aim, during this research work, an invariant-based failure theory was implemented to perform "hot-spot" failure analysis and predict the onset of intralaminar damage of fiber-reinforced polymers in coupons and large-scale models. The selected failure criteria identify the critical failure mode, accounting for general three-dimensional stress states, which is essential for the design and analysis of composite laminates under higher levels of triaxiality. Two test cases involving complex stress states were selected for validation of "hot-spot" analysis, including multidirectional open-hole laminates under quasi-pure bending and a stringer runout loaded in tension.

Then, to predict laminate first-ply failure and last-ply failure under general 3D stress states, the invariant-based failure theory was implemented in the "omni strain" failure envelope approach. This concept enables the generation of safe predictions of failure onset and collapse of multidirectional laminates, by finding the controlling plies in the 3D principal strain space. In this way, the omni strain failure theory provides reliable and fast laminate failure indications that can be particularly useful as a design tool for conceptual and preliminary design of composite structures. The proposed extended omni strain failure envelopes allow not only identification of the controlling plies for first-ply and last-ply failure, but also of the critical failure modes. The predictions of the last-ply failure envelopes and surfaces are compared with experimental data on multidirectional laminates from the first and second World-Wide Failure Exercises, showing a satisfactory agreement and validating the conservative character of omni-strain failure envelopes also under complex triaxial stress states.

Finally, to represent the quasi-brittle behavior of composite materials up to ultimate strength, these failure criteria are coupled with a smeared crack model for transverse cracking and contin-

uum damage mechanics models for fibre-dominated damage, which together account for the kinematics of matrix cracking and fibre tensile or compressive fracture during damage propagation. Furthermore, cohesive elements are used in the finite element framework to predict delamination. A verification study of the developed material model was performed at different levels, from single element tests under multiple loading conditions to off-axis tests of unidirectional coupons. Then, to validate the mesoscale damage model, a series of scaled tests on unnotched specimens and a series of notched specimens were selected, with the aim of validating the prediction of the evolution of damage, as well as size effects. Finally, to complement the validation study and further challenge the developed model, a bolted connection from a stringer runout was analyzed. This detailed analysis confirmed that the proposed material model is a powerful tool that accurately captures the onset and evolution of damage in composite structures.

Resumo

No setor aeroespacial, para cumprir os objetivos em termos de sustentabilidade, o aumento esperado do tráfego aéreo deverá vir com uma nova geração de aeroestruturas e de meios de propulsão. Relativamente às aeroestruturas, estas terão que ser concebidas e construídas para resistir a condições meteorológicas mais extremas, utilizando materiais avançados que possam adaptar-se a diferentes condições, por exemplo, para permitir rotas otimizadas em função do clima. Além disso, espera-se que a certificação baseada no desempenho utilizando técnicas de qualificação e certificação virtuais seja amplamente aplicada. Neste contexto, a investigação em materiais compósitos avançados e a análise da sua resistência desempenham um papel crucial.

Este trabalho faz parte do Doutoramento Industrial Europeu OptiMACS, que se concentra no desenvolvimento e aplicação de novos métodos de otimização de estruturas compósitas aeroespaciais multifuncionais. Em particular, é proposta e validada a aplicação de critérios de rotura avançados e modelos de dano para este tipo de estruturas.

Em primeiro lugar, esta tese apresenta a implementação de um modelo de rotura fenomenológico avançado, baseado em tensores estruturais invariantes, para realizar uma previsão de rotura mais precisa e segura de estruturas compósitas. Em particular, durante este trabalho de investigação, foi implementado um critério de rotura baseado em invariantes para identificação de pontos críticos ("hot-spot analysis") e prever o início de dano intralaminar em provetes e em elementos estruturais de compósitos de matriz polimérica reforçados por fibras contínuas. Os critérios de rotura selecionados identificam o modo crítico de falha, contabilizando estados de tensão gerais tridimensionais, que é essencial para a conceção e análise de laminados compósitos sujeitos a níveis mais elevados de triaxialidade. Dois casos de estudo envolvendo complexos estados de tensão foram selecionados para validação da análise de pontos críticos, o primeiro consistindo em laminados multidirecionais com furos circulares sob flexão, e o segundo consistindo na terminação ("run-out") de um reforçador em "T" ("stringer") solicitado em tração.

Depois, para prever a iniciação da rotura em laminados ("first-ply failure") e a rotura final ("last-ply failure") sob estados gerais de tensão 3D, um critério de rotura invariante foi implementado considerando a abordagem "omni strain". Este conceito permite a geração de previsões seguras de início de falha e colapso de laminados multidirecionais, ao identificar, no campo de tensões principais 3D, as camadas que controlam a rotura. Desta forma, o critério de rotura fornece indicações fiáveis e rápidas de falha do laminado que podem ser particularmente úteis como ferramenta de dimensionamento conceptual e preliminar de estruturas compósitas. Este critério de rotura permite não só a identificação das camadas críticas no laminado, mas também dos modos de falha. As previsões das superfícies de rotura são comparadas com dados experimentais em laminados multidirecionais do primeiro e segundo "World-Wide Failure Exercise", mostrando um acordo satisfatório e validando o caráter conservador das superfícies de rotura também sob com-

plexos estados de tensão triaxial.

Finalmente, para representar o comportamento quasi-frágil dos materiais compósitos até à resistência máxima, estes critérios de rotura são associados a um modelo de fratura difusa para fissuras transversais e modelos de mecânica do dano contínuos para falhas dominadas pelas fibras, que em conjunto são responsáveis pela cinemática da fissuração da matriz e da fratura por tração ou compressão das fibras durante a propagação do dano. Além disso, são implementados elementos coesivos para prever falha por delaminagem. Foi realizado um estudo de verificação do modelo de dano desenvolvido, a diferentes níveis, desde testes de um único elemento em múltiplas condições de carga até testes fora do eixo de provetes unidirecionais. Em seguida, para validar o modelo de dano à mesoscala, foi selecionada uma série de testes em amostras de laminados multidirecionais, visando captar a evolução esperada do dano, bem como efeitos de escala. Finalmente, para complementar o estudo de validação e desafiar ainda mais o modelo desenvolvido, foi analisada uma ligação aparafusada de uma terminação de um reforçador em "T". Esta análise detalhada confirmou que o modelo material proposto é uma ferramenta poderosa que capta com precisão o início e a evolução de dano em estruturas compósitas.

"With our limited senses and consciousness, we only glimpse a small portion of reality. Furthermore, everything in the universe is in a state of constant flux. Simple words and thoughts cannot capture this flux or complexity. The only solution for an enlightened person is to let the mind absorb itself in what it experiences, without having to form a judgment on what it all means. The mind must be able to feel doubt and uncertainty for as long as possible. As it remains in this state and probes deeply into the mysteries of the universe, ideas will come that are more dimensional and real than if we had jumped to conclusions and formed judgments early on."

Robert Greene

Acknowledgements

Firstly, I wish to express my gratitude to my main supervisor, Prof. Albertino Arteiro, for the constant guidance throughout the doctoral programme. I am truly grateful for his technical and moral support, for granting me this opportunity and for providing all the necessary conditions to deliver the present research work. The attention to details in this thesis would not be the same without his feedback.

I would also like to thank Prof. Pedro Camanho, Prof. Antonio Torres Marques, Dr. Fernass Daoud and Florian Glock. They have been very supportive in different stages of my PhD, providing crucial inputs to achieve the research goals we set. Furthermore, I would like to thank Prof. Josè Reinoso for all the help and guidance on the development of the work on failure analysis of large-scale structures.

I gratefully acknowledge the financial support provided by the European Commission, under the Marie Skłodowska-Curie Grant Agreement number 764650. I would also like to acknowledge the institutional support of FEUP and Airbus Defence and Space.

This thesis would not be completed without the support of my colleagues and friends in Porto: Carolina Furtado, Rodrigo Tavares, Luis Pereira, Martim Salgado. I would also like to thank everyone that I met at Airbus Defence and Space and througth the OptiMACS project: George Ntourmas, Alessandro Augusto Gastaldi, Massimo Sferza, Neoklis Traiforos, Weijie Tan, Fabian Volle, Sebastian Deinert, Reinhold Maierl, Gustavo Baños Lapuente, Daniel Nussbaecher, Oegmundur Pertersson, Tim Puehlhofer, Stephan Rechtik, Alexander Hoermann, Verena Heinritzi, Christian Vogt.

To everyone that in some way or another was part of this journey and I forgot to mention, thank you for the support and friendship.

Finally, I dedicate this thesis to my parents, my family and Antonietta.

Giuseppe Corrado

Contents

Abstract i

Resumo iii

Acknowledgements vii

Abbreviations xix

I Introduction and literature review 2

1 Introduction 4
1.1 Motivation and objectives . . . 4
1.2 Outline of the thesis . . . 9

2 State-of-art and literature review 11
2.1 Introduction . . . 11
2.2 Micro-mechanics of failure . . . 11
2.3 Intralaminar failure criteria for composite materials . . . 15
2.3.1 Non-phenomenological failure criteria . . . 16
2.3.2 Phenomenological failure criteria . . . 21
2.4 Failure models to predict delamination . . . 37
2.4.1 Constitutive response of cohesive elements . . . 39
2.5 Strength prediction methods for composite laminates . . . 40
2.6 Summary of the *state-of-art* review . . . 44
2.7 Identification of gaps in the *state-of-art* and goals of the work . . . 45

II Extended failure criteria for composite materials 49

3 Extended omni-strain envelopes for laminate failure predictions 51
3.1 Description of the failure criterion . . . 51
3.1.1 Considerations on the 3D invariant-based failure theory . . . 51
3.1.2 Concept of extended omni strain failure theory . . . 56
3.2 Validation of the extended omni-strain failure envelopes . . . 63
3.3 Strengths and limitations of the extended omni failure concept . . . 75
3.4 Summary of the developed tool for failure predictions under general 3D stress states 77

4 "Hot-spot" ply and laminate failure analysis **79**
4.1 Description of the "hot-spot" failure identification tool . . . 79
4.2 Verification of "hot-spot" identification at the coupon level . . . 81
4.3 Application on a stringer run-out for "hot-spot" failure analysis . . . 97
4.4 Final remarks . . . 100

III Advanced failure models for composite materials **103**

5 Detailed damage model for FRPs **105**
5.1 Description of the meso-scale damage model . . . 106
5.1.1 Smeared crack model for transverse matrix cracking . . . 108
5.1.2 Continuum damage mechanics model for longitudinal damage evolution . 111
5.2 Verification studies . . . 117
5.2.1 Single element tests . . . 117
5.2.2 Verification at the coupon level . . . 125
5.3 Validation studies . . . 130
5.3.1 Validation at the coupon level . . . 130
5.3.2 Validation at the structural detail level . . . 154

IV Conclusions **162**

6 Conclusion and future work **164**
6.1 Conclusions . . . 164
6.2 Future work . . . 167

V Appendix **169**

A Bisection method **171**

Bibliography **173**

List of Figures

1.1 Aeronautics community vision for achieving carbon neutrality [4], from the website of the commercial aviation industry ATAG [5]. 5
1.2 Expected demand of aircraft from Airbus for the next 20 years from Ref. [8]. . . 6
1.3 Global view of the OptiMACS workplan, where the present research work on failure criteria and damage models contributes to an enhanced "Performance-based optimization". 8

2.1 Failure mechanisms involving fibre breakage of a carbon-epoxy cross-ply laminate. Reprinted from [24], copyright (2009), with permission from Elsevier. . . . 12
2.2 (a) 3D kink band model, defining the angle of the kinking plane ψ and the kinking angle φ; (b) Kink band in unidirectional IM6/3501-6 carbon/epoxy composite under longitudinal compressive loading (adapted from Ref. [34]). 13
2.3 Schematic illustration of interfibre fracture (matrix cracking) and corresponding electron microscopy cross-sectional images of a carbon/epoxy material (adapted from Ref. [21]). 14
2.4 Failure mode of unidirectional composite under in-plane shear (10° off-axis carbon/epoxy specimen loaded in axial tension). Figure adapted from Ref. [34]. . . . 14
2.5 Omni FPF envelopes in principal strain space for T700/C-Ply 55 (a) and IM7/977-3 (b) laminates, according to the Tsai-Wu failure criterion [50]. 20
2.6 Rate of use for failure criteria from study conducted by the U.S. Department of Transportation Federal Aviation Administration study, from Ref. [52]. 22
2.7 Failure envelopes obtained using Maximum stress, maximum strain, and Tsai-Hill failure criteria in σ_{11} - σ_{22} space. 23
2.8 Inter-Fibre Fracture modes A, B and C. Reprinted from [17], copyright (1998), with permission from Elsevier. 25
2.9 Biaxial $\sigma_{11} - \sigma_{22}$ failure envelopes of 0° E-glass/MY750 epoxy lamina (from Ref. [30]). 27
2.10 Failure envelopes and WWFE test data for UD E-glass/LY556 [30]. 29
2.11 3D kinking model from LaRC failure criteria [43]. 30
2.12 Failure envelopes and test data for an AS4/55A composite, from Ref. [43]. 31
2.13 3D kinking model with the definition of the kinking angle φ and the angle of the kinking plane ψ [50]. 33
2.14 Linear traction separation response of cohesive elements. 39
2.15 (a) Definition of anchor points for a unit circle failure envelope in principal strain space; (b) unit circle (solid line) and omni strain LPF (dashed line) envelopes for T700/C-Ply 55 carbon/epoxy [50]. 44

3.1 σ_{11} - σ_{22} failure envelopes of S-glass/epoxy with different value of out-of-plane compression (σ_{33}), ranging from zero to 0.8 Y_C. In (a), fibre kinking is predicted by computing the kinking angle φ with a nonzero initial misalignment angle φ^0, while in (b) an alternative micro-mechanical parameter χ is employed. 52
3.2 Failure envelopes in stress space of UD IM7/8552, obtained with the 3D invariant-based failure criteria. 54
3.3 Failure envelopes in strain space of UD IM7/8552, obtained with the 3D invariant-based failure criteria. 55
3.4 Comparison between ε_{11} - ε_{22} failure envelopes in strain space, for a 0° ply, based on the 3D invariant-based failure criteria under plane (green line) and general 3D (blue line) stress states. 56
3.5 Triaxial failure stress states: $\sigma_{22} = \sigma_{33}$ vs. longitudinal stress σ_{11} for a UD carbon/epoxy (after Ref. [50]). 57
3.6 Triaxial failure stress states: $\sigma_{22} = \sigma_{33}$ vs. longitudinal stress σ_{11} for a UD S-glass/epoxy cube (after Ref. [50]). 57
3.7 Triaxial failure stress states: σ_{22} vs. longitudinal stress $\sigma_{11} = \sigma_{33}$ for a UD E-glass/MY750 epoxy (after Ref. [50]). 58
3.8 Triaxial failure stress states: shear stress σ_{12} vs. hydrostatic pressure ($\sigma_{11} = \sigma_{22} = \sigma_{33}$) for a UD T300/PR319 epoxy (after Ref. [50]). 58
3.9 Omni FPF envelope in strain space for IM7/8552, according to the 3D invariant-based failure criteria, with a detailed view on the critical failure modes. 60
3.10 ε_{11} - ε_{22} omni FPF envelope, for UD IM7/8552, obtained with the matrix failure criterion from the 3D invariant-based failure criteria. The omni FPF envelope based on the complete failure theory is also included as benchmark. 60
3.11 Detailed view on the values of kinking angle φ on the omni FPF envelope in principal strain space for IM7/8552, according to the 3D invariant-based failure model. 61
3.12 Omni LPF envelope in principal strain space for IM7/8552, according to the 3D invariant-based failure criteria, with a detailed view of the controlling plies and critical failure modes. 62
3.13 Comparison between omni FPF/LPF envelopes obtained with 3D invariant-based failure criteria under plane (dashed red line) and general 3D stress states (solid black line), in principal strain space for UD IM7/8552. 62
3.14 3D failure surface in stress space for UD IM7/8552, obtained using the 3D invariant-based failure criteria [50]. 63
3.15 3D omni strain FPF (a) and LPF (b) surfaces in strain space for IM7/8552, obtained using the 3D invariant-based failure criteria [50]. 64
3.16 σ_{22} - σ_{11} failure envelopes versus experimental results from the WWFE-I for a $[90/\pm45/0]_s$ AS4/3501-6 carbon/epoxy laminate [50]. 66
3.17 σ_{22} - σ_{11} failure envelopes versus experimental results from the WWFE-I for a $[\pm30/90]_s$ E-glass/LY556/HT907/DY063 laminate [50]. 67
3.18 Omni strain LPF envelope, controlling plies and critical failure modes obtained with the 3D invariant-based failure criteria for E-glass/LY556/HT907/DY063 [50]. 68
3.19 Omni strain LPF envelope, controlling plies and critical failure modes obtained with the 3D invariant-based failure criteria for E-glass/MY750/HY750/DY063 [50]. 69
3.20 Omni LPF envelopes, based on Tsai-Wu, and unit circle envelopes in principal strain space for two different composite material systems [50]. 70

3.21 $\sigma_{22} - \sigma_{11}$ failure envelopes versus experimental results from the WWFE-I for a $[\pm 55]_s$ E-glass/MY750/HY750/DY063 laminate [50]. 72
3.22 3D omni LPF (a) and $[\pm 35]_s$ laminate LPF (b) surfaces versus experimental results from WWFE-II for a $[\pm 35]_s$ E-glass/MY750 epoxy laminate [50]. 73
3.23 $\sigma_{22} - \sigma_{11}$=$\sigma_{33}$ failure envelopes versus experimental results from WWFE-II for a $[\pm 35]_s$ E-glass/MY750 epoxy laminate. The experimental data is available for two different fibre volume fractions (v_f) [50]. 74
3.24 3D omni LPF (a) and $[\pm 35]_s$ laminate LPF (b) predictions under general stress states and plane stress conditions versus experimental results from WWFE-II for a $[\pm 35]_s$ E-glass/MY750 epoxy laminate [50]. 75

4.1 a) Presentation of the compression experimental device with pivots, b) zoom on the jaws with pivots, c) general principle of the quasi-pure bending test, from Ref. [126]. 82
4.2 Computational solid model for an open-hole plate under quasi-pure bending. . . . 84
4.3 Reaction force-applied displacement plot of the 100/0/0 OH laminate under quasi-pure bending. A detailed view is provided for the identification of FPF and the corresponding critical failure mode. 85
4.4 Reaction force-applied displacement plot of the 25/50/25 OH laminate under quasi-pure bending. A detailed view is provided for the identification of FPF and the corresponding critical failure mode. 86
4.5 Reaction force-applied displacement plot of the 50/40/10 OH laminate under quasi-pure bending. A detailed view is provided for the identification of FPF and the corresponding critical failure mode. 86
4.6 Reaction force-applied displacement plot of the 20/60/20 OH laminate under quasi-pure bending. A detailed view is provided for the identification of FPF and the corresponding critical failure mode. 87
4.7 Reaction force-applied displacement plot of the 25/50/25 OH laminate. A detailed view is provided for the identification of the onset of delamination, by means of the Ye's criterion failure index. 88
4.8 Reaction force-applied displacement plot of the 50/40/10 OH laminate. A detailed view is provided for the identification of the onset of delamination, by means of the Ye's criterion failure index. 88
4.9 Reaction force-applied displacement plot of the 20/60/20 OH laminate. A detailed view is provided for the identification of the onset of delamination, by means of the Ye's criterion failure index. 89
4.10 Evolution of interlaminar damage for 25/50/25, 50/40/10 and 20/60/20 OH laminates. 91
4.11 Damage variable of the cohesive elements for the 3 OH laminates investigated, for an applied displacement larger than the one corresponding to the respective delamination onset. 93
4.12 Reaction force-applied displacement curve of the 100/0/0 OH laminate subjected to quasi-pure bending. These numerical results are obtained using an equivalent single-layer discretization. A detailed view is provided for the identification of laminate failure, as predicted by the unit circle failure criterion. 94
4.13 Reaction force-applied displacement curve of the 25/50/25 OH laminate subjected to quasi-pure bending. These numerical results are obtained using an equivalent single-layer discretization. A detailed view is provided for the identification of laminate failure, as predicted by the unit circle failure criterion. 95

4.14 Reaction force-applied displacement curve of the 50/40/10 OH laminate subjected to quasi-pure bending. These numerical results are obtained using an equivalent single-layer discretization. A detailed view is provided for the identification of laminate failure, as predicted by the unit circle failure criterion. 95
4.15 Reaction force-applied displacement curve of the 20/60/20 OH laminate subjected to quasi-pure bending. These numerical results are obtained using an equivalent single-layer discretization. A detailed view is provided for the identification of laminate failure, as predicted by the unit circle failure criterion. 96
4.16 Schematic plot of the model and boundary conditions of the stringer runout. . . . 97
4.17 "Hot-spot" failure analysis in the runout region for the skin. The predictions for failure onset are computed using the 3D invariant-based failure theory and, in this case, the critical failure index is for fibre kinking. 98
4.18 "Hot-spot" failure analysis in the runout region for the stringer. The predictions for failure onset are computed using the 3D invariant-based failure theory and, in this case, the critical failure index is for fibre kinking. 99
4.19 "Hot-spot" failure analysis in the runout region for the stringer. The predictions for failure onset are computed using the 3D invariant-based failure theory and, in this case, the critical failure index is for matrix tensile failure. 99

5.1 Fracture surfaces resulting from the different failure modes and corresponding damage activation and propagation functions. 106
5.2 Flowchart of the meso-scale damage model. 107
5.3 Transverse fracture plane, after Ref. [133]. 109
5.4 Uniaxial response under longitudinal tension (a) and longitudinal compression (b). 112
5.5 Schematic representation of the derivation of the first branch of a bi-linear damage evolution law. 115
5.6 Verification study at the single element level under uniaxial longitudinal tension (a) and longitudinal compression (b). 119
5.7 Evolution of the damage variable for fibre-dominated failure (d_1) and the kinking angle (φ) with longitudinal strain (ε_{11}), for a single C3D8R element under uniaxial compression in the fibre direction. 119
5.8 Verification study at the single element level under triaxial loading, realized by applying biaxial transverse pressure ($\sigma_{22} = \sigma_{33}$ =120.0 MPa) and longitudinal compression. In (a), there is the comparison between the triaxial case and the uniaxial case, while (b) shows the comparison between the proposed and the previous versions of degradation models. 120
5.9 Numerical results of single element test under different loading conditions for matrix-dominated failure. 123
5.10 Verification study at the single element level under biaxial transverse compression with a ratio (σ_{33}/σ_{22}) = 3.0 and different values of frictional coefficient. The evolution of the normal component of the traction with the cracking strain is shown in (a), while the transverse shear component evolution of the traction with cracking strain is shown in (b). 124
5.11 Verification study at the single element level under a constant out-of-plane pressure (σ_{33}) and increasing out-of-plane shear (σ_{13}), with different values of frictional coefficient. The evolution of the in-plane shear component of the traction vs out-of-plane shear is shown in (a), while in (b) the same traction component is shown vs the cracking strain. 125

5.12 Verification study at the single element level involving load reversal with uniaxial loading. In (a) the evolution of the longitudinal stress component with longitudinal strain is shown, while the damage variable for fibre-dominated failure vs longitudinal strain is displayed in (b). 126
5.13 Verification study at the single element level involving load reversal with in-plane shear loading. In (a) the evolution of the in-plane shear component of the traction with the cracking strain is shown, while the damage variable for matrix-dominated failure vs in-plane strain is displayed in (b). 126
5.14 Mesh and boundary conditions for the simulation of off-axis specimens under tension and compression. 128
5.15 Comparison between experimental results and model predictions on failure of off-axis coupons under tension (a) and compression (b). 129
5.16 Overall correlation between experimental results and model predictions of off-axis coupons subjected to axial loading. 129
5.17 Mesh and boundary conditions for the simulation of an UNT specimen under tension, with ply-level scaling and m = 2, leading to the following stacking sequence: $[45_2/90_2/\text{-}45_2/0_2]_s$. 133
5.18 Size effect study on UNT quasi-isotropic ($[45_m/90_m/\text{-}45_m/0_m]_{ns}$) specimens under tension with n-scaling (a) and m-scaling (b). 136
5.19 Size effect study on UNT quasi-isotropic ($[45_m/90_m/\text{-}45_m/0_m]_{ns}$) specimens under compression with n-scaling (a) and m-scaling (b). 137
5.20 Damage progression in sublaminate-level scaled UNT models, subjected to longitudinal tension. 138
5.21 Damage progression in ply-level scaled UNT models, subjected to longitudinal tension. 139
5.22 Damage progression in sublaminate-level scaled UNT models, subjected to longitudinal compression. 140
5.23 Damage progression in ply-level scaled UNT models, subjected to longitudinal compression. 141
5.24 Mesh and boundary conditions of OH models, for the case of compression (depicted above) and tension (depicted below). 144
5.25 Normalized stress-applied displacement curves for 10/80/10 OH laminate under tension, obtained for different sets of material properties. 146
5.26 Overall correlation between experimental results with coefficient of variation and predictions of OH specimens subjected to tension. 149
5.27 Overall correlation between experimental data with coefficient of variation and predictions of OH specimens subjected to compression. 150
5.28 Column plots of the obtained numerical results and experiments with standard deviation for OH laminates, under tension in (a) and under compression in (b). . . 151
5.29 Damage progression in OH models subjected to longitudinal tension. 152
5.30 Damage progression in OH models subjected to longitudinal compression. 153
5.31 Global and local model of a stringer runout, subjected to tensile loading. 155
5.32 Multi-zone modelling strategy for the definition of different mesh and material response. 156
5.33 Definition of contact behaviour between bolt, skin and stiffener. 157
5.34 Stress-displacement curves, obtained applying different levels of pre-loading, for a bolted connection under tension. Below the evolution of intralaminar damage and delamination is showed for the case of 1 kN clamping load. 159

5.35 Matrix damage evolution in a bolted connection subjected to longitudinal tension. 160

A.1 Graphical representation of the bisection method. 172
A.2 Example of identification of failure loci in ε_{11} - ε_{22} strain space, with polar coordinates. 172

List of Tables

3.1 Material properties of the IM7/8552 carbon-epoxy UD tape [33]. 59
3.2 Material properties from WWFE-I [36]. 65

4.1 Material properties of the T700GC/M21 carbon/epoxy UD tape [127, 128, 129]. . 82
4.2 *In-situ* properties of the T700GC/M21 carbon/epoxy UD tape. 83
4.3 Modified solution control parameters to overcome convergence problems related with Abaqus/Standard® cohesive elements. 90
4.4 Interlaminar material properties of T700GC/M21 UD tape. 90

5.1 Determination of the fracture angle α, after Refs. [131, 134, 135]. 108
5.2 Material properties of IM7/8552 UD tape, used for verification of the implemented damage model. 121
5.3 Dimensions and stacking sequence of the scaled UNT quasi-isotropic laminates, tested for the experimental works presented in Refs. [143, 148]. 131
5.4 *In-situ* properties of IM7/8552 carbon-epoxy material system. 132
5.5 Interlaminar properties of the IM7/8552 carbon-epoxy material system. 133
5.6 Comparison between experimental results from Ref. [143, 148] and proposed mesoscale damage model on the UNT strength of scaled QI specimens. 142
5.7 Sets of material properties, normalized on the values of the first set, used for correlation study on OH specimens. 145

List of abbreviations

ACARE Advisory Council for Aviation Research and Innovation in Europe

AIAA American Institute of Aeronautics and Astronautics

ATAG Air Transport Action Group

BBA Building Block Approach

BK Benzeggagh and Kenane

C3D8R cubic 8-node linear hexahedral finite element with reduced integration

CDM Continuum Damage Mechanics

CFRP carbon fibre-reinforced polymer

COH3D8 8-node three-dimensional cohesive element

CPU central processing unit

CTE Coefficient of Thermal Expansion

CV Coefficient of Variation

CZM Cohesive Zone Model

DDM Discrete Damage Mechanics

DOF Degree Of Freedom

EID European Industrial Doctorate

FE Finite Element

FEA Finite Element Analysis

FEM Finite Element Method

FF fibre failure

FI failure index

FPF first-ply failure

FRP fibre-reinforced polymer

GFRP glass fibre-reinforced polymer

IFF inter-fibre fracture

LaRC Langley Research Center

LHS left-hand side

LPF last-ply failure

LPT Laminate Plate Theory

MDO Multidisciplinary Design Optimization

MPC Multi-point constraint

MSCA Marie Skłodowska-Curie Actions

NASA National Aeronautics and Space Administration

NCF Non-Crimp Fabric

NT notched

OH open-hole

OptiMACS Optimization of Multifunctional Aerospace Composite Structures

QI quasi-isotropic

RF reserve factor

RHS right-hand side

RVE Representative Volume Element

S4R 4-node quadrilateral finite element with reduced integration

SCM Smeared Crack Model

SD Standard Deviation

SEM Scanning Electron Microscope

Tr Trace

UD unidirectional

UNT unnotched

VCCT Virtual Crack Closure Technique

WWFE World-Wide Failure Exercise

X-FEM Extended finite element method

Part I

Introduction and literature review

Chapter 1

Introduction

1.1 Motivation and objectives

Materials and structures have been responsible for major improvements in the aerospace sector, mainly in terms of performance and safety. Among the innovative structural concepts and technologies, the development of advanced composite materials, witnessed during the past 40 years, have improved structural performance, reduced operational risk, enhancing the overall capability of aerospace vehicle airframes. This growing interest in using composite materials for aerospace applications is justified by their beneficial mechanical properties, such as their very high specific stiffness and strength, which enable the design of improved light-weight primary structures. Furthermore, as additional beneficial properties, composites are fatigue and corrosion resistant and have tailorable properties, which provide additional design flexibility.

Advanced materials, as fibre-reinforced polymers (FRPs), are among the leading technologies for future sustainable air vehicles, contributing to the design of light-weight structures. Saving fuel consumption by minimizing the structural weight means reducing the environmental impact of aviation, which is one of the most significant challenges that the aeronautical industry is facing. In fact, stimulating goals in terms of environmental impact, concerning CO_2 and NO_x emissions, fuel consumption and noise pollution have been addressed in the Flightpath 2050 issued in 2010 by the European Commission [1] and the associated Strategic Research and Innovation Agenda [2], formulated by the Advisory Council for Aviation Research and Innovation in Europe (ACARE), as well as addressed in the US Aeronautics Strategic Implementation Plan [3] from NASA. Fig. 1.1 shows the aeronautics community vision for achieving carbon neutrality, highlighting the need for biofuels and additional new-generation technologies.

Despite EU research in clean aviation is producing excellent results, the recent events have imposed to rethink Europe's Flightpath 2050 [6]. Indeed, since the publication of Flightpath 2050 the world has changed, and continues to change, at an ever-increasing pace. The COVID-19 pandemic caused aviation's biggest challenge ever: an unprecedented and extended global reduction in demand. Full recovery is still some years away and may be constrained by political crises and conflict [7]. Therefore, according to ACARE, particular attention must be paid to sector

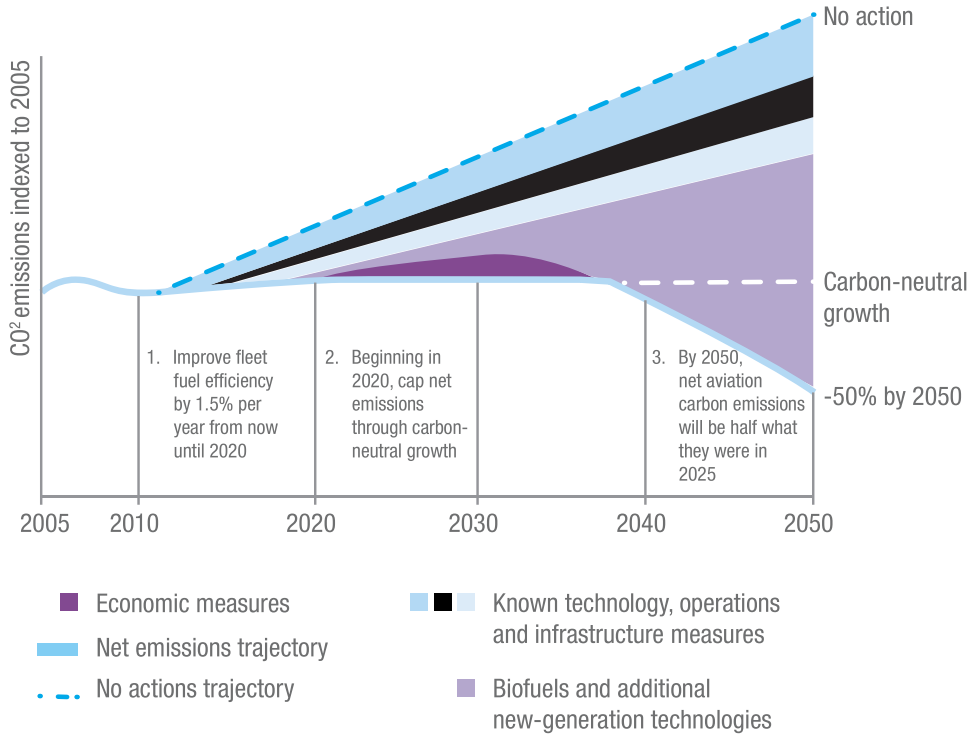


Figure 1.1: Aeronautics community vision for achieving carbon neutrality [4], from the website of the commercial aviation industry ATAG [5].

resilience and passenger health. Escalating and volatile energy prices and uncertainties concerning energy security are also a concern.

ACARE have recently outlined, in "Fly the Green Deal" [7], a set of detailed, quantitative goals to be achieved by 2050 with intermediate milestones in 2030 and 2035. These goals can be summarized in 3 points: i) achieving climate neutral aviation by reducing the impact of CO_2 and non-CO_2 effects, ii) centralizing the role of citizens, protecting travellers' rights in a consistent way across all transport modes and iii) extending global leadership and improving competitiveness.

In spite of the uncertainties on the aviation sector, global market forecasts include positive outlooks. For instance, Airbus is forecasting a need for over 39000 aircraft between 2022 and 2041 [8], of which about 80% are expected to be Typically Single Aisle and the remaining 20% Typically Widebody, as shown in Fig. 1.2. Air traffic is also expected to recover to 2019 levels between 2023 and 2025 and then, to grow at 3.6% until 2041 [8]. This growth rate obviously depends on various social and economic factors, but it may be assumed that the amount of air traffic will increase significantly in the future. In particular it is shown that, as regions around the world expand their aviation industry, their share of the market continues to grow and increases the traffic flow.

In order to cope with the objectives in terms of sustainability, the expected increase of air traffic should come with a new generation of aerostructures and powerplants. Europe's Vision for Sustainable Aviation forecasts that, in 2050, the Europe fleet will contain the highest proportion of sustainable air vehicles in the world. These vehicles are expected to be highly efficient aerody-

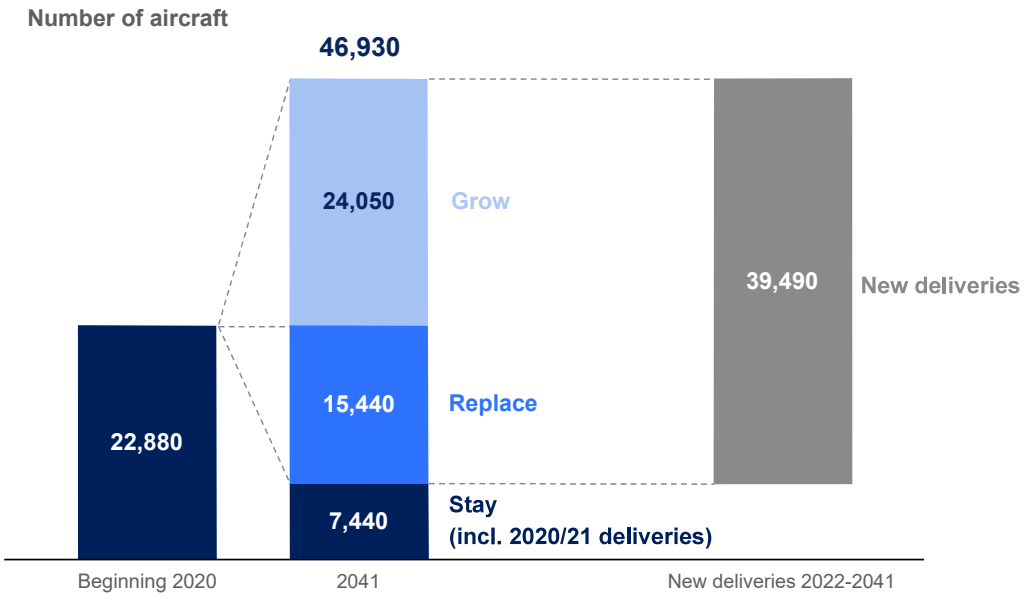


Figure 1.2: Expected demand of aircraft from Airbus for the next 20 years from Ref. [8].

namically, with very low drag, for reduced energy consumption and lower noise impact compared to 2020. They will be designed and built to withstand more extreme weather conditions, by using advanced materials and light-weight structures that can adapt to different conditions, for example to enable climate-optimized routing. Furthermore, performance-based certification using virtual qualification and certification techniques is expected to be widely applied, delivering higher efficiency and reliability than physical testing [7].

In this context, research in advanced composite materials plays a crucial role. Indeed, fibre-reinforced composite materials proved to represent a valid alternative to traditional light metal alloys, being able to reduce the weight of aerospace components, while meeting their operational constraints (i.e. reliability, stability, strength, noise, manufacturability and cost). This material replacement gave to the designer the flexibility to select the fibre orientation on a layer by layer basis, building laminated fibre-reinforced composite materials with load-tailored layups. Additionally, enhanced damage tolerance can be built into the structure, by suppressing critical damage modes for the benefit of more favourable ones [9]. On the other hand, this flexibility comes at the cost of a considerably more complex internal material architecture.

In fact, due to the inherent heterogeneity and anisotropy of laminated composites, their usage is challenged by the resulting increase of complexity of the design process. The additional parameters to be determined include the exact layering design of the structure (i.e. number, sequence, thickness and mechanical characteristics of each ply) and the manufacturing process to be followed for each component. Furthermore, the formulation of the design criteria required for the structural sizing optimization process (consisting of all relevant strength, fatigue, buckling, aeroelasticity, manufacturing and deflections constraints) is more challenging due to the employment of these anisotropic materials. As a direct consequence, a detailed numerical modelling using the Finite Element Method (FEM) for an entire aeronautic product would result in millions of degrees of

freedom, which is prohibitive for optimization purposes. The structural optimization of composite structures is, therefore, nowadays performed at a macroscale level by considering homogenized properties for each laminate, which compromises the level of detailing of the resulting optimal design [10, 11, 12].

These limitations have been fundamental motivations for several investigations conducted by researchers worldwide. Moreover, in order to join forces and realize the most cutting-edge research, an active synergy between industry and academia has been often realized to exploit complementary competences and face the mentioned challenges. With this purpose, among the several research projects funded by the European Union's Horizon 2020 research and innovation programme through the Marie Skłodowska-Curie Actions (MSCA), a European Industrial Doctorate (EID) called OptiMACS, tackles a more efficient multidisciplinary design Optimization of Multifunctional Aerospace Composite Structures [13]. The strategic direction of the OptiMACS project looks towards the industrial need to make aeronautical composite structures more affordable, reducing the cost of their design, by optimization, while meeting all the operational constraints. Novel optimization models, processes and design criteria will be delivered and implemented in the industrial Multidisciplinary Design Optimization (MDO) platform (at Airbus Defence and Space) and the performance of the enhanced platform will be evaluated on the designated industrial and academic case studies. This enhanced industrial MDO platform will be proposed as a new benchmark for MDO of composites in the aeronautical industry worldwide.

A set of sophisticated software tools is currently employed within the European aerospace industry in order to perform structural optimization. The cutting-edge Lagrange aircraft optimization software, developed and extensively employed by Airbus (for the design of civil, military as well as experimental aircraft) currently has a number of design and performance optimization criteria implemented (i.e. structural weight, structural strength, aerodynamic and aeroelastic performance and stability, structural stability, such as analytical buckling criteria, and fundamental failure criteria, such as maximum strain and Tsai-Hill approaches). Within the OptiMACS project, the research work described in this thesis addresses the development of extended and advanced failure models and design criteria for aerospace composites. The contribution of this work is aimed at enhancing the industrial MDO software, by improving the performance-based optimization processes, providing more accurate and safe failure information. However, this is only one of the three main work packages of the project. In fact, OptiMACS will also deliver a set of manufacturing models, constraints and optimization criteria for enhancing the design cycle by feeding manufacturing knowledge early into the design process, as well as novel optimization algorithms to improve the computational efficiency of the industrial MDO. A schematic view of the project, highlighting the work described in this thesis, is provided in Fig. 1.3. A more detailed description of the work packages and preliminary results of the OptiMACS project can be found in Ref. [14].

It is clear that, in this framework, the research work addressed in this thesis plays an important role for the industrial MDO platform, delivering an enhanced optimization against failure of composite structures. In particular, this investigation aims at delivering failure information to the

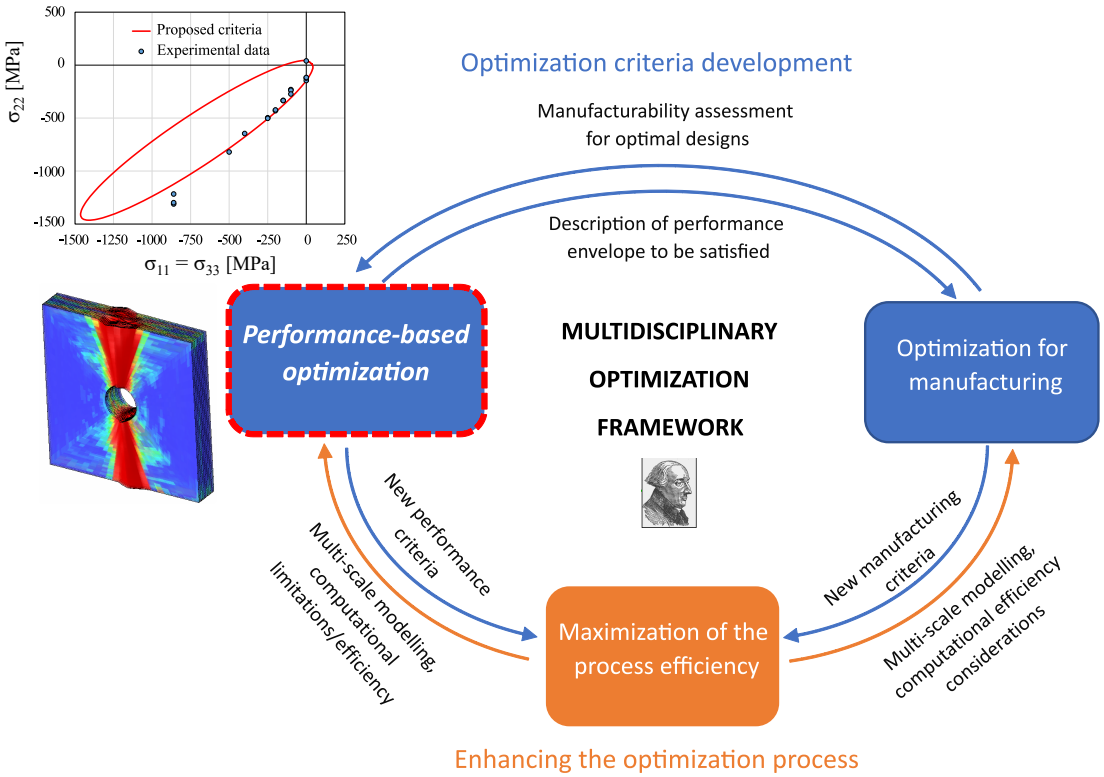


Figure 1.3: Global view of the OptiMACS workplan, where the present research work on failure criteria and damage models contributes to an enhanced "Performance-based optimization".

MDO framework at different scales: i) at the ply and laminate level, assessing and extending the currently implemented intralaminar and interlaminar failure criteria; ii) at the coupon and detail level, to predict the damage behaviour of composite structures, by modelling and implementing 3D damage evolution laws within numerical predictive tools; iii) at the detail and structural level, delivering detailed and accurate predictions of failure onset in a Finite Element (FE) context. The benefits of the integration of these developments in the MDO platform can have a significant impact in the overall design process.

1.2 Outline of the thesis

This thesis is organized in 6 chapters that address the different topics connected to the delivery of the main goal of the present research: the development of extended and advanced failure models and design criteria for aerospace composites.

Following this first introductory chapter, the next one is dedicated to the state-of-art review of the following topics: i) the micro-mechanics of failure initiation in composite materials under quasi-static loadings, ii) phenomenological and non-phenomenological failure criteria for FRPs, iii) failure theories for the onset of delamination and iv) approaches for strength prediction of a general laminate, including analytical methods and damage models. Then, in the same section, the identified gaps in the state-of-art and literature are highlighted. Finally, the main research questions and, in particular, the main hypotheses and strategies to deliver the expected research outcomes are presented.

Chapter 3 introduces a simplified approach to first-ply failure (FPF) and last-ply failure (LPF). The proposed analytical method allows predicting the onset and final failure of a multidirectional laminate under general stress states, given only a set of material properties. Chapter 3 also includes validation studies of the proposed approach, highlighting its main advantages and drawbacks.

Then, Chapter 4 describes the "hot-spot" failure analysis for the prediction of the onset of intralaminar failure and the corresponding failure mode in a FE context based on a layer-wise discretization. The "hot-spot" failure analysis is then implemented to predict final failure when using a FE model with single-layer discretization. Some interesting case studies are described in order to assess the validity of the proposed tool.

Next, Chapter 5 presents a mesoscale damage model for composite material addressing the onset and broadening of fibre- and matrix-dominated failure mechanisms. The formulation of constitutive models are described in detail, with a focus on the development of a damage law for fibre kinking broadening. Additionally, verification and validation studies are presented to assess the suitability and benefits of the implemented mesoscale model.

Lastly, in Chapter 6, the main conclusions of the work carried out in this thesis are presented along with some proposed future research works.

Chapter 2

State-of-art and literature review

2.1 Introduction

The present chapter presents the state-of-the-art review. Firstly, the failure mechanisms of composite materials under quasi-static loadings are described, followed by a deep presentation of the state-of-art methods to predict the onset of these phenomena. Then, the challenges related to the prediction of damage progression, material degradation and ultimate failure are presented.

2.2 Micro-mechanics of failure

Failure criteria are defined to set the the limit values in stress (or strain) space beyond which the material experiences a certain level of structural degradation. Therefore, they provide a robust tool for predicting the loss of integrity that could lead to the structural collapse of the studied component [15]. For instance, failure criteria are crucial at the design stages, especially when providing failure envelopes from relatively simple experimental data. Predictions using the failure envelopes nowadays makes failure analysis of carbon fibre reinforced composite laminates very simple to understand, enabling the calculation of safety factors of composite structures subjected to complex loading and boundary conditions.

Before reviewing the failure theories for FRPs, it is fundamental to describe the complex failure mechanisms of these materials. In fact, the need for failure criteria based on failure mechanisms dates back to 1973, when Hashin used his experimental studies to establish two different formulations to identify fibre failure and matrix failure. According to some reviews, however, the first model distinguishing failure modes was proposed by Puck in 1969 [16], although his theory has found more resonance in the composites community with the work published in 1998 [17].

Thanks to the large experimental campaigns conducted over the last decades, the main failure mechanisms of composite laminae were identified. For a UD ply under plane stress conditions, several experimental studies were needed to understand and identify the micromechanics of failure [18, 19, 20]. These failure mechanisms are listed below for each loading case, providing also the resulting fracture plane and its orientation (α), as defined in Fig. 2.3.

- Longitudinal tension:

  Experimental evidence have shown that, for a unidirectional (UD) ply under longitudinal tension, failure onset is caused by fibre failure, which is the phase having the lower ultimate strain. Not all fibres fail simultaneously, but a single fibre breaks at the weakest points, generating a non-uniform stress state around the failure point [21, 22, 23, 24]. Afterwards, the stress redistribution causes matrix cracking and fibre-matrix decohesions, leading to fibre pull-out. The resulting fracture plane is normal with respect to the fibre direction. A typical fracture surface under quasi-static tensile loading is shown in Fig. 2.1, in an image obtained by Scanning Electron Microscope (SEM) from Ref. [24]. The fracture plane is not perfectly planar as it is characterized by fibre pull-out.

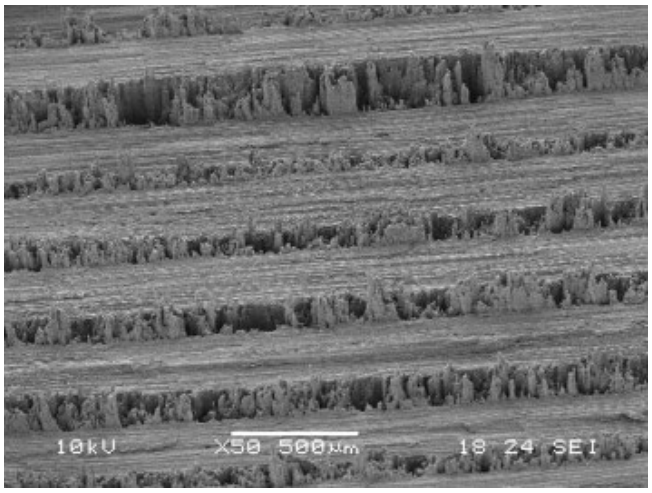


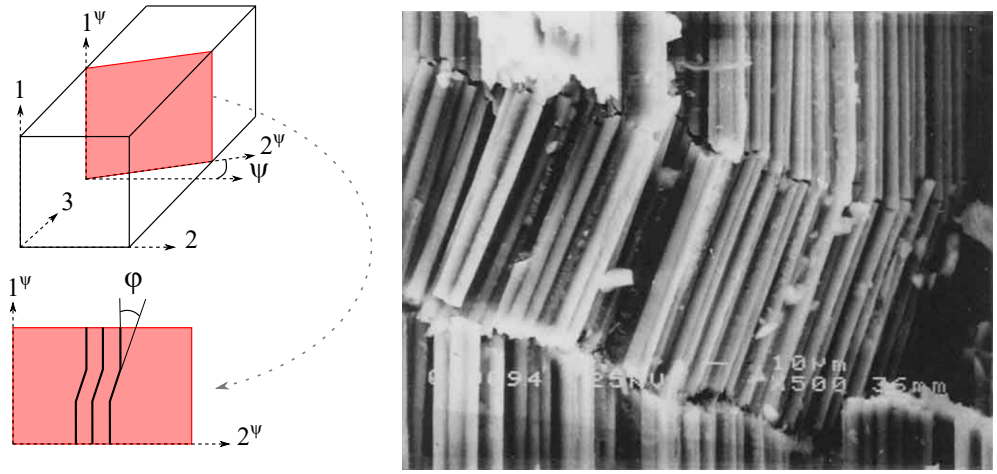
Figure 2.1: Failure mechanisms involving fibre breakage of a carbon-epoxy cross-ply laminate. Reprinted from [24], copyright (2009), with permission from Elsevier.

- Longitudinal compression:

  UD laminates under longitudinal compressive loading have been observed to experience a failure phenomenon that involves the generation of a kink band, being a combination of the microbuckling mechanism and the transferred shear stresses by the interface between matrix and fiber [25, 26]. In other words, fibre kinking commonly occurs as a result of fibre instability due to local cracks in the matrix, which leads to the formation of a kink band.

  Rosen was the first researcher to analyze microbuckling as the main mechanism inducing fibre kinking, being geometric instability of the fibers that causes a transverse displacement when a compressive load is applied [27]. He distinguished two periodic failure modes of fibre compressive failure: an *extension mode*, typically observed in elastic polymer matrices with fibre volume fractions less than about 30%, and a *shear mode*, for fibre volume fractions greater than 30%. For primary aeronautical structures, composites with high volume fractions and well aligned fibres are the commonly used and, thus, shear driven compressive failure is the most interesting failure mode.

The prediction and modelling of compressive failure of UD composites is a challenging problem which has been addressed for several years [19, 27, 28, 29]. Argon [28] developed the first mechanical model for fibre kinking as a separate failure mode. For Argon, fibre kinking is the result of matrix shear failure, prompted by an initial fibre misalignment. For this model, and those that follow it, matrix elastic behaviour and initial material imperfections play an important role. In recent and advanced failure theories [30, 31, 32, 33], the fracture plane generated by kinking failure, and defining a kink band, is modelled using two angles: the angle of the kinking plane ψ and the kinking angle φ, as shown in Fig. 2.2.



(a) (b)

Figure 2.2: (a) 3D kink band model, defining the angle of the kinking plane ψ and the kinking angle φ; (b) Kink band in unidirectional IM6/3501-6 carbon/epoxy composite under longitudinal compressive loading (adapted from Ref. [34]).

- Transverse tension:

  Under transverse tension, the onset of failure of UD laminates takes place in the matrix and fibre-matrix interface, due to high stress concentrations. Failure takes the form of isolated interfacial micro-cracks increasing in number with loading and finally coalescing into a catastrophic transverse crack [21, 34]. Transverse matrix cracking under tensile loading is characterized by a fracture plane parallel to the fibres ($\alpha = 0°$), as represented in Fig. 2.3.

- Transverse compression:

  For pure transverse compression, failure initiation is triggered by the combined action of shear stresses in the fracture plane and by the friction promoted by the normal stress to that plane. Experimental studies identified the presence of numerous hackles in the matrix along the fracture surface proving the failure by shear [21, 34]. The resulting fracture plane has an orientation of approximately 53°, as shown in Fig. 2.3.

- In-plane shear:

Under in-plane shear, a high shear stress concentration develops at the fibre-matrix interface, causing shear failure in the matrix and/or fibre-matrix debonding. A schematic representation of the described phenomena is shown in Fig. 2.4. The orientation of the resulting fracture plane is the same of transverse tension, so parallel to the direction of the fibres, as illustrated in Fig. 2.3.

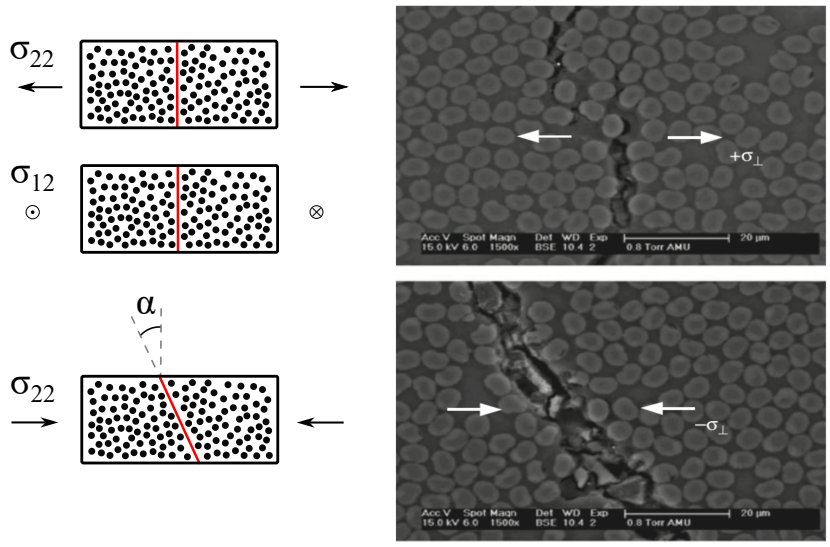


Figure 2.3: Schematic illustration of interfibre fracture (matrix cracking) and corresponding electron microscopy cross-sectional images of a carbon/epoxy material (adapted from Ref. [21]).

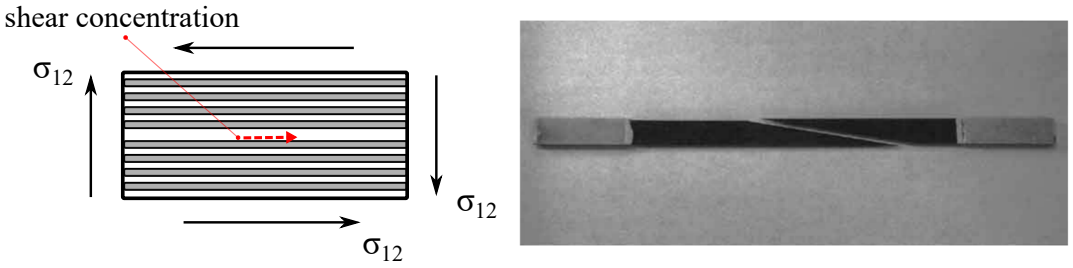


Figure 2.4: Failure mode of unidirectional composite under in-plane shear (10° off-axis carbon/epoxy specimen loaded in axial tension). Figure adapted from Ref. [34].

The case of combined stress applied to FRP laminae is challenging and led to the formulation of advanced failure theories, predicting the corresponding failure mode and the orientation of the fracture plane and the kinking angle. The latter, indeed, depends strongly on the stress state triggering failure initiation.

The next section will introduce failure criteria that are not based on the failure modes, denoted as non-phenomenological failure theories, and failure criteria that distinguish the different failure mechanisms, denoted as phenomenological failure criteria. Most of the former theories for composites have been proposed by extending and adapting isotropic failure criteria to account for the

anisotropy in stiffness and strength of the composite, whereas the latter attempt to represent the different failure modes described above, with specifically developed criteria.

2.3 Intralaminar failure criteria for composite materials

Failure of engineering materials is a phenomenon investigated since the early days of mankind and, after the advent of the industrial age, it has been studied with a modern scientific approach. In order to join all the contributions made until early 2000's, a coordinated study, known as the World-Wide Failure Exercise (WWFE), was organized by Hinton et al. [35, 36]. The aim of the study was to improve the foundation on which failure criteria for composite materials are based and to meet a general need for more reliable criteria. A two-stage approach has been adopted for the exercise. Part A was devoted to providing full details of the theoretical models and failure criteria of the participants. Part B was concerned with comparing the theoretical results with experimental results. Within the Exercise, 19 different failure theories for two-dimensional (2D) stress states were considered and applied to solve 14 challenging problems set by the organizers. Some theories have been shown to give good agreement with experimental results and others to have limited capabilities. Puck, Cuntze, Tsai, Zinoviev and Bogetti failure theories were the best performing in the overall ranking.

However, based on the results of the test cases addressed in the WWFE, a qualitative assessment was made on the confidence of the failure theories to deal with a number of fundamental issues. This assessment, outlined in Ref. [35], highlights the low confidence level of the WWFE theories in predicting the failure modes, leakage events under internal pressure on tubes and multiple non-linearities. Moreover, the first exercise did not provide any clue on the maturity of the failure criteria in two important areas [37]:

1. Prediction of material response under triaxial stress states and
2. Damage/matrix crack development, initiation of delamination and ultimate failure.

For this reason, to have a more complete framework able to assess the status of today's failure theories for FRPs, other two exercises were proposed (WWFE-II and WWFE-III) [37, 38, 39, 40], addressing respectively the first and the second issues enumerated above. The WWFE-II used a set of 12 test cases to investigate the effect of triaxial stress states, while for the WWFE-III 13 test cases have been chosen to address key issues, such as the presence of stress concentrations under in-plane loading conditions.

Although the mentioned studies represented a valuable contribution to the field, they did not succeeded in establishing the most advanced status of failure criteria. In fact, since in the world-wide failure exercises the benchmark was the experimentally-obtained values, it was argued whether the experimental data were reliable enough to be used for comparison [41, 42]. Furthermore, many leading researchers did not participate to the exercises and new failure criteria have been proposed in the meantime [30, 32, 33, 43]. For this reason, to encompass all the reliable

theories predicting the material response until failure of composites, a larger overview is surely required.

In this section, the classification of failure criteria is made by distinguishing non-phenomenological and phenomenological criteria, as common to many reviews of failure theories [44, 45]. The first group includes failure criteria in which a failure envelope is defined by using a mathematical expression, usually a polynomial, that predicts failure by interpolating between a few experimental points. No attempt is made to predict which failure mode is taking place, and the criterion itself does not integrate any physical consideration. Failure theories of the second family frequently provide physical considerations for failure prediction, considering the failure modes in the equation of the criteria.

The application of each failure criterion in both groups to model failure of composite materials is discussed, highlighting the most common and recent models. This section does not aim to review in detail all existing failure criteria. Such an exhaustive study can be found in the literature [46, 44]; therefore, the objective of the section is rather to raise some considerations on the principal theories used, discussing their recent implementations for composite materials by pointing out the validity, advantages, and limitations of each one.

2.3.1 Non-phenomenological failure criteria

The first group of the classification introduced before, presents non-phenomenological failure theories. These criteria include all polynomial and tensorial criteria, using mathematical expressions to describe the failure surface as a function of the material strengths. As mentioned before, these criteria are based on the process of adjusting an expression to a curve obtained by experimental tests.

Most non-phenomenological failure criteria are expressed in the form of polynomials, usually of the second order. For plane stress, they can be expressed as:

$$\mathrm{FI} = F_{11}\sigma_{11}^2 + F_{22}\sigma_{22}^2 + F_{66}\sigma_{12}^2 + 2F_{12}\sigma_{11}\sigma_{22} + F_1\sigma_{11} + F_2\sigma_{22} + F_6\sigma_{12} \tag{2.1}$$

where the coefficients F_{ij} and F_i depend on the specific criterion and the failure initiation point is identified when the failure index FI is equal to 1. In the last equation and for the entire chapter, the index *1* refers to the fibre direction, the index *2* refers to the in-plane transverse direction and the index *3* refers to the through-thickness direction of a generic FRP lamina. Furthermore, X_T, X_C and Y_T, Y_C are the tensile and compressive strengths, in the fibre and transverse directions respectively, while S_L is the in-plane shear strength.

Tsai-Hill failure criterion Hill proposed a failure criterion as an extension of the von Mises criterion for the case of ductile metals with anisotropy. Then, Tsai adapted this criterion by determining the failure strength parameters for unidirectional composite laminae with transverse isotropy. The Tsai-Hill failure criterion is expressed in terms of a single criterion, and it allows for considerable interaction among the stress components. However, no distinction is made between

tensile and compressive strengths, as the equation is applicable for both cases. The strength parameters must be specified according to the signs of the normal stresses. In fact, the coefficients of the polynomial equations are given by:

$$\begin{aligned} F_{11} &= \frac{1}{X^2}, & F_1 &= 0, & F_{12} &= \frac{1}{2X^2}, \\ F_{22} &= \frac{1}{Y^2}, & F_2 &= 0, & & \\ F_{66} &= \frac{1}{(S_L)^2}, & F_6 &= 0, & & \end{aligned} \tag{2.2}$$

with:

$$\begin{aligned} &\sigma_{11} \geq 0 \Rightarrow X = X_T; \quad && \sigma_{11} < 0 \Rightarrow X = X_C; \\ &\sigma_{22} \geq 0 \Rightarrow Y = Y_T; \quad && \sigma_{22} < 0 \Rightarrow Y = Y_C. \end{aligned} \tag{2.3}$$

The Tsai-Hill criterion proved a good correlation with some experimental results and, for instance, failure predictions for the E-glass/epoxy composite material were excellent, outperforming either the maximum stress criterion or the maximum strain failure criterion [47], which will be treated in Chapter 2.3.2. However, its applicability clearly depends on whether the studied material is ductile or brittle, as this theory provides reliable predictions mostly when addressing failure of ductile materials. In fact, brittle materials, such as most advanced composite materials, seem to be better treated with other very simple phenomenological failure criteria, such as the maximum stress criterion or the maximum strain failure criterion [47].

Tsai-Wu failure criterion The most general polynomial failure criterion for composite materials is the Tensor Polynomial criterion proposed by Tsai and Wu. Aiming to overcome the limitations of the previous failure theory in the representation of experimental data, this criterion proposed to increase the number of parameters in the polynomial equation. In addition to a better curve-fitting, the Tsai-Wu criterion has the feature of representing the various strengths in tensor form. Their polynomial equation is defined by using the following coefficients:

$$\begin{aligned} F_{11} &= \frac{1}{X_T X_C}, & F_1 &= \frac{1}{X_T} - \frac{1}{X_C}, \\ F_{22} &= \frac{1}{Y_T Y_C}, & F_2 &= \frac{1}{Y_T} - \frac{1}{Y_C}, \\ F_{66} &= \frac{1}{(S_L)^2}, & F_6 &= 0, \end{aligned} \tag{2.4}$$

and the coefficient F_{12} is given by:

$$F_{12} = \frac{F_{12}^*}{\sqrt{X_T X_C Y_T Y_C}} \tag{2.5}$$

where $-1 < F_{12}^* < 1$ is the interaction term, which can be obtained only with an expensive and difficult-to-perform biaxial test. Because of the difficulty and expense of obtaining a reliable value for F_{12}^*, it was recommended to use a value of -1/2 which leads to safe approximations. It is worth

noticing that, when the normalized interaction term is -1/2, the classical von Mises failure criterion can be recovered if anisotropy is reduced to isotropy and the tensile and compressive strengths are equal. Nevertheless, due to the highly orthotropic strength properties of composite materials, strength predictions are practically insensitive to the value of the interaction term. For this reason, Narayanaswami and Adelman suggested that F_{12} can simply be regarded as zero [48].

Despite the inability to identify failure modes, this criterion has some advantageous features, such as the fact that it is a closed-form, single-valued function. Furthermore, it satisfies the invariant requirements of coordinate transformation, following normal transformation laws, and the strength tensors display similar symmetry properties as the stiffness and compliance terms. Daniel et al. [34] described the computational procedure required for the determination of the lamina strengths using the Tsai-Wu criterion, which includes the determination of the safety factor for a given loading and the computation of the strength components of the lamina referred to any system of coordinates.

Master Ply concept and Omni strain failure envelopes Motivated by the industrial need to reduce the complexity of the failure theories for composites, Tsai and Melo [49] proposed a novel invariant-based approach for the description of the mechanical response of composite laminates. In particular, they pointed out that carbon fibre-reinforced polymers CFRPs share common stiffness properties when normalized by their respective trace of the plane stress stiffness matrix, Tr [Q]. The concept of invariance and trace-based theory were proven useful in the design of laminates, since trace is independent of the loading condition (in-plane versus flexural), stacking sequence (mid-plane symmetric versus asymmetric), and material symmetry (isotropic, orthotropic and anisotropic).

Ten different carbon fibre composites and their trace-normalized stiffness factors were shown to be very close, particularly in the longitudinal direction, parallel to the fibres. The median values of these factors define a Master Ply, which can be used to gain understanding of the laminate behaviour of these composites [49]. Therefore, this Master Ply and trace of the plane stress stiffness matrix becomes the only material properties needed for the elastic characterization. In other words, since the stiffness of CFRPs along the fibre direction is responsible for about 88% of the value of Tr, it is possible to determine the trace of a given material using only the in-plane longitudinal stiffness component, E_1, without the need to measure the transverse and shear moduli: $\mathrm{Tr} = E_1/0.880$. Furthermore, Laminate Plate Theory (LPT) can be employed to generate trace-normalized factors for the stiffness components of multidirectional laminates using the Master Ply. The trace can then be used to estimate the laminate in-plane elastic constants (E_x, E_y, G_{xy} and ν_{xy}), from one elastic lamina property (E_1) and from the Universal Laminate Factors, as described in Ref. [49].

Following this theory, Tsai and Melo proposed also an invariant-based approach for the description of failure initiation of composite laminates [49]. They introduced the omni strain failure envelope, also denoted as minimum FPF envelope, which is the inner failure envelope in strain space, obtained by finding the controlling ply that would fail first for unit loading strain vectors

from 0 to 2π. Since it describes failure of any laminate by covering an infinite number of fibre orientations, it is deemed to be a material property which characterizes failure onset, without requiring information on the laminate layup. Indeed, to get the omni strain FPF envelope for a given material, the only data needed are the ply material properties required to use the employed failure theory and generate a failure envelope. Therefore, in this case, the properties required are: four independent elastic constants for the in-plane stiffness matrix to express the theory in strain space (the Young's moduli in the longitudinal and transverse direction E_1 and E_2, the in-plane shear modulus G_{12}, and the Poisson's ratio ν_{12}) and five strengths (X_C, X_T, Y_C, Y_T, and S_L), which are the properties required to use the Tsai-Wu criterion.

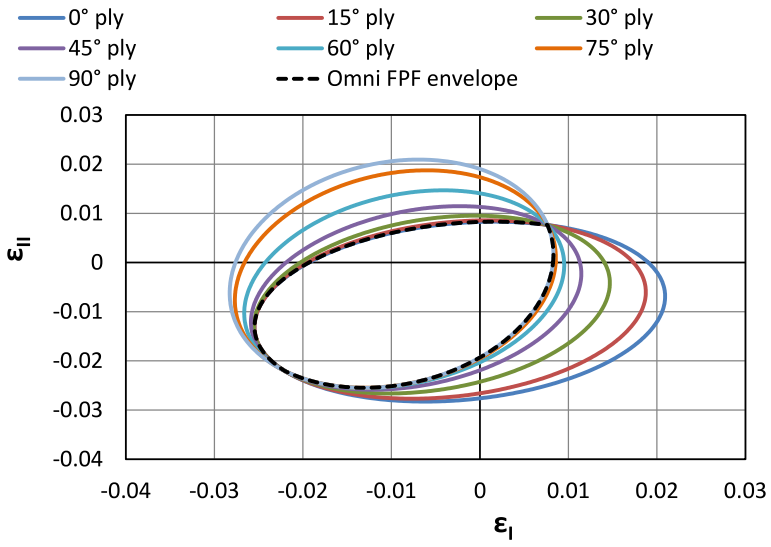
The proposed representation of failure was presented in strain space, since the shape of the envelope remains independent of adding other plies. In strain space, it is possible to superimpose the failure envelopes for the different ply orientations and compute a laminate failure envelope.

Fig. 2.5 shows the omni strain failure envelopes based on the Tsai-Wu failure criterion for two different materials [50]. It can be noted that, with this approach, all laminate data can be displayed on one graph in strain space, realizing a very concise display of the strength of a given composite material. Furthermore, it is a very practical tool, enabling a fast selection of the stacking sequence according to the required mechanical properties, since it covers all the possible ply orientations.

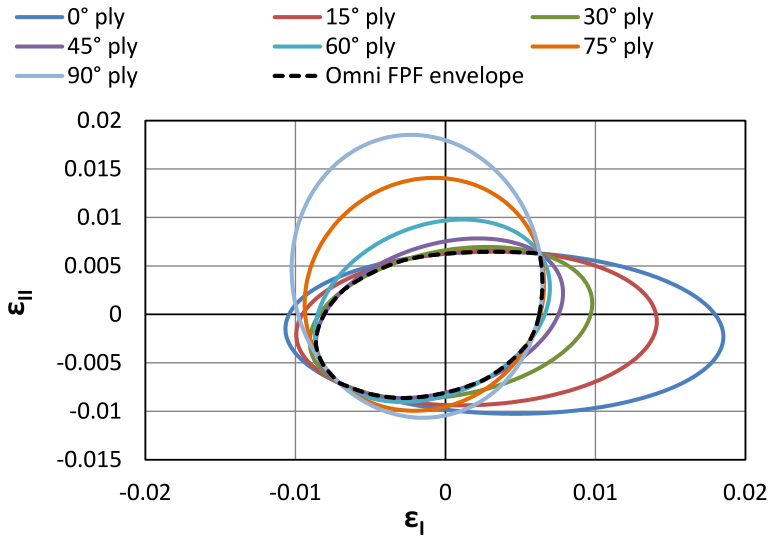
For the implementation of omni strain FPF envelopes, the use of polynomial tensor-based failure criteria is interesting, as there are established transformation relations that enable the reformulation of the criteria from stress space to strain space [50]. These transformation relations are described in Ref. [49], where the Tsai-Wu failure criterion is reformulated in strain space:

$$G_{ij}\varepsilon_i\varepsilon_j + G_i\varepsilon_i = 1 \tag{2.6}$$

where G_{ij} and G_i are the strength parameters in strain space, which can be expressed as a function of the strength parameters in stress space F_{ij} and F_i as follows: $G_{ij} = F_{kl}Q_{ki}Q_{lj}$, $G_j = F_jQ_{ij}$, where Q_{ij} is the in-plane stiffness matrix. However, any failure theory can be applied for the generation of omni (!FPF) envelopes.



(a) T700/C-Ply 55.



(b) IM7/977-3.

Figure 2.5: Omni FPF envelopes in principal strain space for T700/C-Ply 55 (a) and IM7/977-3 (b) laminates, according to the Tsai-Wu failure criterion [50].

The authors verified that the omni strain envelope, based on Tsai-Wu, is safe for all laminates, giving the chance to display all laminate data on a single graph in strain space. Because the failure envelope is independent of the laminate layup (it does not need to be recalculated every time the lay-up changes), it is considered a very promising strategy for the conceptual design and optimization of composite structures.

Since the omni FPF envelopes represent the most conservative design solution, where all the plies are undamaged, Tsai and Melo proposed an extended version of this criterion, to define and predict the continued load-carrying capability of any laminate, after damage initiation. In fact, they have introduced the LPF envelope [51], which is an extension of the concept of omni FPF

envelope to the ultimate failure. The construction of these envelopes follows the same procedure as described before, but with degraded ply properties. However, this part of their work will be addressed in the next section, together with the other strength prediction methods.

Even though the use of non-phenomenological failure criteria give good predictions for some cases, presenting some noticeable features (such as invariance under rotation of coordinates and transformation according to established tensorial relations), they have some limitations when applied to predicting the strength prediction of composite structures. In fact, the knowledge of failure mechanisms is a key requirement for a reliable analysis of non-homogeneous anisotropic materials. The lack of homogeneity plays a key role in strength predictions, since the internal structure of the material governs its failure.

As a final remark, it is worth pointing other issues of polynomial criteria, such as the fact that failure predictions under biaxial tensile stresses depend on the compressive strength. This is questionable from a physical point of view.

2.3.2 Phenomenological failure criteria

For conventional engineering metals, the curve-fitting process works quite well in the generation of failure envelopes. However, for anisotropic materials such as composites, the curve-fitting process is challenged by the different strengths the material exhibits with respect to the loading direction. For this reason, the usage of phenomenological failure criteria in the design phase of laminated composites is more and more common.

In an AIAA Failure Criteria Survey [52] published in 1996, the large majority of the respondents said they utilized one of the four lamina failure criteria shown in Fig. 2.6. Among the phenomenological failure criteria, maximum strain was most commonly used at 30%, with maximum stress next at 22%. Tsai-Hill and Tsai-Wu usage came in at 17% and 12% respectively. From that time, the trend of using phenomenological failure criteria, with a stronger physical basis, has increased in a remarkable way.

The maximum strain and the maximum stress failure criteria are among the simplest failure criteria and they are presented below. Then, an improved accuracy in the failure predictions was obtained by the criteria proposed by Hashin and Puck. More recently, advanced failure theories, such as the ones proposed by Dávila and Camanho [30, 33], are described in detail in the following paragraphs.

Maximum stress failure criterion According to the maximum stress failure criterion, failure occurs when at least one stress component along the principal material axes exceeds the corresponding strength in that direction. This leads to the formulation of five sub-criteria and five failure mechanisms, which can be summarized as follows:

$$\mathrm{FI} = \max\left(\left|\frac{\sigma_{11}}{X}\right|, \left|\frac{\sigma_{22}}{Y}\right|, \left|\frac{\tau_{12}}{S_L}\right|\right), \tag{2.7}$$

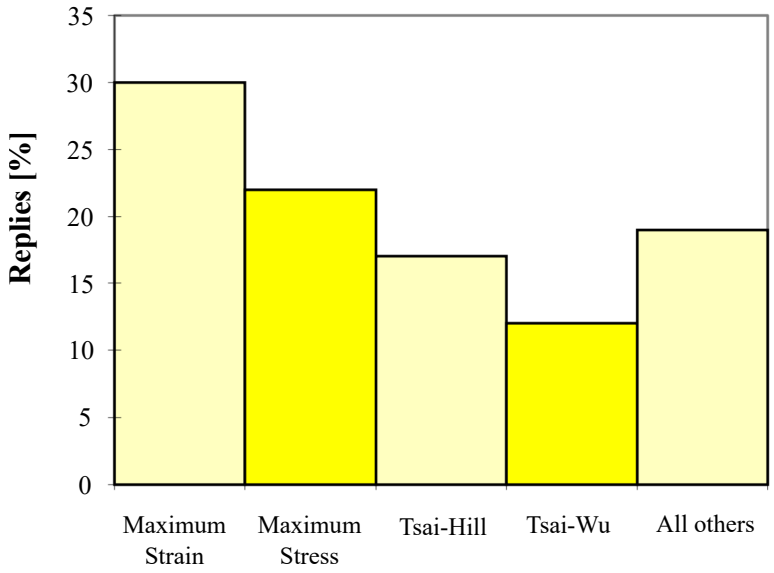


Figure 2.6: Rate of use for failure criteria from study conducted by the U.S. Department of Transportation Federal Aviation Administration study, from Ref. [52].

with:

$$\begin{aligned} &\sigma_{11} \geq 0 \Rightarrow X = X_T\,;\ \sigma_{11} < 0 \Rightarrow X = X_C\,; \\ &\sigma_{22} \geq 0 \Rightarrow Y = Y_T\,;\ \sigma_{22} < 0 \Rightarrow Y = Y_C. \end{aligned} \tag{2.8}$$

The maximum stress criterion is more applicable for the brittle failure modes and does not take into account any interaction under general stress states.

Maximum strain failure criterion The maximum strain failure criterion is quite similar to the maximum stress failure criterion, being a simple and direct way to predict failure of composites. This criterion, in fact, considers that the laminate fails when the strain exceeds the respective allowable. Three different conditions of failure are considered in correspondence with the maximum strain in the fibre or transverse direction and shear strain [53]:

$$\mathrm{FI} = \max\left(\left|\frac{\varepsilon_{11}}{\varepsilon_{11}^{u}}\right|, \left|\frac{\varepsilon_{22}}{\varepsilon_{22}^{u}}\right|, \left|\frac{\gamma_{12}}{\gamma_{12}^{u}}\right|\right), \tag{2.9}$$

with:

$$\begin{aligned} &\varepsilon_{11} \geq 0 \Rightarrow \varepsilon_{11}^{u} = \varepsilon_{11}^{ut}\,;\ \varepsilon_{11} < 0 \Rightarrow \varepsilon_{11}^{u} = \varepsilon_{11}^{uc}\,; \\ &\varepsilon_{22} \geq 0 \Rightarrow \varepsilon_{22}^{u} = \varepsilon_{22}^{ut}\,;\ \varepsilon_{22} < 0 \Rightarrow \varepsilon_{22}^{u} = \varepsilon_{22}^{uc}. \end{aligned} \tag{2.10}$$

The superscript "u" in ε_{11}^{u} and ε_{22}^{u} identifies the ultimate strain in the longitudinal and transverse direction respectively, while γ_{12}^{u} is the ultimate shear strain.

The maximum strain criterion allows for some interaction of stress components due to the Poisson's effect. However, when compared with experimental data, this criterion seems to oversimplify the mechanics of failure, especially under compression and under combined stresses, while giving reliable predictions of fibre failure under longitudinal tension. In fact, more advanced failure criteria, such as LaRC03 and the 3D invariant-based failure theory [30, 33], kept

this criterion to predict fibre tensile failure. Fig. 2.7 shows the failure envelope of the described theory in stress space, compared with the envelopes based on Tsai-Hill and the maximum stress failure criterion.

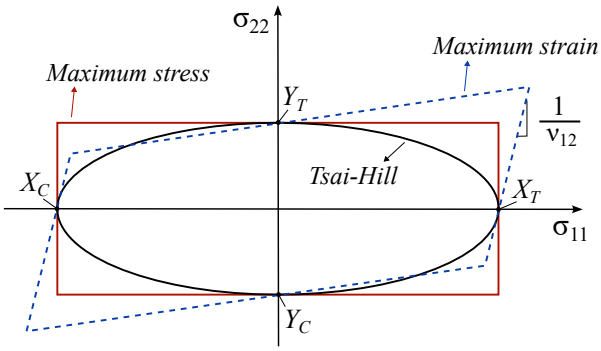


Figure 2.7: Failure envelopes obtained using Maximum stress, maximum strain, and Tsai-Hill failure criteria in σ_{11} - σ_{22} space.

To overcome the limitations of the maximum strain criterion, Hart-Smith developed a failure theory for fibrous composites based on a maximum shear stress criterion with a number of associated cutoff rules [54, 55]. The proposed criteria addresses mainly fibre-dominated failure mechanisms and they are weaker in regard to matrix-dominated failures, as the author has worked mostly with CFRPs [56].

In the WWFE, the failure models proposed by Hart-Smith showed significant weaknesses, especially in predicting failure of glass fibre-reinforced polymers (GFRPs) [56]. Indeed, the failure envelopes for unidirectional laminae were, for some test cases, unconservative (i.e. predicting higher limit values for the onset of material degradation than obtained experimentally).

Hashin failure criteria Hashin and Rotem proposed a criterion which predicts failure initiation under general in-plane loading, distinguishing fibre and matrix failure modes by using two different equations. Fibre failure is predicted as the maximum stress failure theory:

$$\mathrm{FI_F} = \begin{cases} \dfrac{\sigma_{11}}{X_T} & \text{for} \quad \sigma_{11} \geq 0\,, \\ \dfrac{\sigma_{11}}{X_C} & \text{for} \quad \sigma_{11} < 0\,, \end{cases} \tag{2.11}$$

The failure index for matrix failure is formulated using a quadratic equation, as follows:

$$\mathrm{FI_M} = \begin{cases} \left(\dfrac{\sigma_{22}}{Y_T}\right)^2 + \left(\dfrac{\tau_{12}}{S_L}\right)^2 & \text{for} \quad \sigma_{22} \geq 0\,, \\ \left(\dfrac{\sigma_{22}}{Y_C}\right)^2 + \left(\dfrac{\tau_{12}}{S_L}\right)^2 & \text{for} \quad \sigma_{22} < 0\,. \end{cases} \tag{2.12}$$

Few years later, in 1980, Hashin applied some modifications to the Hashin-Rotem theory and proposed a three-dimensional failure criteria in terms of quadratic stress polynomials, expressed

as isotropic invariants [57]. Since the 3D formulation comes from a simple extension of the plane-stress case, obtained by adding additional failure indices for the out-of-plane transverse stress components, hereafter we introduce just the formulation for plane stress states:

$$\mathrm{FI_F} = \begin{cases} \left(\frac{\sigma_{11}}{X_T}\right)^2 + \left(\frac{\tau_{12}}{S_L}\right)^2 & \text{for} \quad \sigma_{11} \geq 0\,, \\ \frac{\sigma_{11}}{X_C} & \text{for} \quad \sigma_{11} < 0\,; \end{cases} \tag{2.13}$$

$$\mathrm{FI_M} = \begin{cases} \left(\frac{\sigma_{22}}{Y_T}\right)^2 + \left(\frac{\tau_{12}}{S_L}\right)^2 & \text{for} \quad \sigma_{22} \geq 0\,, \\ \left(\frac{\sigma_{22}}{2S_T}\right)^2 + \left[\left(\frac{Y_C}{2S_T}\right) - 1\right]\frac{\sigma_{22}}{Y_C} + \left(\frac{\tau_{12}}{S_L}\right)^2 & \text{for} \quad \sigma_{22} < 0\,, \end{cases} \tag{2.14}$$

where S_T is the transverse shear strength.

This set of criteria is surely more interactive, compared to the Hashin-Rotem theory, for tensile failure in the direction of the fibres and for combined transverse compression and shear. However, at that time, Hashin pointed out that there was a general lack of carefully controlled experimental data, so the accuracy of his criterion could not be verified deeply.

Since the Hashin-Rotem criteria have been published, several other failure-mode oriented criteria have been proposed. In particular, Yamada and Sun proposed a criterion for the fibre failure mode which included in-situ effects on the in-plane shear strength [58]. A modified version of this criterion, proposed by Chang et al. [59, 60] has been implemented in LS-Dyna® [61]. Christensen developed a set of criteria for fibre- and matrix-dominated failure modes, which included the effect of hydrostatic pressure [62]. However, the mentioned failure theories showed some weaknesses in the overall description of failure, as highlighted in the WWFE, especially when compared with more advanced failure theories as the one proposed by Puck [36].

Puck failure criteria After being selected as one of the best performing theories in the WWFE [36], the failure criteria proposed by Puck became popular, with several other theories appearing as extensions to these criteria. The most noticeable difference between these criteria and the ones proposed by Hashin is that three modes of matrix cracking are considered, differing in the angle between the fracture plane and the lamina, as well as in the type of load which causes the fracture, as shown in Fig. 2.8.

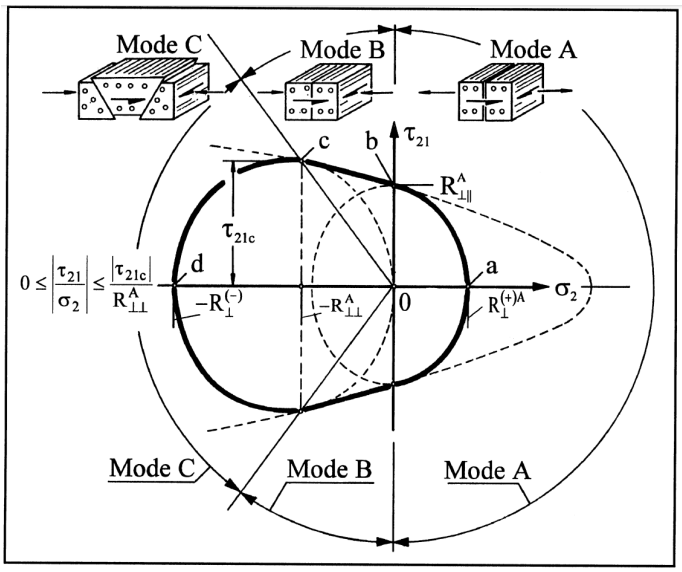


Figure 2.8: Inter-Fibre Fracture modes A, B and C. Reprinted from [17], copyright (1998), with permission from Elsevier.

Puck failure criterion for matrix transverse cracking is based on a modified Mohr-Coulomb theory for brittle transversely isotropic materials. As he mentioned in Ref. [18], the idea of using the failure criteria of Mohr as guidelines was originally formulated by Hashin, who never accomplished his idea (probably due to the limited computational capacities). Indeed, also according to the investigations of Puck and his coauthors, the orientation of the fracture surface of specimens failing by matrix compression suggests that the Mohr-Coulomb criterion is applicable to matrix compression failure [16, 18, 63]. Puck failure theory, besides the stress level which leads to failure, also provides important additional information about the fracture mode and the predicted fracture angle, which brings along a much better assessment of the consequences that transverse (or inter-fibre) failure may have for the laminate.

According to Puck, the failure criteria for fibre failure (FF) are based on a failure hypothesis for fibres instead of one for the UD composites, because the loads are concentrated in the fibres. From this hypothesis, and introducing an empirical shear correction term $(10\gamma_{21})^2$ and a stress magnification factor of the transverse stress on the fibre $m_{\sigma f}$, the FF criterion was formulated as:

$$\mathrm{FI_F} = \begin{cases} \dfrac{1}{\varepsilon_{11}^{ut}}\left(\varepsilon_{11} + \dfrac{\nu_{f12}}{E_{f1}} m_{\sigma f}\,\sigma_{22}\right) & \text{for} \quad \sigma_{11} \geq 0 \\ \dfrac{1}{\varepsilon_{11}^{uc}}\left|\left(\varepsilon_{11} + \dfrac{\nu_{f12}}{E_{f1}} m_{\sigma f}\,\sigma_{22}\right)\right| + (10\,\gamma_{21})^2 & \text{for} \quad \sigma_{11} < 0 \end{cases} \tag{2.15}$$

The formulation of the failure criteria for inter-fibre fracture (IFF) are based on a fundamental hypothesis: fracture of the plane in which the stresses act, causing fracture, is exclusively originated by the stresses which act in this plane. In fact, the traction components acting on the fracture plane, which needs to be determined, are used to assess failure under two fundamental regimes:

transverse tension and transverse compression. The orientation of the fracture plane is determined when the plane of maximum stress effort is found, solving a maximization problem. This is done varying the orientation of the fracture plane, calculating the failure index for every angle, and recording the orientation giving the maximum value of the failure index.

Puck criterion for IFF for each mode reads:

$$\mathrm{FI}_{\mathrm{IFF}} = \begin{cases} \sqrt{\left(\frac{\tau_{21}}{S_L}\right)^2 + \left(1 - p_{\perp\parallel}^{(+)}\frac{Y_T}{S_L}\right)^2 \left(\frac{\sigma_{22}}{Y_T}\right)^2} + p_{\perp\parallel}^{(+)}\frac{\sigma_{22}}{S_L} + \left|\frac{\sigma_{11}}{\sigma_{1D}}\right| & \text{for mode A} \\ \frac{1}{S_L}\left(\sqrt{\tau_{21}^2 + (p_{\perp\parallel}^{(-)}\sigma_{22})^2} + p_{\perp\parallel}^{(-)}\sigma_{22}\right) + \left|\frac{\sigma_{11}}{\sigma_{1D}}\right| & \text{for mode B} \\ \left[\left(\frac{\tau_{21}}{(2(1+p_{\perp\perp}^{(-)})S_L}\right)^2 + \left(\frac{\sigma_{22}}{Y_C}\right)^2\right]\frac{Y_C}{(-\sigma_{22})} + \left|\frac{\sigma_{11}}{\sigma_{1D}}\right| & \text{for mode C} \end{cases} \tag{2.16}$$

where $p_{\perp\parallel}^{(+)}$, $p_{\perp\parallel}^{(-)}$ and $p_{\perp\perp}^{(-)}$ are the inclination parameters, introduced to fit the experimental deduced slope, while σ_{1D} is the longitudinal stress value for linear degradation.

Further details of the Puck criteria can be found in Refs. [17, 18]. The failure envelopes of Puck criteria correlated reasonably well with the test results from the WWFE [36]. However, Puck's semi-empirical approach uses several material parameters that are not physical, such as the curve fitting factors, and may be difficult to quantify without considerable experience with a particular material system.

LaRC failure criteria Dávila, Camanho and Rose at the NASA Langley Research Center (LaRC) proposed new Mohr-Coulomb based phenomenological criteria, known as **LaRC03** failure criteria [30]. Their set of six failure criteria improved the accuracy of the fracture predictions obtained by Hashin or Puck, without curve-fitting parameters. Even though the LaRC failure theory is considered an extension of the Puck criteria, major improvements were included in their formulation, leading to remarkable differences in the failure envelopes. For instance, Fig. 2.9 gives a qualitative idea of these differences, showing the comparison between the failure envelopes in the $\sigma_{11} - \sigma_{22}$ stress space, obtained using Puck and LaRC03 theories for a 0° E-glass/epoxy lamina. The most substantial divergence regards the failure prediction under biaxial compression.

The LaRC03 criteria define the matrix failure index (FI_{M}) distinguishing the expression for matrix failure under compression from the one for matrix failure under tension. The formulation of both criteria relies on *in-situ* strengths, indicating that for general laminates they should be preferred rather than the strength of a unidirectional laminate. Indeed, the authors explained that the constraining effect of adjacent plies (i.e. the in-situ effect) substantially increases the effective strength of a ply and needs to be accounted for. The *in-situ* transverse tensile and longitudinal shear strengths, Y_{is}^T and S_{is}^L respectively, along with the toughness ratio g, for the case of thin and

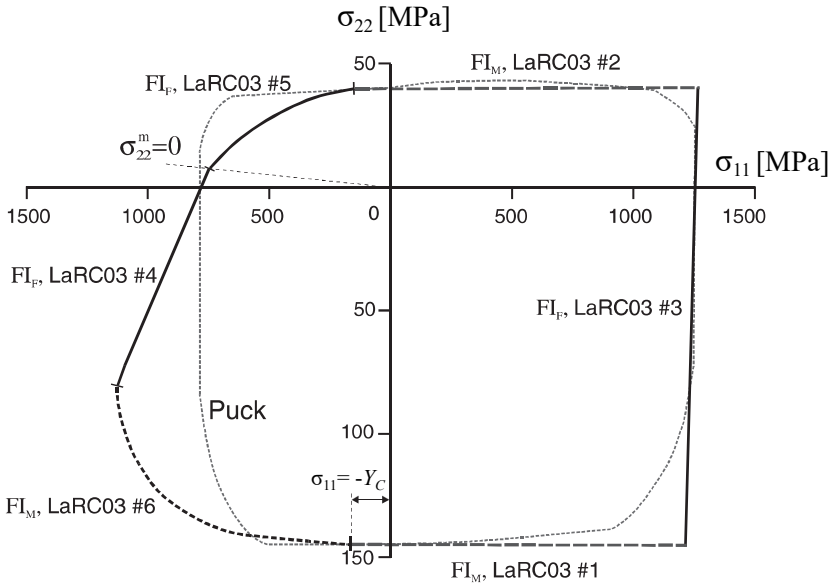


Figure 2.9: Biaxial $\sigma_{11} - \sigma_{22}$ failure envelopes of 0° E-glass/MY750 epoxy lamina (from Ref. [30]).

thick embedded plies, are given as:

$$Y_{\text{is}}^T = \sqrt{\frac{8\mathcal{G}_{\text{Ic}}(L)}{\pi t \Lambda_{22}^0}}, \quad S_{\text{is}}^L = \sqrt{\frac{8\mathcal{G}_{\text{IIc}}(L)}{\pi t \Lambda_{44}^0}}, \quad g = \frac{\mathcal{G}_{\text{Ic}}(L)}{\mathcal{G}_{\text{IIc}}(L)} \qquad \text{for thin plies,} \tag{2.17}$$

$$Y_{\text{is}}^T = 1.12\sqrt{2}Y_T, \quad S_{\text{is}}^L = \sqrt{2}S_L, \qquad g = 1.12^2 \frac{\Lambda_{22}^0}{\Lambda_{44}^0}\left(\frac{Y_T}{S_L}\right)^2 \qquad \text{for thick plies,} \tag{2.18}$$

where: $\Lambda_{22}^0 = 2\left(\frac{1}{E_2} - \frac{\nu_{12}^2}{E_1}\right), \quad \Lambda_{44}^0 = \frac{1}{G_{12}}.$

Therefore, the *in-situ* strengths are expressed as a function of the components of the fracture toughness ($\mathcal{G}_{\text{Ic}}(L)$, $\mathcal{G}_{\text{IIc}}(L)$) in the 1 (longitudinal, L) direction and the parameters Λ_{jj}^0. The details related to the determination of *in-situ* strengths can be found in Ref. [30].

The prediction of matrix failure, according to the LaRC03 criteria, can be now presented in terms of failure indices for matrix tensile and compressive failure as follows:

$$\text{FI}_{\text{M}} = (1-g)\left(\frac{\sigma_{22}}{Y_{\text{is}}^T}\right) + g\left(\frac{\sigma_{22}}{Y_{\text{is}}^T}\right)^2 + \left(\frac{\tau_{12}}{S_{\text{is}}^L}\right)^2 \quad \text{for} \quad \sigma_{22} \geq 0 \tag{2.19}$$

$$\text{FI}_{\text{M}} = \begin{cases} \left(\frac{\tau_{\text{eff}}^{mT}}{S_T}\right)^2 + \left(\frac{\tau_{\text{eff}}^{mL}}{S_{\text{is}}^L}\right)^2 & \text{for} \quad \sigma_{22} < 0, \quad \sigma_{11} < -Y_C \\ \left(\frac{\tau_{\text{eff}}^{T}}{S_T}\right)^2 + \left(\frac{\tau_{\text{eff}}^{L}}{S_{\text{is}}^L}\right)^2 & \text{for} \quad \sigma_{22} < 0, \quad \sigma_{11} \geq -Y_C \end{cases} \tag{2.20}$$

From geometrical considerations on the Mohr-Coulomb criterion and, in particular, on the

Mohr's circle, the effective stress τ_{eff} can be expressed as a function of the in-plane stresses and the angle of the fracture plane α:

$$\begin{cases} \tau_{\text{eff}}^{T} = \left\langle -\sigma_{22}\cos\alpha\left(\sin\alpha - \eta^{T}\cos\alpha\right)\right\rangle \\ \tau_{\text{eff}}^{L} = \left\langle \cos\alpha\left(|\tau_{12}| + \eta^{L}\sigma_{22}\cos\alpha\right)\right\rangle \end{cases} \tag{2.21}$$

where $\langle\cdot\rangle$ is an operand defined as $\langle x\rangle = \frac{1}{2}(x+|x|)$, and the friction parameters η^{T}, η^{L} and the transverse shear strength S_T are given as:

$$\begin{aligned} &\eta^{T} = \frac{-1}{\tan 2\alpha_0} \\ &\eta^{L} \approx -\frac{S_{\text{is}}^{L}\cos 2\alpha_0}{Y_C\cos^2\alpha_0} \quad \text{or from test data} \\ &S_T = Y_C\cos\alpha_0\left(\sin\alpha_0 + \frac{\cos\alpha_0}{\tan 2\alpha_0}\right) \\ &\text{with} \quad \alpha_0 = 53^{\circ} \text{ or from test data} \end{aligned} \tag{2.22}$$

The orientation of the fracture plane (α) is determined when the plane of maximum stress effort is found (i.e., the plane that maximizes the failure index), so in the same way as in Puck criteria.

For the prediction of fibre failure under tension, the simple non-interactive maximum allowable strain criterion is used. This choice comes from the results highlighted by Puck, who reported that using the "effective strain" acting along the fibres instead of the longitudinal stress does not give any significant improvement [18]. Fibre kinking failure is modelled assuming that the collapse of the fibres results from shear kinking and damage of the supporting matrix. The theory of fibre failure under compression requires the formulation of the ply stresses in the misalignment coordinate system m ($\sigma_{11}^{m}, \sigma_{22}^{m}$ and τ_{12}^{m}), assuming a local fibre misalignment, as presented in the equations below the failure criteria:

$$\text{FI}_{\text{F}} = \begin{cases} \dfrac{\varepsilon_{11}}{\varepsilon_{11}^{ut}} & \text{for} \quad \sigma_{11} \geq 0 \\ \left\langle \dfrac{|\tau_{12}^{m}| + \eta^{L}\sigma_{22}^{m}}{S_{\text{is}}^{L}} \right\rangle & \text{for} \quad \sigma_{11} < 0, \quad \sigma_{22}^{m} < 0 \\ (1-g)\left(\dfrac{\sigma_{22}^{m}}{Y_{\text{is}}^{T}}\right) + g\left(\dfrac{\sigma_{22}^{m}}{Y_{\text{is}}^{T}}\right)^{2} + \left(\dfrac{\tau_{12}^{m}}{S_{\text{is}}^{L}}\right)^{2} & \text{for} \quad \sigma_{11} < 0, \quad \sigma_{22}^{m} \geq 0 \end{cases} \tag{2.23}$$

with:

$$\begin{aligned} \sigma_{11}^{m} &= \sigma_{11}\cos^2\varphi + \sigma_{22}\sin^2\varphi + 2\,\tau_{12}\sin\varphi\cos\varphi \\ \sigma_{22}^{m} &= \sigma_{11}\sin^2\varphi + \sigma_{22}\cos^2\varphi - 2\,\tau_{12}\sin\varphi\cos\varphi \\ \tau_{12}^{m} &= -\sigma_{11}\sin\varphi\cos\varphi + \sigma_{22}\sin\varphi\cos\varphi + \tau_{12}\left(\cos^2\varphi - \sin^2\varphi\right) \end{aligned} \tag{2.24}$$

where the total misalignment angle for the general case and for pure longitudinal compression, φ

and φ_c respectively, are calculated as:

$$\varphi = \frac{|\tau_{12}| + (G_{12} - X_C)\,\varphi_c}{G_{12} + \sigma_{11} - \sigma_{22}},\ \varphi_c = \tan^{-1}\left(\frac{1 - \sqrt{1 - 4\left(S_{is}^L/X_C + \eta^L\right)\left(S_{is}^L/X_C\right)}}{2\left(S_{is}^L/X_C + \eta^L\right)}\right) \tag{2.25}$$

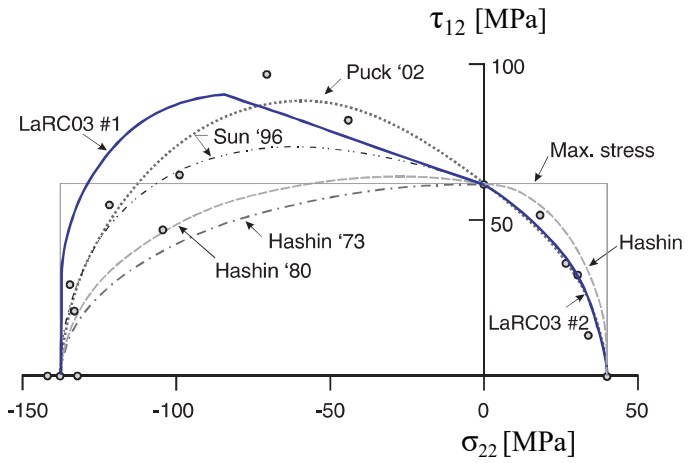


Figure 2.10: Failure envelopes and WWFE test data for UD E-glass/LY556 [30].

A comparison of results from various failure criteria with the experimental results in the $\sigma_{22} - \tau_{12}$ stress plane, obtained from the WWFE [36], is shown in Fig. 2.10. It can be observed that within the positive range of σ_{22}, all the quadratic failure criteria and LaRC03 give satisfactory results. Puck's envelope seems to be the most accurate, but it relies on fitting parameters based on the particular test case, so in general it would need more experimental data for each test case.

The most recent contribution to the field from LaRC, however, is represented by the **LaRC04** failure criteria [43]. These failure theories are based on physical models for each failure mode and take into consideration non-linear matrix shear behaviour, without using empirical factors. The proposed set of criteria are an extension of the LaRC03 plane stress criteria, to account for general three-dimensional (3D) loading and for in-plane shear non-linearity. The idea behind the LaRC04 criteria is to address also the design and analysis of thick composite laminates, where more consistent failure predictions should rely on 3D stress states. For more details, the interested reader can consult Ref. [43].

The formulation of the failure index under matrix tension, proposed by the authors, includes linear and quadratic terms in σ_{22}, a quadratic term in τ_{23}, the *in-situ* strengths and a term on the in-plane shear internal energy $\chi(\gamma_{12})$, defined as:

$$\chi(\gamma_{12}) = 2\int_0^{\gamma_{12}} \tau_{12} d\gamma_{12} \tag{2.26}$$

For the evaluation of the *in-situ* strengths, a fracture mechanics analysis for the propagation of cracks in a constrained ply was performed. Fibre tensile failure is predicted using a non-interacting maximum allowable stress criterion. For fibre kinking, only matrix failure (as well as some form

of instability) is assumed to trigger the failure. This consideration is believed to be accurate for carbon fibre-reinforced composites. In Fig. 2.11, the new 3D kinking model is shown, highlighting the angle of the kinking plane ψ, which has a value between 0 and 180°. Figs. 2.11a and 2.11b show a unidirectional lamina under compressive stress, with a detailed view on the stresses acting on the (2-3) plane, while Figs. 2.11c and 2.11d show the angle of the kink plane, identifying the stress components acting on that plane. The local stresses in the (2-3) plane are found as a function of ψ, using the transformation equations.

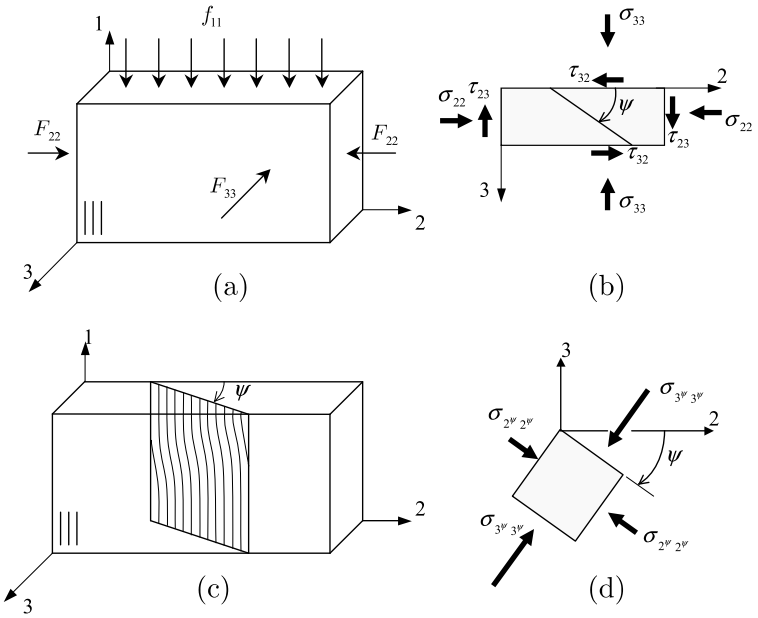


Figure 2.11: 3D kinking model from LaRC failure criteria [43].

The LaRC04 criteria are summarized in equations (2.27)-(2.28), which can be used knowing the following ply material properties: E_1, E_2, G_{12}, ν_{12}, X_T, X_C, Y_T, Y_C, S_L, $\mathcal{G}_{\text{Ic}}$ and $\mathcal{G}_{\text{IIc}}$.

$$\text{FI}_\text{F} = \begin{cases} \dfrac{\sigma_{11}}{X_T} & \text{for} \quad \sigma_{11} \geq 0 \\ \left(\dfrac{\tau_{1^m2^m}}{S_{\text{is}}^L - \eta^L \sigma_{2^m2^m}}\right)^2 & \text{for} \quad \sigma_{11} < 0, \quad \sigma_{2^m2^m} < 0 \\ (1-g)\dfrac{\sigma_{2^m2^m}}{Y_{\text{is}}^T} + g\left(\dfrac{\sigma_{2^m2^m}}{Y_{\text{is}}^T}\right)^2 + \dfrac{\Lambda_{23}^o \tau_{2^m3^\psi}^2 + \chi\left(\gamma_{1^m2^m}\right)}{\chi\left(\gamma_{12\text{is}}^u\right)} & \text{for} \quad \sigma_{11} < 0, \quad \sigma_{2^m2^m} \geq 0 \end{cases} \tag{2.27}$$

$$\mathrm{FI_M} = \begin{cases} (1-g)\dfrac{\sigma_{22}}{Y_{\mathrm{is}}^T} + g\left(\dfrac{\sigma_{22}}{Y_{\mathrm{is}}^T}\right)^2 + \dfrac{\Lambda_{23}^o \tau_{2m3\psi}^2 + \chi(\gamma_{12})}{\chi(\gamma_{12\mathrm{is}}^u)} & \text{for} \quad \sigma_{22} \geq 0 \\ \left(\dfrac{\tau^{tm}}{S_T - \eta^t \sigma_n^m}\right)^2 + \left(\dfrac{\tau^{Lm}}{S_{\mathrm{is}}^L - \eta^L \sigma_n^m}\right)^2 & \text{for} \quad \sigma_{22} < 0, \quad \sigma_{11} < -Y_C \\ \left(\dfrac{\tau^t}{S_T - \eta^t \sigma_n}\right)^2 + \left(\dfrac{\tau^L}{S_{\mathrm{is}}^L - \eta^L \sigma_n}\right)^2 & \text{for} \quad \sigma_{22} < 0, \quad \sigma_{11} \geq -Y_C \end{cases} \tag{2.28}$$

The *in-situ* strengths and the toughness ratio included in the criteria are defined in the same way as in equations (2.17)-(2.18). The ultimate in-plane shear strain, for thin and thick embedded plies respectively, is defined as:

$$\gamma_{12\mathrm{is}}^u = \chi^{-1}\left(\frac{8\mathscr{G}_{IIc}(L)}{\pi t}\right), \quad \gamma_{12\mathrm{is}}^u = \chi^{-1}\left[2\chi(\gamma_{12}^u)\right], \tag{2.29}$$

For the determination of the initial misalignment angle φ^0, the misalignment angle for pure compression φ_c and the shear strain at failure for a pure axial compression case $\gamma_{1^m2^m}^c$, a two-steps solution is required, since kinking can be promoted by instability or matrix failure. The presentation of this analytical procedure is out of the scope of this work and it can be found in Ref. [43].

The failure envelopes in stress space shown in Fig. 2.12 indicate that the predicted strengths using the LaRC04 criteria correlate well with the experimental results from Swanson et al. [64]. A good correlation is also achieved with the Puck failure criteria, but the latter requires curve fitting factors. As a consequence, LaRC04 was selected for the development of the damage models in Refs. [65, 66].

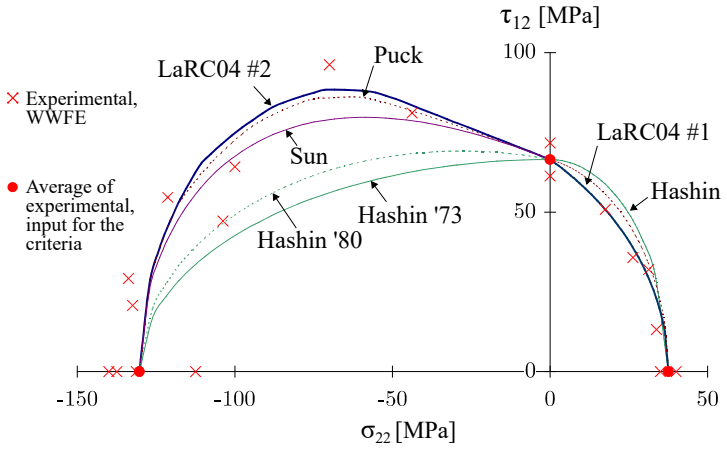


Figure 2.12: Failure envelopes and test data for an AS4/55A composite, from Ref. [43].

Another version of this set of failure criteria, designated as **LaRC05**, was developed and took part of WWFE-II [67]. The formulation of this failure theory is essentially an extension of LaRC04, including a deep study of the non-linear response of constitutive response of FRP composite and the prediction of *in-situ* material strengths. When compared with the experimental

data from the WWFE-II, the failure model was able to capture the influence of hydrostatic pressure on compressive fibre failure and relevant physical mechanisms. More details can be found in Ref. [67].

However, Catalanotti et al. [32] proved that the quadratic interaction criterion for the prediction of transverse tensile failure from LaRC04/05 has fundamental weaknesses in the formulation, leading to a wrong computation of the fracture plane. An additional drawback of LaRC04/05 was pointed out: the strength results are very sensitive to the misalignment angle φ^0 (that represents the manufacture defects and imperfections in the materials). To overcome this limitation, an alternative procedure for the determination of the total misalignment angle φ has been proposed by Catalanotti et al. [32]. In addition, the set of criteria proposed by Catalanotti et al. [32] solved other problems with previous 3D implementations of the LaRC criteria, including inconsistency in the failure envelopes when using *in-situ* strengths.

3D invariant-based failure criteria Among the most recent failure criteria proposed for FRPs, a set of advanced phenomenological failure theories, denoted as 3D invariant-based failure criteria [33, 68], was introduced. These new criteria are based on the transversely isotropic yield function developed by Vogler et al. [69]. The new 3D failure criteria have an invariant quadratic formulation based on structural tensors that accounts for the preferred directions of the anisotropic material. With this formulation, anisotropy is derived using structural tensors and not symmetry conditions based on a reference coordinate system. Furthermore, since the formulations do not depend on coordinate-system transformations, the search for the fracture plane is not necessary. These advantageous features enable a simpler and elegant description of failure of laminated composites.

The invariant-based failure criterion for transverse failure of unidirectional composites is given as:

$$\mathrm{FI_M} = \begin{cases} \alpha_1 I_1 + \alpha_2 I_2 + \alpha_3^t I_3 + \alpha_{32}^t I_3^2 & \text{for} \quad I_3 > 0 \\ \alpha_1 I_1 + \alpha_2 I_2 + \alpha_3^c I_3 + \alpha_{32}^c I_3^2 & \text{for} \quad I_3 \leq 0 \end{cases} \tag{2.30}$$

where the stress invariants (I_1, I_2, I_3) for matrix failure are defined as:

$$I_1 = \frac{1}{4}\sigma_{22}^2 - \frac{1}{2}\sigma_{22}\sigma_{33} + \frac{1}{4}\sigma_{33}^2 + \sigma_{23}^2, \qquad I_2 = \sigma_{12}^2 + \sigma_{13}^2, \qquad I_3 = \sigma_{22} + \sigma_{33} \tag{2.31}$$

and the failure parameters α are given by:

$$\alpha_1 = \frac{1}{(S_T)^2}, \quad \alpha_2 = \frac{1}{(S_L)^2}, \quad \alpha_{32}^t = \frac{1 - \dfrac{Y_T}{2Y_{BT}} - \alpha_1 \dfrac{Y_T^2}{4}}{Y_T^2 - 2Y_{BT}Y_T}, \quad \alpha_3^t = \frac{1}{2Y_{BT}} - 2\alpha_{32}^t Y_{BT},$$

$$\alpha_{32}^c = \frac{1 - \dfrac{Y_C}{2Y_{BC}} - \alpha_1 \dfrac{Y_C^2}{4}}{Y_C^2 - 2Y_{BC}Y_C}, \quad \alpha_3^c = \frac{1}{2Y_{BC}} - 2\alpha_{32}^c Y_{BC}. \tag{2.32}$$

S_T and S_L are respectively the transverse and in-plane shear strengths, Y_C and Y_{BC} are respectively the transverse uniaxial and biaxial compressive strengths, and Y_T and Y_{BT} are respectively the transverse uniaxial and biaxial tensile strengths. Through the sign of the third invariant I_3, this criterion is able to address failure under biaxial stress states.

Fibre failure under tension is predicted using the non-interactive maximum allowable strain criterion, following the LaRC03 criteria [30]. Since the failure mechanism under longitudinal compression of CFRPs involves mainly the formation of a kink band, resulting from micro-buckled fibres and local matrix cracking, Camanho et al. [68] proposed a 3D kinking model by recalling the invariant-based failure criterion for the transverse case, but in a misalignment frame. In fact, by determining the angle of the kinking plane ψ and the kinking angle φ, it is possible to formulate the invariant-based failure criterion for kinking failure prediction in the misalignment frame.

Fig. 2.13 shows the kinking plane and the 3 coordinate systems: the initial coordinate system ($1^0 2^0 3^0$), associated with the material axes of the composite, the coordinate system related with the kinking plane ($1^\psi 2^\psi 3^\psi$) and the coordinate system related with the misaligned fibres ($1^\varphi 2^\varphi 3^\varphi$).

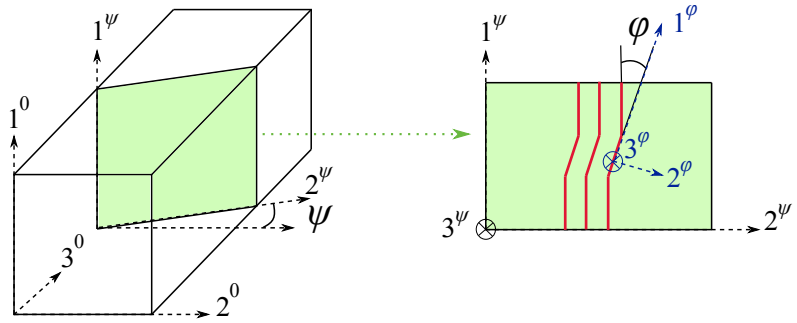


Figure 2.13: 3D kinking model with the definition of the kinking angle φ and the angle of the kinking plane ψ [50].

The invariant-based failure criterion for fibre kinking is formulated in the latter coordinate system. In a compact form, the failure criteria for fibre failure can be presented in the following way:

$$\begin{cases} \text{FI}_\text{F} = \dfrac{\varepsilon_1}{\varepsilon_1^{ut}} & \text{for} \quad \sigma_{11} \geq 0 \\ \text{FI}_K = \alpha_1 I_1 + \alpha_2 I_2 + \alpha_3^t I_3 + \alpha_{32}^t I_3^2 \leq 1 & \text{for} \quad \sigma_{11} < 0 \quad \text{and} \quad I_3 > 0 \\ \text{FI}_K = \alpha_1 I_1 + \alpha_2 I_2 + \alpha_3^c I_3 + \alpha_{32}^c I_3^2 \leq 1 & \text{for} \quad \sigma_{11} < 0 \quad \text{and} \quad I_3 \leq 0 \end{cases} \tag{2.33}$$

To formulate the stress tensors, the definition of the preferred direction $\mathbf{a}$, corresponding to the fibre direction for a unidirectional laminate, is required. This direction is obtained by performing two transformations of coordinate system to get to the initial $(1^0 2^0 3^0)$ system:

$$\mathbf{a}^{(0)} = \begin{bmatrix} \cos\varphi \\ \cos\psi \sin\varphi \\ \sin\psi \sin\varphi \end{bmatrix} \tag{2.34}$$

The structural tensor $\mathbf{A}$ that represents the transversely isotropic properties of the material is defined as:

$$\mathbf{A} = \mathbf{a} \otimes \mathbf{a} \tag{2.35}$$

The stress invariants needed for the coordinate system-free formulation of the invariant-based criteria can be now formulated as a function of the preferred direction $\mathbf{a}$, the structural tensor $\mathbf{A}$, and the stress tensor $\boldsymbol{\sigma}$ based on its crack inducing components $\boldsymbol{\sigma}^p$ and the reaction components $\boldsymbol{\sigma}^r$:

$$I_1 = \frac{1}{2}\text{tr}\,(\boldsymbol{\sigma}^p)^2 - \mathbf{a}\,(\boldsymbol{\sigma}^p)^2\,\mathbf{a}, \qquad I_2 = \mathbf{a}\,(\boldsymbol{\sigma}^p)^2\,\mathbf{a}, \qquad I_3 = \text{tr}\,\boldsymbol{\sigma} - \mathbf{a}\boldsymbol{\sigma}\mathbf{a} \tag{2.36}$$

with:

$$\boldsymbol{\sigma}^r = \frac{1}{2}(\text{tr}\,\boldsymbol{\sigma} - \mathbf{a}\boldsymbol{\sigma}\mathbf{a})\mathbf{1} - \frac{1}{2}(\text{tr}\,\boldsymbol{\sigma} - 3\mathbf{a}\boldsymbol{\sigma}\mathbf{a})\mathbf{A}, \qquad \boldsymbol{\sigma}^p = \boldsymbol{\sigma} - \boldsymbol{\sigma}^r \tag{2.37}$$

To complete the definition of the analytical framework needed to predict the failure initiation for fibre kinking, the only missing parameters are the angles, defining the misalignment frame of the kink band. For the definition of the angle of the kinking plane ψ, a pragmatic approach is used, based on the work available in the literature [32, 43]. This angle is formulated as a function of the shear stresses (if the latter are not zero):

$$\psi = \arctan\left(\frac{\sigma_{13}}{\sigma_{12}}\right) \tag{2.38}$$

Otherwise the angle of the kinking plane is calculated as:

$$\psi = \frac{1}{2}\arctan\left(\frac{2\sigma_{23}}{\sigma_{22} - \sigma_{33}}\right) \tag{2.39}$$

The kinking angle φ is defined as a sum of two components: a constant initial misalignment angle φ^0 and an angle resulting from the applied shear loading φ^R. The methodology to find both contributions is described in detail in Ref. [33]. Although this approach gives reliable results, an alternative method to determine the kinking angle φ was proposed in Refs. [33, 70], based on the observations from Catalanotti et al. [32]. As suggested by the authors of the formulation in Ref. [32], there may be physical inconsistencies when using an initial nonzero misalignment angle. Therefore, the kinking angle φ can be found assuming the initial misalignment angle to be zero and representing the imperfections that trigger fibre kinking by a micro-mechanical parameter χ. In particular, imposing the stress equilibrium in the frame of a kink band, the kinking angle φ is expressed as a function of the sign of the shear applied in the frame of the kinking plane and the angle γ_R resulting from the applied shear loading:

$$\varphi = \operatorname{sgn}\left\{\sigma_{12}^{(\psi)}\right\}\gamma_R \tag{2.40}$$

Assuming linear shear behaviour, the shear constitutive law can be expressed as follows [32]:

$$\sigma_{12}^{(\varphi)} = \chi\,\gamma_R \tag{2.41}$$

where $\sigma_{12}^{(\varphi)}$ is the applied shear in the misalignment frame and the micro-mechanical parameter χ can be obtained assuming failure by pure longitudinal compression [32]:

$$\chi = -\frac{\sin(2\varphi_c)\,X_C}{2\,\varphi_c} \tag{2.42}$$

where φ_c is the kinking angle under pure longitudinal compression and X_C is the longitudinal compressive strength.

For a generic loading scenario, γ_R is calculated using Eq. 2.41 and then, the kinking angle φ is obtained from Eq. 2.40. However, a suitable numerical method should be employed. Catalanotti et al. [32] proposed to use the Newton-Raphson method, expressing Eq. 2.41 as:

$$F = \chi\,\gamma_R + \frac{1}{2}(\sigma_{11}-\sigma_{22})\sin(2\,\gamma_R) - |\sigma_{12}|\cos(2\,\gamma_R) \tag{2.43}$$

and its derivative with respect to γ_R gives [32]:

$$\frac{\mathrm{d}F}{\mathrm{d}\gamma_R} = \chi + (\sigma_{11}-\sigma_{22})\cos(2\,\gamma_R) + 2|\sigma_{12}|\sin(2\,\gamma_R) \tag{2.44}$$

Finally the angle γ_R can be approximated using the following formula [32]:

$$\gamma_{Ri+1} = \gamma_{Ri} - \frac{F\big|_{\gamma_R=\gamma_{Ri}}}{\left.\frac{\mathrm{d}F}{\mathrm{d}\gamma_R}\right|_{\gamma_R=\gamma_{Ri}}} \tag{2.45}$$

The determination of the kinking angle φ_c is made by reformulating the invariant-based failure criteria for a pure longitudinal compressive stress state, starting from the stress invariants [33, 68]:

$$I_1 = \frac{1}{4}\sigma_{11}^2 \sin^4\varphi, \qquad I_2 = \sigma_{11}^2 \sin^2\varphi\cos^2\varphi, \qquad I_3 = \sigma_{11}\sin^2\varphi \tag{2.46}$$

So the invariant-based failure criterion can be now rewritten for the pure longitudinal compression case, as follows [33, 68]:

$$\begin{aligned} \mathrm{FI}_K = {} & \frac{1}{16}\alpha_1\,\sigma_{11}^2\left(1-2\cos 2\varphi+\cos^2 2\varphi\right)+\frac{1}{4}\alpha_2\,\sigma_{11}^2\left(1-\cos^2 2\varphi\right)+ \\ & +\frac{1}{2}\alpha_3^c\,\sigma_{11}(1-\cos 2\varphi)+\frac{1}{4}\alpha_{32}^c\,\sigma_{11}^2\left(1-2\cos 2\varphi+\cos^2 2\varphi\right) \end{aligned} \tag{2.47}$$

At failure this function is equal to 1, $\sigma_{11} = X_C$ and the resulting kinking angle $\varphi = \varphi_c$ is given by [33, 68]:

$$\begin{aligned} \varphi_c = \frac{1}{2}\arccos\Big\{ & \Big[4\sqrt{\alpha_1-4\alpha_2+\alpha_2^2X_C^2+\left(\alpha_3^c\right)^2+2\alpha_2\alpha_3^cX_C+4\alpha_{32}^c}+ \\ & +\left(\alpha_1+4\alpha_{32}^c\right)X_C+4\alpha_3^c\Big]\cdot\left[\left(\alpha_1-4\alpha_2+4\alpha_{32}^c\right)X_C\right]^{-1}\Big\} \end{aligned} \tag{2.48}$$

It is important to emphasize that this set of invariant-based failure criteria is completely formulated in a 3D setting, unlike other phenomenological failure criteria that were initially formulated in a 2D setting and then extended to the 3D case. Further details, such as the pragmatic approach for the determination of the fracture plane and the definition of the *in situ* properties, can be found in Ref. [33].

Several validation studies of these criteria were performed, comparing the predictions with experimental data obtained for different material systems under various scenarios of multiaxial loading. The validation tests performed by Camanho et al. [33, 68] include experimental results from open literature (such as the first WWFE, where only biaxial tests are discussed) and additional data obtained using computational micro-mechanics to complement the available database, without requiring very expensive test setups.

These validation studies have shown that this set of criteria is capable of predicting the evolution of the shear stress with hydrostatic pressure, which no previous failure criteria have been able to achieve. Furthermore, a good agreement between the failure envelopes predicted by computational micro-mechanics and the 3D invariant-based failure criteria was reported. While Hashin's criteria show an open failure envelope for the biaxial transverse compression quadrant, thus making it unsuitable for representing the fracture of composites subjected to high hydrostatic stresses, the 3D invariant-based failure criteria accurately represented the failure envelopes under both tension-tension and compression-compression biaxial stress states [33, 68].

A more recent work from Li et al. [71] has highlighted that the need for material strengths under biaxial tension and compression reduces the applicability of the 3D invariant-based failure theory from Camanho. Indeed, biaxial data is rarely available and experimental measurement is

still restricted to unsatisfying accomplishment of biaxial testing. Despite Camanho has alternatively suggested to use off-axial test data to overcome the inaccessibly of biaxial experiments, the accuracy of this alternative approach suffers from the underestimation of transverse strengths caused by the longitudinal stress (σ_{11}) [71].

In order to overcome above-mentioned drawbacks, Li et al. [71] proposed improved failure criteria for matrix failure by formulating the invariant-based theory as a function of uniaxial strengths and, therefore, eliminating the need of biaxial strength parameters. Transverse shear strength and biaxial tensile strengths (S_T, Y_{BT}) are obtained from Mohr's fracture hypothesis, while biaxial compressive strength (Y_{BC}) is formulated using the theory of ductile/brittle transition. The proposed approach based on the assumption of ductile behaviour under equi-biaxial transverse compression allows to predict a finite strength, eliminating the irrational prediction of infinite strength under equi-biaxial transverse compression.

Finally, the predictions are validated based on computational micromechanics, showing that more reasonable and more accurate predictions under various stress conditions can be achieved by the developed stress invariant-based criteria [71].

2.4 Failure models to predict delamination

Delamination is one of the most common types of damage in laminated fibre-reinforced composites, which takes place between two layers of dissimilar orientation within the laminate, due to high interlaminar stresses acting on the interface between upper and lower layers defining the interface. It can be originated by different factors, such as design features prone to develop interlaminar stresses (curved sections, drop-offs, free edges, etc.), manufacturing defects (interlaminar inclusions, resin-rich areas, etc.) or accidental circumstances (low velocity tool impacts, etc.) [72]. Following the onset of damage, delamination growth occurs usually when compression and out-of-plane loads (static or fatigue) are applied to the structure.

While, on one hand, for intralaminar damage, very advanced phenomenological failure criteria have been proposed, allowing the identification of failure onset under the most complex stress states with great accuracy [30, 32, 33, 43], on the other hand, the proposed failure criteria to capture the onset of delamination have an easier formulation. The first failure theory, i.e. average interlaminar normal stress failure criterion, was proposed in 1974 by Whitney and Nuismer [73] and implemented by Kim and Soni [74] to investigate a CFRP laminate under in-plane tensile and compressive loading. When interlaminar shear stress are not negligible, stress-based criteria such as the Ye's delamination criterion or the quadratic interaction criterion proposed by Brewer and Lagace, are normally used [75, 76, 77, 78]. The formulation of the Ye's criterion is given as:

$$\begin{cases} \left(\frac{\sigma_{33}}{Y_T}\right)^2 + \left(\frac{\sigma_{13}}{S_L}\right)^2 + \left(\frac{\sigma_{23}}{S_L}\right)^2 \leq 1 & \text{for} \quad \sigma_{33} > 0\,, \\ \left(\frac{\sigma_{13}}{S_L}\right)^2 + \left(\frac{\sigma_{23}}{S_L}\right)^2 \leq 1 & \text{for} \quad \sigma_{33} \leq 0\,, \end{cases} \tag{2.49}$$

where Y_T is the transverse tensile strength, S_L is the in-plane shear strength, σ_{23} and σ_{13} are the out-of-plane shear stresses and σ_{33} is the out-of-plane normal stress.

Even though more recent failure theories account for the enhancement effect of through-thickness compression on mode II shear [79, 80], these improvements are considered relevant just for those cases where there is a relatively high stress level acting on a large area, such as overlap joints and short beam shear tests. For this reason, only simple quadratic stress criteria are commonly used and embedded in more general computational frameworks. For instance, stress-based criteria can be used to perform "hot-spot" identification, as a qualitative measure to predict the location where the onset of delamination is likely to occur. However, to investigate delamination growth, other approaches have been developed and gained a more relevant position. Among the methods for capturing the onset and growth of delamination, the Finite Element Analysis (FEA) is a method used extensively, by means of two techniques: the Virtual Crack Closure Technique (VCCT) and the Cohesive Zone Mode (CZM) approach.

The VCCT was proposed for the first time by Rybicki et al. [81], as a modified version of the Irwin's crack closure integral. This technique calculates the mixed-mode energy-release rates based on the computed forces and displacements obtained from FEA and it is based on the assumption that the energy released during delamination propagation equals the work required to close the crack back to its original position. Then, delamination growth is captured by comparing a combination of the components of the energy release rate to a critical value. Although the VCCT has been considered one of the most accurate methods to predict delamination, it has important limitations, such as the need to include a crack or delamination in the model as a discrete discontinuity [82, 83, 84].

The concept of CZM was introduced for the first time by Dugdale in 1960 [85], and revised by Barrenblatt few years later [86]. Their theory was then implemented by Hillerborg for the first time, in a pioneering work for the several subsequent implementations. Indeed, cohesive finite elements have been widely implemented for several applications, mainly because they offer the advantage of predicting both onset and propagation of delamination without the need of a pre-existing initial crack and without previous knowledge of the crack propagation direction. On the other hand, the simulation of progressive delamination using cohesive elements is challenging due to numerical difficulties related to the proper definition of the stiffness of the cohesive layer, the requirement of refined meshes, and the convergence problem when dealing with material softening responses [87, 88, 89, 90, 91].

In the following section, the constitutive response of cohesive elements based on a traction-separation law is presented in detail. The idea of this section is to give more details to the reader

on an advanced method to predict the onset and propagation of interlaminar damage, as well as presenting the approach that has been implemented in this thesis for several case studies.

2.4.1 Constitutive response of cohesive elements

The implementation of cohesive elements requires the definition of failure criterion for the onset of delamination and softening law to model propagation of interlaminar damage. State-of-art approaches on this topic achieve a good confidence level, predicting accurately the propagation of delamination under mixed-mode fracture. Robust numerical models are also able to account for frictional effects, which plays an important role in the propagation phase [91, 92, 93]. However, the research work of this thesis does not focus on modelling interlaminar damage and frictional effects are neglected in most of the cases.

For the present work, the constitutive response of the cohesive elements is defined using a traction-separation law, which relates cohesive surface tractions, τ, to displacement jumps, Δ. A typical traction-separation response is shown in Fig. 2.14, where K is the slope of the first linear regime representing the interface stiffness, $\mathcal{G}_c$ is the fracture toughness, i.e. the area under the traction displacement jump relation, and τ^0 is the interfacial strength. In the present thesis, the FE solver used to simulate the mechanical behaviour of composite materials is Abaqus® and finite-thickness COH3D8 cohesive elements were selected to model delamination. The available traction-separation model in Abaqus® assumes initially linear elastic behaviour followed by the initiation and evolution of damage [94].

The criterion to predict the onset of delamination is the quadratic nominal stress criterion (Abaqus®' Quads Damage), which is given as:

$$\left(\frac{\langle \tau_3 \rangle}{\tau_3^0}\right)^2 + \left(\frac{\tau_1}{\tau_1^0}\right)^2 + \left(\frac{\tau_2}{\tau_2^0}\right)^2 = 1 \tag{2.50}$$

where the Macaulay bracket, $\langle\ \rangle$, is used to specify that the compressive stress does not contribute to damage initiation, while τ_3 is the traction stress acting in the normal through-thickness direction, τ_1 and τ_2 are the shear stresses and τ_1^0, τ_2^0, τ_3^0 are the corresponding strengths.

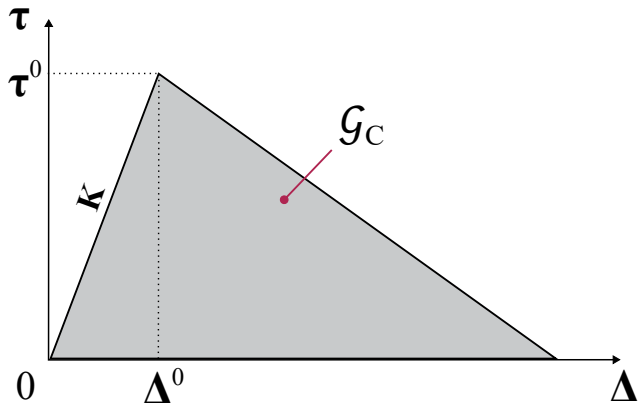


Figure 2.14: Linear traction separation response of cohesive elements.

Once delamination has initiated, it is controlled by a propagation criterion based on the fracture energy (or critical energy release rate), which is specified as a material property. As shown in Fig. 2.14, the material response is supposed to degrade according to a linear softening law and the total crack opening takes place when the fracture toughness is completely dissipated. The variation of fracture toughness as a function of mode ratio in epoxy composites is calculated using the Benzeggagh and Kenane (BK) criterion extended to the 3D case [95]. The BK fracture criterion is particularly useful when the critical fracture energies during deformation along the first and the second shear directions are the same, and it is given as:

$$\mathscr{G}_{\mathrm{Ic}} + (\mathscr{G}_{\mathrm{IIc}} - \mathscr{G}_{\mathrm{Ic}}) \left(\frac{\mathscr{G}_{\mathrm{II}} + \mathscr{G}_{\mathrm{III}}}{\mathscr{G}_{\mathrm{I}} + \mathscr{G}_{\mathrm{II}} + \mathscr{G}_{\mathrm{III}}} \right)^{\eta} = \mathscr{G}_{\mathrm{c}} \tag{2.51}$$

where η is an experimentally derived parameter, $\mathscr{G}_{\mathrm{Ic}}$ and $\mathscr{G}_{\mathrm{IIc}}$ are the mode I and II fracture toughness and $\mathscr{G}_{\mathrm{I}}$, $\mathscr{G}_{\mathrm{II}}$ and $\mathscr{G}_{\mathrm{III}}$ are the energy release rates corresponding to the fracture modes I, II and III and their sum is the total energy release rate.

For linear softening, Abaqus® uses an evolution of the damage variable, D_k, that enables to track the state of an interface element (from 0, the undamaged state, to 1, fully damaged), which was proposed by Camanho and Dávila [96], namely:

$$D_k = \frac{\Delta^{\mathrm{f}} \left(\Delta - \Delta^0 \right)}{\Delta \left(\Delta^{\mathrm{f}} - \Delta^0 \right)} \tag{2.52}$$

where Δ is the maximum relative displacement at a given increment, Δ^{f} is the displacement at failure and Δ^0 is the displacement at the onset of delamination.

To use this method properly, a minimum number of elements within the cohesive zone is required. A quantitative study on this topic can be found in Ref. [90], where a procedure to use coarser FE meshes is described, identifying a minimum of 3 elements within the length of the cohesive zone to predict delamination growth without losing accuracy in the results. However, this procedure should be used with care, since the results are very sensitive to the interface parameters. Another possibility offered by implicit FE solvers is to use a viscous regularization parameter, which can aid numerical analyses to achieve convergence. On the other hand, this parameter can affect the global material response, so a preliminary sensitivity study is required for assessing its reliability.

2.5 Strength prediction methods for composite laminates

The failure criteria described in Chapter 2.3 deal with lamina failure. To predict laminate strength, the progressive accumulation of damage leading to final failure needs to be taken into account. Clearly, this is a difficult task, since additional damage mechanisms, such as delamination, and complex interactions between intralaminar and interlaminar damage mechanisms may occur in a laminate. However, the effects of delamination are usually treated separately from intralaminar damage mechanisms as explained in the previous section.

Experimental evidence has shown that failure in a laminated composite is very often progressive in nature, occurring by a process of damage accumulation [97]. Therefore, the progressive loss of lamina stiffness must be taken into account as a function of the type of predicted damage. The typical procedure to predict the strength of a laminate, when intralaminar damage mechanisms are dominant, follows this list:

1. Lamina strain and stress analysis.
2. Lamina failure criteria.
3. Damage evolution models (as a function of type of failure predicted at lamina level).
4. Laminate failure criterion.

The damage evolution (point 3) is usually performed using a reduction of ply elastic properties, typically reducing E_1 for fibre failures and both E_2 and G_{12} for matrix cracking [72, 98]. This degradation may be sudden or progressive. For transverse matrix cracking, the progressive degradation of elastic properties has a good physical basis, since it represents the progressive accumulation of transverse cracks until the crack density saturation is achieved. The reduction of the transverse elastic properties can also be a function of the stress state. This consideration is also reasonable, since a matrix crack under compressive stresses can still carry some load.

A number of approaches have been proposed to determine ultimate laminate failure (point 4). A common strategy is to assume ultimate laminate failure when fibre fracture occurs in any lamina. This strategy is inadequate when stress concentrations are present, like in access holes and bolted joints, since localized fibre fracture, actually relieving stress concentrations, occur without laminate failure. Furthermore, in laminates where the main failure mechanism involves the matrix, such as $[\pm 45]$s laminates, failure may occur without fibre fracture. However, the described procedure is just a common example to give an idea of the required steps for the general failure prediction of a laminate at the meso-scale level, but other approaches have been recently considered.

The progress in computational power has allowed the research community to perform deeper studies, considering a level of accuracy that was not possible before. Exploiting these technological advancements, reliable numerical models representing the different types of damage mechanisms, with the respective damage evolution laws, have been developed at different mechanical scales. In fact, the ability of damage models to predict physical phenomena such as the initiation and propagation of damage strongly depends on the scale (or resolution) at which the damage mechanisms under consideration are modelled. Aiming to the smallest scale of composites idealization, the only choice would be a numerical modelling at micro-mechanics scale. This would allow to treat the constituent materials as homogeneous, considering separately fibres and matrix. However, the available models at this scale have a low degree of maturity and, at the same time, are computationally demanding [99, 100, 101, 102, 103, 104, 105, 106, 107]. Approaches at the micro-scale, therefore, are still considered not suitable to model damage evolution up to final collapse of composite laminates.

So far, the meso-mechanics scale proved to be a successful trade-off, able to accurately represent quasi-brittle behaviour of laminated composite structures within a reasonable computational cost. At this scale, plies are the building blocks of the model. Models at the meso-mechanical scale are typically divided into two different approaches, the Continuum Damage Mechanics (CDM) approach and the Discrete Damage Mechanics (DDM) approach. The framework of continuum damage mechanics, introduced for the first time by Kachanov [108] for the description of creep in metals, is a widespread approach for the description of the inelastic response of materials with damage. In general, the formulation of the CDM model starts by the definition of a potential (the complementary free energy density) as a function of damage variables associated to the different failure modes. It is also necessary to define the damage activation functions, i.e., the conditions that lead to the onset of inelastic response, and the damage evolution functions. A complete definition of a CDM model for the simulation of intralaminar damage can be found, for instance, in Refs. [65, 66]. The CDM model simulates localized intralaminar damage using strain softening constitutive models. To avoid mesh dependent solutions, the energy dissipated is regularized for each damage mechanism using a modification of the crack band model. Additionally, a maximum allowable element size is defined to avoid physically unacceptable snap-backs of the material response [66].

However, continuum approaches alone cannot realistically simulate the response of the laminates that are dominated by delamination and splitting mechanisms, which are discrete in nature and are sensitive to the local stress fields and boundary conditions. A more effective computational approach in such cases would have to include a concurrent combination of smeared and discrete models to capture the interaction between the material and structural (or local and global) behaviour. For this reason, DDM can be a suitable approach to progressive failure modelling when matrix cracks and delamination are explicitly introduced into the model via displacement discontinuities, which they create [109]. Alternatively, embedded discontinuity models, such as the extended finite element method (X-FEM), are used to insert cracks (and delamination) in locations that are independent of the mesh orientation and without the need of re-meshing [110].

To predict of the ultimate strength of composite structures, it is necessary to have an accurate numerical representation of all damage modes and their interactions. Some of the most complex damage models available rely on CDM to represent the intralaminar damage modes (e.g., transverse matrix cracking and fibre failure) and use cohesive zone models to capture delamination between ply interfaces. However, despite advances in progressive damage modelling, recent studies indicate that CDM models coupled with cohesive zone models may not always represent laminate failure sequences properly [111].

The multiscale nature of damage and failure in composite structures has been the motivation for recently proposed multiscale models. In multiscale modelling, macroscopic and microscopic models are coupled to take advantage of the efficiency of macroscopic models and the flexibility of the microscopic models [112]. The scope of such multiscale modelling is to design combined macroscopic-microscopic computational methods that are more efficient than solving the full microscopic model and at the same time give the information needed to the desired flexibility.

Multiscale models can be categorized into two groups: *hierarchical* and *concurrent*. In hierarchical models, homogenization is employed to transfer the predicted behaviour of the material from a lower scale (e.g., micromechanical Representative Volume Element (RVE)) to a higher scale. Models based on this approach have been implemented in commercial FE packages. In concurrent multiscale models, on the other hand, instead of applying homogenization to bridge the scales, both scales are concurrently present in the model. In undamaged areas, a macro-model with effective homogenized behaviour is employed, while in damaged areas, the model resolution is increased and meso/micro features are explicitly accounted for [109].

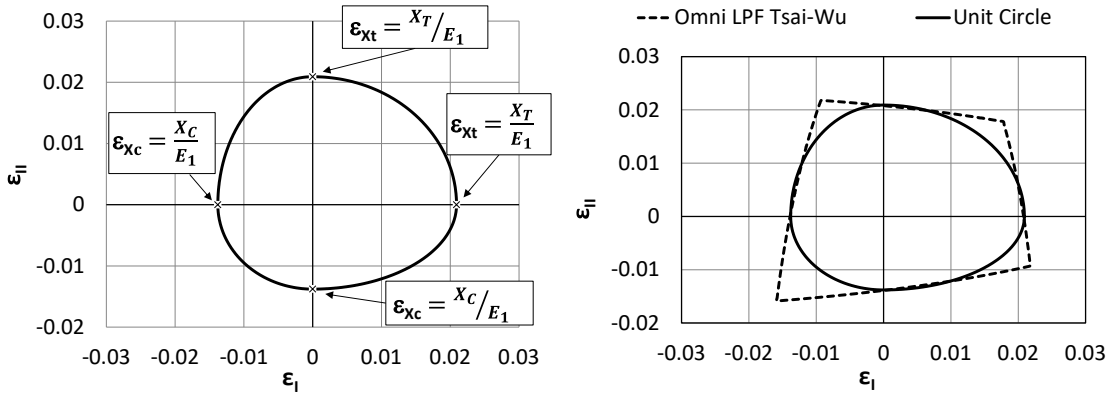
Despite significant progress, a number of outstanding challenges have so far limited the impact of this approach on the composites industry and the state of the practice. First is the issue of computational complexity: multiscale modelling requires performing (coupled or uncoupled) simulations at multiple time and length scales. Significant computational resources are typically needed to predict the response using multiscale approaches. Second, multiscale models require calibration of model parameters that operate at multiple time and length scales [109].

Recently, few global-local FEM approaches have been proposed to predict the global ply failure and local skin-stiffener debonding of reinforced panels, while reducing the computational time [113, 114, 115]. In particular, these methods proved to be reliable and efficient tools to study localized nonlinearities, such as onset and evolution of damage, minimizing the computational effort. For instance, a two-way coupling global-local approach, described by Akterskaia et al. [115], enabled to address delamination phenomena through a local analysis based on cohesive elements and to ensure that the energy dissipated due to delamination evolution at the local level was captured at the global level, with special attention to the exchange of information between the global and local models. The validation of this method established a reliable procedure of dissipated energy calculation for the global model due to delamination based on the dissipated energy in the local model [115]. However, so far, only delamination is modelled with higher resolution, while ply damage has not been properly incorporated in these global-local frameworks.

On the other hand, to meet the industrial need for fast and practical tools at an early design stage, simplified and reliable approaches for the prediction of last-ply failure of any CFRPs have been developed. With this aim, Tsai and Melo [51] proposed an extended version of the omni strain criterion, as described in Chapter 2.3.1, to predict the continued load-carrying capability of any laminate after damage initiation. While the omni strain FPF envelopes are obtained using intact ply properties, omni strain LPF envelopes are defined using degraded ply properties, based on a matrix degradation factor (E_m^*) and micro-mechanics relations. Moreover, the authors observed that, for all CFRP laminates, the inner LPF envelope is controlled by the 0° and 90° plies loaded in the fibre direction. Because the analysis is conducted for LPF conditions, it is assumed that the matrix is already degraded, and, therefore, ultimate failure is governed by fibre-dominated longitudinal failure.

Following these observations, a further simplification of the failure analysis was performed introducing the unit circle failure envelopes for CFRPs, which can be easily represented by defining the “anchor points” as shown in Fig. 2.15a. Comparing the omni strain LPF envelope and the

unit circle failure envelope of the same material, as shown in Fig. 2.15b, the unit circle envelope is inscribed in the omni LPF envelope. Although the failure predictions related with this criteria are intentionally conservative, this theory is extremely useful. In particular, the great advantage of using the unit circle failure envelope is that it only requires the strains-to-failure of a 0° coupon measured in tension and in compression, instead of complete characterization of the ply properties required by the omni strain LPF envelope [50, 51].



(a) Anchor points.

(b) Unit circle and omni LPF envelope.

Figure 2.15: (a) Definition of anchor points for a unit circle failure envelope in principal strain space; (b) unit circle (solid line) and omni strain LPF (dashed line) envelopes for T700/C-Ply 55 carbon/epoxy [50].

2.6 Summary of the *state-of-art* review

To address failure phenomena and strength of a lamina, it is helpful to understand the underlying failure mechanisms and processes within and between the constituents of the composite and their effect on the ultimate macroscopic behavior. The failure mechanisms on a micromechanical scale vary with the type of loading and are intimately related to the properties of the constituents, that is, fiber, matrix, and interface. Experimental evidence was presented to describe common failure events, such as: fibre breakage and pull-out under tensile loading, the generation of a kink band under compression, matrix cracking and failure in the fibre-matrix interface under transverse loading and/or in-plane shear.

Several theories had been proposed in the literature to predict the onset of failure in composite materials, but only some give good agreement with experimental results under general stress states.

Non-phenomenological failure criteria are generally based on closed form solutions, which are operationally simple and readily amenable to computational procedures. However, they do not allow the identification of failure modes. In fact, their aim is not to improve the accuracy as compared to existing failure theories or the ability to capture the detailed physics associated with the various failure mechanisms, but rather to improve the simplicity, as measured by the number

of tests required to define the failure envelope. For this reason, they are considered very robust tools, giving reliable and fast indications for the conceptual design of composite materials.

Phenomenological failure criteria provide not only the predictions for the onset of ply damage, but also additional information regarding the type of failure. Recently, advanced phenomenological failure criteria have been proposed, allowing the identification of failure under the most complex stress states with great accuracy while taking into account the different failure modes. Furthermore, they have been implemented as damage initiation functions in advanced computational models that predict the inelastic and fracture behaviour of composites. However, this accuracy in the failure initiation process, provided by advanced failure criteria, is paid by a more extensive material characterization.

Delamination is a very common failure mode in composite structures. It takes place between plies, usually with different orientation, due to high interlaminar stresses. The onset of this type of failure can be predicted using interlaminar failure criteria, such as the Ye's criterion or simple quadratic stress criteria. However, for detailed and accurate analyses, advanced approaches are usually employed, such as the Virtual Crack Closure Technique (VCCT) and the Cohesive Zone Model (CZM) approach. The first allows the accurate prediction of interlaminar damage but it requires to include a crack or delamination in the model as a discrete discontinuity. For this reason, usually the implementation of cohesive elements is preferred.

As a concluding remark, it must be highlighted the beneficial contribution of failure theories to different stages of the design of composite structures. In fact, failure criteria have a key role not only as initiation functions for damage models that predict the inelastic response of composite materials, but also for "hot-spot" identification and for conceptual and preliminary design. For this reason, the choice of the most appropriate failure criteria can have a strong impact on the performance of the components, their structural function and their design efficiency and time to market.

Finally, the challenges related to the prediction of laminate failure were presented. When addressing final collapse of composite laminates, the accumulation of damage events needs to be taken into account for most of the cases. Indeed, except for unidirectional laminates, composite structures are able to carry more load after damage initiation. *State-of-art* damage models for composite material were briefly introduced, ranging from the ones representing failure at the smallest scale of idealization (i.e., micro-scale), considering matrix and fibres separately, to the approaches that treat laminates as homogenous materials, at the macro-scale. The successful trade-off was achieved by models at the meso-scale, where plies are the building blocks of the model. Alternative approaches, such as global-local and multiscale models, were also introduced, given their recent significant progress.

2.7 Identification of gaps in the *state-of-art* and goals of the work

State-of-art approaches related to ply failure initiation have achieved a high degree of accuracy, being able to represent several relevant aspects of the failure process of laminated composites,

e.g., the increase on apparent shear strength when applying moderate values of transverse compression, or the detrimental effect of the in-plane shear stresses in failure by fibre kinking. The most advanced set of phenomenological failure criteria account for the effect of ply thickness, fibre misalignment in compression, the effect of hydrostatic stresses and the effect of shear nonlinearity on fibre kinking and in-situ strength, as described in this Chapter.

Despite these recent developments, some challenges requiring additional research can be identified, including (i) the development of models across different length and time scales, which are required for the effective design and optimization of aircraft structures, and (ii) the study of the effect of triaxiality in fibre-dominated failure modes, which is relevant, e.g., for fastened connections in aircraft structures. For this reason, this research work will address the mentioned issues, while assessing the impact of the implemented advanced models to the overall design process, in order to find the most appropriate trade-off solution. Therefore, exploiting the recent findings on advanced failure criteria from the literature review, the first objective of this research work is to develop a tool for failure prediction in a FE context, by implementing a set of phenomenological three-dimensional failure criteria, based on invariants, for aerospace applications. The idea of this work is to assess the accuracy of the obtained predictions when compared with available experimental data.

Then, in addition to advanced failure criteria implementation in an FE context, these criteria will be used to establish new laminate strength analysis models based on the concept of omni envelopes to allow more efficient laminate optimization while reducing complexity and size of the experimental programs required at the preliminary design stage.

Indeed, an additional challenge of this thesis is to develop a laminate strength analysis method suitable for optimization frameworks. Strength constraints for MDO are required to outline safe failure envelopes for different loading conditions that do not compromise the efficiency of the optimization process. Another desirable aspect regarding failure criteria for MDO is their formulation in strain space, mainly because they can benefit from invariant laminate failure predictions with respect to ply orientations, simplifying the design of composite laminates. In fact, the failure envelope for a given ply angle is fixed in strain space independently of the orientation of the other plies in the laminate, unlike ply failure envelopes in stress space. Failure envelopes in strain space, therefore, enable an invariant description of failure with respect to the ply orientation, which is essential for a continuous optimization with lamination parameters [116, 117], and to quickly compare against the maximum allowables obtained experimentally.

Furthermore, for detailed analysis on the accumulation of damage in composite laminates, efficient tools have been developed to perform geometrical nonlinear analyses combined with material nonlinearities like delamination and ply damage, minimizing the computational time. A novel FE approach, based on a global-local framework, and its integration in the MDO platforms is of great interest for the aerospace industry. However, so far, only delamination has been properly addressed into these global-local frameworks, as discussed in Section 2.5.

Therefore, to propose the integration of ply damage into an efficient global-local FE approach, a meso-scale composite material model will be extended in order to account for general 3D stress

states. In particular, the effect of out-of-plane stress components must be accounted in the initiation and broadening of fibre kinking, which allows to study triaxiality in fibre-dominated failure modes. The validation of such advanced material model would be highly beneficial for detailed analysis of composite structures. However, additional considerations regarding the computational cost of its application are required.

Part II

Extended failure criteria for composite materials

Chapter 3

Extended omni-strain envelopes for laminate failure predictions

This chapter deals with the development of a laminate failure theory for composite materials, suitable for industrial optimization frameworks. The proposed laminate failure theory will be based on the concept of omni-strain failure envelopes, firstly introduced in Ref. [49] and presented in the previous chapter. The motivation for this novel contribution is to extend the omni-strain LPF theory to allow safe failure predictions under general 3D stress states. The objective of this section is to give an overview on the developed theory and to present the validation studies, assessing the obtained results.

3.1 Description of the failure criterion

3.1.1 Considerations on the 3D invariant-based failure theory

Reviewing the *state-of-art* failure criteria for composite materials, it can be observed that, after almost sixty-years of efforts, the desirable aspects of a failure theory have been identified and they can be summarized in: (i) the ability to generate failure envelopes close to experimental data for different material systems and loading conditions, (ii) consistency in physics and mathematics, meaning that the criteria should, for instance, not allow open envelopes (i.e. infinite strength) and (iii) a stress invariant-based formulation to avoid the inclusion of additional parameters (e.g. the inclination parameters from Puck theory).

For the reasons above, the 3D invariant-based failure criteria from Refs. [33, 68] were selected for the development of a laminate failure theory suitable for optimization purposes. This set of failure criteria is outlined in detail in Section 2.3.2.

Before presenting the novel contribution on the invariant based approach to laminate failure, few remarks and considerations on the 3D invariant-based failure criteria are made for a full assessment of the foundation of new developments.

Firstly, regarding the computation of the kinking angle φ, two methods were proposed with the presentation of the fibre kinking failure model [33]. Both define the kinking angle as a sum of

two components: a constant initial misalignment angle φ^0 and an angle resulting from the applied shear loading φ^R. The difference between the two approaches lies in the assumption of linear or non-linear shear response [33, 68].

However, the assumption of a constant initial misalignment angle to compute the kinking angle φ leads to physical incompatibilities. As pointed out in Refs.[32, 70, 118], the application of a nonzero transverse compression (σ_{22} or σ_{33}) results in a variation in the axial compressive strength, which has no supporting evidence. For instance, Fig. 3.1 illustrates the failure envelopes of UD S-glass/epoxy [36] in the σ_{11} - σ_{22} stress space, for different values of applied through-thickness compression σ_{33}. Fig. 3.1a shows the "non-physical" variation in axial compressive strength (X_C) when fibre kinking is computed assuming a nonzero initial misalignment angle φ^0 and a linear shear response. For this reason, the alternative approach, firstly introduced in Ref. [32], is preferred because it calculates φ imposing the stress equilibrium in the frame of a kink band using a micro-mechanical parameter χ, instead of a nonzero initial misalignment angle.

As presented in Section 2.3.2, Catalanotti et al. [32] proposed the implementation of the Newton-Raphson method as a numerical approach to approximate the value of φ. However, considering that the kinking angle φ is calculated using a linear combination between a trigonometric and a linear function (Eq. 2.43), the proposed algorithm does not always converge. For this reason, in this work, the bisection method was implemented, exploiting the known bounds of the solution.

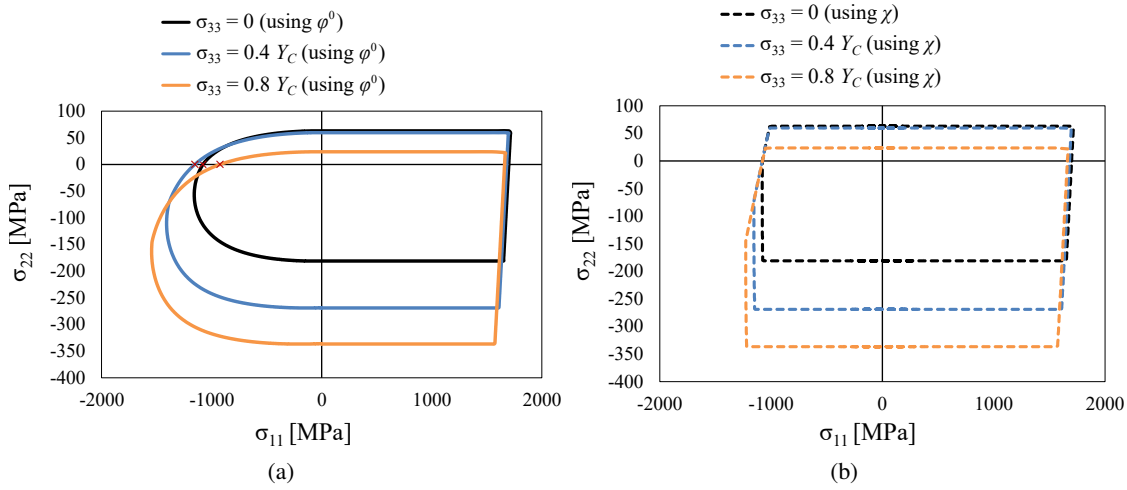


Figure 3.1: σ_{11} - σ_{22} failure envelopes of S-glass/epoxy with different value of out-of-plane compression (σ_{33}), ranging from zero to 0.8 Y_C. In (a), fibre kinking is predicted by computing the kinking angle φ with a nonzero initial misalignment angle φ^0, while in (b) an alternative micro-mechanical parameter χ is employed.

Following these minor modifications, the failure envelopes obtained with the 3D invariant-based failure criteria can be presented and compared with failure predictions from the original envelopes (outlined in Ref. [68]). For this aim, the material used in the original manuscript (UD IM7/8552) is considered, and thus all the material properties can be found in Ref. [68]. In order to calculate the failure loci of each failure envelope, the bisection method was numerically

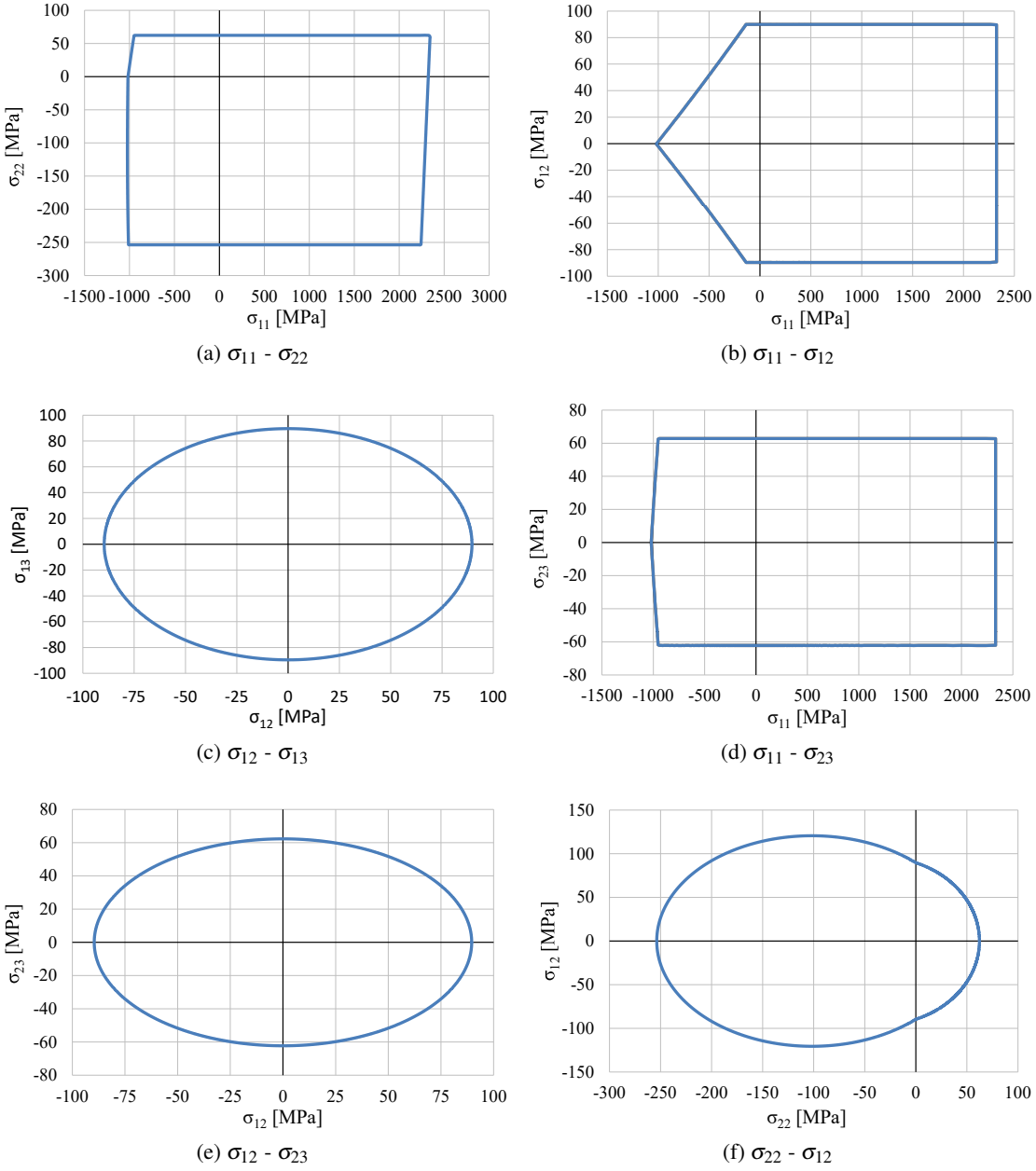
implemented and additional details on the implementation are included in Appendix A. Fig. 3.2 shows the predicted envelopes in stress space, for several stress states. It can be observed that, for complex stress states, the invariant-based theory still generates closed envelopes. Furthermore, the envelopes in strain space are provided in Fig. 3.3, considering pairs of nonzero strain components and general 3D stress states.

To enrich the verification of the invariant-based theory, the obtained ε_{11} - ε_{22} failure envelope for a single UD ply has been compared with the failure envelope for the same material, but under plane stress conditions, as shown in Fig. 3.4. The failure envelope under 3D stress states predicts correctly fibre failure under longitudinal tension as the one for plane stress. In addition, the increase of strength under applied biaxial compressive strain is well captured, with a larger envelope area, due to the beneficial effect of negative values of σ_{33} as explained in Ref. [33]. Furthermore, the reduction of strength under pure longitudinal applied tensile strain is justified by a consequential 3D stress state, composed by $\sigma_{11} > 0$ and $\sigma_{22} = \sigma_{33} > 0$. A totally similar justification can be given for the reduction of strength applying pure transverse tensile strain.

To further challenge the 3D invariant-based theory in the prediction of failure under triaxial stress states, experimental results from the WWFE-II [119] are considered here. Figs. 3.5-3.8 show the correlation of the predicted envelopes against experimental results from the WWFE-II for UD S-glass/epoxy, carbon/epoxy, E-glass/MY750 and T300/PR319 respectively. The predictions of the 3D invariant-based theory are also compared with those obtained using the popular Tsai-Wu and Hashin failure surfaces for the same test cases [50].

The mechanical properties of the tested materials are found in Ref. [119]; however, since biaxial strengths are not provided, they have been assumed after assessing their effect on the predicted envelopes. Furthermore, the transverse shear strength S_T is assumed equal to the transverse tensile strength Y_T, following the observations from Refs. [17, 120]. The influence of Y_{BC} on the strength predictions of the invariant-based theory was investigated for each case and it is included in the respective figures. With the same scope, the effect of the interaction term F_{12}^* from the Tsai-Wu theory was studied and it is also shown. All the test cases highlight that the 3D invariant-based theory offers a remarkable flexibility in fitting complex results with Y_{BC}, while the interaction term from Tsai-Wu cannot always help the correlation with experimental data. Indeed, except for the third case (Fig. 3.7) where the strength predictions are very sensitive to the value of the interaction term, a nonzero F_{12}^* results in open envelopes for the first 2 cases (Figs. 3.5-3.6) and in almost coincident predictions in the last case (Fig. 3.8) [50].

On the other hand, the implementation of Hashin criteria results in open envelopes when addressing triaxial test cases, such as the ones in σ_{11} - σ_{22}=σ_{33} in Figs. 3.5- 3.6. Indeed, when applying biaxial transverse compression and the value of longitudinal stress does not exceed the allowables in tension or compression (i.e. $X_C < \sigma_{11} < X_T$), an infinite strength is predicted, which is obviously an unacceptable result from the physical point of view. Then, the failure predictions for the other two cases (UD E-glass/MY750 in σ_{22} - σ_{22}=σ_{33} stress space in Fig. 3.7 and UD T300/PR319 under shear stress and hydrostatic pressure in Fig. 3.8), the correlation with the available experimental data is excellent.

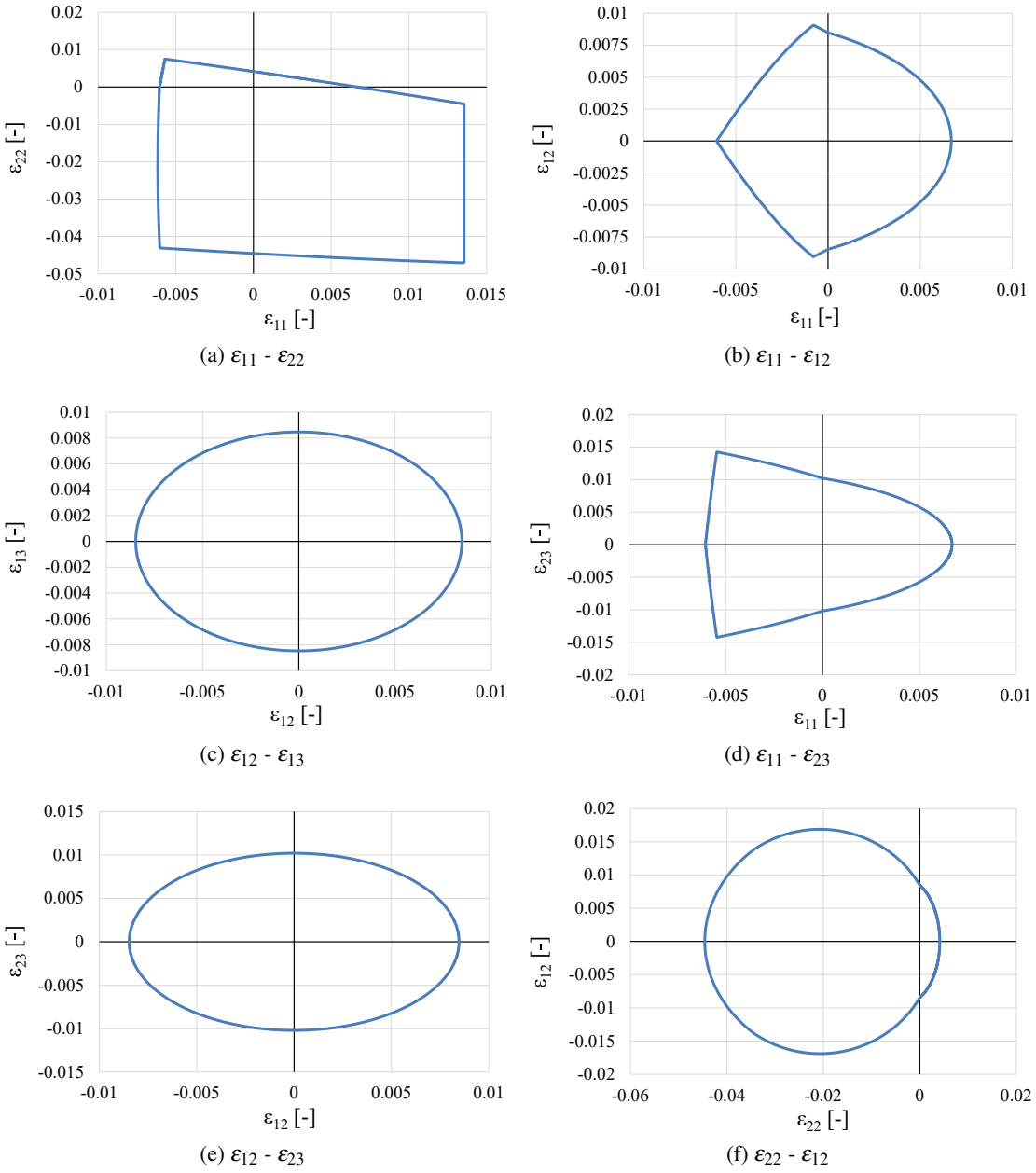


(a) σ_{11} - σ_{22} (b) σ_{11} - σ_{12}

(c) σ_{12} - σ_{13} (d) σ_{11} - σ_{23}

(e) σ_{12} - σ_{23} (f) σ_{22} - σ_{12}

Figure 3.2: Failure envelopes in stress space of UD IM7/8552, obtained with the 3D invariant-based failure criteria.



(a) ε_{11} - ε_{22} (b) ε_{11} - ε_{12}

(c) ε_{12} - ε_{13} (d) ε_{11} - ε_{23}

(e) ε_{12} - ε_{23} (f) ε_{22} - ε_{12}

Figure 3.3: Failure envelopes in strain space of UD IM7/8552, obtained with the 3D invariant-based failure criteria.

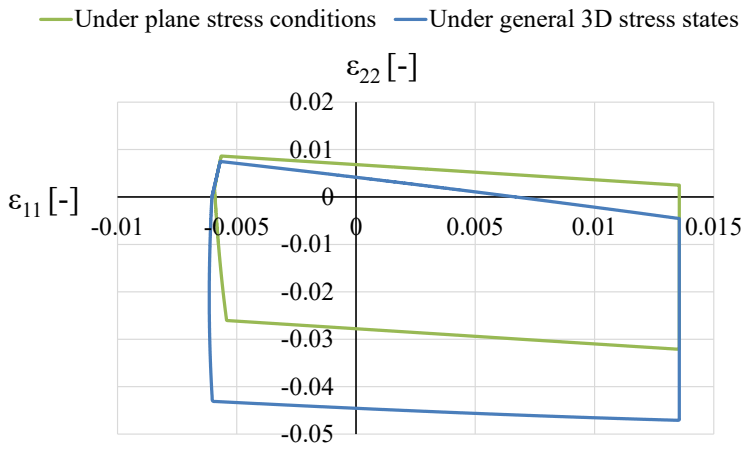


Figure 3.4: Comparison between ε_{11} - ε_{22} failure envelopes in strain space, for a 0° ply, based on the 3D invariant-based failure criteria under plane (green line) and general 3D (blue line) stress states.

In general, the failure predictions based on Tsai-Wu criterion exhibited some deviations with respect to the experimental data when dealing with triaxial failure stress states. Similarly, Hashin criteria is not suitable to address complex stress states, as open envelopes are generated under biaxial transverse compression.

In spite of the large scatter of the test results and the complexity of the considered test cases, a generally good fit is observed when using the 3D invariant-based failure criteria [50]. Indeed, for all test cases, the invariant-based criteria generate closed envelopes and account for the effect of hydrostatic pressure by using suitable values for Y_{BC}.

3.1.2 Concept of extended omni strain failure theory

Exploiting the fully 3D description of failure provided by the invariant-based theory outlined in Sec. 2.3.2, omni strain failure envelopes can be extended by finding the controlling plies in the 3D principal strain space [50]. Indeed, with this extension, the resulting design space can predict laminate failure under complex 3D stress states and address, for instance, the design of bolted joints or thick composite laminates, where through-thickness stress states cannot be neglected. Furthermore, in this case, the envelopes allow the identification of the critical failure modes for each controlling ply, which cannot be investigated with the original omni strain envelopes, based on Tsai-Wu.

An example of omni FPF envelope, obtained using the invariant-based failure model for IM7/8552, is shown in Fig. 3.9. This research work is carried out using the material properties of IM7/8552 from Ref. [33], which are listed in Table 3.1.

In Fig. 3.9a, several ply failure envelopes are represented with different colours, from which the omni strain FPF envelope (outlined with a black dotted line) can be obtained. Fig. 3.9b provides a detailed view of the omni FPF envelope only, where the failure loci are represented using different markers in order to identify the critical failure modes for each controlling ply ([0], [90],

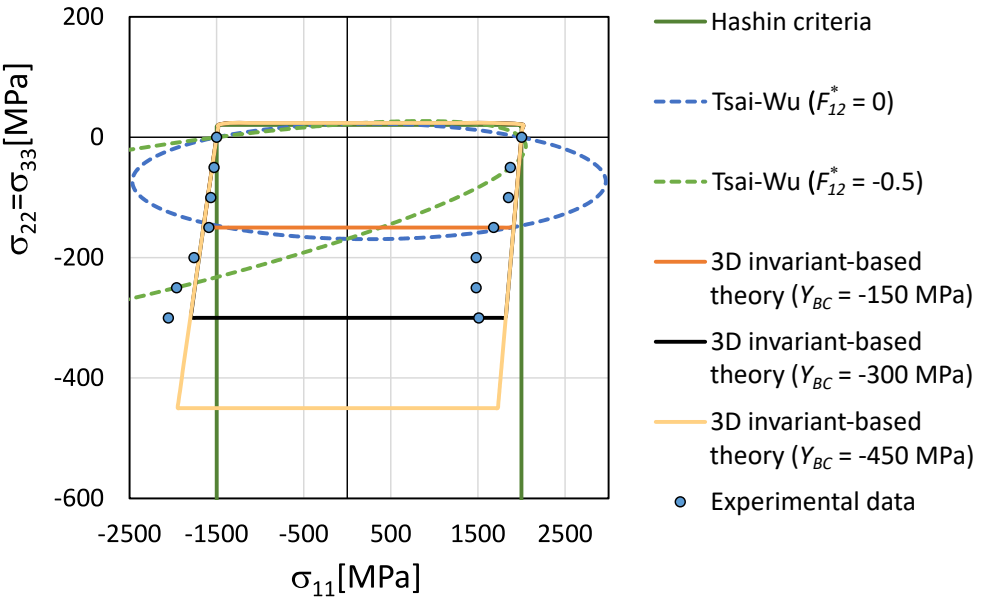


Figure 3.5: Triaxial failure stress states: $\sigma_{22} = \sigma_{33}$ vs. longitudinal stress σ_{11} for a UD carbon/epoxy (after Ref. [50]).

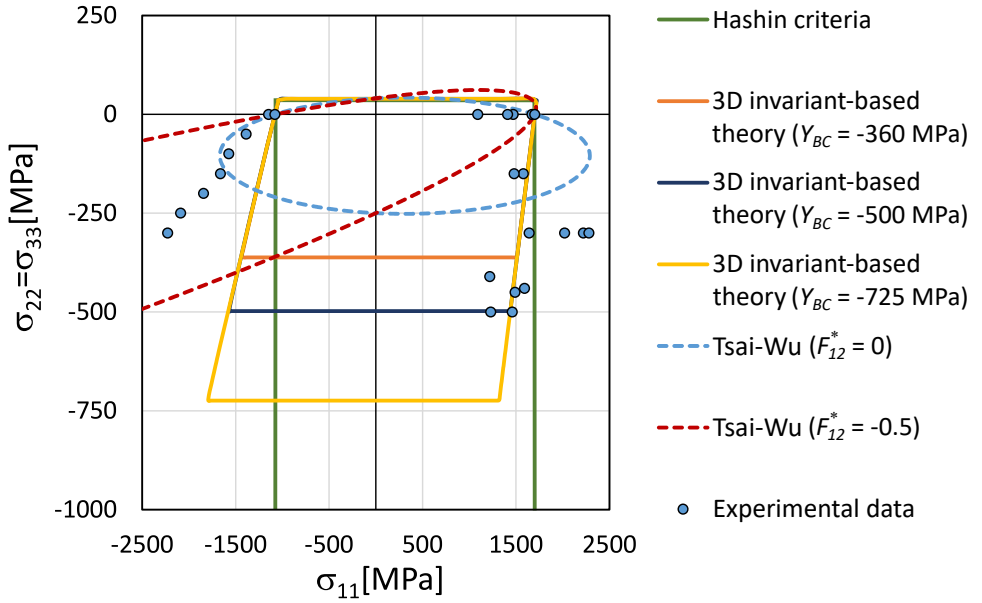


Figure 3.6: Triaxial failure stress states: $\sigma_{22} = \sigma_{33}$ vs. longitudinal stress σ_{11} for a UD S-glass/epoxy cube (after Ref. [50]).

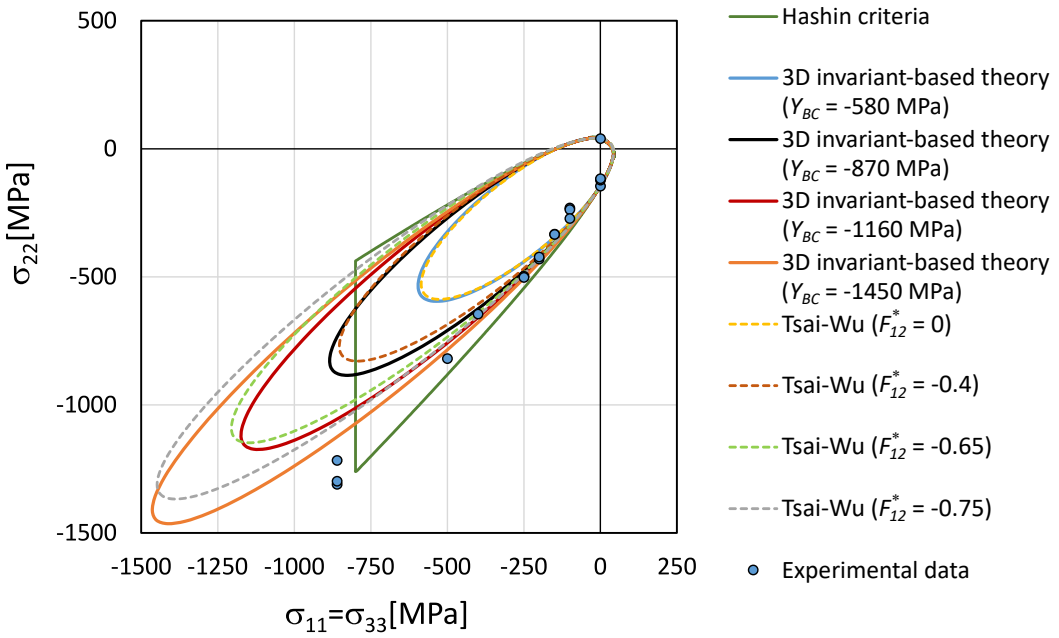


Figure 3.7: Triaxial failure stress states: σ_{22} vs. longitudinal stress $\sigma_{11} = \sigma_{33}$ for a UD E-glass/MY750 epoxy (after Ref. [50]).

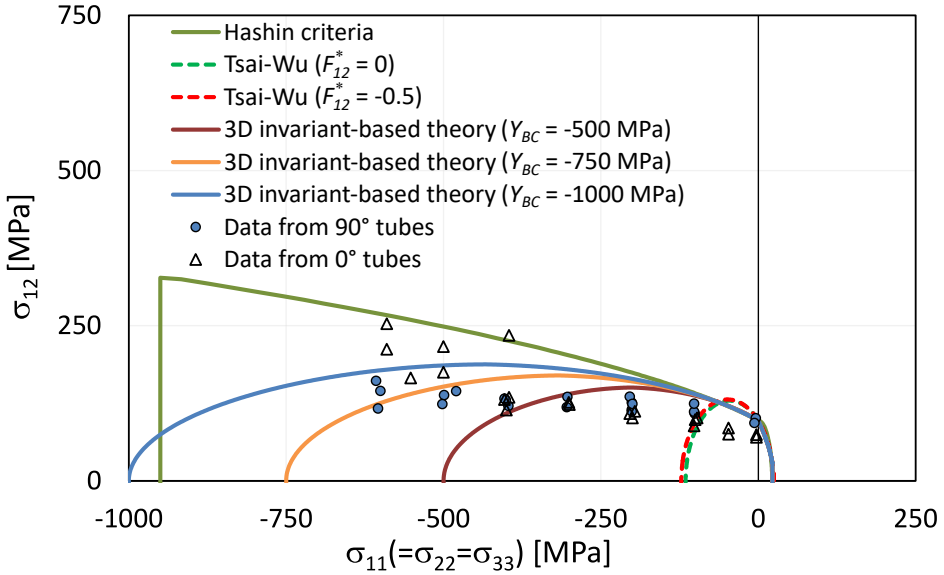


Figure 3.8: Triaxial failure stress states: shear stress σ_{12} vs. hydrostatic pressure ($\sigma_{11} = \sigma_{22} = \sigma_{33}$) for a UD T300/PR319 epoxy (after Ref. [50]).

Table 3.1: Material properties of the IM7/8552 carbon-epoxy UD tape [33].

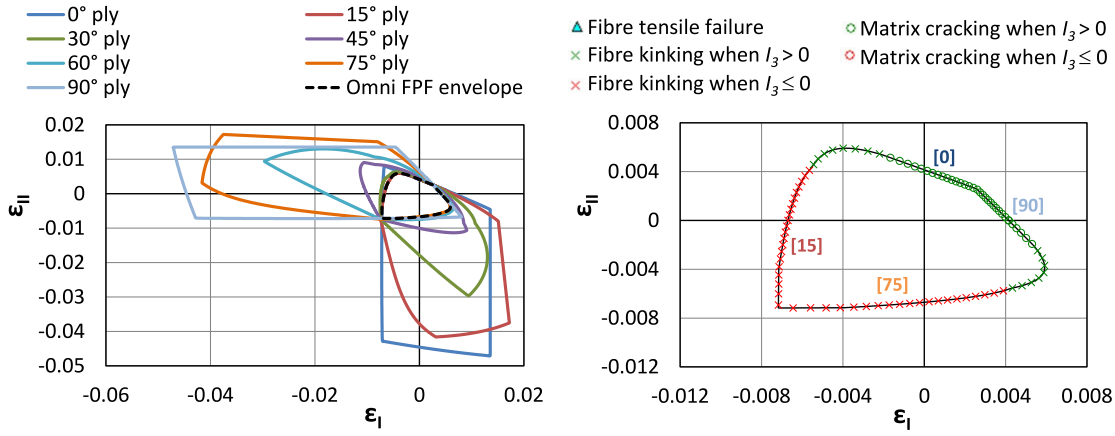
Property	Value	Units
E_1	171.42	GPa
E_2	9.08	GPa
G_{12}	5.29	GPa
ν_{12}	0.32	-
ν_{23}	0.487	-
β	2.12E-08	MPa^{-3}
X_T	2323.5	MPa
X_C	-1017.5	MPa
Y_T	62.3	MPa
Y_{BT}	38.7	MPa
Y_C	-253.7	MPa
Y_{BC}	-600.0	MPa
S_L	89.6	MPa
S_T	62.3	MPa

[75] and [15]). In this way, it is possible to identify fibre failure as the most prominent FPF mode shaping the omni FPF envelope of IM7/8552. Finally, it can be also observed that, when $\varepsilon_{11} > \varepsilon_{22}$ the [75] or [90] plies are responsible for failure initiation, otherwise the controlling plies are the [15] or [0] ones.

An additional detailed plot to verify the critical failure modes (alternative to the one in Fig. 3.9b) can be obtained exploiting the two different formulations of the invariant-based failure criteria to distinguish transverse, matrix-dominated failure mechanisms from longitudinal, fibre-dominated failure mechanisms. In particular, plotting the failure envelopes for matrix failure mode (FI_M from Eq. 2.30) and the complete omni FPF envelope (which includes fibre failure), as shown in Fig. 3.10, the critical failure modes can be easily identified. Indeed, in Fig. 3.10, it can be observed how the matrix is responsible for failure initiation under applied biaxial tensile strain, i.e., the first quadrant. Moreover, this analysis confirms that the failure mode that actually shapes the omni FPF envelope of IM7/8552, for most of the strain space, is fibre compressive failure.

Furthermore, when fibre kinking occurs, the kinking angle φ and the angle of the kinking plane ψ, computed as described in the failure model, can be recorded and added to the plot. To give an example, Fig. 3.11 shows the evolution of the kinking angle on the omni FPF envelope for IM7/8552. It can be observed that the predicted kinking angle in the minimum FPF envelope ranges, in absolute values, from 0° to 8.6°, reaching the maximum absolute value in the compression-compression quadrant, under the highest value of applied biaxial compressive strain [50].

Following Ref. [51], the degraded ply properties of IM7/8552 are computed using micromechanics relations and a matrix degradation factor equal to 0.15. The omni LPF envelope can be finally generated, as shown in Fig. 3.12. In a similar illustrative scheme as for the omni FPF envelope, the controlling plies and the critical failure modes are highlighted in the figure. In particular,



(a) Omni FPF envelope.

(b) Controlling plies and failure modes.

Figure 3.9: Omni FPF envelope in strain space for IM7/8552, according to the 3D invariant-based failure criteria, with a detailed view on the critical failure modes.

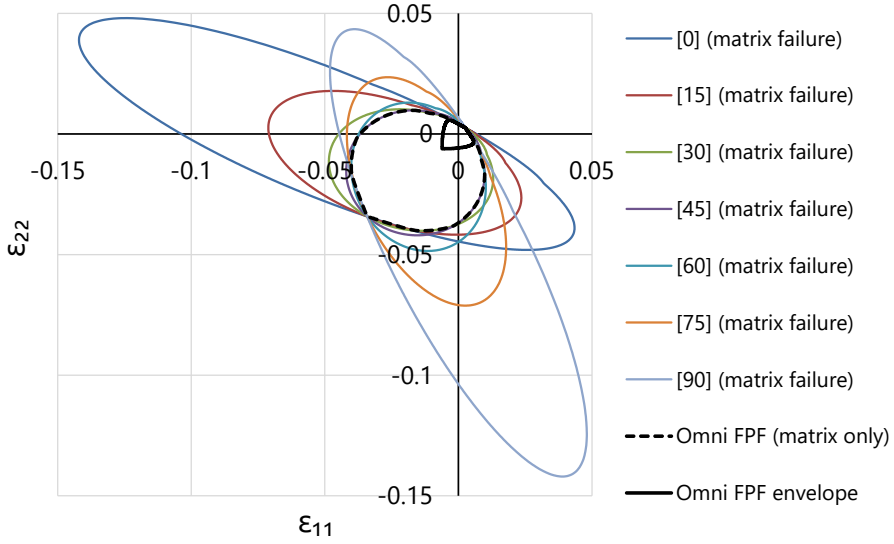


Figure 3.10: ε_{11} - ε_{22} omni FPF envelope, for UD IM7/8552, obtained with the matrix failure criterion from the 3D invariant-based failure criteria. The omni FPF envelope based on the complete failure theory is also included as benchmark.

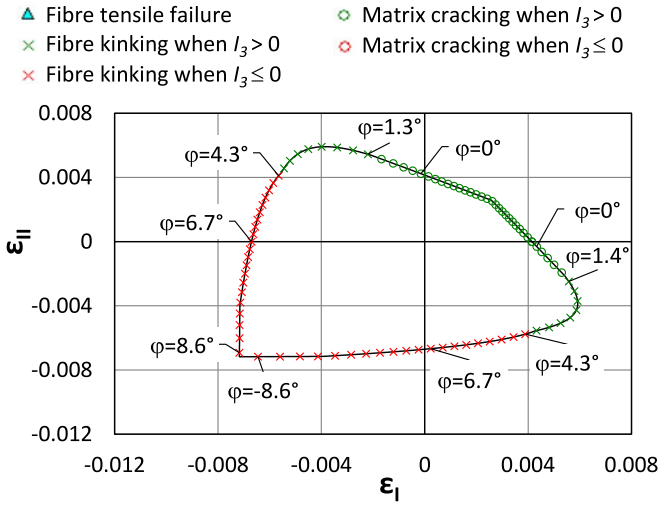


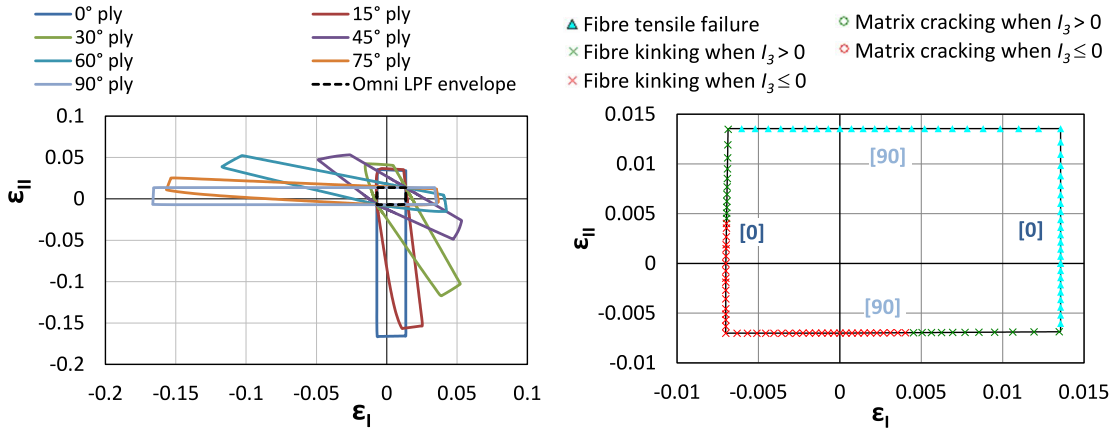
Figure 3.11: Detailed view on the values of kinking angle φ on the omni FPF envelope in principal strain space for IM7/8552, according to the 3D invariant-based failure model.

Fig. 3.12b shows that LPF is dominated by fibre failure, in agreement with the observations of Tsai and Melo [51].

The presented extension of the omni strain FPF/LPF envelope was made under the assumption of general 3D stress states, in order to exploit the fully 3D failure description of the implemented set of phenomenological criteria. However, for the sake of completeness, it is interesting to compare these omni FPF/LPF envelopes with the ones obtained under the assumption of plane stress conditions.

The comparison for FPF, shown in Fig. 3.13a, recalls the differences found and justified for the [0] ply (Fig. 3.4), which result in a significant shift in the failure loci of the omni envelope, especially in the first quadrant. This means that for thick plies, where the assumptions of plane stress cannot be made, the selection of a safe stacking sequence, for this material, should account for a reduced strength under applied tensile principal strains, and a slightly increased strength under applied compressive ε_I - ε_{II}. However, for final collapse, despite significant differences are found for each ply orientations, the obtained omni LPF predictions do not reflect any influence from out-of-plane stresses, as shown in Fig. 3.13b. This result is valid for IM7/8552, but it should be verified for other materials.

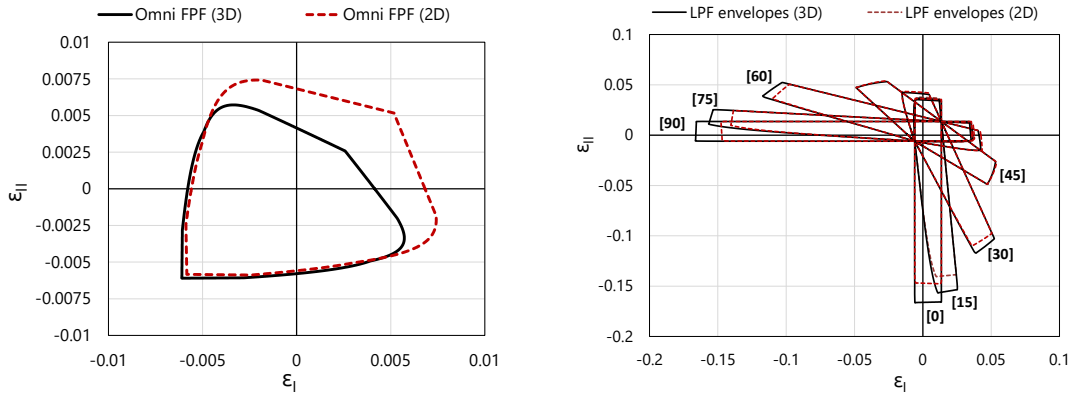
This invariant-based description of failure can be represented in 3D, as the set of invariant-based failure criteria captures well the effect of the out-of-plane direction. For IM7/8552, the failure surface in stress space is shown in Fig. 3.14, while the omni FPF and LPF surfaces are represented in Figs. 3.15a and 3.15b, respectively. As a remark, these surfaces predict membrane FPF or LPF of any laminate, independently of layup or stacking sequence, while considering the effect of out-of-plane stresses, and can be obtained using only the material properties of the UD material required by the failure model. For this reason, this approach can be very effective in guiding the conceptual design of composite structures subjected to any stress state [50].



(a) Omni LPF envelope.

(b) Identification of controlling plies and failure modes.

Figure 3.12: Omni LPF envelope in principal strain space for IM7/8552, according to the 3D invariant-based failure criteria, with a detailed view of the controlling plies and critical failure modes.



(a) Omni FPF envelopes

(b) Omni LPF envelopes

Figure 3.13: Comparison between omni FPF/LPF envelopes obtained with 3D invariant-based failure criteria under plane (dashed red line) and general 3D stress states (solid black line), in principal strain space for UD IM7/8552.

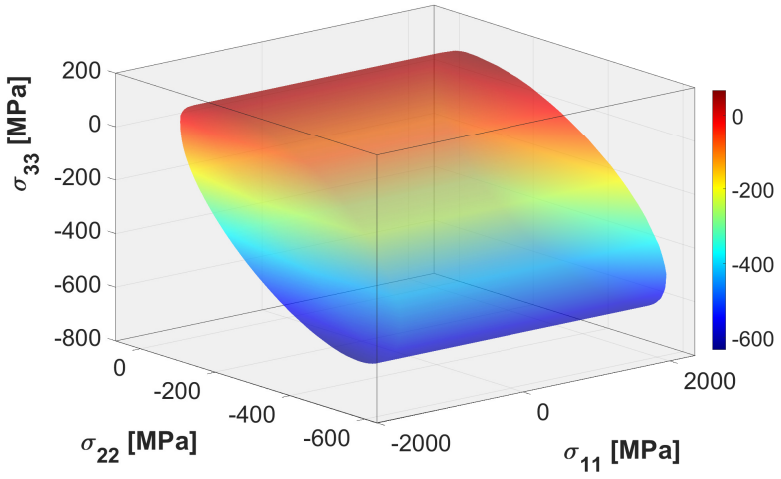


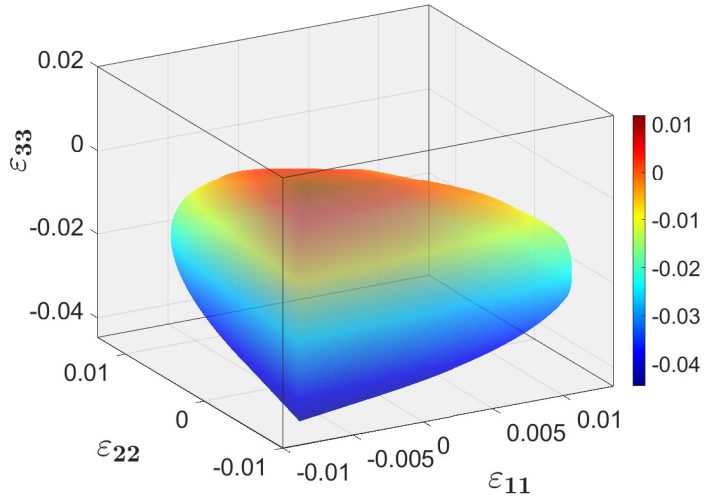
Figure 3.14: 3D failure surface in stress space for UD IM7/8552, obtained using the 3D invariant-based failure criteria [50].

It is also important to stress that, for typical CFRP laminates, such as aerospace industry-standard "quad" laminates characterized by different percentage of [0], [±45] and [90] plies [121], omni LPF and laminate LPF envelopes (the latter obtained from superposing in strain space only the envelopes of the ply orientations contained in the selected laminate) will lead to the same laminate failure predictions. This is justified by the presence of the [0] and [90] plies in these laminates, which will govern LPF according to both approaches. Therefore, for all CFRP quad laminates, the omni LPF envelopes ensure the same degree of conservatism as the laminate LPF envelopes, but without the need to recompute the failure envelope every time the layup changes. On the other hand, when tackling LPF of angle-ply laminates, omni LPF envelopes will have a certain degree of conservatism that will depend on the ply angles [50].

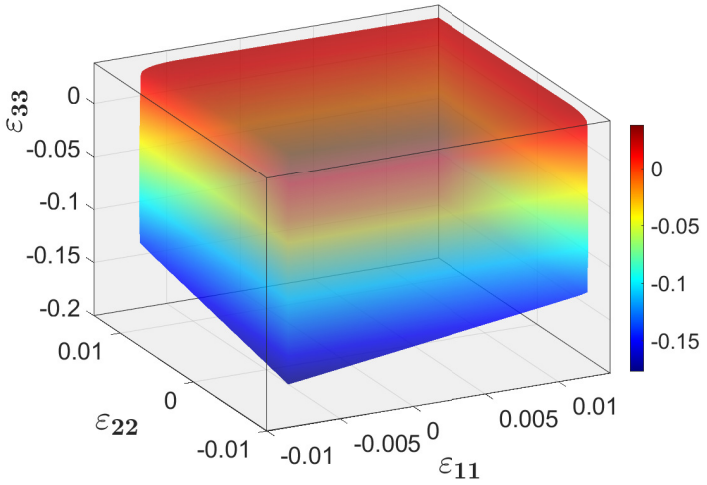
3.2 Validation of the extended omni-strain failure envelopes

In this section, the reliability and the overall performance of these "extended" omni strain LPF envelopes in predicting laminate failure is assessed using experimental data from the first and the second WWFE [36, 39, 119]. For the validation studies involving biaxial experimental data, omni LPF envelopes are generated using the Tsai-Wu and the 3D invariant-based failure criteria outlined in Sec. 2.3.2. For all the considered criteria, the envelopes are calculated using a matrix degradation factor of 0.15, which however lowers the differences in the failure predictions between the different criteria. In fact, when the matrix degradation factor approaches to zero, the predictions of the criteria in 2D become coincident. The degraded elastic properties used for omni LPF envelopes are: $E_2(=E_3)$, G_{12} and ν_{12}. The interaction term F_{12}^* of the Tsai-Wu failure theory is considered equal to -0.5 for all the considered test cases.

The first WWFE provides several test cases including biaxial failure stress envelopes for different laminates [36]. In this validation study, the following laminates have been considered: AS4/3501-6 $[90/\pm45/0]_s$, E-glass/LY556/HT907/DY063 $[\pm30/90]_s$ and E-glass/MY750/HY750/



(a) 3D omni strain FPF surface.



(b) 3D omni strain LPF surface.

Figure 3.15: 3D omni strain FPF (a) and LPF (b) surfaces in strain space for IM7/8552, obtained using the 3D invariant-based failure criteria [50].

Table 3.2: Material properties from WWFE-I [36].

Material	E_1[GPa]	E_2[GPa]	ν_{12}	G_{12}[GPa]	X_T-X_C[MPa]	Y_T-Y_C[MPa]	S_L[MPa]
AS4/3501-6	126.0	11.0	0.28	6.6	1950 - 1480	48 - 200	79
E-glass/LY556	53.48	17.7	0.28	5.83	1140 - 570	35 - 114	72
E-glass/MY750	45.6	16.2	0.28	5.83	1280 - 800	40 - 145	73

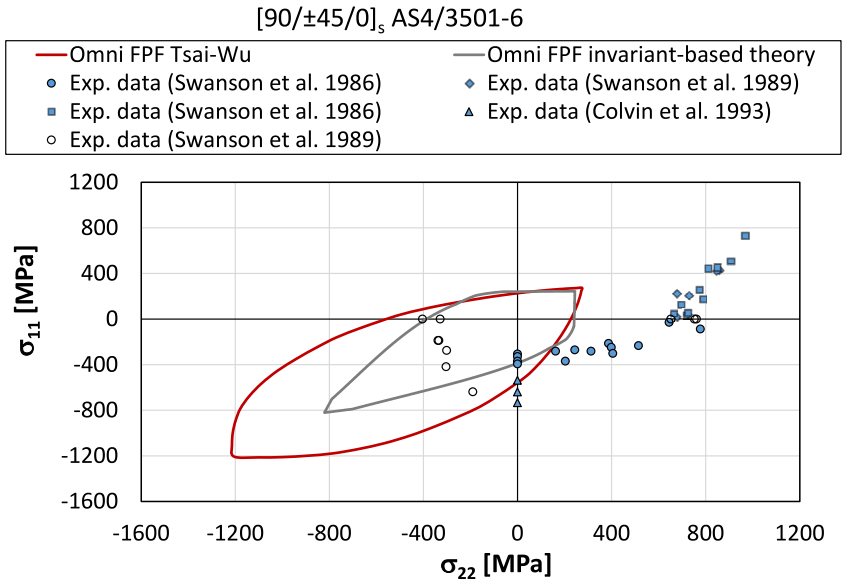
DY063 $[\pm 55]_s$. The material properties of their unidirectional plies are provided in Table 3.2. The additional mechanical properties required for the 3D invariant-based failure theory (Y_{BC}, Y_{BT}) are not provided in the WWFE-I, but they are scaled following the observations from Ref. [69]. Since the experimental data from literature are presented in stress space, laminate stress-strain relations have been used to represent omni LPF envelopes in stress space and compared with the available data.

Fig. 3.16 presents the comparison between experimental results and the proposed envelopes for an AS4/3501-6 $[90/\pm 45/0]_s$ laminate. On the left-hand side, Fig. 3.16a shows the omni FPF envelopes obtained with Tsai-Wu and the invariant-based theory, while in Fig. 3.16b the omni LPF envelopes based on the same criteria and the unit circle predictions are included. The conservatism of the omni FPF approach can be observed when using both theories and, in particular, in the strength predictions in the first and fourth quadrant. This can be explained by the critical failure mode under those stress states, which is matrix cracking for FPF.

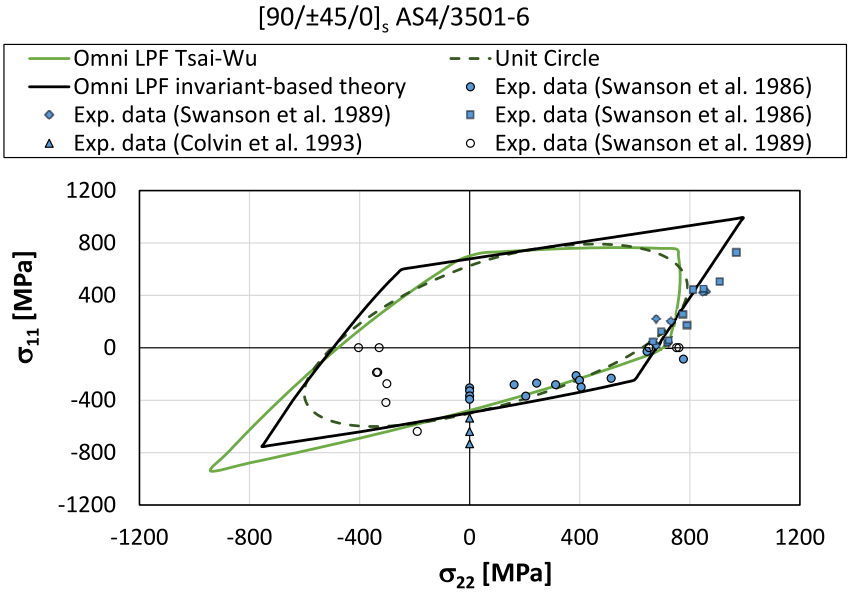
Small differences can be observed between the two omni LPF envelopes (obtained using the 3D invariant-based failure criteria in black and Tsai-Wu in green solid line), but in general, the predictions obtained with Tsai-Wu and the unit circle envelope are slightly more conservative compared with the invariant-based theory. The correlation between test data and predictions is excellent, except for the third quadrant where the predictions seem to overestimate the laminate strength under biaxial compression. However, those experimental results from Swanson and Colvin cannot be considered 100% reliable, as pointed out also by the organizers of the first WWFE [36]. In fact, those results are characterized by a large scatter in the mean axial compressive strength, probably affected by buckling when testing longer specimens. Thus, the predictive capability of the considered approaches cannot be reliably assessed in the compression-compression quadrant.

The correlation between the failure predictions using omni FPF envelopes and experimental data for a $[\pm 30/90]_s$ laminate made of E-glass/LY556/HT907/DY063, shown in Fig. 3.17a, highlights the remarkable conservatism of the approach and the large difference when compared with omni LPF and unit circle envelopes shown in Fig. 3.17b. The failure predictions obtained with the two omni LPF envelopes are almost coincident, while the unit circle is less conservative than the omni LPF envelopes. Unlike CFRPs, fibre failure is not always the critical failure mode for GFRPs.

To confirm this observation, Figs. 3.18 and 3.19 show the omni LPF envelopes in strain space for the E-glass composites herein (Table 3.2), highlighting that the controlling plies are not always

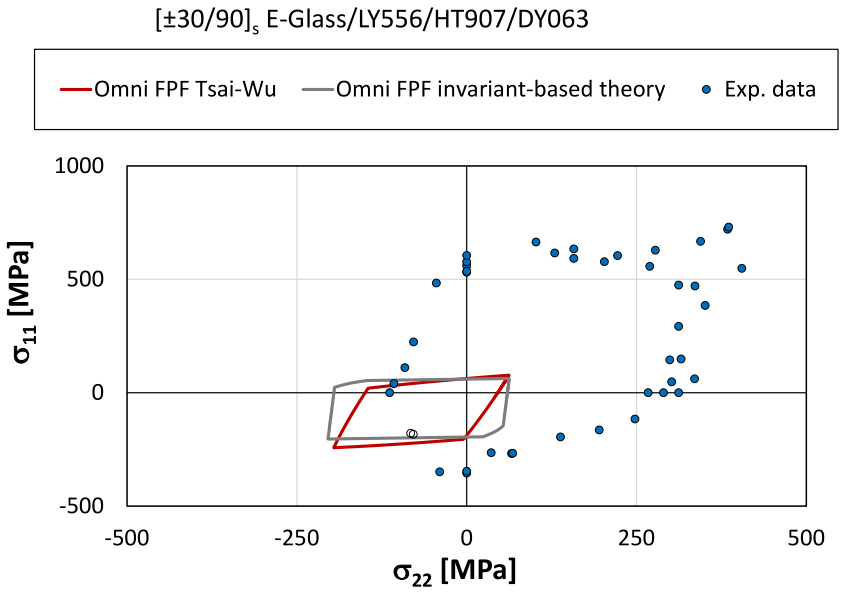


(a) Omni FPF envelopes.

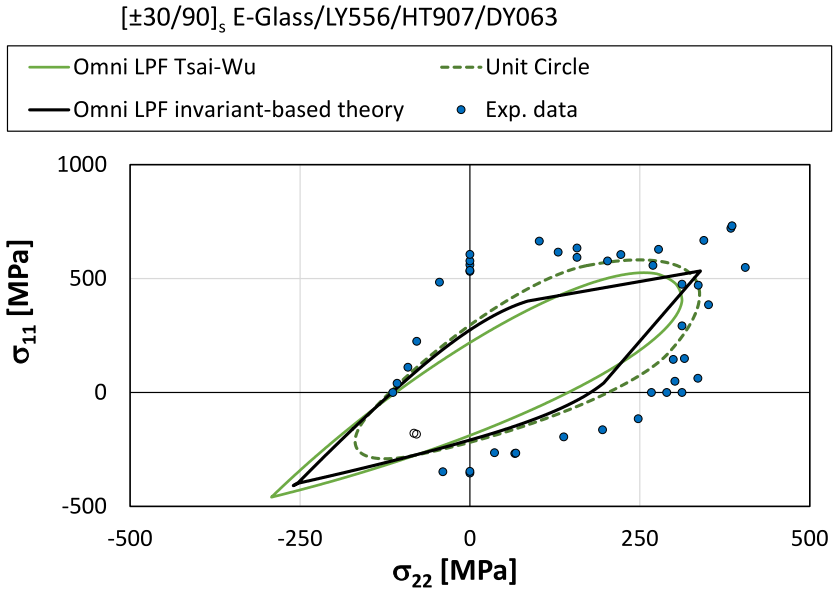


(b) Omni LPF envelopes and unit circle.

Figure 3.16: σ_{22} - σ_{11} failure envelopes versus experimental results from the WWFE-I for a $[90/\pm45/0]_s$ AS4/3501-6 carbon/epoxy laminate [50].

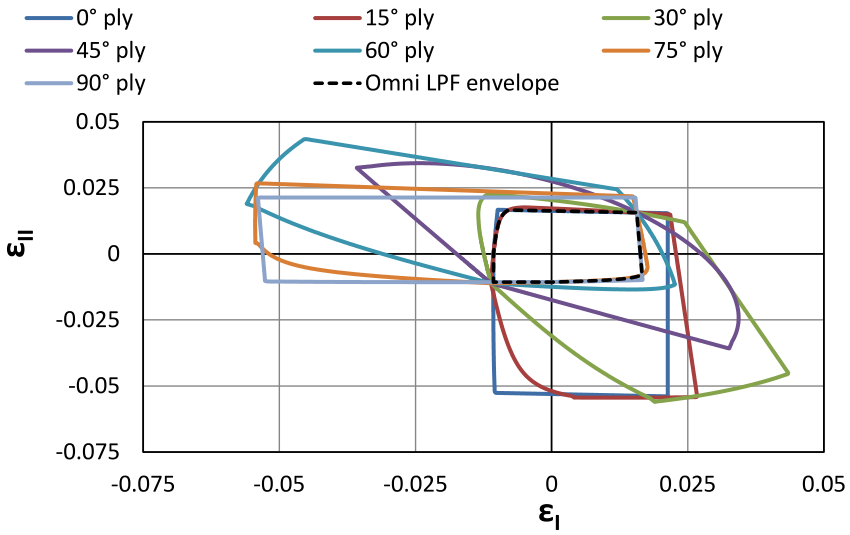


(a) Omni FPF envelopes.

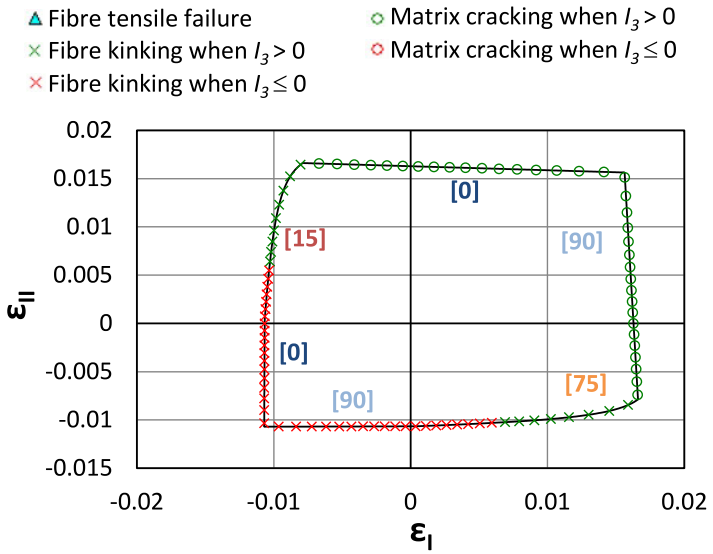


(b) Omni LPF envelopes and unit circle.

Figure 3.17: σ_{22} - σ_{11} failure envelopes versus experimental results from the WWFE-I for a $[\pm 30/90]_s$ E-glass/LY556/HT907/DY063 laminate [50].



(a) Omni LPF envelope.

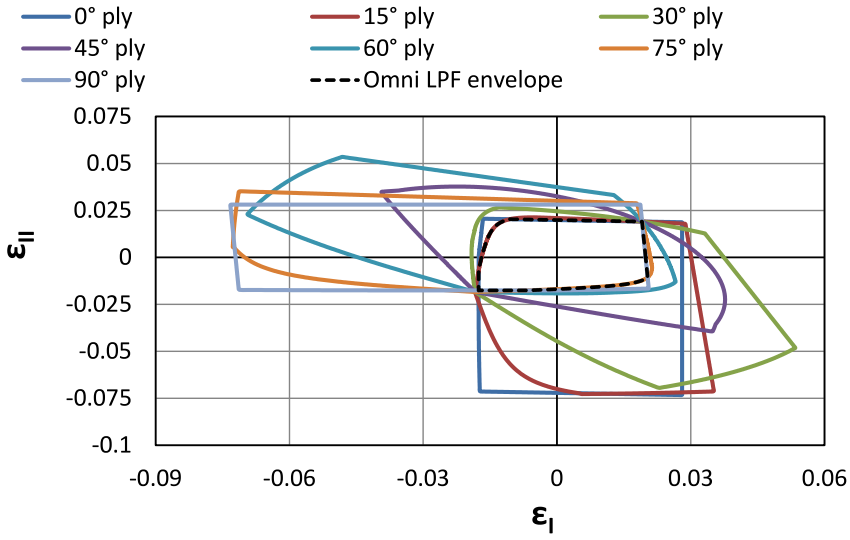


(b) Controlling plies and failure modes.

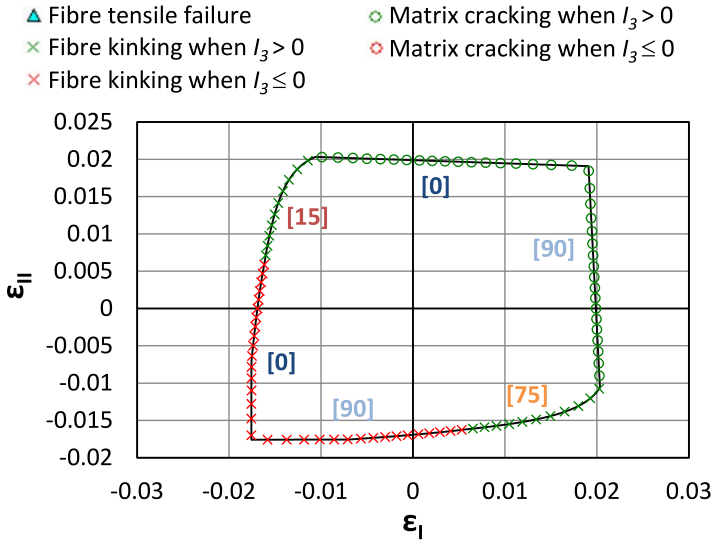
Figure 3.18: Omni strain LPF envelope, controlling plies and critical failure modes obtained with the 3D invariant-based failure criteria for E-glass/LY556/HT907/DY063 [50].

[0] and [90], and that matrix failure defines almost half of the envelopes for these materials. This confirms that the assumption of fibre failure for LPF is only true when studying CFRP laminates. As direct consequence of these remarks, the resulting unit circles for the same materials are no longer inscribed in the omni LPF envelopes, as represented in Fig. 3.20. Thus, for the considered GFRPs, with a lower degree of anisotropy, the tensile and compressive strains-to-failure of a [0] coupon cannot be considered the only anchor properties to define omni failure analysis. In other words, the simplification of the unit circle does not apply to GFRPs [50].

Finally, it is noted that, as in the previous case (Fig. 3.16), the failure envelopes in Fig. 3.17

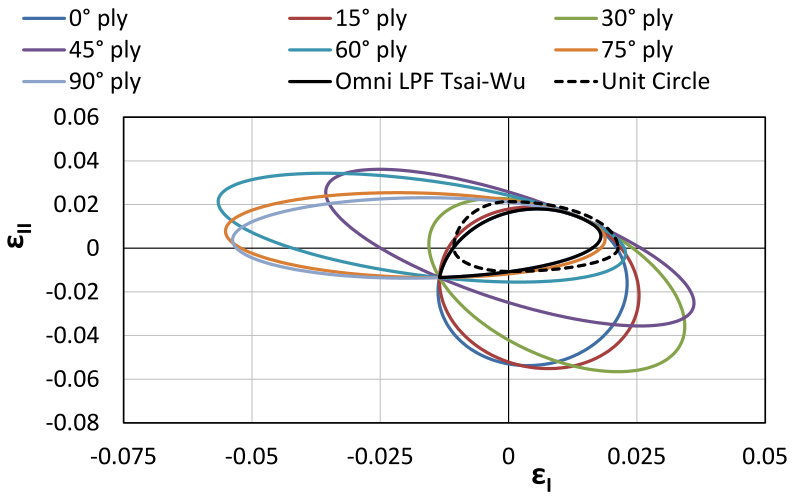


(a) Omni LPF envelope.

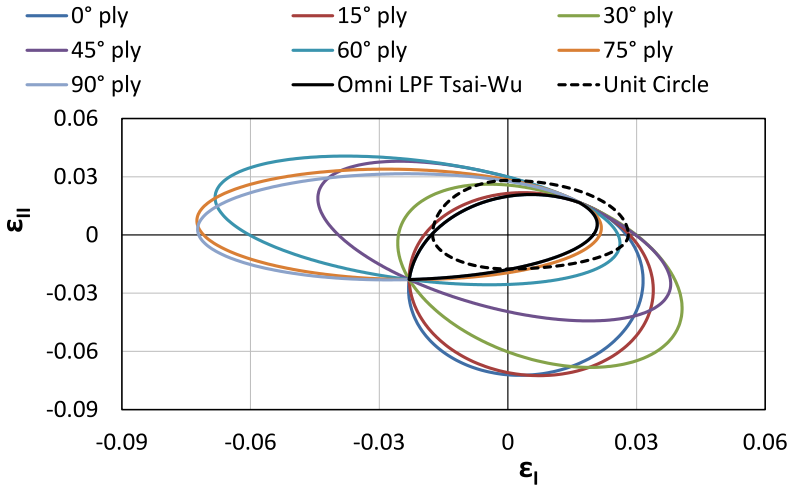


(b) Controlling plies and failure modes.

Figure 3.19: Omni strain LPF envelope, controlling plies and critical failure modes obtained with the 3D invariant-based failure criteria for E-glass/MY750/HY750/DY063 [50].



(a) E-glass/LY556/HT907/DY063.



(b) E-glass/MY750/HY750/DY063.

Figure 3.20: Omni LPF envelopes, based on Tsai-Wu, and unit circle envelopes in principal strain space for two different composite material systems [50].

underpredict the experimental data in the compression–compression quadrant, which can be attributed to compression instability of the specimens under that loading condition.

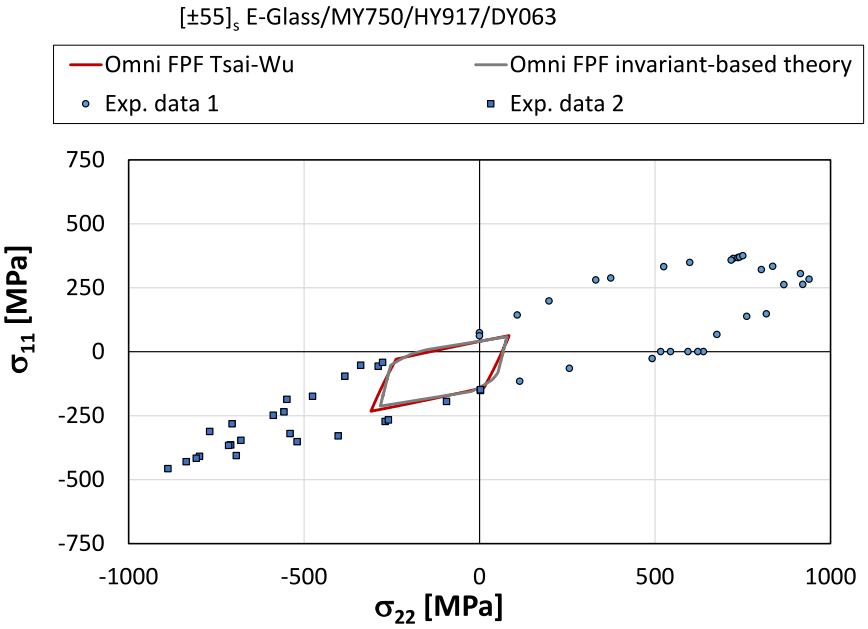
The experimental results for a $[\pm 55]_s$ E-glass/MY750/HY750/DY063 laminate are compared with the proposed omni LPF and unit circle envelopes in the σ_{22} - σ_{11} stress space, as illustrated in Fig. 3.21a. The conservatism of omni FPF envelopes is confirmed in this test case, as shown in Fig. 3.21b, while the predictive capability of omni LPF envelopes can be acknowledged also in this study.

These three test cases provide clear indications on the huge benefits in using a LPF approach instead of FPF predictions. The larger domain when using LPF predictions allows to reduce conservatism in a remarkable way, without incurring additional computational time. These benefits can be exploited immediately from the conceptual design stage of composite aerostructures, since the presented tool is invariant with respect to the laminate layup. The beneficial impact of this approach on the composites industry, where the consolidated practice in early design stage is to use FPF theories, such as maximum strain or Tsai-Wu, can be significant.

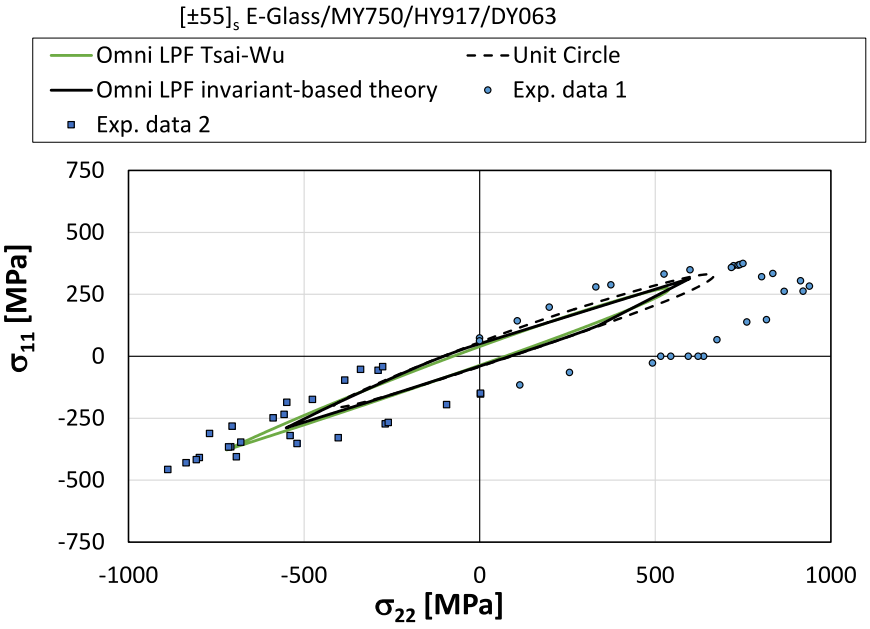
A triaxial test case for laminate failure is also available from the WWFE-II. Due to the complexity of imposing a triaxial stress state with suitable load introduction systems, there is lack of reliable experimental results involving triaxiality. For UD laminates, such validation studies have been supported in the past by computational micromechanics; however, for multidirectional laminates, computational micromechanics is still not suitable for similar studies due to the computational cost of running a micro-scale representative volume element of a multidirectional laminate. Herein, the aim is to assess the reliability of the proposed quick analytical approach to composite laminate failure, accepting a certain degree of conservatism. In the selected test case, glass/epoxy tubes were first subjected to an equal internal and external pressure, and then an axial compression load was incrementally applied up to failure, while keeping the pressure constant during the test [119]. The mechanical properties of E-glass/MY750/HY750/DY063 in the out-of-plane direction can be found in Ref. [119].

In order to predict the variation of the compressive strength σ_{22} with through-thickness stress σ_{33} (where σ_{11}=σ_{33}), a fully 3D omni LPF surface in stress space was generated for this material, to extract the envelope in the relevant section. To assess the conservatism of the proposed 3D omni LPF surface, a laminate failure envelope, obtained superposing only ply failure envelopes of the relevant orientations ($\pm 35°$) and the same failure model, was included in this study. Both surfaces and experimental data are shown in Fig. 3.22.

The predictions using the full 3D omni surface and the $[\pm 35°]_s$ LPF surface in the relevant section are illustrated with a blue solid line and a dotted red line, respectively, and compared with experimental results in Fig. 3.23. This comparison shows that the laminate LPF envelope allows to reduce the conservatism of 3D omni LPF surfaces, with more accurate predictions, in the case of angle-ply laminates. However, in spite of providing conservative predictions, the omni LPF envelopes define, in a physically-based setting, a safe approach for laminate failure prediction that is independent of the particular layup sequence, thus making its application straightforward for any laminate of a given material system. It can, therefore, be used for preliminary design, analysis and

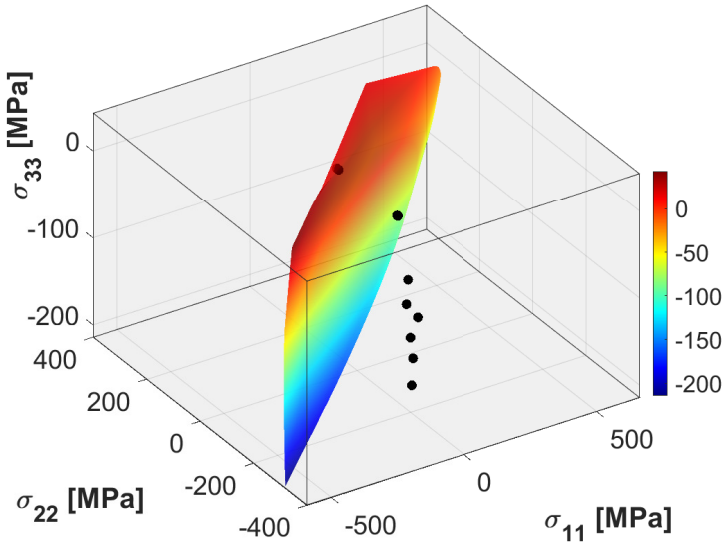


(a) Omni FPF envelopes.

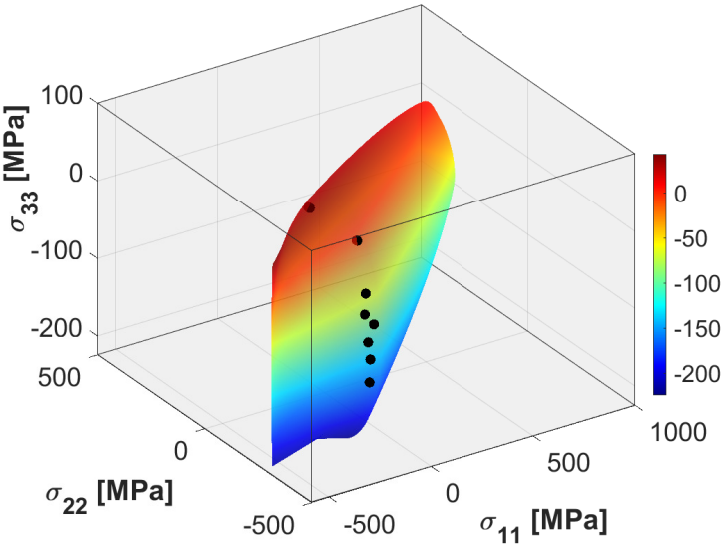


(b) Omni LPF envelopes and unit circle.

Figure 3.21: $\sigma_{22} - \sigma_{11}$ failure envelopes versus experimental results from the WWFE-I for a $[\pm 55]_s$ E-glass/MY750/HY750/DY063 laminate [50].



(a) 3D omni LPF surface.



(b) 3D $[\pm 35]_s$ LPF surface.

Figure 3.22: 3D omni LPF (a) and $[\pm 35]_s$ laminate LPF (b) surfaces versus experimental results from WWFE-II for a $[\pm 35]_s$ E-glass/MY750 epoxy laminate [50].

optimization of composite structures without the need for recalculating the failure envelope. This allows simple generalization of ply-based criteria to laminate-based criteria, which is expected to contribute to significant time savings during the massive operations taking place, for instance, in multidisciplinary design optimization of composite aerostructures [50].

Finally, in order to assess the importance of including the out-of-plane stresses in the failure analysis, the triaxial test case for a $[\pm 35]_s$ E-glass/MY750 epoxy laminate from WWFE-II is again considered. In this case, the omni LPF envelopes assuming plane stress conditions are compared with the ones under general 3D stress states as shown in Fig. 3.24a. In Fig. 3.24b, laminate LPF envelopes under 2D and 3D stress states are shown [50].

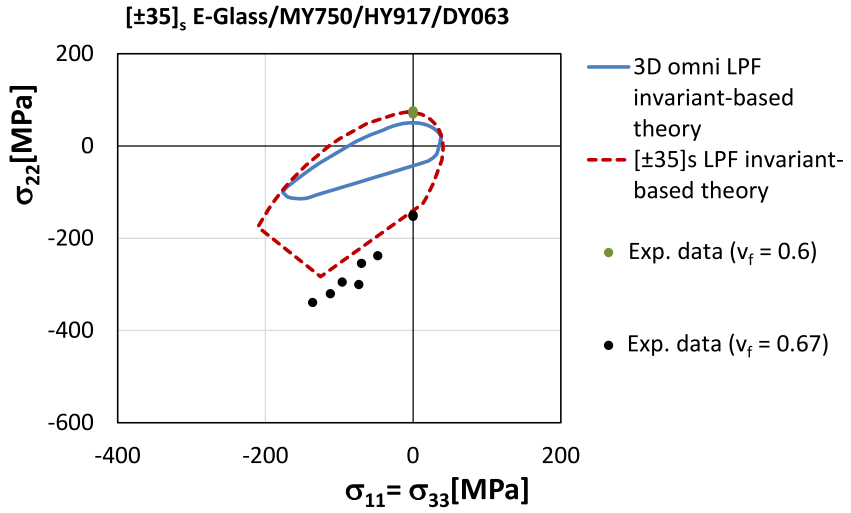
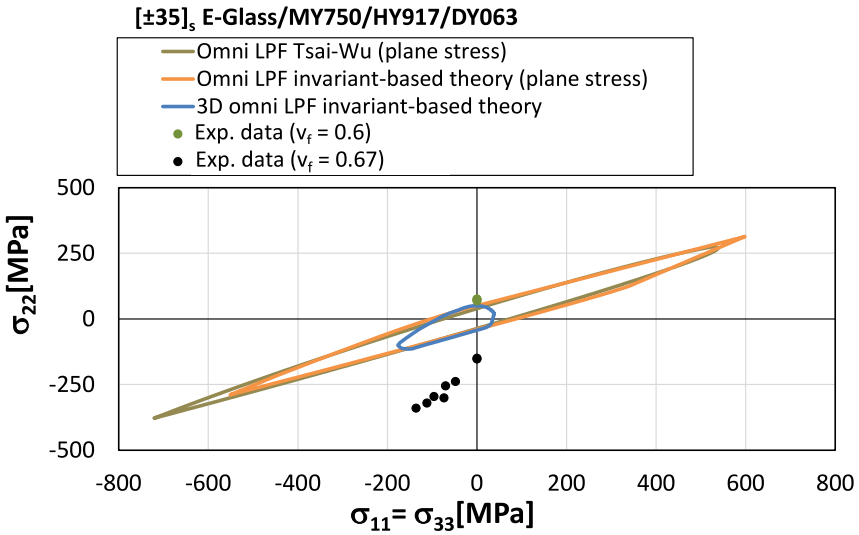


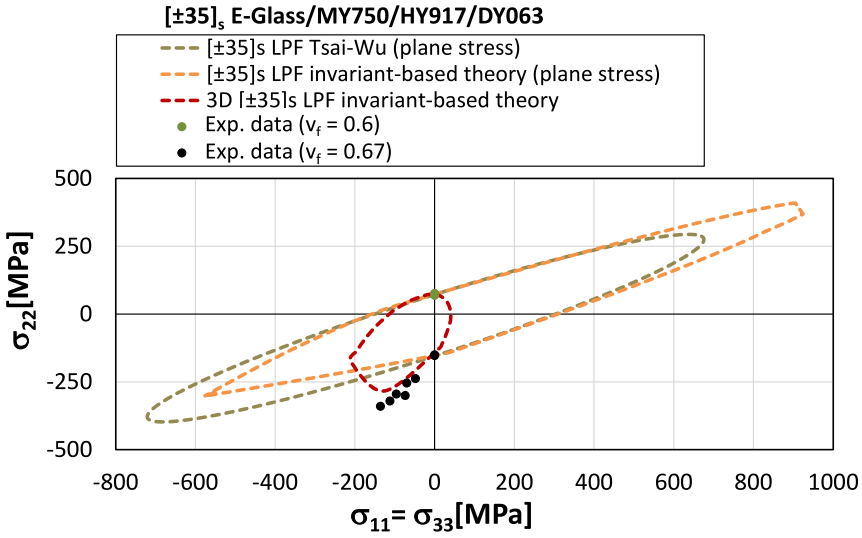
Figure 3.23: $\sigma_{22} - \sigma_{11}$=$\sigma_{33}$ failure envelopes versus experimental results from WWFE-II for a $[\pm 35]_s$ E-glass/MY750 epoxy laminate. The experimental data is available for two different fibre volume fractions (v_f) [50].

The omni LPF envelopes under plane stress provide similar predictions for both theories, as observed for the biaxial test cases from WWFE-I. When comparing these envelopes with the omni LPF surface, generated with the invariant-based theory, the design space is considerably reduced in the first and third quadrant, as a result of the effect of the out-of-plane stress. Although the available test data do not allow to assess with rigour how overestimated are the predictions of the plane stress models, the remarkable difference suggests that accounting for the effect of hydrostatic pressure can be very important in obtaining safe failure predictions for general laminates [50].

This becomes clear by analyzing the laminate LPF envelopes shown in Fig. 3.24b. The failure envelope from the $[\pm 35]_s$ LPF surface confirms that the influence of the out-of-plane stress allows to capture the increase of strength under hydrostatic pressure and the reduced strength under triaxial tension/compression, and therefore, to achieve an improved correlation with the experimental data [50].



(a) Omni LPF predictions.



(b) $[\pm 35]_s$ LPF predictions.

Figure 3.24: 3D omni LPF (a) and $[\pm 35]_s$ laminate LPF (b) predictions under general stress states and plane stress conditions versus experimental results from WWFE-II for a $[\pm 35]_s$ E-glass/MY750 epoxy laminate [50].

3.3 Strengths and limitations of the extended omni failure concept

Omni strain failure envelopes, extended with recourse to fully 3D phenomenological failure criteria, represent the original contribution introduced with this research work. The goal of this implementation was to address two unanswered questions arising from the omni strain failure envelope concept, firstly proposed by Tsai and Melo [49, 51]: (i) whether this concept could be used to predict FPF and LPF of general laminates in the presence of high levels of triaxiality, and (ii)

whether this concept could account for the influence of layup on the FPF and LPF modes, and predict them [50].

The extension of omni strain failure envelopes was realized by implementing the 3D invariant-based failure theory. The failure predictions from the first and second WWFE were selected as a suitable benchmark to validate this method, since they describe challenging biaxial and triaxial experimental data and the performance of competing failure theories involved in the WWFE was available for comparison. In this way, the application of this concept to scenarios of general 3D stress states was analyzed, while predicting the FPF and LPF modes, and assessing its conservatism compared with other approaches [50].

The validation study has shown that the extended omni LPF concept is a reliable method to address laminate failure under biaxial and triaxial stress states. The benefits of this implementation can be appreciated especially when predicting laminate failure under high values of hydrostatic pressure, where omni LPF envelopes based on non-phenomenological failure criteria give over-conservative predictions, leading to reduced design spaces. On the other hand, extended omni LPF envelopes under membrane loading generated similar predictions compared to the ones obtained with Tsai-Wu, but the extended approach provided also the critical failure modes [50].

An additional observation was made after assessing the effect of the stacking sequence on the prediction of omni LPF envelopes. This study has shown that LPF envelopes obtained superposing only ply failure envelopes contained in the considered laminate allow to reduce the conservatism of omni LPF envelopes, with more accurate predictions, in the angle-ply laminates. However, typical structural laminates are often characterized by the presence of [0] and [90] plies, and, consequently, omni LPF envelopes will typically provide satisfactory predictions in those cases [50].

Thus, the extended omni failure approach resulted to be a simple and generic framework that leads to safe prediction of the strength of general multidirectional laminates, independently of the stress state and level of triaxiality imposed on the composite. And despite its simplicity, the strength predictions are either equally good or better than other methods, for instance, considered in the first and second WWFE. Hence, the proposed extended method provides reliable and fast failure indications of composite laminates that can be particularly useful as a design tool for conceptual and preliminary design of composite structures [50].

3.4 Summary of the developed tool for failure predictions under general 3D stress states

In the present work, an extension of a recently introduced concept, called omni strain failure envelope, is proposed by implementing a set of 3D phenomenological failure theories, known as the 3D invariant-based failure criteria, in order to address laminate failure under general 3D stress states and to identify critical failure modes. This concept allows simple generalization of ply-based criteria to laminate-based criteria, overcoming two important constraints in multidisciplinary design optimization of composite aerostructures: (i) computing time, by establishing laminate failure criteria independently of ply discretization, and (ii) excessive conservatism, by incorporating safe LPF criteria instead of overconservative FPF criteria.

A validation study of the predicting capability of omni LPF envelopes was performed using experimental results from the first and second WWFE. A good agreement was observed for the 2D cases, where the added value brought by the proposed envelopes was highlighted when analyzing glass-fibre composites, whose LPF is governed by different failure modes; LPF of CFRP laminates, on the other hand, is always governed by fibre failure.

Finally, a triaxial test case was studied. The proposed 3D omni LPF surface presented some degree of conservatism with respect to experimental data on an angle-ply laminate, providing, nevertheless, a safe design space with minimal analysis cost due to its laminate invariant character. However, this conservatism will not be observed in industry-standard CFRP quad laminates, containing [0], [$\pm$45] and [90] plies. Moreover, it is shown that the influence of the out-of-plane stress cannot be neglected to properly capture laminate failure under hydrostatic pressure and to obtain safe LPF predictions under general 3D stress states.

So, the described method proves to be a very robust tool, giving reliable and fast failure indications in either 2D or complex 3D stress states. Being a quick tool, it can be used for preliminary design and integrated in multidisciplinary design optimization platforms, meeting the industrial need for computational efficiency, while simplifying the failure analysis and sizing of composite laminates.

Chapter 4

"Hot-spot" ply and laminate failure analysis

This Chapter presents the "hot-spot" failure analysis, which is a method to identify the critical locations for failure initiation (or final collapse) and corresponding failure modes in FRP structures, using FEA. Most of the popular failure criteria are already implemented in commercial FE softwares, such as Ansys® or Abaqus®, allowing the user to get fast indications on failure of composite structures. However, recent and advanced failure criteria are rarely included and they need the development of a special-purpose subroutine to customize the simulation, providing more results by computing additional failure indices. For this reason, the implementation of advanced failure criteria to perform "hot-spot" failure identification is presented in this Chapter. After the presentation of the implemented methods for failure analysis, the proposed tools will be verified against experimental data for different test cases.

4.1 Description of the "hot-spot" failure identification tool

The implementation of failure criteria in a FE software for "hot-spot" failure analysis has been recently proposed to accurately predict critical locations in large global models [122, 123, 124]. Exploiting the indications obtained from a "hot-spot" failure analysis, it is possible to increase the modelling resolution only where required, enabling a more efficient and reliable global-local analysis, especially when addressing large-scale composite structures. Lopes et al. [125] implemented the LaRC04 failure criteria to compare the strength of variable-stiffness and traditional straight-fibre composite panels. The implementation of this advanced phenomenological failure theory allowed to predict FPF, accounting for *in-situ* strengths. Molker et al. proposed the implementation of LaRC05 for the prediction of failure initiation and critical failure modes of laminated composite structures [122], while in Ref. [123] a novel LaRC05-based failure theory was implemented to address damage onset of Non-Crimp Fabric (NCF) reinforced composites. These implementations were done in the commercial FE code Abaqus/Standard®, by means of a user-defined subroutine

creating new element output variables showing the computed failure indices for each integration point.

The target of this type of analysis is usually the initiation of intralaminar failure mechanisms, so matrix and fibre failure. However, interlaminar failure criteria can also be implemented to predict the onset of delamination in a FE model. Furthermore, "hot-spot" failure identification can be also employed to predict final collapse, by means of laminate LPF theories and FE models discretized using an equivalent single-layer along the laminate thickness. Indeed, when the computational time is a strict constraint or for large global models, shell elements are commonly selected for the discretization of the model and, for design purposes, reserve factors (RFs) are usually computed using simple failure criteria at the laminate level.

In this work, intralaminar failure is predicted using the 3D invariant-based failure criteria [33, 68] and the onset of delamination is predicted with Ye's failure theory [75]. The description of these failure theories can be found in Chapter 2.

The formulation of both sets of criteria was implemented in a post-processing Python script, compatible with Abaqus/Standard® and Abaqus/Explicit®, to generate new element field outputs, by recovering the full stress tensor of each element and computing the failure index for each of the failure modes addressed by the criteria. Thus, this approach allows the identification of "hot-spots" and the corresponding failure mechanisms for damage initiation, creating 4 element output variables to predict fibre and matrix failure, under tension and compression, and an additional variable for the onset of delamination.

Besides this post-processing script, the same failure theories were implemented in a user subroutine, UVARM, written in FORTRAN, with the same scope of the script, so to generate new output field presenting the failure indices on the FE model. This subroutine is run at every load increment for every integration point of the model. However, there is a substantial difference between the two tools: the post-processing script is a tool that the user can run offline, so it reads the results from the database after the simulation is completed and, for linear-elastic analyses, this offers more flexibility; while the UVARM subroutine obviously, works only if it runs within the FEA.

For "hot-spot" failure analysis, both tools can be used since the mechanical behaviour of the model is assumed to be linear-elastic until damage initiation and it will not be modified after failure initiation. In fact, the non-linear progressive damage behaviour is out of the scope of this part of the work and will be addressed in the next Chapter. Therefore, a refined step-wise load incrementation is required in order to accurately predict the load level at the onset of failure (i.e. when the failure index is equal to one).

On the other hand, when the aim is to perform "hot-spot" failure analysis at laminate level addressing LPF, a FE model with an equivalent single-layer discretization and a laminate failure criterion should be used instead. With this purpose, an additional post-processing script was developed to compute and show the failure indices of the unit circle failure theory, as presented in Section 2.5.

Finally, to assess the results of the Ye's criterion for the prediction of delamination, cohesive elements have been implemented between plies with different orientation, as a parallel study. Indeed, although the linear-elastic analytical framework based on Ye's delamination onset criterion can give useful details about the delamination onset, it is not suitable for the prediction of delamination propagation because interlaminar failure in composite materials is a highly non-linear phenomenon, that usually starts at interfaces along the free edges or at defects. For this reason, to investigate accurately the onset and propagation of interlaminar damage, the implementation of the CZM has been chosen.

To verify and evaluate these tools, two test cases will be presented in the following sections, assessing their predictions at the coupon level and at the detail level. The first test case involves open-hole (OH) laminates subjected to quasi-pure bending, while the second case addresses an aeronautical reinforced panel under tensile loading. For both test cases, experimental results are available.

These case studies are presented to show: i) the implementation of the 3D invariant-based failure criteria and the Ye's criterion for the prediction of the onset of intralaminar failure and delamination, respectively, addressing models discretized with volumetric elements; ii) the suitability of laminate failure criteria, such as the unit circle, for models discretized with an equivalent single-layer.

4.2 Verification of "hot-spot" identification at the coupon level

Herein, an experimental investigation from Ref. [126] was selected as a test case for "hot-spot" failure analysis. The cited work involves the mechanical response of several coupons under quasi-pure bending, realized using an original device of compression with pivots. The authors introduced this device as an alternative to four-point bending tests, since it enables performing the test without contact between cylindrical bars and the sample and, thus, avoiding local indentation.

In particular, the bending is realized through a couple of wedges, inserted in the jaws of the tabs (as shown in Fig. 4.1), which define the offset of the mid-surface of the plate and the eccentricity of the test. For a large eccentricity, the specimen is subjected to a quasi-pure bending moment (as encountered with the four-point-bending test device), while for small eccentricity the test tends to a pure compression test. In the present study, large eccentricities, equal to half of the total thickness of the tested specimen, are used in order to obtain a quasi-pure bending moment in the gauge length. Furthermore, this test case has been selected because it is quite interesting for advanced modelling due to the two stress gradients generated in the sample: a *through-thickness* gradient due to the applied bending and an *in-plane* gradient due to the geometrical discontinuity at the hole.

The material used in these tests is T700GC/M21 carbon/epoxy, whose mechanical properties for a UD tape can be found in Refs. [127, 128, 129], except for the transverse biaxial compressive and tensile strengths (Y_{BC}, Y_{BT}), which are scaled following the observations from Ref. [69]. These material properties are listed in Table 4.1. Furthermore, the *in-situ* properties (S^L_{is}, S^T_{is}, Y^C_{is}, Y^T_{is} and

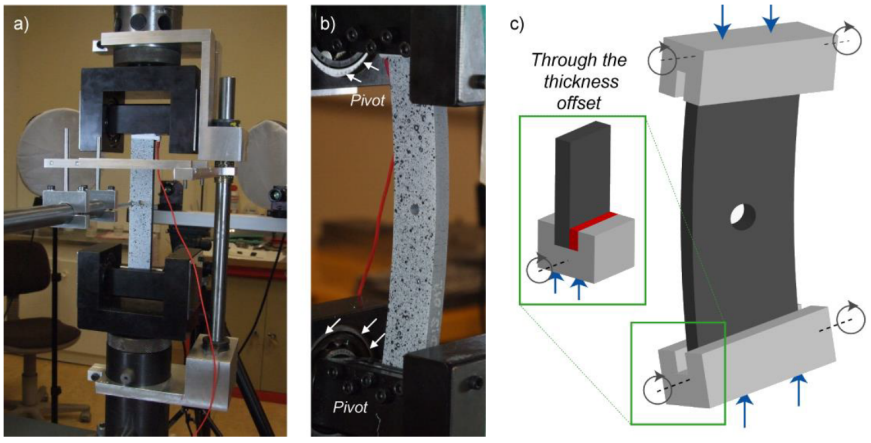


Figure 4.1: a) Presentation of the compression experimental device with pivots, b) zoom on the jaws with pivots, c) general principle of the quasi-pure bending test, from Ref. [126].

Y_{is}^{BT}), required to account for the effect of ply thickness on the strengths of each ply, are calculated following the analytical models described in Ref. [33].

Table 4.1: Material properties of the T700GC/M21 carbon/epoxy UD tape [127, 128, 129].

Property	Value	Units
E_1	122.00	GPa
E_2	8.30	GPa
G_{12}	4.50	GPa
ν_{12}	0.32	-
ν_{23}	0.54	-
X_T	2000.0	MPa
X_C	-1300.0	MPa
Y_T	76.0	MPa
Y_C	-256.0	MPa
Y_{BT}	47.2	MPa
Y_{BC}	-605.4	MPa
S_L	81.0	MPa
S_T	51.0	MPa

The open-hole plates have symmetric layups and the following geometrical characteristics:

- gauge length: $L = 130.0$ mm,
- hole diameter: $d = 6.35$ mm,
- width-to-hole-diameter ratio: $w/d = 5$,
- ply thickness: $t = 0.262$ mm.

The numerical analysis is conducted on four different layups, having the following stacking sequences, also denoted as X/Y/Z with X% of 0° plies, Y% of ±45° plies and Z% of 90°

Table 4.2: *In-situ* properties of the T700GC/M21 carbon/epoxy UD tape.

Ply position (thickness)	*In-situ* strengths [MPa]					
	Y_T	Y_{BT}	Y_C	Y_{BC}	S_L	S_T
Embedded (t_{ply})	120.4	83.7	-313.5	-605.4	104.1	65.6
Embedded ($2 \cdot t_{ply}$)	120.4	87.2	-299.6	-605.4	98.3	61.9
Outer (t_{ply})	76.0	46.1	-268.8	-605.4	85.9	51.0

plies: (i) a unidirectional $[0_{16}]$, (ii) a quasi-isotropic $[45/90/\text{-}45/0]_{2s}$ laminate (where the subscript "s" denotes the laminate symmetry with respect to the central inner ply) denoted 25/50/25, (iii) a highly-oriented $[45/0_2/\text{-}45/90/45/0_2/\text{-}45/0]_s$ laminate denoted 50/40/10, and (iv) a highly-disoriented $[45/90/\text{-}45_2/0/45_2/90/\text{-}45/0]_s$ laminate denoted 20/60/20 [126].

The idea behind this numerical study is to simulate the linear-elastic response of these 4 laminates, using two modelling strategies: (i) one based on C3D8R solid elements to spot the critical locations prone to the onset of ply intralaminar damage and delamination; (ii) the other following an equivalent single-layer discretization consisting of conventional S4R shell elements to predict laminate failure. The Abaqus/Standard® implicit solver is used to perform the numerical analyses. It is important to note that the propagation of intralaminar damage and the resulting material degradation is not part of this study.

The entire simulation setup is built by means of a Python script, to automate the complete process. In particular, the developed script was programmed to draw the part, assign the materials, apply loads, boundary conditions, create interactions, mesh parts, define the simulation steps and run the job. The quasi-pure bending load is simulated using two reference points, with the assigned eccentricity, and imposing a suitable displacement from one side. This modelling assumption was applied for both types of discretization (layerwise and equivalent single-layer), as it allows to save a considerable amount of computational time, compared to the case of modelling the complete experimental device. Furthermore, in order to increase the computational efficiency of the model based on solid elements, a finer mesh is used only in the central region, where the stress gradient is higher and it is expected to be the region where damage initiates. This central region is tied with the remaining parts using Abaqus®' Tie constraint. As the idea of this numerical study is to predict FPF with a ply failure criterion, one element per ply is implemented in all laminates. A schematic picture of the generated model is shown in Fig. 4.2.

"Hot-spot" FPF analysis Herein, the results of the "hot-spot" analysis to predict the onset of intralaminar failure in OH laminates under quasi-pure bending are presented.

In this first investigation, the objective is to identify the ply in the laminate that fails first and the corresponding failure mechanism. For this reason, the point of failure initiation is highlighted for each of the 4 investigated laminates, in the respective reaction force-displacement curves shown in Figs. 4.3-4.6. The obtained curves are very non-linear due to the geometric non-linearity of the test case, which is accounted in this numerical study. The first-ply failure mode is specified by means of a close view of the critical region for failure onset, to perform a "hot-spot" identification

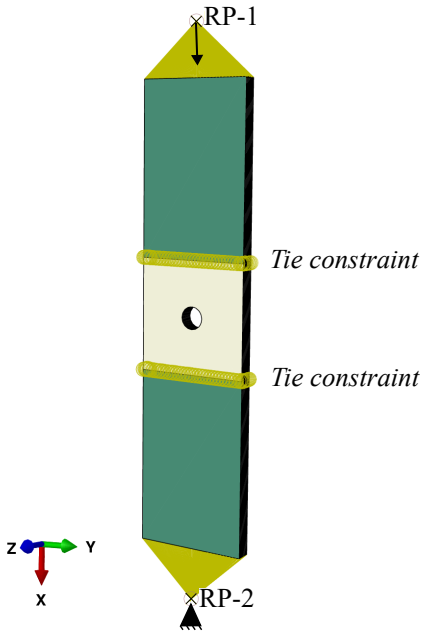


Figure 4.2: Computational solid model for an open-hole plate under quasi-pure bending.

analysis. The position of the critical ply within the laminate is an important information for this study, as bending generates local stress states in tension or compression through the thickness.

It can be observed that in the 3 laminates presented in Figs. 4.3-4.5, fibre compression FPF is predicted. Indeed, the onset of failure for these laminates is predicted at the face under local compression, due to fibre kinking. The closest ply to the surface under compression is [0] for the UD laminate, while it is [45] for the quasi-isotropic 25/50/25 and highly-oriented 50/40/10 laminates. Finally, for the 20/60/20 OH laminate, the predicted damage initiation mechanism is matrix cracking under compression of the outer 90° ply, as shown in Fig. 4.6. However, in the same laminate, the failure index of fibre kinking in the 45° ply close to the face under compression was very close to one, which means that damage is predicted to affect multiple plies from its early stage.

It should be noted that, accounting for the effect of ply thickness and position on the strengths of each ply in multidirectional laminates (i.e., *in-situ* effect), embedded plies increase the resistance to matrix cracking thanks to the constraining effect exerted by the adjacent plies with the fibres aligned along different orientations. Indeed, for most of the studied laminates, the onset of failure of the embedded plies is predicted under higher load levels, as compared to the mode inducing FPF. The correct physical representation of the mechanical response of an embedded ply in a multidirectional laminate assumes a key role for this study as the influence of the stress gradient through the thickness is predominant as compared with the in-plane stress gradient due to the presence of the hole.

The predicted failure mechanisms for damage onset are in agreement with the experimental observation from Ref. [126]. In fact, fibre kinking was observed to govern the failure scenario of all these open-hole laminates. For the multidirectional laminates, due to load redistribution,

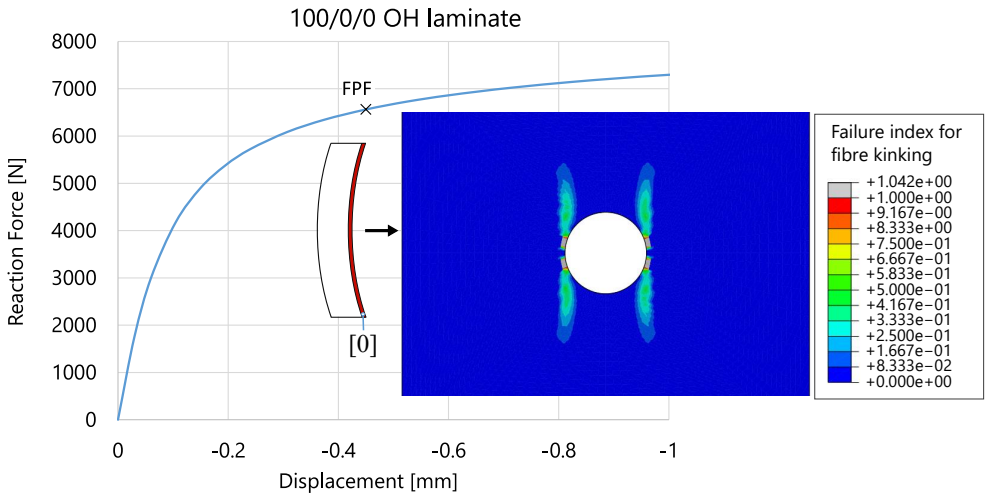


Figure 4.3: Reaction force-applied displacement plot of the 100/0/0 OH laminate under quasi-pure bending. A detailed view is provided for the identification of FPF and the corresponding critical failure mode.

failure was then suddenly observed in the experiments on the face under tension due to tensile fibre failure and transverse cracking.

"Hot-spot" failure analysis for delamination onset and growth Following the study on intralaminar failure, a first numerical approach to delamination onset is presented. It uses the computed stresses, obtained from a linear-elastic analysis, to determine the critical locations where interlaminar damage is expected to initiate. Since it is a very fast analysis tool, it is suggested for every delamination assessment study, in order to have a good starting point before performing any additional detailed investigation.

As delamination in UD laminates is unlikely to occur before ply damage, the objective of this numerical study is to simulate only the mechanical response of the 3 multidirectional laminates investigated before (quasi-isotropic 25/50/25, highly-oriented 50/40/10 and highly disoriented 20/60/20), spotting the critical location prone to delamination onset. With this aim, an additional output field is written on the FE analyses performed for FPF, in order to identify the onset of interlaminar damage by computing the failure index of Ye's stress-based criterion [75]. Then, to compare the obtained results with a more accurate method, cohesive elements are included in the numerical model to predict delamination onset and growth. To implement the latter, the resulting model uses 2 types of elements, namely C3D8R solid elements representing the plies and COH3D8 cohesive elements representing the interfaces. Both numerical approaches were run with Abaqus/Standard® implicit solver.

For the first numerical study, it is important to note that the interlaminar failure criterion is applied at the integration points of the C3D8R finite elements representing the plies, where actually intralaminar damage takes place. This is one of the reasons why this approach cannot be considered for reliable quantitative predictions, and usually provide qualitative results only. Indeed,

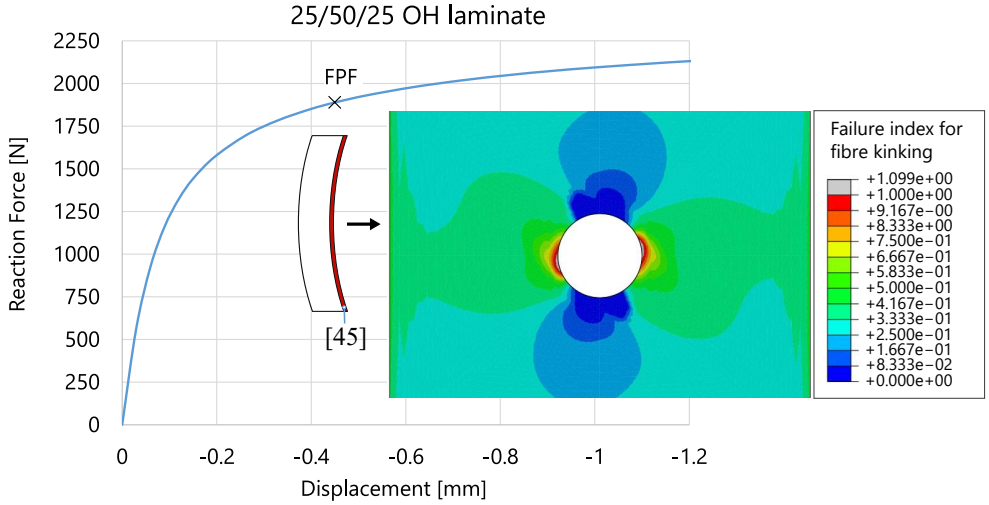


Figure 4.4: Reaction force-applied displacement plot of the 25/50/25 OH laminate under quasi-pure bending. A detailed view is provided for the identification of FPF and the corresponding critical failure mode.

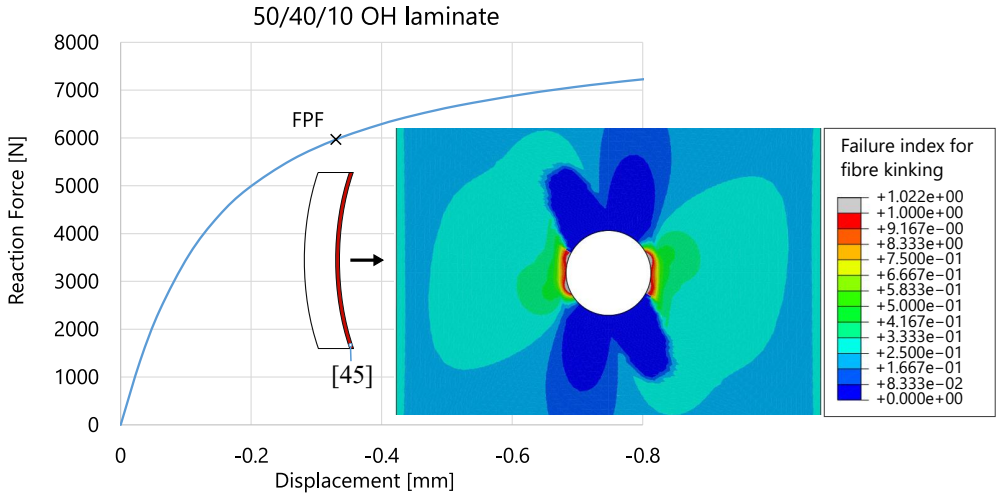


Figure 4.5: Reaction force-applied displacement plot of the 50/40/10 OH laminate under quasi-pure bending. A detailed view is provided for the identification of FPF and the corresponding critical failure mode.

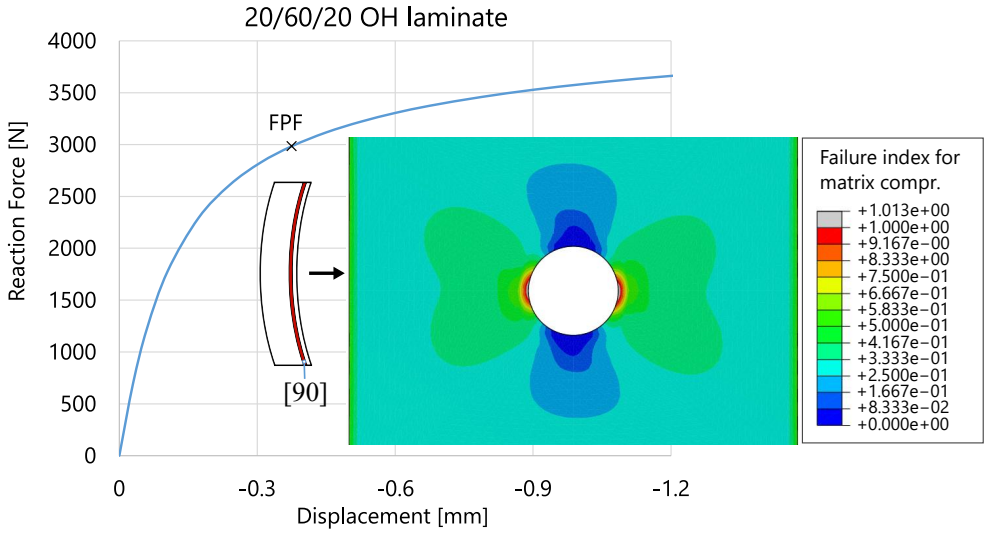


Figure 4.6: Reaction force-applied displacement plot of the 20/60/20 OH laminate under quasi-pure bending. A detailed view is provided for the identification of FPF and the corresponding critical failure mode.

to perform a quantitative study, Ye's criterion would need to be applied with a calibration procedure, based on experimental data to refine the element size. This data on the load level inducing delamination, however, is not available in Ref. [126].

Figs. 4.7-4.9 show the predicted onset of delamination, as highlighted for each of the 3 investigated laminates, in the respective reaction force-displacement curves. Furthermore, the FPF point is specified to compare the different load levels required to initiate ply damage and delamination. A close view of the critical region for each failure onset is provided in the figure, for a clear identification of the locations where the failure index is equal to one. The face on the top surface, in Figs. 4.7-4.9, is the face subjected to local compression due to bending. As a reminder for the reader, the evolution of damage and the resulting material degradation is not part of this study.

The obtained results show that, for each of the 3 cases, delamination is not a critical failure mode, as FPF is predicted to occur with a lower applied displacement. Neglecting the effect of ply damage broadening, high out-of-plane stresses due to quasi-pure bending are predicted for the quasi-isotropic and highly-disoriented laminates, in the vicinity of the outer 90° plies, and to promote delamination cracks. The onset of delamination in these 90° plies can be observed in Fig. 4.7 and Fig. 4.9. On the other hand, in the highly-oriented laminate shown in Fig. 4.8, delamination is predicted to initiate in the vicinity of the two blocked 0° plies close to the face under local compression. This kind of results are very useful for structural applications, as they allow a preliminary assessment of the importance of a detailed analysis on delamination events. Therefore, as a final remark for this test case, interlaminar damage is not critical in the first stage of failure but it can contribute to the propagation phase.

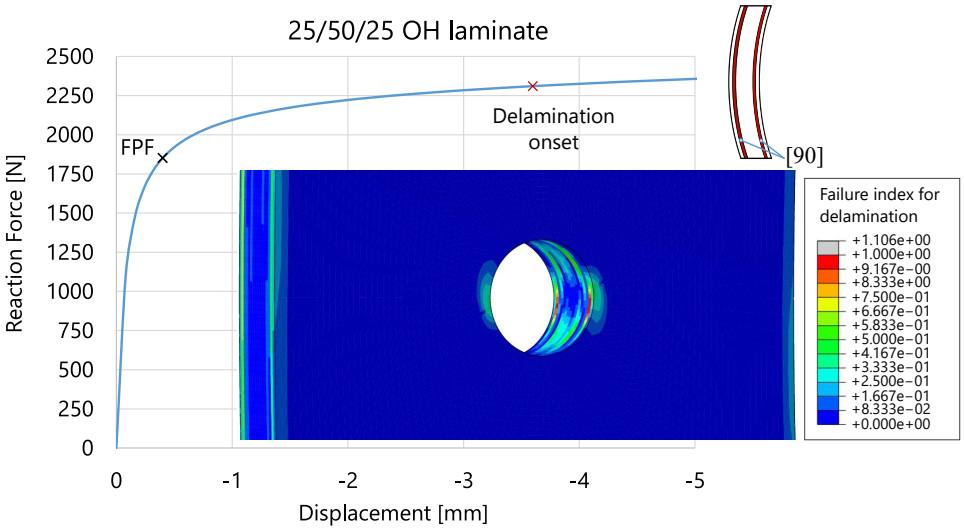


Figure 4.7: Reaction force-applied displacement plot of the 25/50/25 OH laminate. A detailed view is provided for the identification of the onset of delamination, by means of the Ye's criterion failure index.

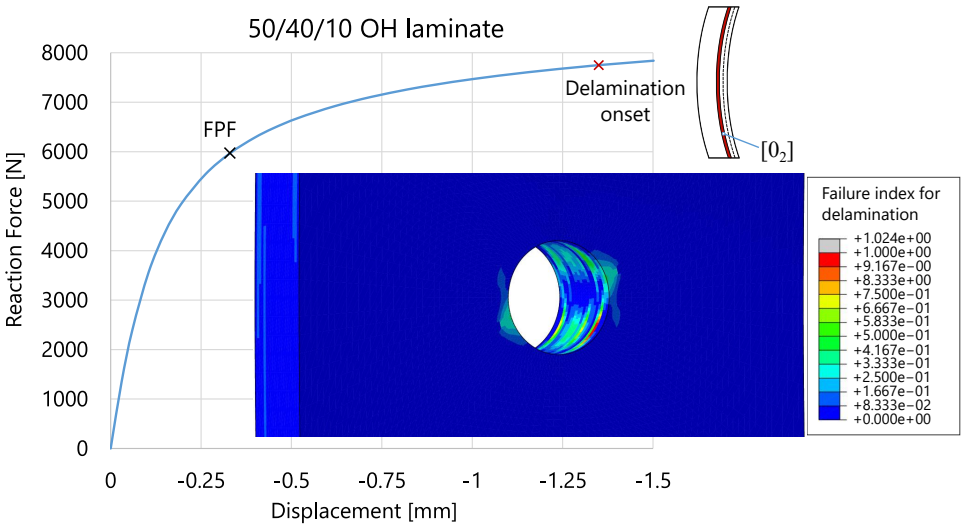


Figure 4.8: Reaction force-applied displacement plot of the 50/40/10 OH laminate. A detailed view is provided for the identification of the onset of delamination, by means of the Ye's criterion failure index.

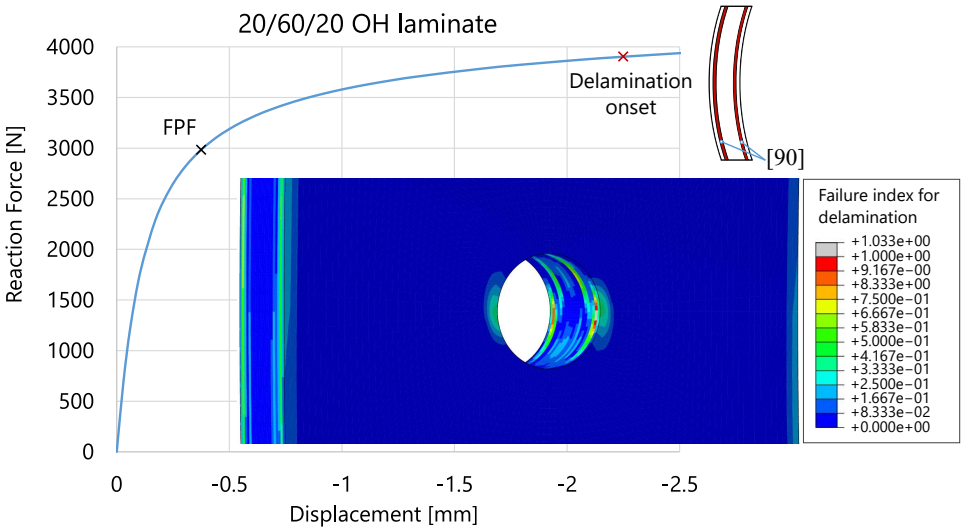


Figure 4.9: Reaction force-applied displacement plot of the 20/60/20 OH laminate. A detailed view is provided for the identification of the onset of delamination, by means of the Ye's criterion failure index.

To complement this numerical study on delamination, an additional FEA was performed including cohesive elements between plies with different orientations. The constitutive response of cohesive elements, as described in Section 2.4.1, was implemented for an accurate representation of the onset of delamination and its propagation.

As explained in Section 2.4.1, damage propagation leads to convergence issues in implicit FE solvers and a common option offered by the solvers is to use a viscous regularization parameter, which can aid numerical analyses to achieve convergence. On the other hand, this parameter can affect the global material response, so a preliminary sensitivity study is required for assessing its reliability. For the present analysis, just few modifications in the general solution controls were implemented and the modified parameters are shown in Table 4.3.

To perform this work, additional material properties need to be defined, complementing the ones introduced in Table 4.1. These properties, defined in Table 4.4, are the interlaminar properties required for the implementation of cohesive elements. In particular, they include: the penalty stiffness (K) that theoretically tends to infinity but due to numerical constraints it is assumed 10^6 N/mm^3, the thickness of cohesive elements (t_c), the mode I and mode II interlaminar fracture toughness (respectively $\mathcal{G}_{\mathrm{Ic}}$ and $\mathcal{G}_{\mathrm{IIc}}$), the BK mixed-mode interaction parameter (η) [95] and the through-thickness strengths (τ_3^0 and τ_1^0), assuming that τ_1^0 and τ_2^0 have the same value.

Fig. 4.10 shows the predicted evolution of interlaminar damage for the considered multidirectional OH laminates, for different levels of applied displacement. Delamination can be identified through the damage variable on cohesive elements, SDEG, implemented in Abaqus®. Note that the damage variable of the cohesive elements is calculated using Eq. (2.52). The state variable ranges from 0, identifying the undamaged state, to 1, when the element is fully damaged.

For the quasi-isotropic OH laminate, delamination is predicted to initiate between the 0° and 45° plies, being the fourth and fifth ply from the side under local compression. The 50/40/10

Table 4.3: Modified solution control parameters to overcome convergence problems related with Abaqus/Standard® cohesive elements.

Parameter	Description	Value
Field equations - displacement		
R_n^α	convergence criterion for the ratio of the largest residual to the corresponding average flux norm for convergence (default: 5×10^{-3})	0.10
C_n^α	convergence criterion for the ratio of the largest solution correction to the largest corresponding incremental solution value (default: 10^{-2})	1.0
Time incrementation		
I_0	number of equilibrium iterations (without severe discontinuities) after which the check is made whether the residuals are increasing in two consecutive iterations (minimum: 3; default: 4)	10
I_R	number of consecutive equilibrium iterations (without severe discontinuities) at which logarithmic rate of convergence check begins (default: 8)	10
I_C	upper limit on the number of consecutive equilibrium iterations (without severe discontinuities), based on prediction of the logarithmic rate of convergence (default: 16)	500
I_A	maximum number of cutbacks allowed for an increment (default: 5)	50
Line search control		
N^{ls}	maximum number of line search iterations (default: 0 for steps that use the Newton method and 5 for steps that use the quasi-Newton method)	4.0
S_{max}^{ls}	maximum correction scale factor (default: 1.0)	4.0
S_{min}^{ls}	minimum correction scale factor (default: 0.0001)	0.25
η^{ls}	ratio of new to old correction scale factors below which line searching terminates (default: 0.10)	0.15

Table 4.4: Interlaminar material properties of T700GC/M21 UD tape.

Property	Value	Units
K	1.0×10^6	N/mm^3
τ_3^0	46.0	MPa
τ_1^0	Calculated from Ref. [90]	MPa
$\mathcal{G}_{\mathrm{Ic}}$	0.35	N/mm
$\mathcal{G}_{\mathrm{IIc}}$	1.50	N/mm
η	2.0	-
t_c	1.0×10^{-2}	mm

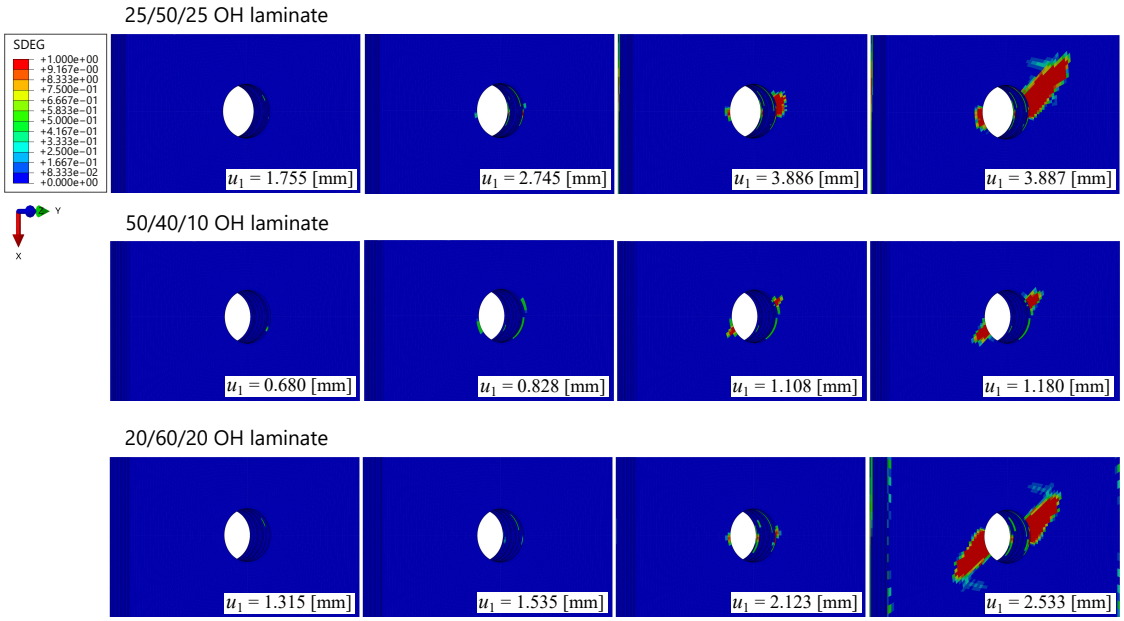


Figure 4.10: Evolution of interlaminar damage for 25/50/25, 50/40/10 and 20/60/20 OH laminates.

laminate contains blocked 0° plies which trigger the onset of delamination, which indeed starts between the two 0° plies and -45° ply, as shown in Fig. 4.10. Finally, for the 20/60/20 OH laminate, the onset of interlaminar damage is predicted to take place between the 0° and 45° plies, being the fifth and sixth ply from the face under local compression. Despite degradation initiates in different locations, the evolution of delamination is predicted to take place in the outer interface under compressive stress state for all the investigated laminates.

Fig. 4.11 shows a more detailed view of the predicted delamination for the three investigated multidirectional laminates. Using a visualization option in Abaqus®, it was possible to select different colors for highlighting the cohesive elements partially damaged (in green, with a damage variable between 0.10 and 0.99), the ones where damage is in its early stage (in blue, with a damage variable between 0.001 and 0.10) and the ones severely damaged (in red, with a damage variable greater than 0.99). The elements that are not damaged take an initial color which has been set as white. Furthermore, a suitable global translucency value has been selected to allow the reader to have a complete overview of the interlaminar damage in the laminate.

The results show clearly that the first interface, from the top surface subjected to local compressive stress state, is the one expected to delaminate quickly for each of the considered stacking sequences. This means that the layup has a lower influence to delamination growth with respect to the stress gradients imposed by the test. In fact, the three lamination sequences are very dissimilar, as well as the applied displacement at delamination onset. Additionally, we can observe few differences in the predicted broadening of interlaminar damage. In particular, the 20/60/20 laminate represents the only case where a considerable interlaminar damage is predicted at the free edges, while in the quasi-isotropic laminate (Fig. 4.11a) the delamination is predicted to grow mainly from the hole towards one side, instead of a symmetric propagation as for the other two cases.

Although the reliability of the first method (based on Ye's criterion) is arguable, as discussed in the previous paragraphs, the predicted onset of delamination can be exploited as a first indication for a detailed study on the propagation of interlaminar damage, using cohesive elements. In fact, it can be observed that the applied displacement corresponding to delamination onset in the "hot-spot" analysis is similar to the one inducing a quick delamination growth on the outer interface, predicted with recourse to cohesive elements. This methodology enables to assess the differences in predictions between Ye's failure criterion and the quadratic nominal stress criterion (Abaqus®' Quads Damage), even if the Ye's criterion is computed on the plies and the second criterion on the interfaces. Observing the results, it is possible to appreciate a good agreement between the two criteria for identification of the location of delamination onset.

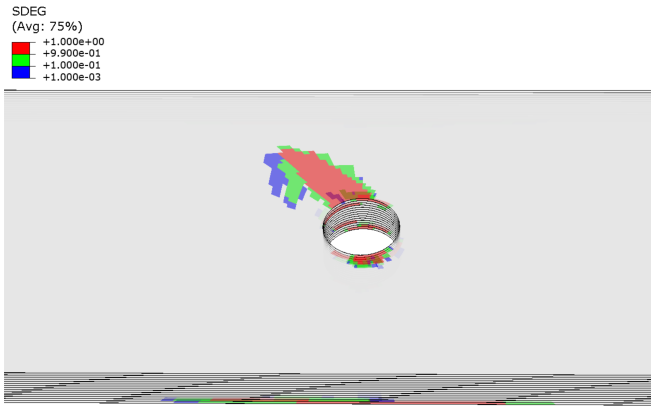
"Hot-spot" LPF analysis The research work on OH laminates subjected to quasi-pure bending has been an interesting test case for "hot-spot" failure tools predicting the onset of ply damage and delamination. As a final investigation, "hot-spot" failure analysis will be applied to predict the load level corresponding to final failure, as predicted by the unit circle failure theory presented in Section 2.5.

With this aim, OH laminates are modelled with an equivalent single-layer discretization, with 5 integration points along the thickness to capture the through-thickness stress gradient. The numerical results for the same open-hole laminates (UD 100/0/0, quasi-isotropic 25/50/25, highly-oriented 50/40/10 and highly-disoriented 20/60/20) are shown in Figs. 4.12-4.15. For these laminates, the plots include the respective reaction force-displacement curve in green and a detailed view of the output field at laminate failure.

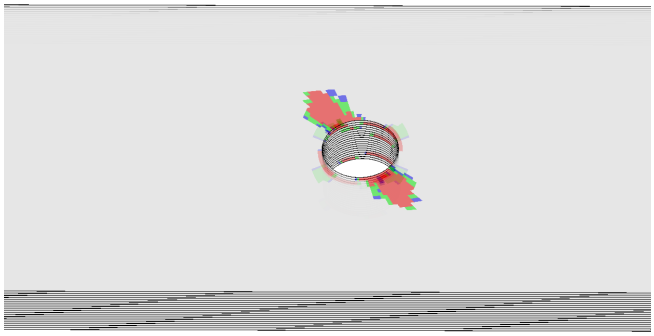
It should be noted that the implemented 4-node quadrilateral finite elements with reduced integration (S4R) are formulated under the assumption of plane stress conditions, therefore, the resulting model does not account for the out-of-plane component of the stress. Moreover, the unit circle criterion is a strain-based laminate failure theory which does not account for damage evolution in the stress concentration in open-hole laminates.

Laminate failure for all the studied layups is predicted to occur when applying a higher displacement than the one predicted to lead to FPF. This is coherent with the formulation of the failure theories, predicting FPF and LPF. The failure locations for the 100/0/0 laminate are the same as the one predicted with the detailed meso-scale model based on solid elements. Therefore, fibre kinking is predicted to govern failure onset and lead to laminate collapse, as expected in UD laminates. For multidirectional layups, the equivalent single-layer discretization based on shell elements does not predict the exact location (or multiple locations) within the laminate leading to catastrophic failure, but it highlights, at a macroscopic level, the critical locations and stress level leading to laminate failure.

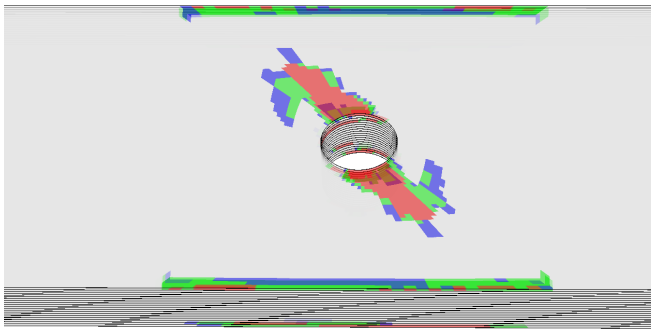
As a final and important remark, the computational cost of these simulations is compared. As expected, the computational cost of the model with solid elements is remarkably higher than the computational cost of the shell-based models. In fact, using 8 CPUs and the same computer system, the CPU time is around 60 minutes when using solid elements, while only about 40 seconds



(a) Damage variable of the cohesive elements for the 25/50/25 OH laminate. The applied displacement is 3.89 mm.



(b) Damage variable of the cohesive elements for the 50/40/10 OH laminate. The applied displacement is 1.98 mm.



(c) Damage variable of the cohesive elements for the 20/60/20 OH laminate. The applied displacement is 2.53 mm.

Figure 4.11: Damage variable of the cohesive elements for the 3 OH laminates investigated, for an applied displacement larger than the one corresponding to the respective delamination onset.

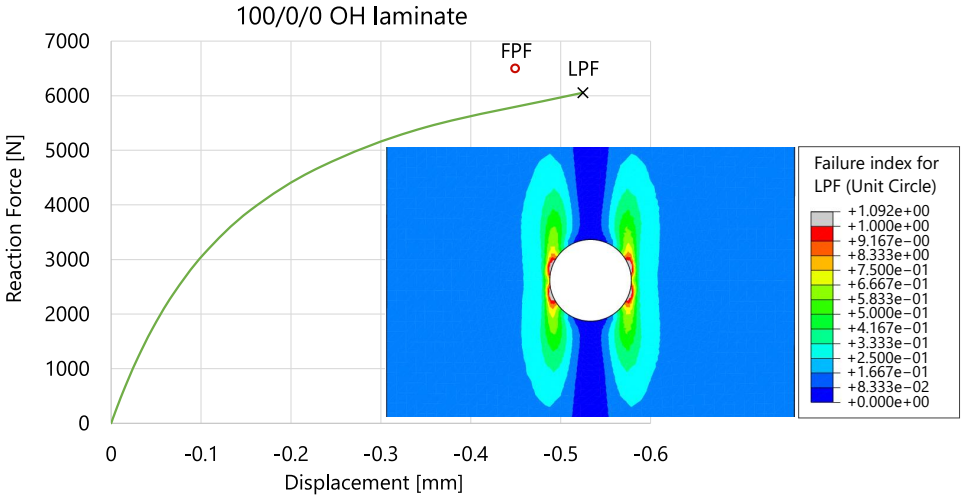


Figure 4.12: Reaction force-applied displacement curve of the 100/0/0 OH laminate subjected to quasi-pure bending. These numerical results are obtained using an equivalent single-layer discretization. A detailed view is provided for the identification of laminate failure, as predicted by the unit circle failure criterion.

with shell elements, which allows a huge saving in terms of computational time.

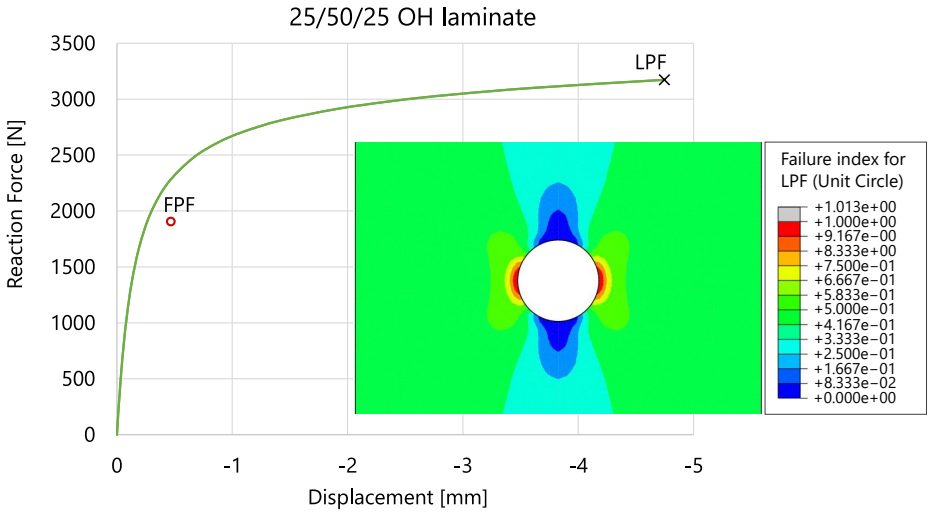


Figure 4.13: Reaction force-applied displacement curve of the 25/50/25 OH laminate subjected to quasi-pure bending. These numerical results are obtained using an equivalent single-layer discretization. A detailed view is provided for the identification of laminate failure, as predicted by the unit circle failure criterion.

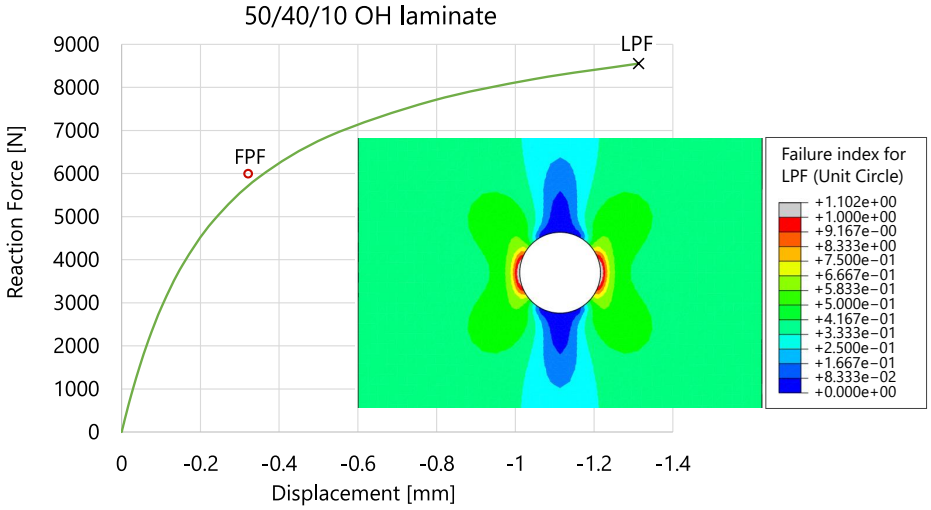


Figure 4.14: Reaction force-applied displacement curve of the 50/40/10 OH laminate subjected to quasi-pure bending. These numerical results are obtained using an equivalent single-layer discretization. A detailed view is provided for the identification of laminate failure, as predicted by the unit circle failure criterion.

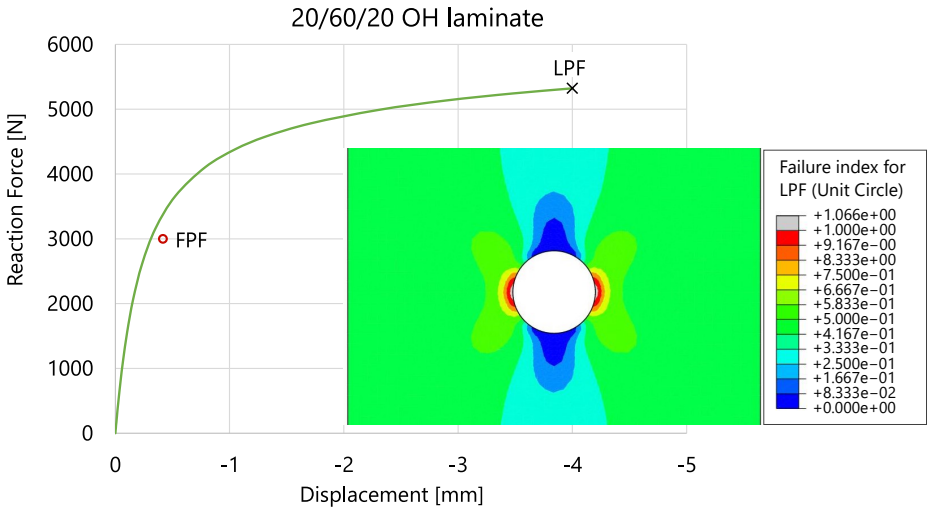


Figure 4.15: Reaction force-applied displacement curve of the 20/60/20 OH laminate subjected to quasi-pure bending. These numerical results are obtained using an equivalent single-layer discretization. A detailed view is provided for the identification of laminate failure, as predicted by the unit circle failure criterion.

4.3 Application on a stringer run-out for "hot-spot" failure analysis

In this section, the "hot-spot" failure analysis is applied to an aeronautical reinforced panel, targeting the identification of the critical locations for damage onset in the runout region. The structure under analysis is composed of a flat composite skin, a composite T-stringer and two bolts. The skin and the stringer are made from unidirectional CFRP pre-preg material IMA/M21E, while the bolts are made from stainless steel.

The stringer in this case is manufactured by joining two L-shaped components, each of them characterized by the following stacking sequence: [45/-45/90/-45/45]. The layup of the skin is defined as: $[45/0/-45/0_2/90/-45/0/45/0]_s$. The interaction between skin and stringer is simulated by using the "Tie constraint" available on Abaqus®.

Due to the main assumption of plane stress states, standard shell models cannot accurately estimate the full stress state, crucial for the runout region where a change of load path takes place [130]. For this reason, first-order solid elements C3D8R are used to discretize all the parts of the structure considered for this analysis. Furthermore, first-order solid elements allow to properly set the contact behaviour between stringer and bolts, and skin and bolts.

The analysis of this model is performed in two different steps: (i) a bolt load is applied to the two bolts included in the runout panels, by defining the "Pre-tension load" option of Abaqus® and using low-stiffness dummy springs attached to the head of the bolts to prevent rigid body motions in this pre-load step; and (ii) an external tensile loading is introduced by defining "Multi-point constraints" (MPCs) of Abaqus® at the two ends of the structure, one to apply the tensile loading and the other to apply the constraints, as schematically shown in Fig. 4.16. These numerical constraints couple the degrees of freedom of the master node with those identified as slave nodes, using the perfectly rigid option for this study.

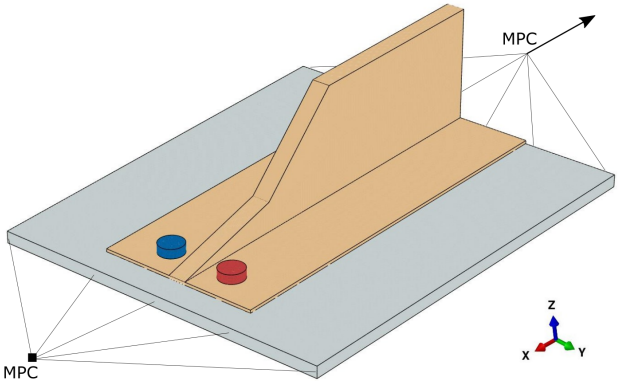


Figure 4.16: Schematic plot of the model and boundary conditions of the stringer runout.

The discretization of the model is done using one element per ply and a smaller element size in the vicinity of the bolts, where a stress concentration is expected. Then, after running a linear-elastic analysis using Abaqus/Standard® and including the effect of geometric non-linearities, a postprocessing script was run to perform a "hot-spot" failure analysis with the 3D invariant-based

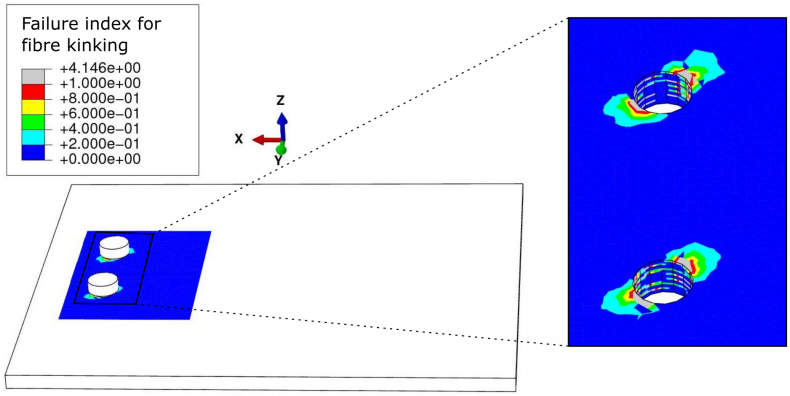


Figure 4.17: "Hot-spot" failure analysis in the runout region for the skin. The predictions for failure onset are computed using the 3D invariant-based failure theory and, in this case, the critical failure index is for fibre kinking.

failure theory. Given the large dimension of the model, this study was perform in the regions close to the runout for both skin and stringer, where FPF was expected to take place.

The results of the "hot-spot" failure analysis are shown in Figs. 4.17-4.19. In particular, Fig. 4.17 shows that the onset of damage in the skin region close to the runout is triggered by fibre kinking. As it can be observed in the zoomed view, failure initiation takes place in all the plies of the laminate, in the vicinity of the bolts. A similar failure scenario can be seen when plotting the output field of the critical failure indices of the stringer. In fact, Figs. 4.18 and 4.19 show that the critical failure locations at the bottom surface of the stringer are matching the ones at the top surface of the skin, as expected. However, in this case, fibre kinking is not the only critical failure mode but it occurs together with matrix tensile failure. Fibre kinking is predicted to initiate in the last three plies (90°/-45°/45°), while matrix cracking is expected only in the middle 90° ply. Experimental results validated the qualitative predictions obtained with this approach[1].

[1]This research work was carried out during the virtual secondment at the University of Seville and the confidential experimental study used for the validation analysis cannot be disclosed in this thesis.

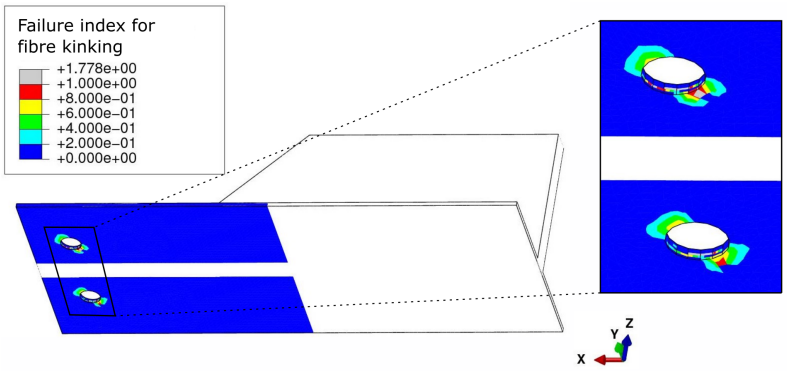


Figure 4.18: "Hot-spot" failure analysis in the runout region for the stringer. The predictions for failure onset are computed using the 3D invariant-based failure theory and, in this case, the critical failure index is for fibre kinking.

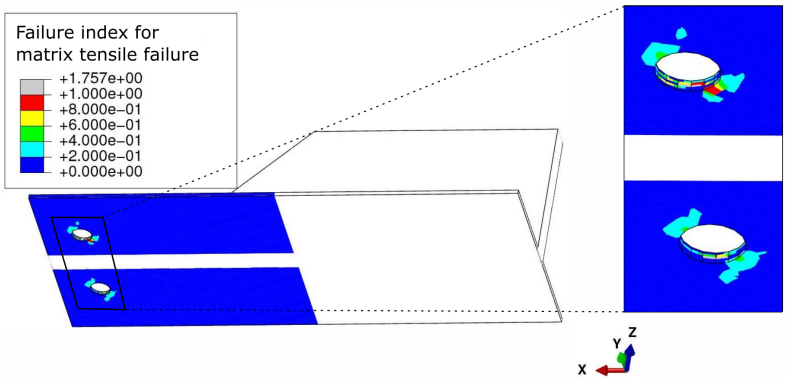


Figure 4.19: "Hot-spot" failure analysis in the runout region for the stringer. The predictions for failure onset are computed using the 3D invariant-based failure theory and, in this case, the critical failure index is for matrix tensile failure.

4.4 Final remarks

In this work, a numerical approach to predict failure of FRPs at the ply and laminate level, within a FE framework, was presented. In particular, a failure prediction method, known as "hot-spot" failure identification, was implemented to predict the onset of intralaminar failure (or FPF), delamination and final collapse (or LPF). The described methodology has the aim to predict the stress level corresponding to failure events and to highlight the regions in the FE model where the failure index is equal to one.

For this scope, a set of 3D invariant-based failure criteria, was implemented in a FE code to perform "hot-spot" FPF analysis and identify the critical locations for damage onset and the corresponding ply failure modes. Then, to identify the onset of delamination, the Ye's failure criterion was implemented in an additional numerical tool. Furthermore, a simplified failure theory to be applied at the laminate level, called unit circle, was also implemented to perform "hot-spot" LPF analysis, with recourse to models with an equivalent-single layer discretization. Two test cases were selected for the validation of "hot-spot" failure analysis at two different levels: at the coupon level, open-hole laminates with different layups were tested under quasi-pure bending; at the structural level, a stringer runout loaded in tension was analyzed. For both cases, experimental results were available to assess the performance of the implemented methods.

The "hot-spot" failure analysis resulted satisfactorily accurate in predicting the critical locations for FPF in both test cases, confirming the experimental observations on critical failure modes and locations triggering the initiation of damage. A good agreement was also achieved when predicting the critical locations for the onset of delamination. These results were confirmed using a more accurate numerical model predicting interlaminar damage, based on cohesive elements. However, since the approach based on Ye's failure theory is applied to the plies and not to the interfaces, the obtained results can be considered only qualitative and no reliable conclusions can be made from them. Finally, the "hot-spot" LPF analysis, based on the unit circle criterion, gave useful indications, with a low computational cost, on the critical stress level leading to laminate failure. The main limitation of the latter method regards the equivalent single-layer discretization using shell (S4R) elements, which does not account for the out-of-plane stress components and it is not suitable for test cases involving triaxial stress states.

Then, more complex analysis, based on cohesive elements, have been implemented for the multidirectional OH laminates under quasi-pure bending. In spite of the convergence problems characterizing this approach and the required experience in the use of non-linear FE codes, this method is the only one giving reliable predictions of delamination growth, without the need to include a pre-existing crack or delamination. The obtained results showed that the initiation of interlaminar damage was well predicted by the first analysis tool, but this approach identified the interfaces (where cohesive elements are implemented) providing more reliable predictions. Furthermore, the propagation of interlaminar damage was investigated. The obtained predictions show that, for all the studied laminates, the outer interface, from the face subjected to local compression, is the one where interlaminar damage tends to grow very quickly. In particular, the

delamination is predicted to initiate from the side edges of the hole and to propagate towards the lateral free edges in a symmetric way, except for the quasi-isotropic laminates, where the delamination grows only towards one side.

However, the influence of interlaminar stresses on failure of the investigated cases is not very high, since they first experience ply failure in the fibre compression mode considerably earlier than delamination onset. This was predicted using the 3D invariant-based failure criteria and confirmed by the experimental results from literature.

The proposed methods for "hot-spot" failure analysis are useful preliminary tools that can be used to obtain quick indications about intralaminar failure onset, the corresponding failure modes, without going through complex analysis and numerical problems. Additionally, the accurate prediction of delamination is of interest for detailed analysis and, for FRP structures where delamination is a critical failure mode. In particular, using a global-local FE approach, the computational cost of this large-scale analyses based on these methods can be drastically reduced, and their integration into an optimization process is of great interest for industrial applications.

Part III

Advanced failure models for composite materials

Chapter 5

Detailed damage model for FRPs

Although advanced failure criteria can be implemented to perform "hot-spot" FPF analysis, identifying the most critical areas for failure onset, it is not sufficient to predict the ultimate load of composite multidirectional laminates, since failure of these materials is governed by a progressive evolution of damage. Furthermore, although laminate failure theories can be used for "hot-spot" LPF analysis and predict the ultimate load of composite structures, the obtained predictions are not suitable for detailed analysis and accurate design of FRP structures, e.g., in the presence of stress concentrations. For this reason, this chapter is dedicated to detailed damage models for composite materials, aiming to address the topic of damage evolution up to collapse in laminated FRP structures.

Section 2.5 introduced the *state-of-art* approaches to model the phenomena of damage propagation. As mentioned, non-linear constitutive models defined in the context of the mechanics of continuum mediums have been developed and implemented in FE codes in recent years [65, 66]. However, CDM approaches alone cannot realistically simulate the response of the laminates that are dominated by delamination, which is discrete in nature and sensitive to the local stress fields and boundary conditions. A more effective computational approach in such cases would have to include a concurrent combination of smeared and discrete models to capture the interaction between the material and structural (or local and global) behavior. Indeed, DDM can be a suitable approach to progressive failure modelling when delamination is explicitly introduced into the model via displacement discontinuities, which they create [109].

The methodology introduced in this work consists of a composite material model proposed in the literature [131], representing the quasi-brittle behaviour of composite structures, and its extension to account for the effect of general 3D stress states in the initiation and broadening of fibre kinking using the 3D invariant-based failure theory. The formulation of the constitutive model implemented for this work is described in the following sections.

5.1 Description of the meso-scale damage model

For the present constitutive model, the mechanical behaviour prior to damage initiation was assumed to be linear-elastic. Then, for the definition of the damage model, suitable damage activation functions need to be formulated for each of the addressed failure modes. Herein, the meso-scale damage model aims at representing 3 failure mechanisms, schematically represented in Fig. 5.1: longitudinal tensile fracture, longitudinal fibre kinking failure, and transverse matrix cracking with a fracture angle α, parallel to the fibre direction and dependent on the applied stress state (σ). The micro-mechanics of these failure modes are described in detail in Section 2.2.

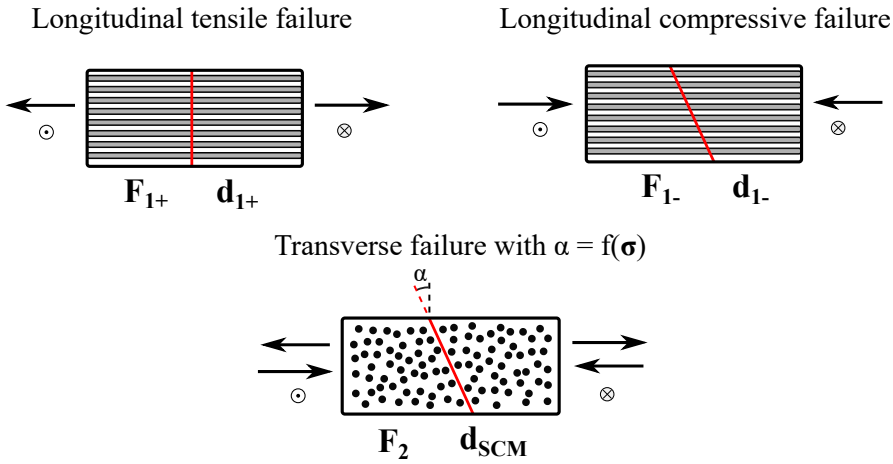


Figure 5.1: Fracture surfaces resulting from the different failure modes and corresponding damage activation and propagation functions.

To account for the effect of complex 3D stress states, the 3D invariant based failure criteria were implemented as damage activation functions, which can be found in Section 2.3.2. This set of criteria are coupled with a Smeared Crack Model (SCM) for transverse cracking and CDM models for fibre-dominated damage, which together account for the kinematics of matrix cracking and fibre tensile or compressive fracture during damage propagation. Furthermore, to predict delamination, cohesive elements are used at the interfaces between layers with different orientation. The description of the constitutive response of the implemented cohesive elements can be found in Section 2.4.1.

This mesoscale damage model was implemented in the FE package Abaqus/Explicit® [132], which is an explicit dynamics analysis solver based on the implementation of an explicit integration rule. The flowchart of the implemented model is presented in Fig. 5.2, with the cracking strain tensor being computed (iteratively as presented in Ref. [133]), while the CDM model from Refs. [65, 66] predicts the damage evolution for longitudinal failure mechanisms.

The novelty of this work on detailed failure analysis is mainly related to the description of longitudinal failure mechanisms, so in the CDM model. In particular, in the previous version of the CDM model presented in Ref. [131, 134], the 3D invariant-based kinking model (Section 2.3.2)

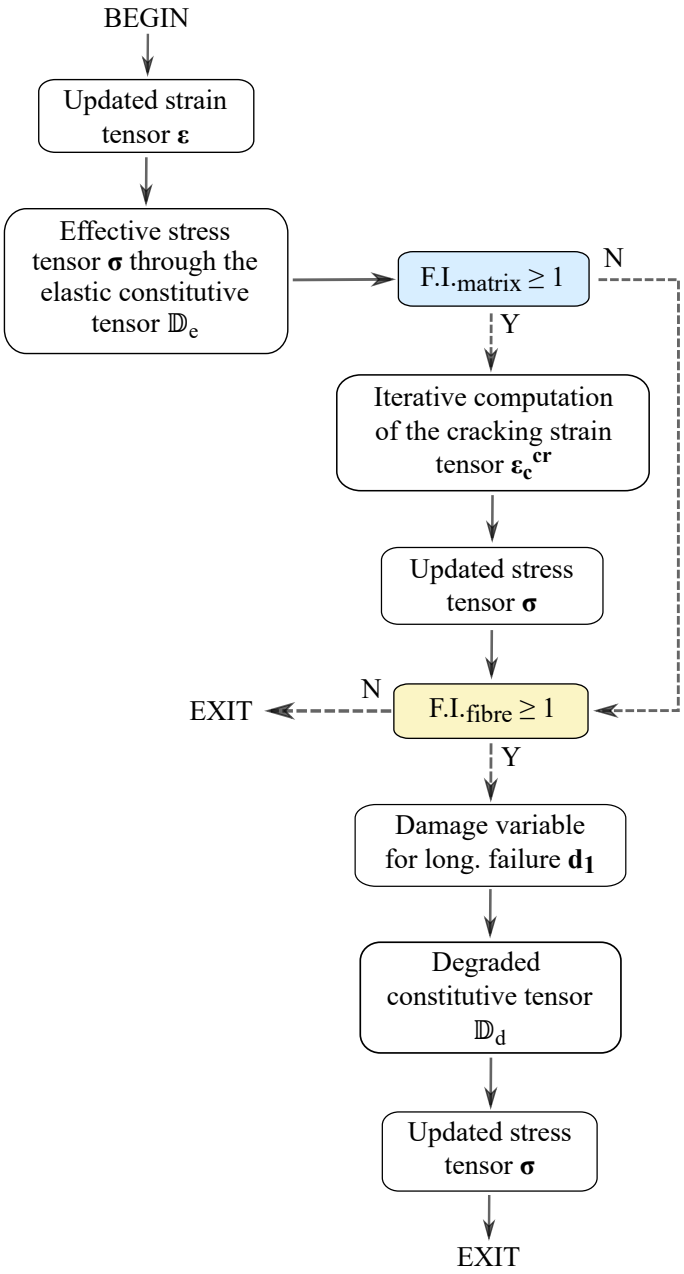


Figure 5.2: Flowchart of the meso-scale damage model.

was implemented as a damage activation function, while the damage evolution law for longitudinal compressive failure was formulated using the maximum stress criterion.

This represented a limitation of the CDM for the description of fibre-dominated damage and, for this reason, a modification in the corresponding damage evolution law is proposed in this work to account for the effects of general 3D stress states. The following sections describe the entire mesoscale damage model as illustrated in Fig. 5.2, starting with the SCM and then presenting the CDM model, including the details of the latest developments.

5.1.1 Smeared crack model for transverse matrix cracking

In this section, the formulation of the SCM for the prediction of transverse crack onset and propagation, as proposed by Camanho et al. [133] and extended by Zhuang et al. [131, 134], is presented.

The onset of transverse failure is predicted using the 3D invariant based failure criterion for matrix-dominated failure, as presented in Section 2.3.2. To ensure that transverse cracking initiates at the intersection with the failure surface, i.e., when the condition $f_M(\boldsymbol{\sigma}) = 1$ is met, an iterative scheme based on the Newton-Raphson method was employed, following Ref. [70, 135].

Exploiting the accurate prediction of the stress state at the intersection with the failure surface, the fracture angle α is calculated by means of a pragmatic approach proposed in Refs. [33, 135]. It is worth noting the orientation of the matrix-dominated fracture plane is not known in advance, as it depends on the stress state triggering matrix cracking and the material properties. However, the present model assumes the fracture plane is always parallel to the fibre direction, as suggested by the morphology of FRPs. Furthermore, the present model assumes that the angle of the fracture plane α remains constant after damage initiation. The pragmatic approach for the determination of the fracture angle α is summarized in Table 5.1.

Table 5.1: Determination of the fracture angle α, after Refs. [131, 134, 135].

Conditions	Determination of fracture angle α
$\{I_3 < 0,\ \sigma_{22} < -\lvert S_T\rvert,\ \lvert\sigma_{33}\rvert > \lvert\sigma_{22}\rvert\}$ or $\{I_3 < 0,\ \sigma_{22} > -\lvert S_T\rvert,\ \sigma_{33} < -\lvert S_T\rvert\}$	$\alpha = \operatorname{sgn}\{\sigma_{23}\}\arcsin\sqrt{\dfrac{S_T}{\min\{\lvert\sigma_{22}\rvert, \lvert Y_C\rvert\}}}$
$\{I_3 < 0,\ \sigma_{22} < -\lvert S_T\rvert,\ \lvert\sigma_{22}\rvert > \lvert\sigma_{33}\rvert\}$ or $\{I_3 < 0,\ [\sigma_{22}, \sigma_{33} > -\lvert S_T\rvert],\ [\lvert\sigma_{23}\rvert, \lvert\sigma_{22} - \sigma_{33}\rvert, \lvert\sigma_{12}\rvert, \lvert\sigma_{13}\rvert \approxeq 0]\}$	$\alpha = \operatorname{sgn}\{\sigma_{23}\}\arccos\sqrt{\dfrac{S_T}{\min\{\lvert\sigma_{33}\rvert, \lvert Y_C\rvert\}}}$
$\{[I_3 < 0,\ \sigma_{22}, \sigma_{33} > -\lvert S_T\rvert]$ or $[I_3 > 0]$ and $\lvert\alpha_1 I_1 + \alpha_3 I_3 + \alpha_{32} I_3\rvert > \lvert\alpha_2 I_2\rvert\}$	$\alpha = \arctan\left(\dfrac{\sigma_{13}}{\sigma_{12}}\right)$
$\{I_3 < 0$ and $[\lvert\sigma_{23}\rvert, \lvert\sigma_{22} - \sigma_{33}\rvert, \lvert\sigma_{12}\rvert, \lvert\sigma_{13}\rvert \approxeq 0]\}$	$\alpha = 0$
$\{[I_3 < 0,\ \sigma_{22}, \sigma_{33} > -\lvert S_T\rvert]$ or $[I_3 > 0]$ and $\lvert\alpha_1 I_1 + \alpha_3 I_3 + \alpha_{32} I_3\rvert < \lvert\alpha_2 I_2\rvert\}$	$\alpha = \dfrac{1}{2}\arctan\left(\dfrac{2\sigma_{23}}{\sigma_{22} - \sigma_{33}}\right)$

A schematic illustration of the transverse fracture plane is shown in Fig. 5.3, where the coordinate system $x_1\,x_2\,x_3$ is aligned with the material axes and the $x_1^{cr}\,x_2^{cr}\,x_3^{cr}$ cracking coordinate system ($x_1^{cr}\,x_2^{cr}\,x_3^{cr}$) is obtained with a rotation of an angle α around the x_1 axis. Therefore, the unit vector normal to the fracture plane can be expressed as follows:

$$\mathbf{n}_2 = \{0,\ \cos\alpha,\ \sin\alpha\}^T \tag{5.1}$$

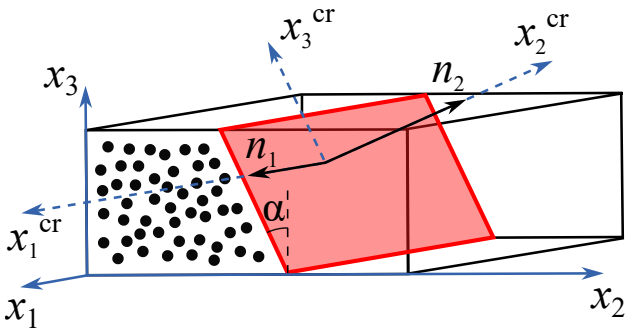


Figure 5.3: Transverse fracture plane, after Ref. [133].

The SCM uses an additive decomposition of the strain tensor, which is divided into an elastic strain $\boldsymbol{\varepsilon}_e$ and a cracking strain $\boldsymbol{\varepsilon}_c$, and it is based on a cohesive law that relates the tractions acting on the fracture plane with the corresponding displacement jumps across the crack faces. Therefore, the definition of the strain tensor by additive decomposition can be expressed as:

$$\boldsymbol{\varepsilon} = \boldsymbol{\varepsilon}_e + \boldsymbol{\varepsilon}_c = \boldsymbol{\varepsilon}_e + \mathbf{R} \cdot \boldsymbol{\varepsilon}_c^{cr} \cdot \mathbf{R}^T \tag{5.2}$$

where $\boldsymbol{\varepsilon}_c^{cr}$ is the cracking strain projected in the crack coordinate system and $\mathbf{R}$ is the rotation matrix relating the global coordinate system to that associated to the fracture plane.

The stress-strain relation is given as [133]:

$$\boldsymbol{\sigma} = \mathbb{D}_e : (\boldsymbol{\varepsilon} - \boldsymbol{\varepsilon}_c) = \mathbb{D}_e : \boldsymbol{\varepsilon} - \mathbb{D}_e : \left(\mathbf{R} \cdot \boldsymbol{\varepsilon}_c^{cr} \cdot \mathbf{R}^T\right) \tag{5.3}$$

Therefore, the tractions acting on the fracture plane, using Eq. 5.3, can be expressed as [133]:

$$\mathbf{t}^{cr} = \mathbf{R}^T \cdot (\sigma \cdot \mathbf{n}_2) = \mathbf{R}^T \cdot \left[\mathbb{D}_e : \boldsymbol{\varepsilon} - \mathbb{D}_e : \left(\mathbf{R} \cdot \boldsymbol{\varepsilon}_c^{cr} \cdot \mathbf{R}^T\right)\right] \cdot \mathbf{n}_2 \tag{5.4}$$

Following Ref. [133], the tractions can be also obtained from the cohesive law of the cracking band with the displacement jump on the fracture plane (ω^{cr}), where the latter are calculated as a function of the cracking strain tensor and the characteristic length of the finite element (l^*):

$$\omega^{cr} = \left[(2\boldsymbol{\varepsilon}_c^{cr} : \mathbf{n}_1^{cr} \otimes \mathbf{n}_2^{cr})\,\mathbf{n}_1^{cr} + (\boldsymbol{\varepsilon}_c^{cr} : \mathbf{n}_2^{cr} \otimes \mathbf{n}_2^{cr})\,\mathbf{n}_2^{cr} + (2\boldsymbol{\varepsilon}_c^{cr} : \mathbf{n}_2^{cr} \otimes \mathbf{n}_3^{cr})\,\mathbf{n}_3^{cr}\right] l^* \tag{5.5}$$

In the present implementation, l^* is taken as the square root of the in-plane area of the finite element. By expressing the cohesive law as $\mathbf{t}^{cr} = g(\omega^{cr})$ and combining Eq. 5.4 and Eq. 5.5, it results in a system of non-linear equations that can be solved for the cracking strain using an iterative method:

$$\begin{aligned} &\mathbf{R}^T \cdot \left[\mathbb{D}_e : \boldsymbol{\varepsilon} - \mathbb{D}_e : \left(\mathbf{R} \cdot \boldsymbol{\varepsilon}_c^{cr} \cdot \mathbf{R}^T\right)\right] \cdot \mathbf{n}_2 \\ &\quad = \mathbf{g}\left\{\left[(2\boldsymbol{\varepsilon}_c^{cr} : \mathbf{n}_1^{cr} \otimes \mathbf{n}_2^{cr})\,\mathbf{n}_1^{cr} + (\boldsymbol{\varepsilon}_c^{cr} : \mathbf{n}_2^{cr} \otimes \mathbf{n}_2^{cr})\,\mathbf{n}_2^{cr} + (2\boldsymbol{\varepsilon}_c^{cr} : \mathbf{n}_2^{cr} \otimes \mathbf{n}_3^{cr})\,\mathbf{n}_3^{cr}\right] l^*\right\} \end{aligned} \tag{5.6}$$

Camanho et al. [133] proposed a modified version of the constitutive model, originally proposed by Turon et al. [136], based on a linear softening cohesive law in the context of a SCM. This cohesive law defines the tractions acting on the fracture plane as follows [131]:

$$\mathbf{t}^{cr} = t_i^{cr}(d_{SCM}) = \begin{bmatrix} (1-d_{SCM})\,\dfrac{|\omega_1^{cr}|}{\omega_f^m}\,\bar{t}_1^{cr} \\ (1-d_{SCM})\,\dfrac{|\omega_2^{cr}|}{\omega_f^m}\,\bar{t}_2^{cr} \\ (1-d_{SCM})\,\dfrac{|\omega_3^{cr}|}{\omega_f^m}\,\bar{t}_3^{cr} \end{bmatrix} + \frac{\langle -\omega_2^{cr}\rangle}{|\omega_2^{cr}|} \begin{bmatrix} d_{SCM}\,\mu_L\,\dfrac{\omega_1^{cr}}{\omega_f^m}\,|t_2^{cr}| \\ t_2^{cr} - (1-d_{SCM})\,\dfrac{|\omega_2^{cr}|}{\omega_f^m}\,\bar{t}_2^{cr} \\ d_{SCM}\,\mu_T\,\dfrac{\omega_3^{cr}}{\omega_f^m}\,|t_2^{cr}| \end{bmatrix} \tag{5.7}$$

where d_{SCM} is a scalar damage variable, $\bar{t}_i^{cr}$ are the scalar components of the traction tensor on the failure plane at the onset of transverse failure, ω_i^{cr} are the scalar components of the displacement jump vector, ω_f^m is the equivalent displacement jump at failure under mixed-mode loading conditions, ε_{22}^{cr} and $\varepsilon_{c_{22}}^{cr}$ are respectively the scalar components of the total and cracking strain tensors, μ_L and μ_T are respectively the frictional coefficients in longitudinal and transverse directions, which are assumed to be the same ($\mu_L = \mu_T = \mu$), and $\langle\cdot\rangle$ is the Macauley brackets defined as $\langle x\rangle = \frac{1}{2}(x+|x|)$.

To obtain the damage variable for the SCM (d_{SCM}), a suitable loading function $\mathscr{L}$, as proposed in Ref. [136], is used:

$$d_{SCM} = \max\{0, \max[\mathscr{L}(\omega^{cr})]\} \tag{5.8}$$

with:

$$\mathscr{L}(\omega^{cr}) = \min\left\{\frac{\lambda}{\omega_f^m}, 1\right\} \tag{5.9}$$

where λ is the equivalent displacement jump defined as [133]:

$$\lambda = \sqrt{(\omega_1^{cr})^2 + (\omega_3^{cr})^2 + \langle\omega_2^{cr}\rangle^2} \tag{5.10}$$

The equivalent displacement jump at failure, ω_f^m, is defined using the BK criterion for crack propagation under mixed-mode loading conditions [133]:

$$\omega_f^m = \frac{2\,(\mathscr{G}_{\mathrm{Ic}} + AB^{\eta})}{\bar{t}^{cr}} \tag{5.11}$$

where $A = \mathscr{G}_{\mathrm{IIc}} - \mathscr{G}_{\mathrm{Ic}}$, B is the mode ratio and η is the mixed-mode interaction parameter used in the BK law, $\mathscr{G}_{\mathrm{Ic}}$ and $\mathscr{G}_{\mathrm{IIc}}$ are respectively the mode I and mode II intralaminar fracture toughness associated with transverse failure mechanisms, and $\bar{t}^{cr}$ is the norm of the traction tensor at the onset of transverse failure:

$$\bar{t}^{cr} = \sqrt{(\bar{t}_1^{cr})^2 + (\bar{t}_3^{cr})^2 + \langle\bar{t}_2^{cr}\rangle^2} \tag{5.12}$$

The subroutine including the numerical solution of Eq. 5.6 using Newton's method to solve for the cracking strain is presented in Ref. [133]. The residual for this system of non-linear equations is given as:

$$\mathbf{r}(\varepsilon_c^{cr}) = \mathbf{f}(\varepsilon_c^{cr}) - \mathbf{g}(\varepsilon_c^{cr}) \tag{5.13}$$

where $\mathbf{f}(\varepsilon_c^{cr})$ and $\mathbf{g}(\varepsilon_c^{cr})$ are respectively the left-hand side (LHS) and right-hand side (RHS) of Eq. 5.6. After reaching convergence of the iterative method, with the obtained cracking strains, the stress tensor is easily updated using Eq. 5.3.

5.1.2 Continuum damage mechanics model for longitudinal damage evolution

Following the definition of the analytical framework related to transverse matrix cracking, the onset of fibre-dominated failure is predicted using the 3D invariant-based failure theory, as illustrated in the flowchart of the implemented model (Fig. 5.2). Initiation of fibre failure activates the longitudinal damage variable d_1, which is calculated within the framework of CDM.

The damage propagation functions for longitudinal failure mechanisms must account for the different energy dissipating mechanisms associated with the propagation of a crack perpendicularly to the reinforcing fibers, which include fibre and matrix fracture and fibre-matrix debonding [133]. For this reason, Camanho et al. [133] suggest the use of the bi-linear softening laws proposed by Maimí et al. [65, 66]. This bi-linear softening is defined by the maximum stress, i.e. the longitudinal strengths (X_T and X_C), by the stress corresponding to the modification of the softening slope (the pull-out stress $X_T^{PO} = f_{XT} X_T$ in tension and the residual stress plateau $X_C^R = f_{XC} X_C$ in compression), and by the partition of the dissipated energy per unit volume associated with each linear softening regime [131]. The idea behind the formulation of the cited model relies on the fulfillment of the second law of the thermodynamics and, thus, preventing physically inadmissible damage evolution without energy dissipation.

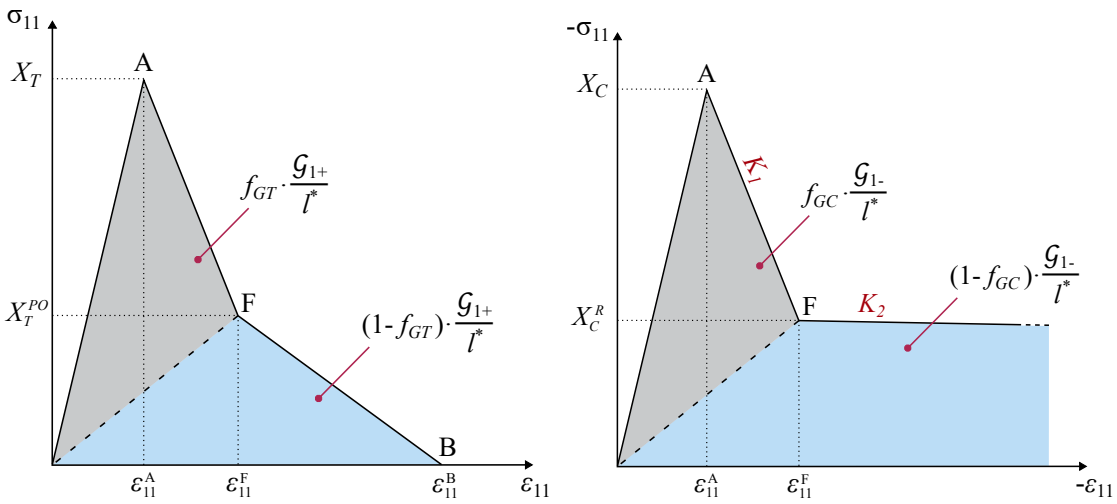
The characteristic length, l^*, introduced for the SCM, is also used for this model to ensure that the numerical solution is independent of mesh refinement, recalling the Bazant's crack band model as reference [137]. The implemented model accounts for this characteristic length by using a normalized value of the fracture toughness, which is the energy dissipated per unit volume g_M, mentioned before and defined as follows:

$$g_M = \frac{\mathcal{G}_M}{l^*}$$

where $\mathcal{G}_M$ is the fracture toughness and M allows to identify the two longitudinal damage law, under tension ($M = +1$) or compression ($M = -1$) [66].

The full details of the theoretical background and the implementation of the damage model for longitudinal failure mechanisms are given in Refs. [65, 66].

Following this damage model, Zhuang et al. [131, 134] proposed a modification to enhance the accuracy of the failure predictions using a fully 3D failure theory, such as the 3D invariant-based failure theory. However, as mentioned above, the theories defining the limit of the elastic region



(a) Bi-linear softening under longitudinal tension. (b) Bi-linear softening under longitudinal compression.

Figure 5.4: Uniaxial response under longitudinal tension (a) and longitudinal compression (b).

and the ones for the bi-linear softening law were coherent for the tensile case, being the maximum strain criterion, but not in compression, where the 3D kinking model was used only for failure onset and the maximum stress criterion for damage evolution.

This was a simplification to employ similar damage evolution laws for longitudinal tensile and compressive failure and to avoid the numerical computation of the parameters of the damage evolution law for longitudinal compressive failure mechanisms. However, this simplification suffered from the following disadvantages:

- The damage threshold variable (failure index) used for the onset of longitudinal compressive failure mechanisms may be significantly different from the one used in the propagation phase;
- Even though the effect of the stress components other than the longitudinal stress is taken into account for the onset of fibre kinking, it is not taken into account in the propagation of the kink band (this may not represent the actual physics of kink band propagation on complex, compression-dominated stress states).

To overcome these limitations in the description of kink band formation and broadening, the 3D invariant-based fibre kinking model was implemented in the corresponding damage evolution law. Therefore, for the first time, the full set of 3D invariant-based failure criteria was implemented for the onset and propagation of intralaminar damage, within a meso-scale damage model.

The details of these developments on the bi-linear longitudinal compressive softening law (Fig. 5.4b) are presented following section.

5.1.2.1 Development of a bi-linear softening law based on a 3D kink band model

Following the experimental findings of Moran et al. [138], the damage model for longitudinal compressive failure targets the prediction of the formation of a kink band, followed by linear softening until reaching a plateau, corresponding to kink band broadening at constant stress.

For a complete definition of the constitutive model, it is necessary to introduce the internal variables and the relation between the latter and the damage variables. The internal variables r_N ($N = 1+$ for longitudinal tension, $N = 1-$ for longitudinal compression) represent the elastic domain thresholds, so the level of elastic strains that can be achieved before the accumulation of additional damage, and they are also related to the damage state of each variable by the damage evolution laws [66]. When the material is undamaged, the value of r_N is lower than 1 before damage onset, where the damage variable is still equal to zero $d_N(r_N < 1) = 0$. In this model, the internal variables are implemented using the 3D invariant-based failure criteria for predicting the full post-peak response of the material.

For the definition of the bi-linear softening formulation for kink band broadening, it is required to consider separately the numerical description of each linear branch of the damage evolution law. The first branch can be characterized by the maximum stress and the stress at the inflection point (point F from Fig. 5.4b), respectively X_C and X_C^R, and by the first portion of energy dissipated per unit area, $\mathscr{G}_{XC}$. The portions of mode-I longitudinal compressive fracture energy in a kink band ($\mathscr{G}_{1-}$) are given as:

$$\mathscr{G}_{XC} = f_{GC}\mathscr{G}_{1-}$$

$$\mathscr{G}_{X_C^R} = (1 - f_{GC})\mathscr{G}_{1-}$$

where f_{GC} is the fraction of the mode-I longitudinal compressive fracture energy corresponding to the initial slope of the respective damage law, $\mathscr{G}_{XC}$ is the fracture energy for the first branch of the softening law and $\mathscr{G}_{X_C^R}$ is the fracture energy for the second branch [139]. It is noted that, to achieve a damage evolution law as shown in Fig. 5.4b, $\mathscr{G}_{XC} = \mathscr{G}_{1-}$ and $\mathscr{G}_{X_C^R}$ is given a large number [140].

In this implementation, the longitudinal component of the stress tensor at the intersection with the failure surface is used, which is denoted as X_C^*. The location of the intersection of the elastic stress vector with the failure surface is determined using an iterative scheme based on the Newton-Raphson method. This allows to compute the exact longitudinal stress (σ_{11}) triggering the onset of fibre kinking, which, for instance, coincides with X_C when the other stress components are negligible. Hence, this value will be the "effective" maximum stress of the first branch of the bilinear softening law.

The value of the strain at the deflection point F can be easily determined by considering the corresponding area of dissipated energy:

$$\varepsilon_{11}^{\mathrm{F}} = -\frac{2\mathscr{G}_{XC}E_1 + l^* X_C^* X_C^R}{l^* E_1 |X_C^*|} \tag{5.14}$$

Since the previous parameters are given from the material properties and the longitudinal stress component at failure, the characterization of the first linear softening law requires only an additional ingredient: its slope. Therefore, the slope of the first softening branch is calculated as follows:

$$K_1 = \frac{|X_C^*| - |X_C^R|}{|\varepsilon_{11}^{\mathrm{F}}| - |\varepsilon_{11}^{\mathrm{A}}|} = \frac{l^* X_C^* E_1 (X_C^* - X_C^R)}{2\mathscr{G}_{XC} E_1 - l^* X_C^* (X_C^* - X_C^R)} \tag{5.15}$$

Using a similar procedure, the second slope can be easily obtained as:

$$K_2 = \frac{0 - |X_C^R|}{|\varepsilon_{11}^{\mathrm{B}}| - |\varepsilon_{11}^{\mathrm{F}}|} = \frac{l^* (X_C^R)^2 E_1 (1 - d_{C1F})}{2\mathscr{G}_{X_C^R} E_1 (1 - d_{C1F}) - l^* (X_C^R)^2} \tag{5.16}$$

where d_{C1F} is the damage variable at the inflection point F, which is defined to be a function of just material properties. It can be noted that the slope of the first branch K_1 can be also expressed as a function of d_{C1F}:

$$K_1 = \frac{|X_C^*| - |X_C^R|}{|\varepsilon_{11}^{\mathrm{F}}| - |\varepsilon_{11}^{\mathrm{A}}|} = \frac{|X_C^*| - |X_C^R|}{\dfrac{|X_C^R|}{(1 - d_{C1F}) E_1} - \dfrac{|X_C^*|}{E_1}} \tag{5.17}$$

The determination of d_{C1F} is obtained combining Eq. 5.15 and Eq. 5.17, which is given as:

$$d_{C1F} = \frac{2\mathscr{G}_{XC} E_1}{2\mathscr{G}_{XC} E_1 - l^* X_C^* X_C^R} \tag{5.18}$$

Simple geometrical considerations allow the determination of the strain at final failure (point B):

$$\varepsilon_{11}^{\mathrm{B}} = -\frac{2\mathscr{G}_{X_C^R}}{l^* |X_C^R|} \tag{5.19}$$

It should noted that, for relatively large finite elements, the fulfillment of energy dissipation leads to a snap-back in the constitutive response. To avoid this, a critical finite element size has been introduced in the model [66], which leads to the verification of the following condition:

$$l^* \leq \frac{2E_1 \mathscr{G}_{1-}}{(X_C^*)^2} \tag{5.20}$$

where X_C^* can be approximated to X_C, since the critical FE size is required to build the FE model and, therefore, before knowing the stress state at the onset of failure. It should be noted that a critical FE size is defined in the same way for the tension case.

For the formulation of the first damage evolution law, a generic point P on the first branch of the bi-linear softening model (Fig. 5.5) can be considered. The stress at P is given as:

$$\sigma_{11}^{\mathrm{P}} = |X_C^*| - K_1 \left(|\varepsilon_{11}^{\mathrm{P}}| - \frac{|X_C^*|}{E_1} \right) \tag{5.21}$$

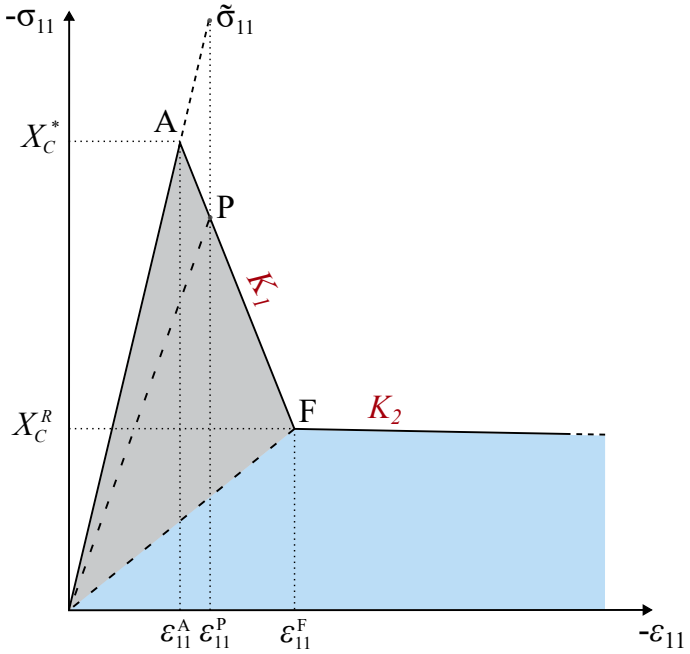


Figure 5.5: Schematic representation of the derivation of the first branch of a bi-linear damage evolution law.

Then, the constitutive relation can be written for the generic point P as follows:

$$E_1(1-d_{1-}) = \frac{\sigma_{11}^{\mathrm{P}}}{\varepsilon_{11}^{\mathrm{P}}} = \frac{|X_C^*| - K_1\left(|\varepsilon_{11}^{\mathrm{P}}| - \dfrac{|X_C^*|}{E_1}\right)}{\dfrac{|\tilde{\sigma}_{11}|}{E_1}} \tag{5.22}$$

where $\tilde{\sigma}_{11}$ is the compressive effective stress calculated as a function of the invariant-based kinking failure criterion.

Therefore, from the previous relation, the damage evolution law for the post-peak response of the material until the inflection point reads:

$$d_{1-} = \left(1 + \frac{K_1}{E_1}\right)\left(1 - \frac{|X_C^*|}{|\tilde{\sigma}_{11}|}\right) \tag{5.23}$$

The derivation of the damage law related to the second branch of the bi-linear damage law is made in a similar way, considering a point P along the second branch. The stress at generic point P on the second branch of the linear softening law is given as:

$$\sigma_{11}^{\mathrm{P}} = |X_C^R| - K_2\left(|\varepsilon_{11}^{\mathrm{P}}| - \frac{|X_C^R|}{E_1(1-d_{C1F})}\right) \tag{5.24}$$

Therefore, for a generic point P along the second branch of the damage law, the constitutive relation can be expressed as:

$$E_1(1-d_{1-}) = \frac{\sigma_{11}^{\mathrm{P}}}{\varepsilon_{11}^{\mathrm{P}}} = \frac{|X_C^R| - K_2\left(|\varepsilon_{11}^{\mathrm{P}}| - \dfrac{|X_C^R|}{E_1(1-d_{C1F})}\right)}{\dfrac{|\tilde{\sigma}_{11}|}{E_1}} \tag{5.25}$$

Then, using the previous relation, the damage propagation law after the inflection point of the bi-linear softening law is formulated as follows:

$$d_{1-} = 1 - \frac{|X_C^R|}{|\tilde{\sigma}_{11}|} + \frac{K_2}{E_1\,(1-d_{C1F})}\left(1 - d_{C1F} - \frac{|X_C^R|}{|\tilde{\sigma}_{11}|}\right) \tag{5.26}$$

It should be noted that the implementation of the damage evolution law relies on the invariant-based failure criterion for fiber kinking through the longitudinal component of the stress tensor at failure onset (X_C^*). This implementation has, therefore, a low computational cost as, after the onset of damage, the calculation of the internal variable for fibre kinking is not required.

After computing the damage variable d_1 for fibre-dominated failure mechanisms, which can be triggered by longitudinal tensile or compressive failure (depending on the sign of σ_{11} inducing damage), the updated stress tensor is calculated from the degraded constitutive tensor $\mathbb{D}_{\mathrm{d}}$. The nonzero components of the degraded constitutive tensor are given as:

$$\begin{aligned}
D_{11} &= \frac{E_{11}^2(\nu_{23}-1)(1-d_1)}{E_{11}(\nu_{23}-1)+2\nu_{12}^2E_{22}(1-d_1)}\\
D_{12} &= D_{21} = \frac{-E_{11}E_{22}\nu_{12}(1-d_1)}{E_{11}(\nu_{23}-1)+2\nu_{12}^2E_{22}(1-d_1)}\\
D_{13} &= D_{31} = D_{12}\\
D_{22} &= D_{33} = \frac{-E_{22}\left[E_{11}-\nu_{12}^2E_{22}(1-d_1)\right]}{E_{11}(\nu_{23}^2-1)+2\nu_{12}^2(1+\nu_{23})E_{22}(1-d_1)}\\
D_{23} &= D_{32} = \frac{-E_{22}\left[\nu_{23}E_{11}+\nu_{12}^2E_{22}(1-d_1)\right]}{E_{11}(\nu_{23}^2-1)+2\nu_{12}^2(1+\nu_{23})E_{22}(1-d_1)}\\
D_{44} &= D_{66} = G_{12}\\
D_{55} &= G_{23}
\end{aligned} \tag{5.27}$$

5.2 Verification studies

This Section presents the verification studies of the mesoscale damage model proposed in this work, as described in Section 5.1, and implemented in Abaqus/Explicit® by means of a VUMAT user subroutine.

The goal of these quantitative studies is to assess the numerical results for simple test cases, performed on single cubic elements under different loading conditions. This is an important step that is required to check multiple aspects of implemented numerical model, such as the obtained solutions and the rate of convergence of the implemented numerical methods. Then, as an intermediate step before addressing multidirectional laminates, a verification study was performed at the coupon level, predicting failure of unidirectional off-axis specimens.

5.2.1 Single element tests

5.2.1.1 Verification tests for fibre-dominated failure mechanisms

A preliminary verification study of the meso-scale damage model was firstly performed at the single element level, to check its correct numerical implementation. Herein, the tests involving fibre-dominated failure mechanisms are presented. Therefore, the objective of this Section is to verify the implementation of the CDM model, by analyzing the obtained results, mainly focussing on the onset and broadening of fibre failure.

Firstly, single elements under longitudinal tension and compression were tested, being the uniaxial cases involving fibre-dominated failure and longitudinal damage progression. These simple stress states were imposed by means of null-displacement and velocity boundary conditions applied to the surfaces of the element. The material selected for the present verification studies is IM7/8552 carbon-epoxy UD tape. The properties of this material are reported in Table 5.2, where: E_1, E_2, E_3 are the Young's moduli, G_{12}, G_{23}, G_{13} are the shear moduli, ν_{12}, ν_{23}, ν_{13} are the Poisson's ratios and ρ is the material density. S_T and S_L, are respectively the transverse and in-plane shear strengths, X_C and X_{BC} are respectively the longitudinal uniaxial and biaxial compressive strengths, X_T and X_{BT}, are respectively the longitudinal uniaxial and biaxial tensile strengths, Y_C and Y_{BC} are respectively the transverse uniaxial and biaxial compressive strengths, and Y_T and Y_{BT}, are respectively the transverse uniaxial and biaxial tensile strengths. Then, $\mathcal{G}_{\mathrm{Ic}}$ and $\mathcal{G}_{\mathrm{IIc}}$ are respectively the fracture toughness under pure mode I and under pure mode II loading, $\mathcal{G}_{1-}$ and $\mathcal{G}_{1+}$ are respectively the steady state propagation values of the fracture toughness for tensile fracture propagation and for kinkband formation, while η is the mixed-mode interaction parameter used in the BK law and μ is the frictional coefficient implemented in the SCM.

For these single element tests, a cubic 8-node linear hexahedral finite element with reduced integration (C3D8R) was used. Abaqus/Explicit® [132] FE code was used to mechanical behaviour of the element up to collapse, by means of the damage model implemented in a VUMAT subroutine, written in "FORTRAN 90". The obtained results are shown in Fig. 5.6, including the evolution of longitudinal stress σ_{11} and fibre-dominated damage variable d_1 with longitudinal

strain ε_{11} for a single element of 1 mm^3 (1.0 $\times$ 1.0 $\times$ 1.0 mm^3), under longitudinal tension and compression.

It can be observed that the evolution of the longitudinal stress and damage variable are correctly captured up to collapse. In particular, the stress level at onset of failure under uniaxial tension and compression are well predicted and the evolution of the damage variable d_1 follows the expected curve. The change in softening slope can be appreciated mainly in the tensile case, as the portion of dissipated energy in the first branch $(f_{GT} \cdot \mathscr{G}_{1+})$ is assumed to be significantly higher than the one in the second branch $((1 - f_{GT}) \cdot \mathscr{G}_{1+})$. In fact, on the other hand, the bilinear softening law under compression is characterized by two branches with a similar slope (i.e. K_1 is similar to K_2, from Fig. 5.5), as well as the two portions of dissipated fracture energy.

Additionally, the uniaxial compression test was used to verify that the damage variable for fibre-dominated failure (d_1) and the kinking angle (φ) grow exponentially with longitudinal strain until final failure, which occurs when d_1 is equal to 1. These results are shown in Fig. 5.7. The first predicted kinking angle, at failure onset, is equal to 19.2°, which triggers the computation of the material degradation by using the damage variable d_1.

It should be noted that damage variable for fibre-dominated failure under compression is not expressed as a function of its internal variable r_{1-}, which would require the calculation of the kinking angle. This is just the case of softening under longitudinal tension, where the damage variable d_{1+} is defined using its internal variable r_{1+}. Hence, both variables, d_{1-} and φ, are characterized by an exponential law but they are not coupled. Indeed, after the initiation of fibre kinking, the degradation model only uses the longitudinal component of the stress tensor at the intersection with the failure surface (X_C^*) to determine d_1; therefore the kinking failure model is no longer required. Furthermore, the exponential evolution of the kinking angle with longitudinal strain is not supported by experimental evidence, which actually proves that the kinkband width and orientation remain constant [141]. Moreover, it was not in the initial scope of the 3D invariant-based failure criteria, that simply predict FPF and the corresponding fracture angle.

Then, a more complex test was run to verify the material response of IM7/8552 under an increasing level of longitudinal compression and constant biaxial transverse pressure. This verification study is performed on a single C3D8R element of 100 µm^3 (0.1 $\times$ 0.1 $\times$ 0.1 mm^3).

The results of this test are shown in Fig. 5.8. In particular, in Fig. 5.8a, the obtained results for this test are compared to the ones under uniaxial longitudinal compression, in order to highlight the effect of the applied biaxial transverse pressure. Fig. 5.8b then, provides the comparison between the results obtained with the proposed damage model and its previous version.

It can be observed, in Fig. 5.8a, that the implemented damage model is able to capture the increase of longitudinal compressive strength due to hydrostatic effect, by means of the implemented 3D invariant-based failure criteria as damage activation functions. Furthermore, the softening curves are well approximated until final collapse, which occurs at two different longitudinal strains, confirming that the energy dissipated due to degradation is the same. The exact values of strain at failure (calculated using Eq. 5.19) are verified by means of a numerical script. Finally, Fig. 5.8b shows how the previous model was also able to capture the onset of fibre kinking, but the

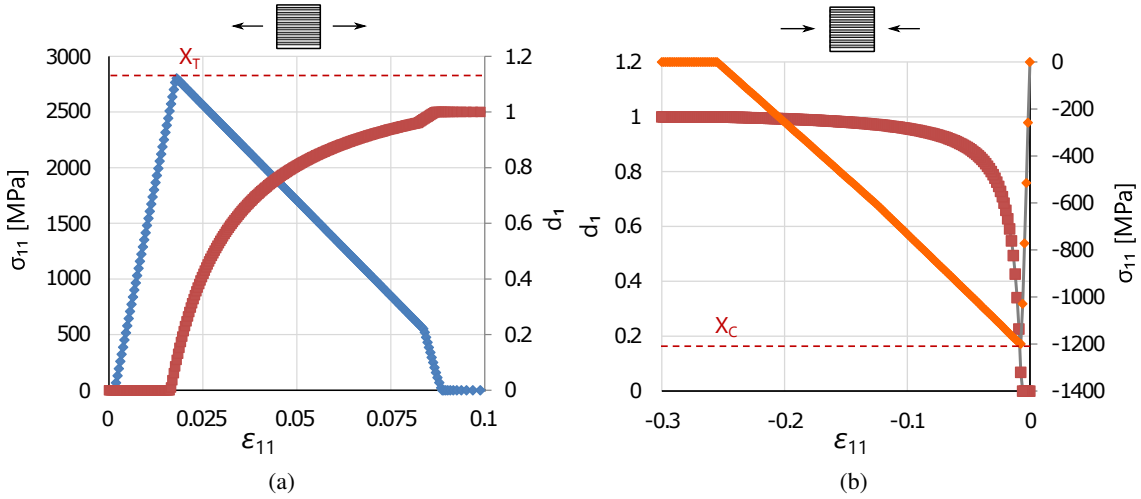


Figure 5.6: Verification study at the single element level under uniaxial longitudinal tension (a) and longitudinal compression (b).

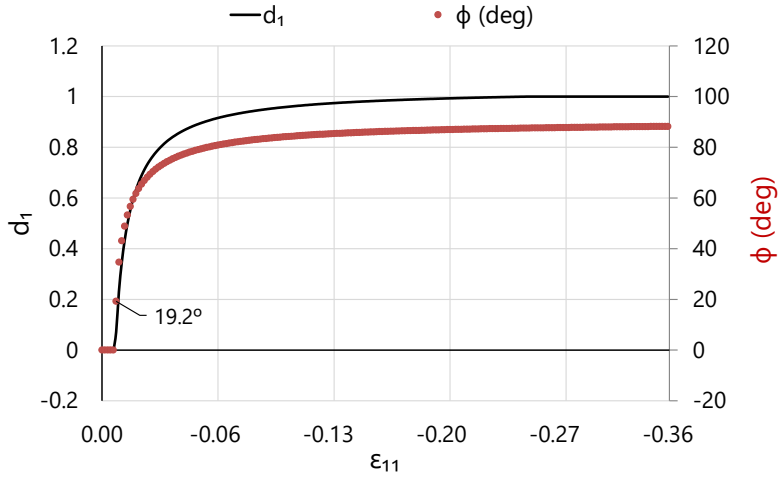
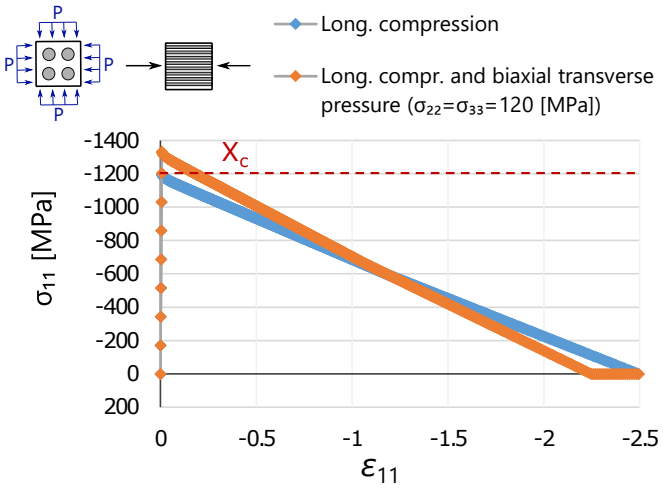
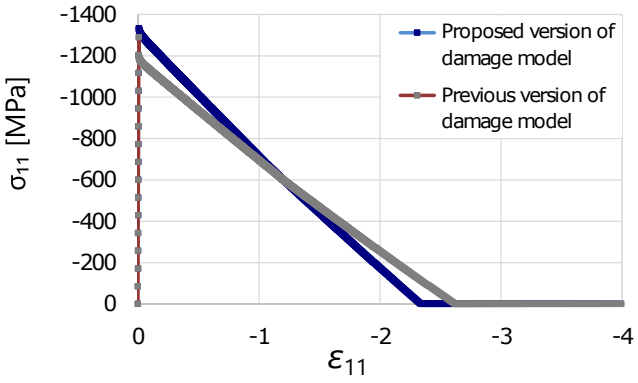


Figure 5.7: Evolution of the damage variable for fibre-dominated failure (d_1) and the kinking angle (φ) with longitudinal strain (ε_{11}), for a single C3D8R element under uniaxial compression in the fibre direction.



(a)



(b)

Figure 5.8: Verification study at the single element level under triaxial loading, realized by applying biaxial transverse pressure ($\sigma_{22} = \sigma_{33}$ =120.0 MPa) and longitudinal compression. In (a), there is the comparison between the triaxial case and the uniaxial case, while (b) shows the comparison between the proposed and the previous versions of degradation models.

Table 5.2: Material properties of IM7/8552 UD tape, used for verification of the implemented damage model.

Property	Value	Units	References/Equation
Young's moduli			
E_1	171.42	GPa	[142]
$E_2 = E_3$	9.08	GPa	[142]
Poisson ratios			
$\nu_{12} = \nu_{13}$	0.32	-	[142]
ν_{23}	0.487	-	[142]
Shear moduli			
$G_{12} = G_{13}$	5.29	GPa	[142]
G_{23}	3.05	GPa	$G_{23} = \frac{E_2}{2+2\cdot\nu_{23}}$
Density			
ρ	1.59	$g \cdot cm^{-3}$	[142]
Longitudinal strengths			
X_T	2806.0	MPa	[143]
X_C	-1200.1	MPa	[142]
Transverse strengths			
Y_T	62.3	MPa	[142]
Y_{BT}	38.7	MPa	[144]
Y_C	-253.7	MPa	[145]
Y_{BC}	-600.0	MPa	[144]
S_L	89.6	MPa	[32]
S_T	62.3	MPa	[142]
Longitudinal fibre-dominated fracture			
$\mathscr{G}_{1-}$	150.0	kJ/m^2	assumed
$\mathscr{G}_{1+}$	134.7	kJ/m^2	[133]
f_{GC}	0.484	-	assumed
f_{GT}	0.824	-	assumed
Transverse matrix-dominated fracture			
$\mathscr{G}_{Ic}$	0.277	kJ/m^2	[142]
$\mathscr{G}_{IIc}$	0.788	kJ/m^2	[142]
η	1.634	-	[133]
μ	0.4	-	assumed

softening curve could not account for this different longitudinal compressive strength, dropping suddenly to X_C. Hence, the previous version of CDM could not exploit the enhancement in the prediction of fibre kinking due to the inability to reflect the predicted compressive strength in the softening curve.

Additional tests were performed for different material systems and element sizes to verify the robustness of the model. The results of these tests confirmed the correct implementation of the numerical model and the expected mechanical response in the fibre-direction of FRPs was captured for all cases.

5.2.1.2 Verification tests for matrix-dominated failure mechanisms

Following the verification tests on the CDM model for damage propagation in the longitudinal direction, herein, the goal is to verify the implementation of the SCM, where the evolution of matrix-dominated failure is modelled using a cohesive law, as described in Section 5.1.1.

With this aim, single C3D8R elements were subjected to simple pure uniaxial and pure shear stress states, in order to trigger matrix cracking and its broadening. In particular, five tests were performed by applying the following loading conditions: transverse tension, transverse compression, in-plane shear, out-of-plane shear and transverse shear. The material used for these studies is IM7/8552 UD tape and its properties can be found in Table 5.2. For all tests, the element dimensions are $0.1 \times 0.1 \times 0.1$ mm^3.

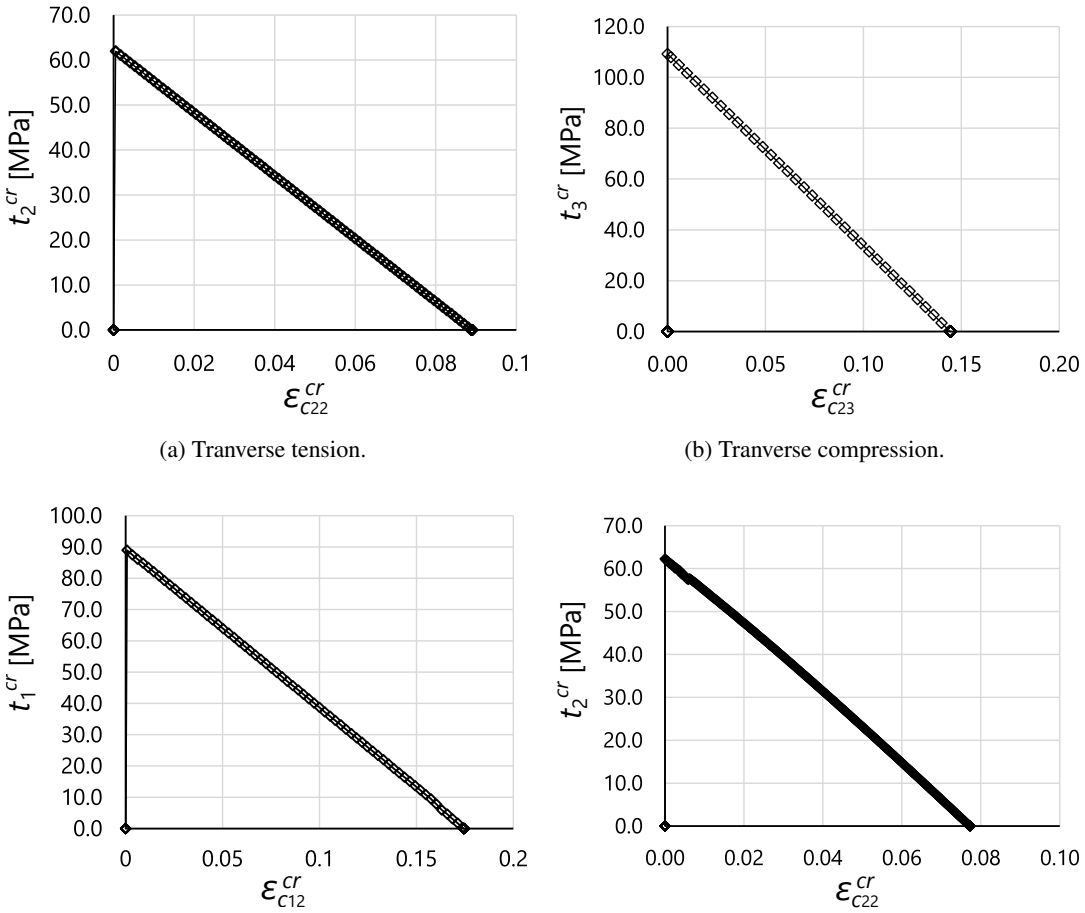
The obtained results are shown in Fig. 5.9, where traction-cracking strain curves are provided for each of the performed test. In all cases, the model was able to correctly predict the onset of transverse damage mechanisms, as well as the computed fracture energy up to final failure. The latter was verified by comparing the area below the traction-cracking strain relations with the expected dissipated energy. For each of the cases, the predicted fracture angle α was also correctly computed.

Then, more complex test cases were run to perform a more comprehensive verification of the implemented material model. Firstly, biaxial transverse compression was applied by imposing two different velocity boundary conditions in the direction 2 and 3, and the influence of friction during growth of matrix cracks was studied. For this test, the element dimensions and the material properties are kept the same as implemented in the previous test.

Fig. 5.10 shows this validation study performed for a C3D8R element under biaxial transverse compression with a ratio $\sigma_{33}/\sigma_{22} = 3.0$ and different values of the frictional coefficient μ (from Eq. 5.7), ranging from 0 to 0.4. It can be observed that the implemented SCM is able to account for the frictional effect on the evolution of transverse matrix cracking. Indeed, since friction acts as an obstacle to the crack propagation for this test case, a higher value of frictional coefficient μ is reflected on a slower reduction of the traction components with the cracking strains. In other words, increasing the friction means raising the overall fracture energy, therefore the tractions required to dissipate the fracture energy by increasing the cracking strains are also higher.

In Fig. 5.11, a test case involving mode II crack broadening is shown. To realize this verification test, the imposed boundary conditions included the application of a constant out-of-plane pressure $\sigma_{33} = 50$ MPa and an increasing out-of-plane shear σ_{13}, setting a suitable velocity boundary condition. Different values of frictional coefficient were included in the test for a further verification of the implemented cohesive law. For this test, the element dimensions are $0.28 \times 0.28 \times 0.28$ mm^3, while the material is still IM7/8552.

It can be observed that the onset and evolution of damage is correctly captured. Recalling the failure envelopes for this material in Fig. 3.2, it can be checked that transverse compression delays failure initiation under transverse shear. Moreover, the predicted frictional effect is well represented and, as previously explained, the evolution of the in-plane shear component of the



(a) Tranverse tension.

(b) Tranverse compression.

(c) In-plane shear.

(d) Tranverse shear.

Figure 5.9: Numerical results of single element test under different loading conditions for matrix-dominated failure.

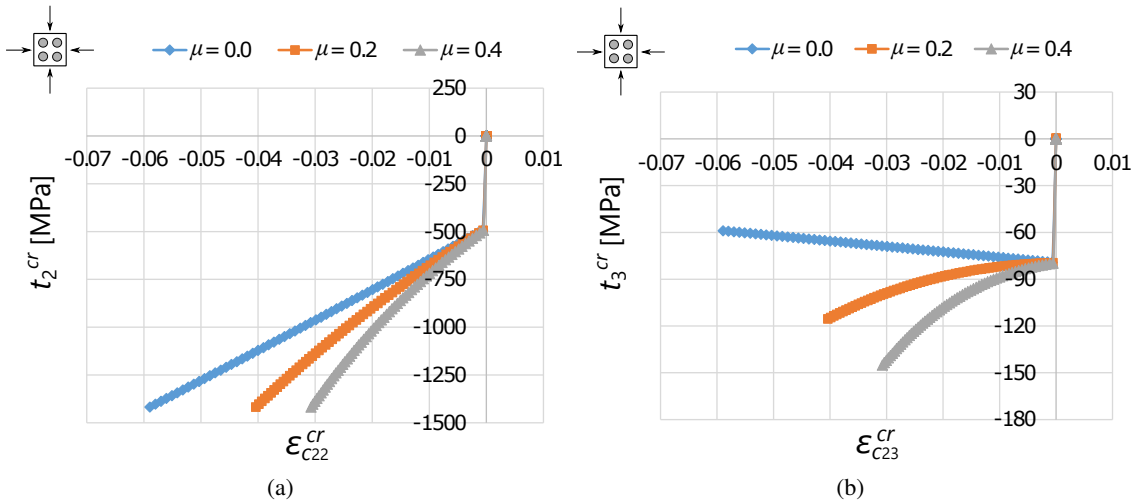


Figure 5.10: Verification study at the single element level under biaxial transverse compression with a ratio $(\sigma_{33}/\sigma_{22})$ = 3.0 and different values of frictional coefficient. The evolution of the normal component of the traction with the cracking strain is shown in (a), while the transverse shear component evolution of the traction with cracking strain is shown in (b).

traction tensor is slower with the cracking strain. Furthermore, the fracture angle α was correctly calculated also for this test case, being equal to 90°.

5.2.1.3 Verification tests with load reversal

As a final test at the single element level, the case of load reversal was addressed. This type of test is generally significant for any damage model, but it is crucial when addressing fatigue, which is out of the scope of this work. However, load reversal is still an essential test to investigate the robustness of the model when, for instance, after the onset of degradation, the redistribution of stress lead to a change of sign or when running a numerical study with multiple steps characterized by different loading conditions.

This verification study was performed on C3D8R elements of several sizes, but herein, the results refer to elements of 0.1 × 0.1 × 0.1 mm^3 and the material selected was IM7/8552 UD tape. Firstly, the pure uniaxial case in the longitudinal direction was analyzed, imposing a tensile loading up to a certain degree of material degradation, corresponding to $d_1 = 0.34$, and then, reversing the load direction to apply compression and to give rise to fibre kinking. The resulting longitudinal stress-strain and longitudinal damage-strain relations are shown in Fig. 5.12.

After analyzing the results, it can be concluded that the model is able to properly capture the onset of failure after damage initiation and load reversal. Moreover, the evolution of damage is well represented in both directions. It can be also noted that the damage variable under tension is uncoupled to the one under compression. This option was selected for the scope of the developed damage model, which is not intended to address cases in which degradation will occur on the same elements due to tensile and compressive stress states. However, it should be pointed out

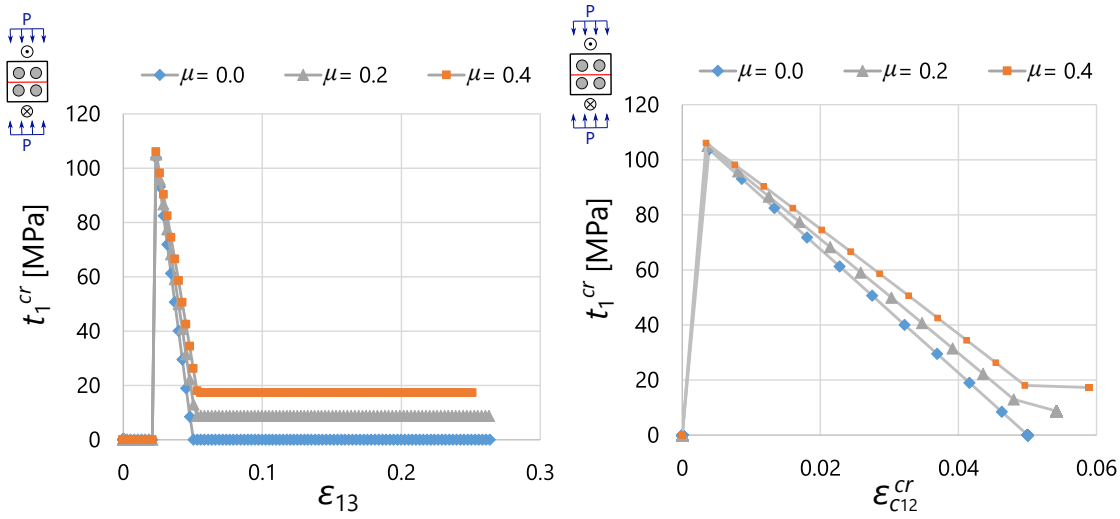


Figure 5.11: Verification study at the single element level under a constant out-of-plane pressure (σ_{33}) and increasing out-of-plane shear (σ_{13}), with different values of frictional coefficient. The evolution of the in-plane shear component of the traction vs out-of-plane shear is shown in (a), while in (b) the same traction component is shown vs the cracking strain.

that experimental evidence exists on the negative influence of fibre kinking on the mechanical behaviour of composite plies under tension and vice-versa.

For the sake of completeness, the pure in-plane shear test is also included in this report. In this way, the effect of load reversal can be investigated also for transverse damage. Similarly to the pure uniaxial case, this test involves multiple steps: firstly positive in-plane shear is applied to trigger matrix cracking and subsequent damage evolution up to a certain extent, then reversing the load to create damage in the other direction and finally, reversing the load up to final failure.

Fig. 5.13 shows the obtained results of this test, including the in-plane shear component of traction tensor-cracking strain curve as well as the damage variable of the SCM-shear strain relation. The material model is observed to be able to capture the evolution of matrix-dominated damage after load reversal until final collapse. Furthermore, unlike the CDM model, the damage variable of the SCM is only one, without storing the information of the loading direction.

After achieving this consistency for several test cases at the single element level, in the next Sections an upscaling of this investigation will be made in order to understand how well the damage model represents the inelastic response and failure behaviour of composite laminates and structural details subjected to different loading conditions.

5.2.2 Verification at the coupon level

This section addresses failure of off-axis specimens subjected to uniaxial loading, with the aim of assessing the predictions of the proposed damage model. Therefore, the analysis presented herein is an upscaling of the preliminary verification started in the previous Section, shifting the focus

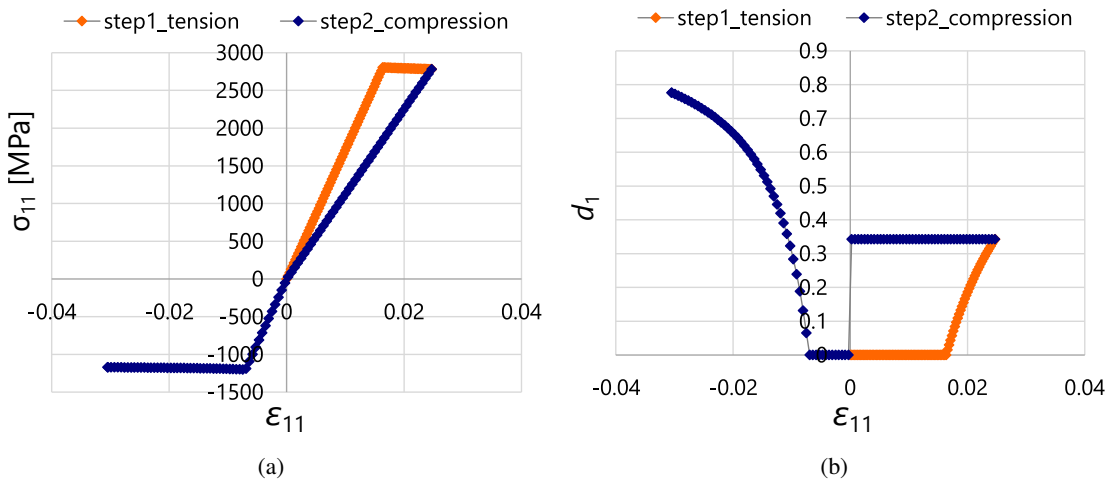


Figure 5.12: Verification study at the single element level involving load reversal with uniaxial loading. In (a) the evolution of the longitudinal stress component with longitudinal strain is shown, while the damage variable for fibre-dominated failure vs longitudinal strain is displayed in (b).

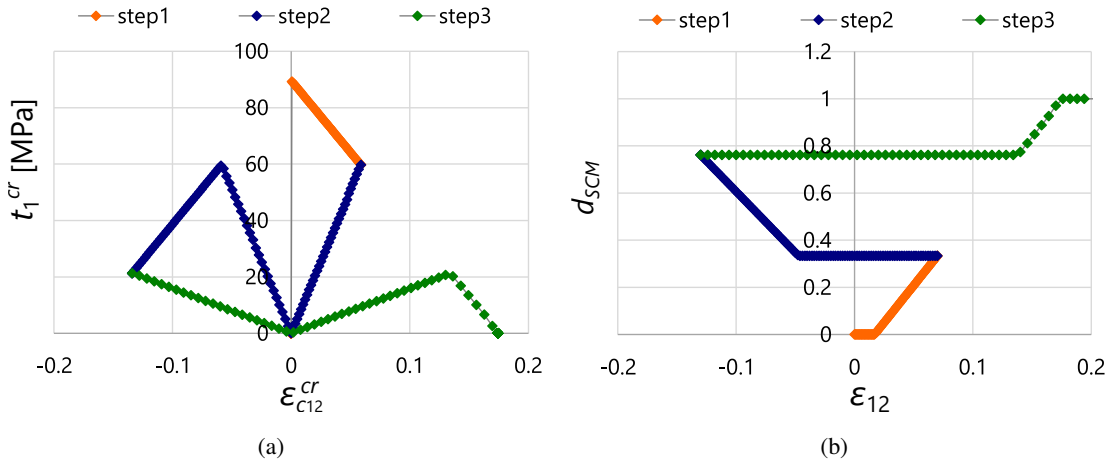


Figure 5.13: Verification study at the single element level involving load reversal with in-plane shear loading. In (a) the evolution of the in-plane shear component of the traction with the cracking strain is shown, while the damage variable for matrix-dominated failure vs in-plane strain is displayed in (b).

from single element level to the coupon level. Indeed, the objective of these tests is to analyze, for the first time, the outcomes of the mesoscale damage model when predicting failure of UD specimens subjected to simple loading conditions.

The experimental data used for this study can be found in Refs. [145, 146], where Koerber et al. presented off-axis and transverse compression and tension tests under quasi-static and dynamic loading to investigate the viscoplastic behavior of the IM7-8552 carbon–epoxy. However, for this work, only the quasi-static tests will be addressed. Thus, the following types of experimental test will be considered:

- off-axis tension at 15°, 30°, 45°;
- transverse tension (i.e. off-axis tension at 90°);
- off-axis compression at 15°, 30°, 45°, 60°, 75°;
- transverse compression (i.e. off-axis compression at 90°).

The geometry of the specimens for off-axis compression is characterized by nominal dimensions of $20 \times 10 \times 4$ mm^3, while for off-axis tension tests, the nominal dimensions of the 15° off-axis specimens were $72 \times 8 \times 1.5$ mm^3 and $62 \times 8 \times 1.5$ mm^3 for all other specimens. The material used for these specimens is IM7/8552 carbon-epoxy UD tape, with a nominal ply thickness of 0.125 mm. The material parameters are shown in Table 5.2, except for the longitudinal compressive and tensile strength, which differ from the Table, being: $X_C = -1017.5$ MPa and $X_T = 2323.5$ MPa.

The generated models are built up using C3D8R finite elements and the simulations are done with the FE commercial software Abaqus/Explicit®. The laminates are discretized using one element per ply through the thickness and each ply of IM7/8552 tape is modelled as a homogeneous material. The in-plane finite element size used for the present models is 0.22 mm, which is lower than the critical element size l^* (Eq. 5.20), in the longitudinal and transverse direction.

The boundary conditions include: the restriction of the translational degree of freedom (DOF) in the fibre direction on one end, while imposing a suitable velocity on the nodes of the other end along the same direction, using a smooth step amplitude. Furthermore, a zero lateral displacement was imposed on one face of the specimen, to avoid bending under compression, and the displacement in the y-direction was restricted only on one edge of the specimens. These boundary conditions are summarized in Fig. 5.14.

The comparison between experimental data and predictions of peak compressive and tensile stress, for the considered off-axis specimens, are shown in Fig. 5.15. The overall results are then summarized in Fig. 5.16, including also the case of pure shear to get a closed envelope. For the latter test, the shear strength was obtained modelling a symmetric $\pm 45°$ laminate and imposing a tensile loading. The in-plane shear stress and transverse shear, in Fig. 5.15, are obtained by transforming the applied axial stress from the global coordinate system (i.e. the laminate system), where *xx* is loading direction, into the material coordinate system, where the 1-direction coincides with the fibre direction and the 2-direction is perpendicular to the previous one and in-plane [145]:

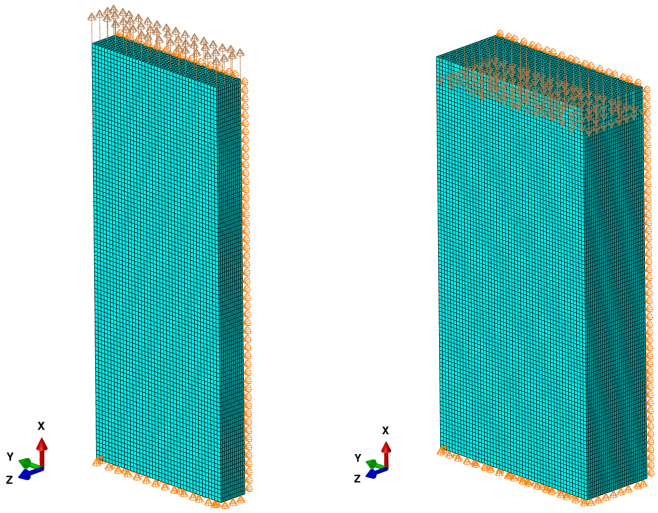


Figure 5.14: Mesh and boundary conditions for the simulation of off-axis specimens under tension and compression.

$$\begin{aligned} \sigma_{22} &= \sigma_{xx} \sin^2 \theta \\ \tau_{12} &= -\sigma_{xx} \sin \theta \cos \theta \end{aligned} \tag{5.28}$$

Good agreement between the experimental results and the model predictions was achieved. In particular, the developed damage model was able to capture the general trends of the recorded stress level at failure for different off-axis angles. It is to be noted that the prediction for these quasi-static cases are very accurate, within the acceptable deviation, except for the 15° under tension and the 60° under compression, where the deviation is slightly more significant. However, the experimental variability is important for this study, for instance, due to the change in fibre orientation with increasing the applied loading, as pointed out in Ref. [146].

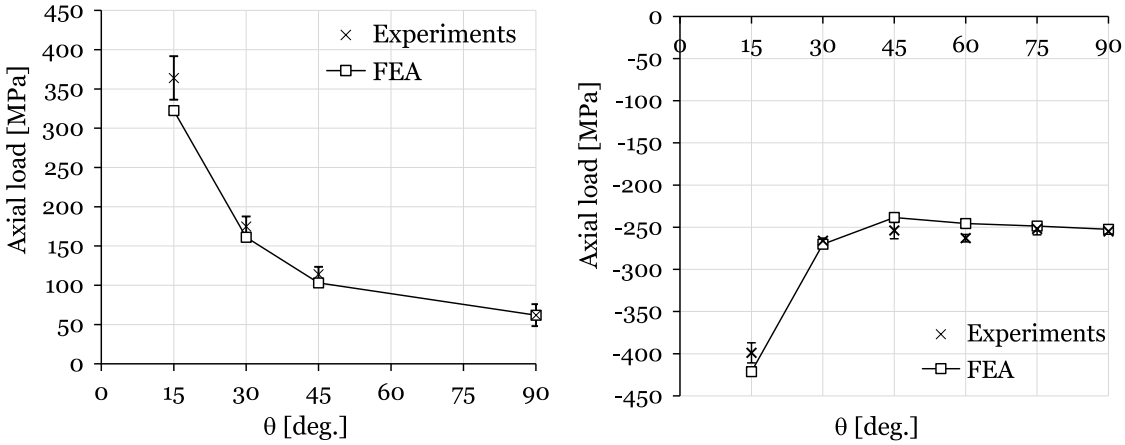


Figure 5.15: Comparison between experimental results and model predictions on failure of off-axis coupons under tension (a) and compression (b).

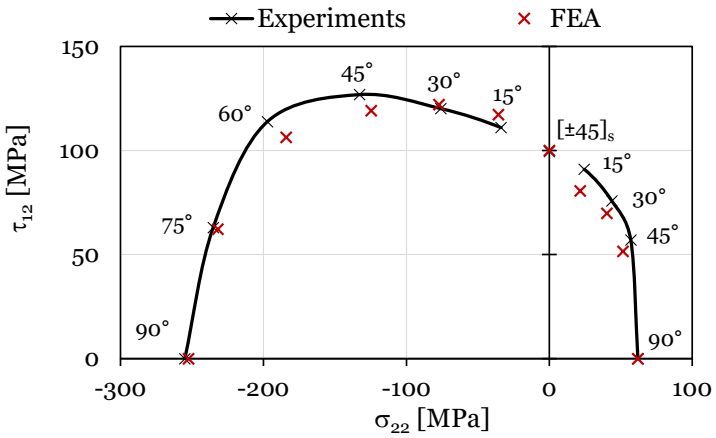


Figure 5.16: Overall correlation between experimental results and model predictions of off-axis coupons subjected to axial loading.

5.3 Validation studies

In structural testing, the Building Block Approach (BBA) is the main reference used for the certification of composite structures [140]. Following this approach, several tests are performed on small size specimens under different conditions and fewer when moving upward in the structural testing pyramid. The goal of this process is to gain a deep understanding of the structural behaviour under simple loading conditions at the early stages of the design process, where any change in the design can still be made without incurring in unfeasible costs. Therefore, in the BBA, the investigation of the mechanical behaviour of coupons is crucial as it is representative of the mechanics of large-scale structures.

This approach is implemented for experimental campaigns as well as for virtual testing. In this framework, the use of FE models to simulate failure of composite laminates assumes a key importance as it can be used to complement, or potentially replace, the purely experimental determination of the design parameters. This would allow to mitigate the cost of the design of new structures [139].

In the present Section, the BBA is employed in the validation of the proposed mesoscale model, performing a comprehensive numerical investigation of coupons and then, upscaling the analysis to address a structural detail. Indeed, this work includes mainly two analysis: one conducted at the coupon level, where failure of several notched and unnotched multidirectional laminates is investigated in detail, followed by a validation study at the detail level, addressing damage progression in the bolted connection of a stringer run-out.

5.3.1 Validation at the coupon level

5.3.1.1 Size effect study on unnotched laminates

Size effect (or scaling effect) in FRP laminates has increasingly become an important area of research. Since the design of composite structures is mostly based on the mechanical behaviour of small coupons (as supported by the BBA), understanding the effect of up-scaling on the strength and failure behaviour of continuous FRP structures is fundamental.

A significant effort has been made to document and predict the scaling effect on unnotched (UNT) and notched (NT) specimens, with experimental and numerical studies [25, 143, 147, 148, 149, 150, 151, 152, 153, 154]. Thanks to this comprehensive research work, important trends have been outlined, highlighting how the strength of composite laminates changes applying a specific geometrical scaling. Moreover, these studies have developed an understanding of the failure mechanisms controlling the strength of composite specimens of different dimensions, to enable the prediction of scaling effects without recurring to empirical laws.

As part of the validation of the mesoscale damage model proposed in this work, a numerical analysis on scaling effects in UNT coupons has been carried out. Therefore, the idea of this work is to test the developed damage model in capturing the size effects in UNT tensile and compressive strength of quasi-isotropic (QI) carbon-epoxy laminates. The experimental findings

on scaling effects of UNT specimens, considered for this validation study, are described in detail in Refs. [143, 148].

In particular, Wisnom et al. [143] found a significant size effect in IM7/8552 carbon-epoxy laminates, particularly: (i) the increase in tensile strength of QI specimens when the size was scaled up by repeating the sublaminate stacking sequence ("n-scaling", $[45/90/-45/0]_{ns}$) and (ii) the decrease in tensile strength when the specimen size was scaled up increasing the ply thickness ("m-scaling", $[45_m/90_m/-45_m/0_m]_s$). On the other hand, for QI UNT specimens under longitudinal compression, Lee and Soutis [148] presented the following results for the same material: no evidence of a size effect when the specimens are scaled up at the sublaminate level (i.e. with "n-scaling") and the decrease in compressive strength of ply-level scaled (i.e. "m-scaled") specimens. Table 5.3 summarizes the geometry for the multidirectional laminates tested to study the UNT strength of scaled specimens [143, 148].

Table 5.3: Dimensions and stacking sequence of the scaled UNT quasi-isotropic laminates, tested for the experimental works presented in Refs. [143, 148].

Specimen type ($[45_m/90_m/-45_m/0_m]_{ns}$)	Layup	Gauge length × width [mm × mm]	Nominal thickness [mm]
Tension [143]			
(sublaminate-level scaling)			
n, m = 1	$[45/90/-45/0]_s$	30 × 8	1.0
n = 2	$[45/90/-45/0]_{2s}$	60 × 16	2.0
n = 4	$[45/90/-45/0]_{4s}$	120 × 32	4.0
(ply-level scaling)			
m = 2	$[45_2/90_2/-45_2/0_2]_s$	60 × 16	2.0
m = 4	$[45_4/90_4/-45_4/0_4]_s$	120 × 32	4.0
m = 8	$[45_8/90_8/-45_8/0_8]_s$	240 × 64	8.0
Compression [148]			
(sublaminate-level scaling)			
n = 2	$[45/90/-45/0]_s$	30 × 30	2.0
n = 4	$[45/90/-45/0]_{2s}$	60 × 60	4.0
n = 8	$[45/90/-45/0]_{4s}$	120 × 60	8.0
(ply-level scaling)			
m = 2	$[45_2/90_2/-45_2/0_2]_s$	30 × 30	2.0
m = 4	$[45_4/90_4/-45_4/0_4]_s$	60 × 60	4.0
m = 8	$[45_8/90_8/-45_8/0_8]_s$	120 × 120	8.0

The material properties of IM7/8552 UD tape, as presented in Table 5.2, are used for this work. Additionally, for this study, it is important to account for *in-situ* strengths, as they can affect remarkably the mechanical response of laminates, especially when addressing the effect of ply-thickness scaling. Indeed, for the case of m = 8, the thickness of the embedded 0° ply is 2 mm and the corresponding *in-situ* strengths are significantly lower than the ones for embedded single plies. These properties are derived using the approach proposed by Camanho et al. [33, 142] and the obtained *in-situ* strengths for IM7/8552 are presented in Table 5.4.

Finite element modelling The FE models were built up using C3D8R solid elements for the prediction of the ply response. Furthermore, for each test case, a study of the influence of delam-

Table 5.4: *In-situ* properties of IM7/8552 carbon-epoxy material system.

Ply position (thickness)	*In-situ* strengths [MPa]					
	Y_T	Y_{BT}	Y_C	Y_{BC}	S_L	S_T
Embedded (t_{ply})	160.2	160.0	-437.6	-600.0	179.2	124.6
Embedded ($2 \cdot t_{ply}$)	113.3	82.7	-364.0	-600.0	140.0	97.3
Embedded ($4 \cdot t_{ply}$)	98.7	63.5	-297.6	-600.0	108.6	75.5
Embedded ($8 \cdot t_{ply}$)	98.7	63.5	-297.6	-600.0	108.6	75.5
Embedded ($16 \cdot t_{ply}$)	98.7	63.5	-297.6	-600.0	108.6	75.5
Outer (t_{ply})	100.8	64.3	-364.0	-600.0	140.0	97.3
Outer ($2 \cdot t_{ply}$)	71.3	43.1	-293.8	-600.0	106.9	74.3
Outer ($4 \cdot t_{ply}$)	62.3	38.7	-253.7	-600.0	89.6	62.3
Outer ($8 \cdot t_{ply}$)	62.3	38.7	-253.7	-600.0	89.6	62.3

ination in the evolution of damage up to collapse was performed generating an additional model with interlaminar layers of COH3D8 cohesive elements between plies with different orientation. Therefore, multidirectional laminates are discretized using one element along the thickness per ply or blocked plies, defined as composite consecutive plies having the same orientation. This layer-wise discretization allowed to assign, for each ply block, the correct *in-situ* strengths (Table 5.4), calculated as a function of the position and thickness of plies, by means of different material cards.

Following Ref. [131], a multi-zone strategy was employed for an accurate definition of in-plane FE sizes, to minimize the computational cost of this numerical study. In this way, laminates were divided three regions: a central zone with a constant element size, lower than the critical value l^*, where material degradation was included and two side regions, with biased mesh size growing from the centre to the edge, where the material response was kept linear-elastic for the entire simulation. The element size in the refined zone was selected to be lower than the minimum critical value in both longitudinal and transverse direction (equal to 0.19, calculated using Eq. 5.20), considering the respective *in-situ* strengths and fracture properties.

As mentioned above, delamination is predicted using COH3D8 cohesive elements, available in Abaqus/Explicit®, with the same discretization used for modelling the intralaminar mechanical behaviour and a thickness of 0.01 mm. Their constitutive response is defined using a traction-separation law, as described in Section 2.4.1. The interlaminar material properties of IM7/8552 were assumed to be equal to the corresponding values of the matrix-dominated intralaminar damage, given the similarity in the fracture modes. These parameters are presented in Table 5.5.

The numerical study was performed using Abaqus/Explicit® with a VUMAT user subroutine to run the meso-scale damage model. The applied loading was simulated by using a suitable velocity boundary conditions introduced using Smooth step amplitude on the upper end of the laminate and clamping the lower end. The symmetry with respect to the laminate midplane was exploited by setting symmetry boundary conditions. As an example, the overall imposed boundary conditions for the case of ply-level scaled UNT specimen, with m = 2 under tensile loading, are shown in Fig. 5.17.

To suppress spurious energy modes (such as zero-energy mode), an enhanced hourglass and distortion control (length ratio equal to 0.80) were employed in the elements where intralaminar

Table 5.5: Interlaminar properties of the IM7/8552 carbon-epoxy material system.

Property	Value	Units	References/Equation
Interface stiffness			
K	1.0×10^6	N/mm^3	assumed
Interface maximum strengths			
$\tau_1^0 = \tau_2^0$	89.6	MPa	assumed equal to S_L
τ_3^0	62.3	MPa	assumed equal to S_T
Interface critical energy release rate			
$\mathcal{G}_{\mathrm{Ic}}$	0.277	kJ/m^2	[142]
$\mathcal{G}_{\mathrm{IIc}} = \mathcal{G}_{\mathrm{IIIc}}$	0.788	kJ/m^2	[142]
Mixed-mode interaction parameter			
η	1.634	-	[133]

damage is simulated. Furthermore, an efficient strategy to delete excessively distorted elements was implemented, based on the element volume change which is tracked by the determinant of the deformation gradient tensor (det $\mathbf{F}$): det $\mathbf{F}= V/V_0$. Therefore, with the aim of imposing limits on large changes in element volume and allowing reliable results, the following conditions were specified for the deletion of intralaminar elements [155, 156]:

$$\text{Delete element if: } \begin{cases} d_1 > 0.999 \\ d_{SCM} > 0.999 \\ 0 < \det \mathbf{F} < 0.8 \ \text{ or } \ \det \mathbf{F} > 1.2 \end{cases} \tag{5.29}$$

This simulation strategy prevents a premature job termination due to excessive element distortion, before the final structure failure. When cohesive elements where included in the analysis, they were set to be deleted only when fully damaged, i.e. when their damage variable (Eq. 2.52) was equal to one.

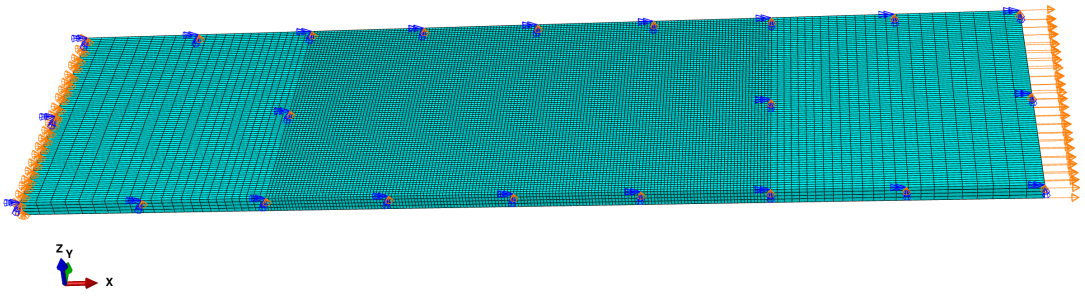


Figure 5.17: Mesh and boundary conditions for the simulation of an UNT specimen under tension, with ply-level scaling and m = 2, leading to the following stacking sequence: $[45_2/90_2/\text{-}45_2/0_2]_s$.

Numerical results The numerical results for ply-level and sublaminate-level scaled tests on QI UNT specimens under tension and compression are shown in Fig. 5.18 and Fig. 5.19, respectively. A summary of the results of scaled tensile and compressive strengths, compared with experimental data and the associated standard deviation, is provided in Table 5.6.

It can be observed that the numerical predictions fit quite well the experimental results for ply-level and sublaminate-level scaled specimens, for the two loading cases involving tension and compression. In fact, the scaling effect is well predicted by the proposed modelling strategies. In particular, relative errors between the mean strength measured experimentally and the one predicted numerically, including or neglecting the effect of delamination, are nearly always within the standard error and below 15%. Indeed, in a set of 12 cases, the only test where the predicted strength is above 15% error is the m = 4 specimen under compression, where a significant scatter was detected in the experiments, with a Coefficient of Variation (CV) of 19%.

Additionally, this work allowed to challenge the proposed mesoscale model in the prediction of damage progression in thick multidirectional laminates, with a nominal thickness of 8 mm. Moreover, these cases are characterized by the numerical oscillations that are an artefact of explicit dynamic modelling. This can be clearly observed for the case of n = 8 under compression. In general, a good agreement with experimental data was achieved also for thick UNT specimens.

Furthermore, it should be noted that delamination plays an important role in the prediction of the UNT strengths, especially for the cases with blocked plies (ply-level scaling). Indeed, the numerical models predicted an earlier failure driven by delamination, due to the higher interlaminar stresses generated by thick embedded blocked plies and lower *in-situ* strengths. In general, the modelling strategy with cohesive elements allows to minimize the overprediction of UNT strength and thus, it proved to be suitable for this type of studies.

Regarding critical failure mechanisms, experimental results about sublaminate scaled tests under tension showed that all specimens exhibited no visible (superficial) damage prior to ultimate failure, with a clean break across the width in the gauge section. The smallest n = 1 specimen is the only case where final failure involved also delamination [143]. The numerical studies on damage progression in sublaminate-level scaled UNT models are shown in Fig. 5.20. It includes the output fields showing the evolution of: (i) matrix-dominated failure through the user-defined damage variable of the SCM ("SDV_D_SCM"), (ii) fibre-dominated failure by means of the user-defined damage variable of the CDM ("SDV_D1_CDM") and (iii) delamination using the Abaqus®' internal damage variable ("SDEG").

The simulations confirm that transverse matrix cracks are the governing failure mechanisms. Indeed, they start developing before reaching ultimate failure, providing less and less support to the 0° plies. Final collapse is predicted to be driven by delamination and fiber tensile failure, after the large development of matrix cracks across the width of the specimens. These predictions are in line with the experimental results, as delamination is found to have little influence on the UNT tensile strengths.

Unlike sublaminate-scaling, ply-level scaled specimens under tensile loading behaved differently according to the size [143]. In the m = 2 specimen, superficial matrix cracks were observed

to occur in the range 343 – 396 MPa, followed by delamination at the free edges which propagates until catastrophic fibre failure. A similar pattern in the initiation of failure took place for the m = 4 specimens, but matrix cracks in the 90° plies and delamination between the 90° and -45° plies were also observed. The final failure occurred as a combination of the complete delamination between the -45° and 0° plies and subsequent fibre failure. The sequence of failure events in m = 8 specimens are the same as the m = 4 case, with some initial transverse cracking observed on the surface [143].

Fig. 5.21 shows that, for m = 2, the predicted failure events are in line with the experimental findings. Indeed, transverse matrix cracks develop slowly until delamination occurs at the interface between the 90° and -45° plies, which quickly leads to catastrophic failure. The predictions for the m = 4 case are also in agreement with the experiments, since a large delamination occurred between the -45° and 0° plies resulted in a drop in load. Finally, in the m = 8 specimen, transverse matrix cracks develop earlier due to the lower *in-situ* strengths of the 1 mm thick ply. Subsequently, as seen in the experiments, delamination was predicted to grow forming small triangular patches, starting from the matrix cracks at the free edge.

The experimental findings on compressive strength of QI UNT specimens showed that no size effects was obtained with ply-level and sublaminate-level scaling. For all cases, failure took place in the gauge length, driven by the compressive strength of the inner blocked 0° plies. However, the extensive matrix cracking that was introduced during the cutting process of the test pieces could contribute to the initiation of edge delamination and premature specimen failure [148]. These defects led to conservative results, especially in the 8 mm thick IM7/8552 blocked laminate, as explained in Ref. [148]. Further, a tendency of failures near the grip for the n > 4 specimens was pointed out, which suggests that blocking the plies makes the laminate more susceptible to stress concentrations developed in the tab region.

Numerical results on UNT compressive strength, shown in Figs. 5.22-5.23, highlights that the failure scenario is always dominated by fibre kinking, usually starting from the free edges. For ply-level scaled specimens (m-scaling), the influence of delamination is relevant in the progressive evolution of damage, contributing to an earlier collapse. The issues found in the experiments result in a difficult correlation, but the overall size effect is in agreement with the predictions. Furthermore, since these failure events grow in a dynamic way, it resulted challenging capturing the full progression of damage and often, only the initial stage was available for post processing. However, a clear load drop was obtained for all the cases.

Finally, it can be concluded that the developed mesoscale damage model proved to capture the size effect in UNT tensile and compressive strength. However, this work is only part of a preliminary validation and additional test cases need to be addressed to further challenge and explore the predictive capabilities of the proposed mesoscale damage model. Moreover, to evaluate the added value of the included developments within the mesoscale damage model, test cases with significantly high through-thickness stresses need to be considered.

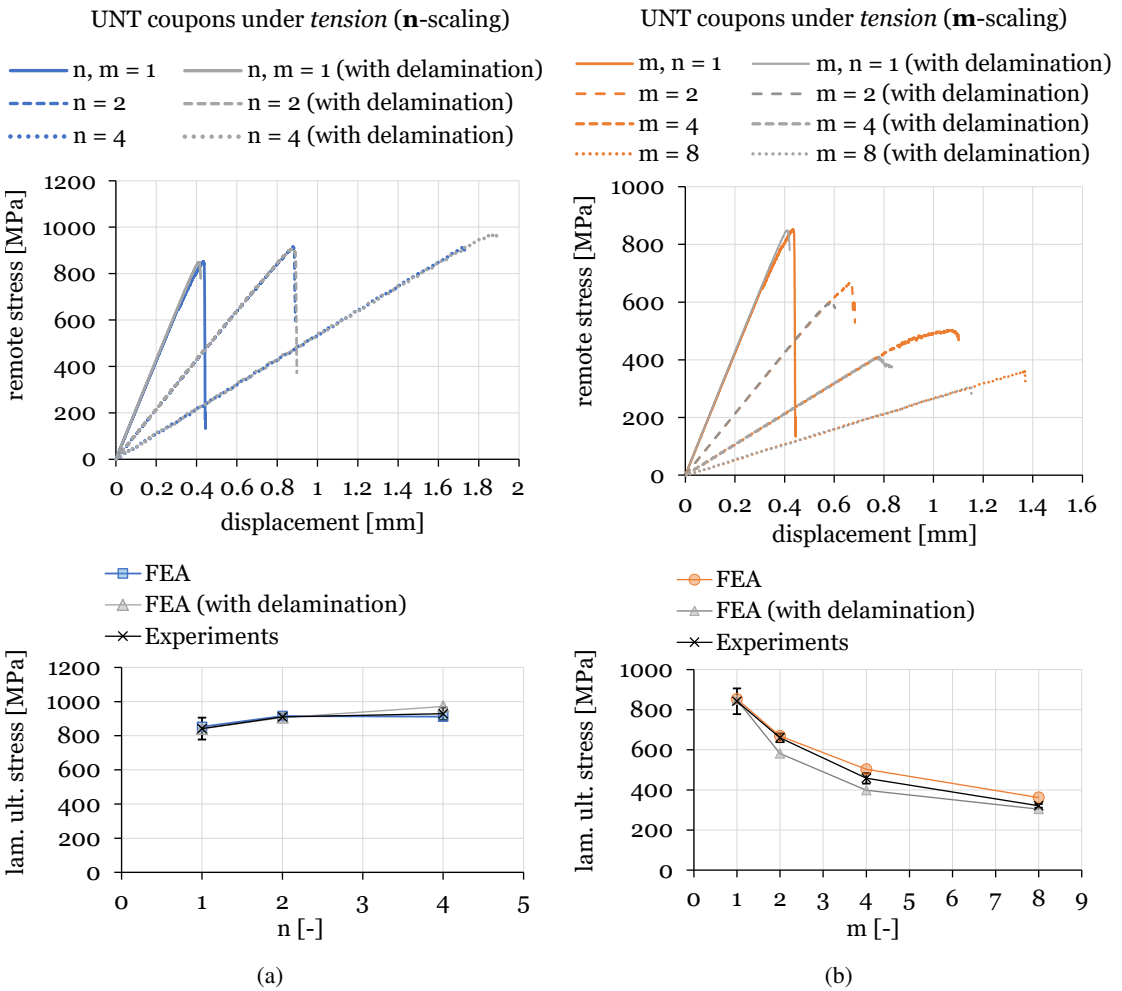


Figure 5.18: Size effect study on UNT quasi-isotropic ($[45_m/90_m/\text{-}45_m/0_m]_{ns}$) specimens under tension with n-scaling (a) and m-scaling (b).

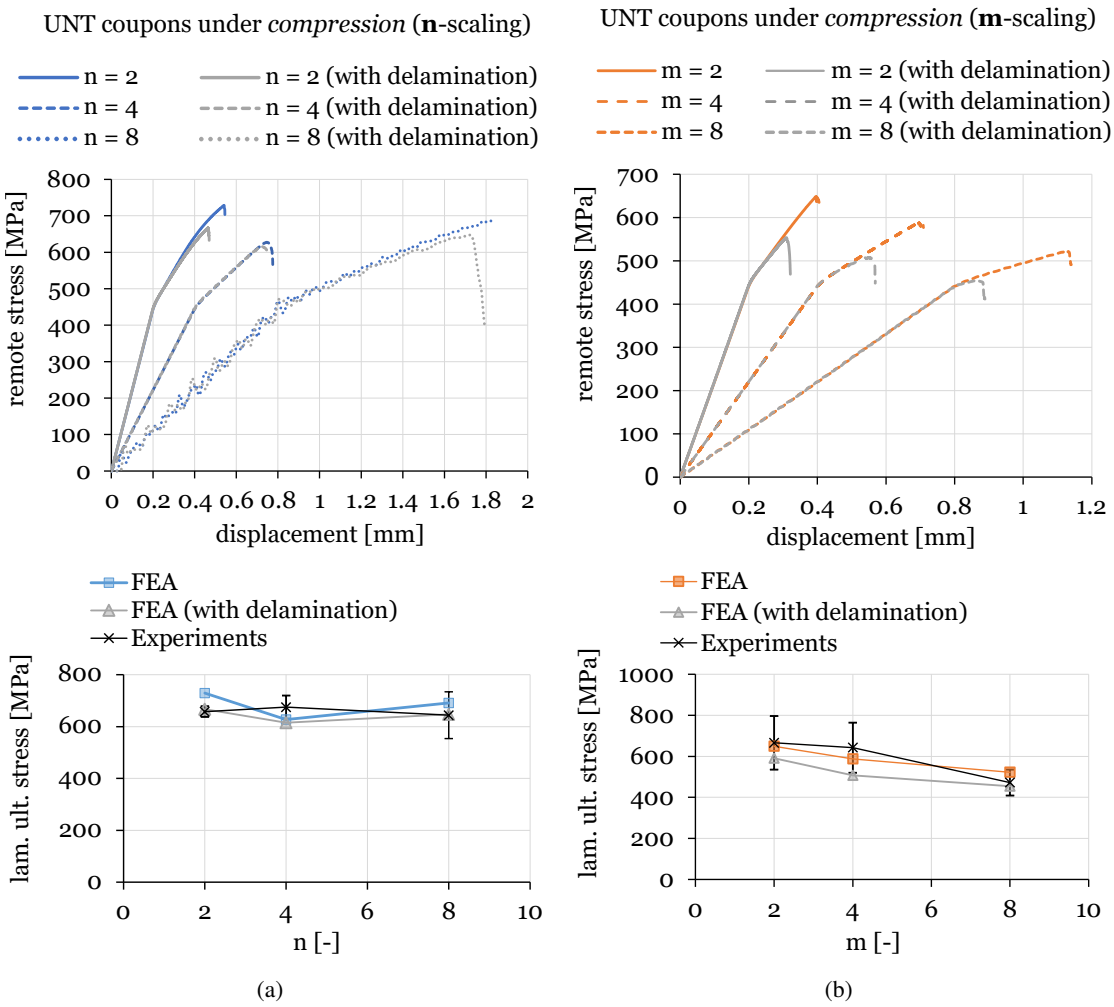


Figure 5.19: Size effect study on UNT quasi-isotropic ($[45_m/90_m/\text{-}45_m/0_m]_{ns}$) specimens under compression with n-scaling (a) and m-scaling (b).

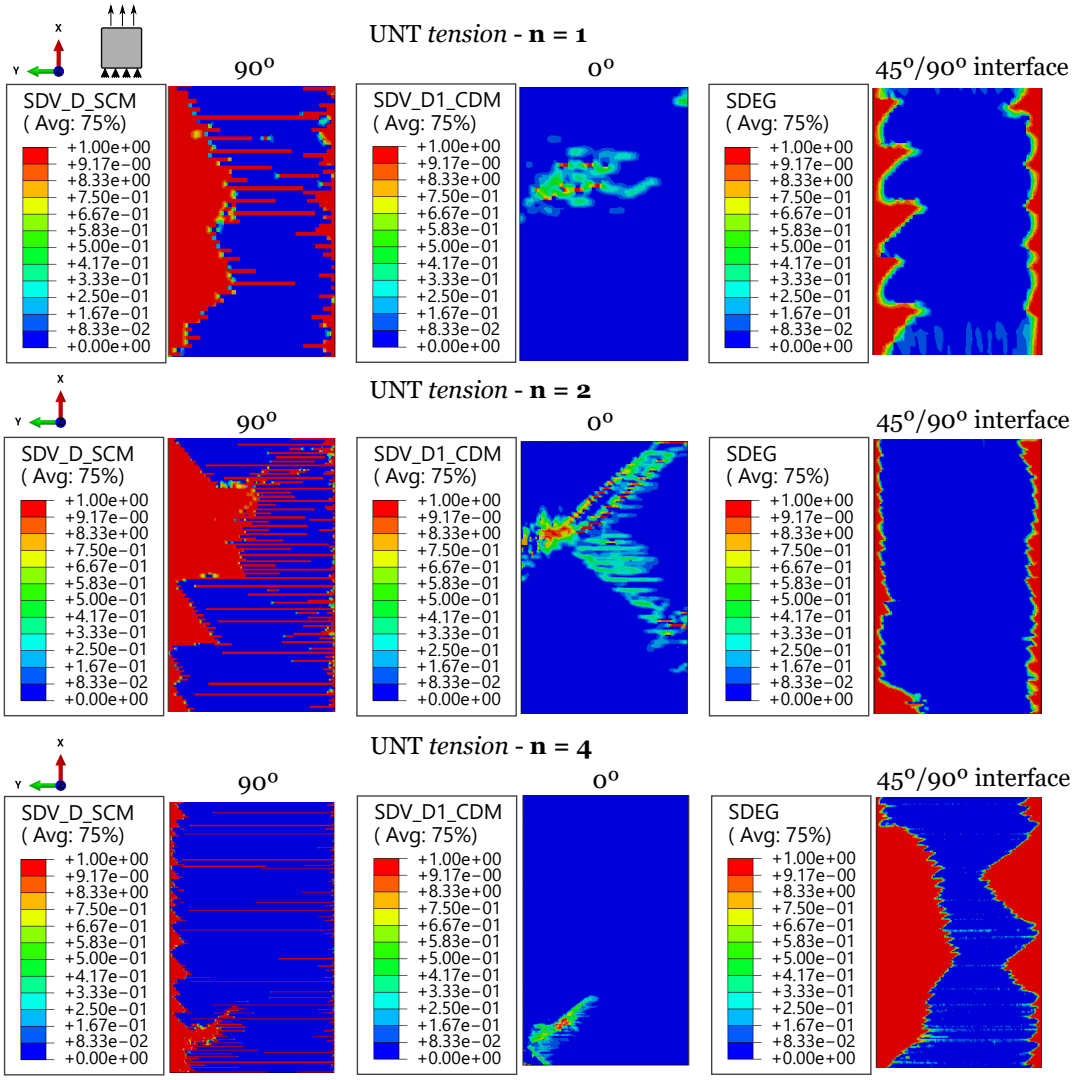


Figure 5.20: Damage progression in sublaminate-level scaled UNT models, subjected to longitudinal tension.

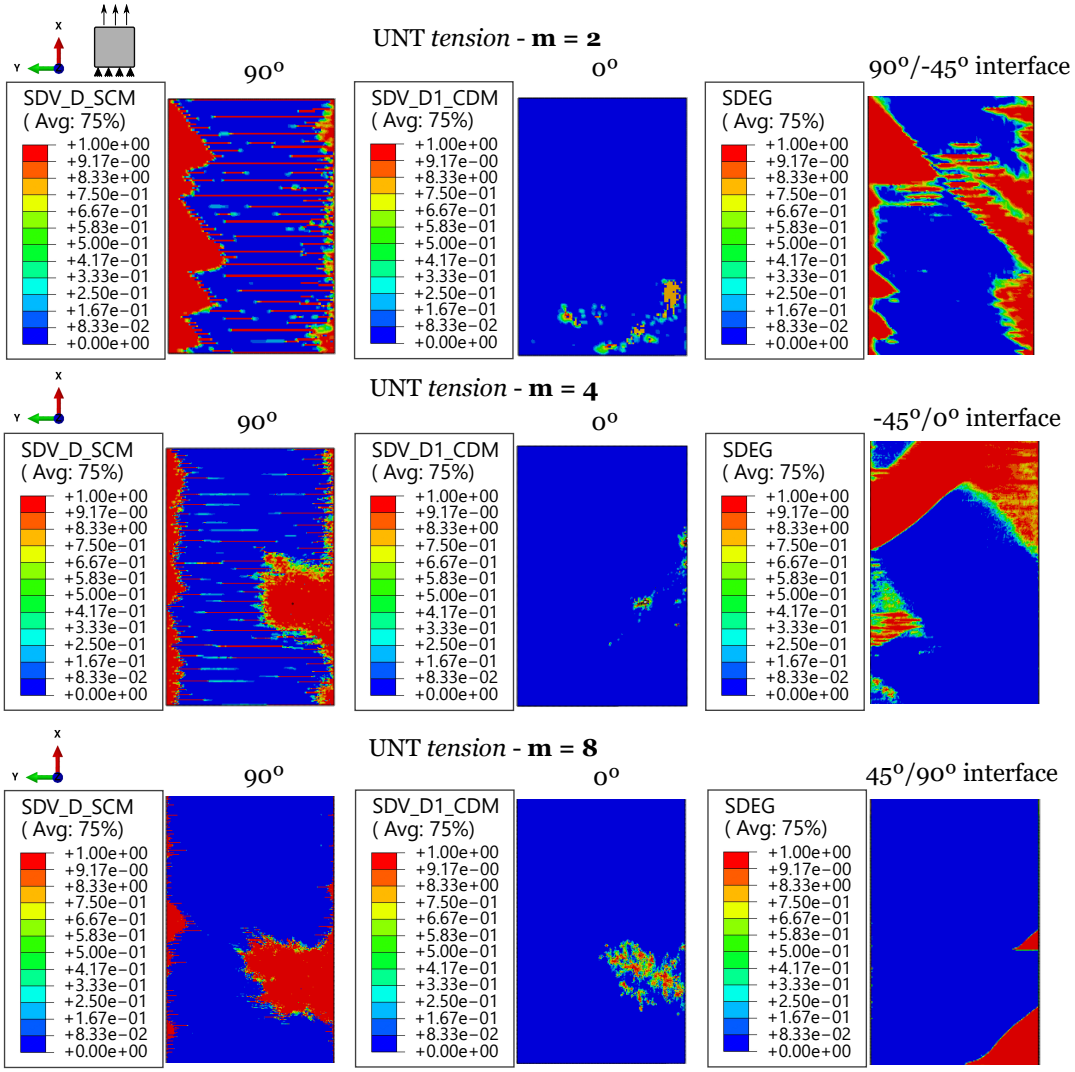


Figure 5.21: Damage progression in ply-level scaled UNT models, subjected to longitudinal tension.

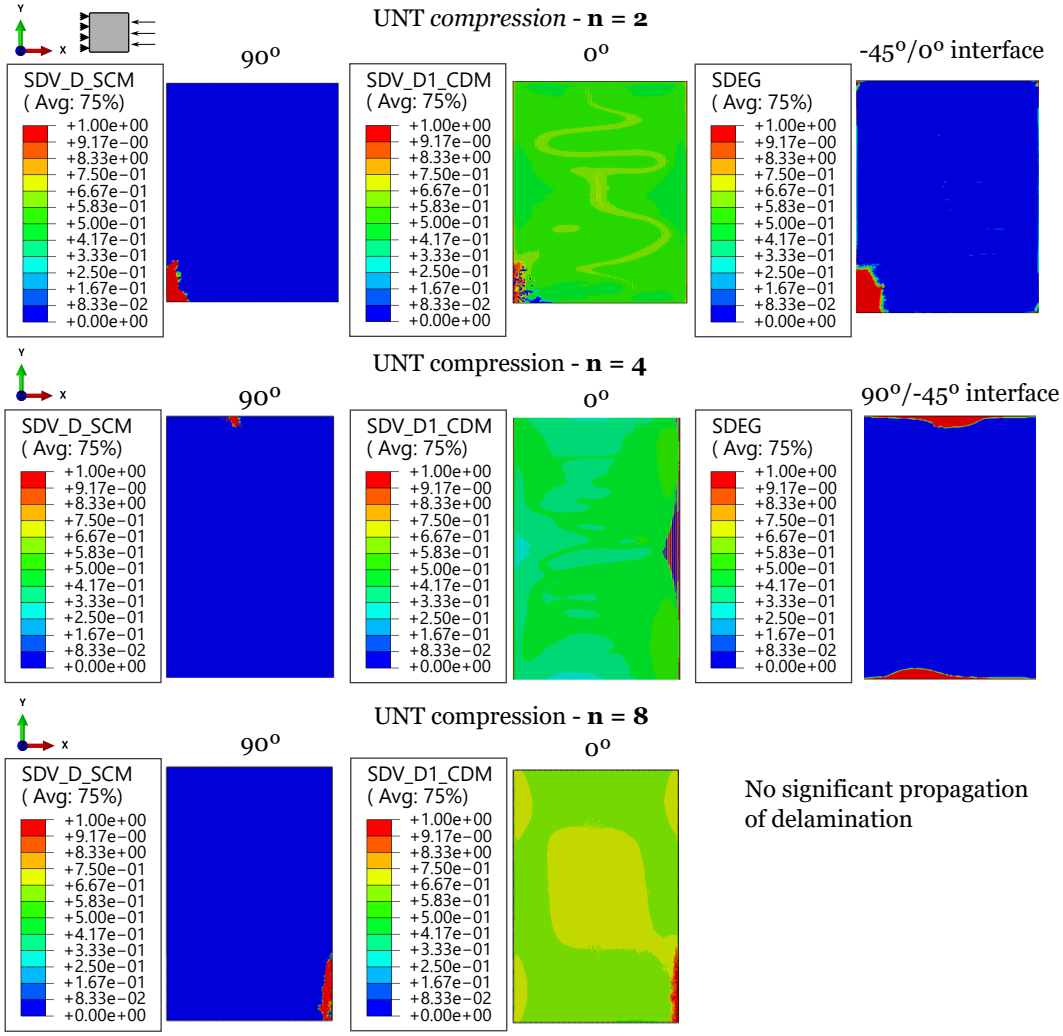


Figure 5.22: Damage progression in sublaminate-level scaled UNT models, subjected to longitudinal compression.

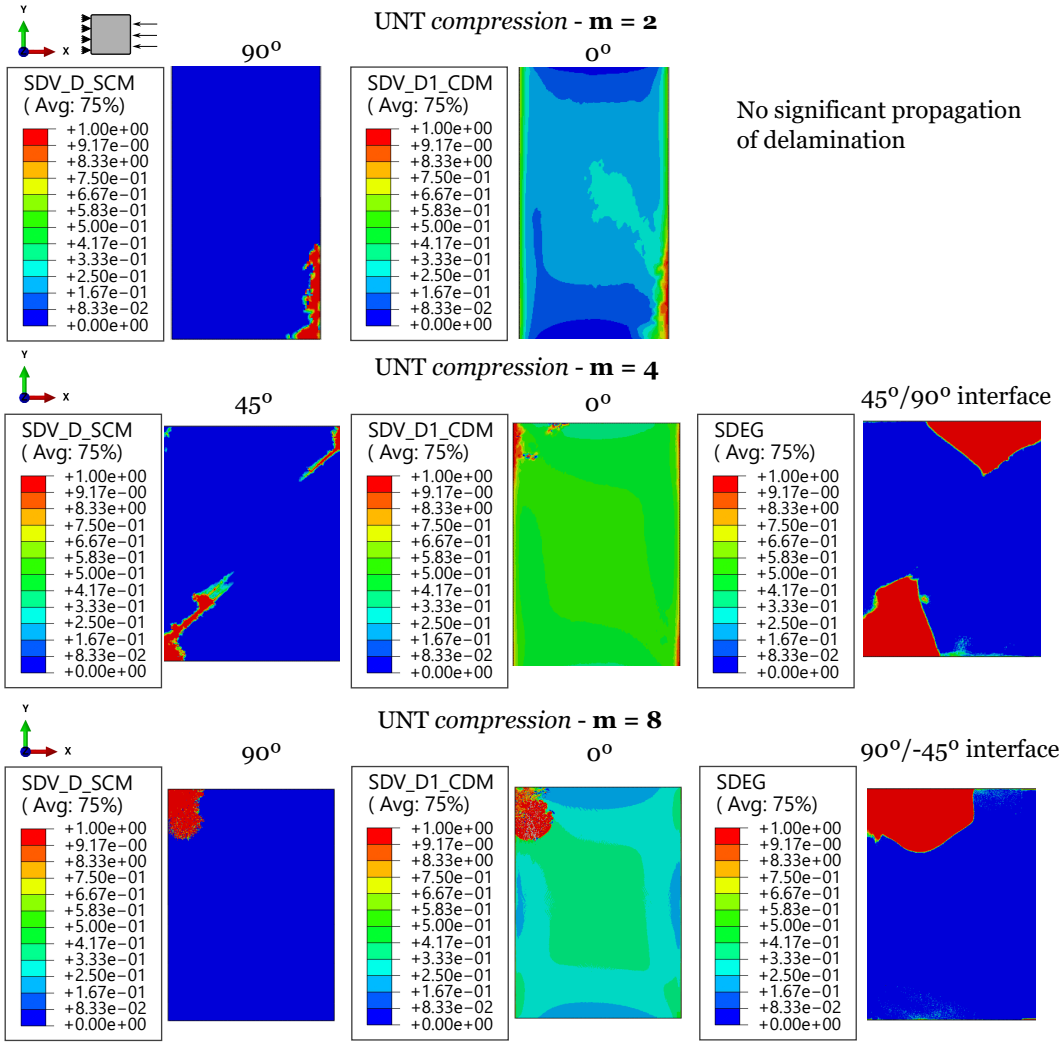


Figure 5.23: Damage progression in ply-level scaled UNT models, subjected to longitudinal compression.

Table 5.6: Comparison between experimental results from Ref. [143, 148] and proposed mesoscale damage model on the UNT strength of scaled QI specimens.

Specimen type ($[45_m/90_m/-45_m/0_m]_{ns}$)	Experiments [MPa]	CV [%]	Predictions [MPa]	Error [%]	Predictions with delam. [MPa]	Error [%]
Tension						
(sublaminate-level scaling)						
n, m = 1	842	±7.6	853	+1.3	841	-0.2
n = 2	911	±2.0	915	+0.4	906	-0.5
n = 4	929	±3.9	911	-1.9	971	+4.5
(ply-level scaling)						
m = 2	660	±3.3	669	+1.3	582	-11.8
m = 4	458	±5.8	503	+9.7	398	-13.1
m = 8	321	±2.9	362	+12.9	304	-5.3
Compression						
(sublaminate-level scaling)						
n = 2	658	±3.15	729	+10.8	667	+1.3
n = 4	675	±6.6	627	-7.1	615	-8.8
n = 8	644	±14.0	691	+7.2	647	+0.5
(ply-level scaling)						
m = 2	666	±19.6	649	-2.5	591	-11.3
m = 4	642	±19.0	587	-8.5	508	-20.9
m = 8	472	±13.4	522	+10.7	454	-3.7

5.3.1.2 Strength of open-hole laminates

Continuous FRPs have a number of characteristics that are typical of brittle materials. They lack plasticity to reduce the influence of stress concentrations arising from discontinuities introduced either intentionally as cut-outs and fastener holes, or unintentionally due to in-service damage (impact damage) and defects induced during the manufacturing process [149]. For this reason, research on the mechanical response and failure of OH specimens play an important role in the design of composite structures, as it allows to study the effect of stress concentration on laminate strength and critical failure mechanisms.

This Section presents an additional validation study, based on the experimental data on OH tensile and compressive strengths provided by Airbus. In the presentation of this work, details on material properties and OH strengths will not be disclosed in absolute terms, as they are protected by intellectual property. Normalized values will be used instead, which still allows to understand and analyze the obtained results. The aim of this study is to complement the validation of the proposed meso-scale damage model, exploiting the extensive experimental results on collapse of OH laminates. The available data include the strength and the standard deviation of 4 different OH laminates, presented with X/Y/Z, which refers respectively to the percentage of 0°, ±45°, 90° plies. These OH laminates are: a quasi-isotropic 25/50/25, a highly-oriented 50/40/10, a hard 40/40/20 and a soft highly-disoriented 10/80/10.

Finite element modelling For the present study, the numerical analysis was performed considering 3 sets of material properties, presented with normalized values in Table 5.7. These properties have been used to tackle different types of analysis with different scopes, and herein, their suitability to represent the mechanical response of hard and soft OH laminates is discussed. In addition to the previously defined properties, in this case further elastic properties are used to distinguish the tensile Young's modulus E_{1T} from the compressive one E_{1C}, as well as the elastic modulus in the transverse direction under tension E_{2T} and compression E_{2C}. Following the strategy implemented in the previous section, *in-situ* strengths are calculated and accounted for in the analysis, for each of the studied material sets, using different material cards based on the position and thickness of the ply.

The numerical models are built in a similar way as done to study scaling effects on UNT coupons (Section 5.3.1.1). Indeed, C3D8R solid elements are used to model the plies, with one element per ply block in the thickness direction, while COH3D8 cohesive elements are implemented between plies of different orientation to study the effect of delamination. The OH laminates are clamped on the lower end and a tensile/compressive loading is applied to the upper end of the laminate, using appropriate smooth step amplitudes, to implement a quasi-static loading. These boundary conditions, as applied on OH models for tension and compression, are schematically shown in Fig. 5.24.

Fig. 5.24 also shows the discretization of the models, which implement the multi-zone strategy presented in the previous Section, to minimize the computational cost increasing the resolution only in the region close to the hole. The finite element size characterizing this region, where

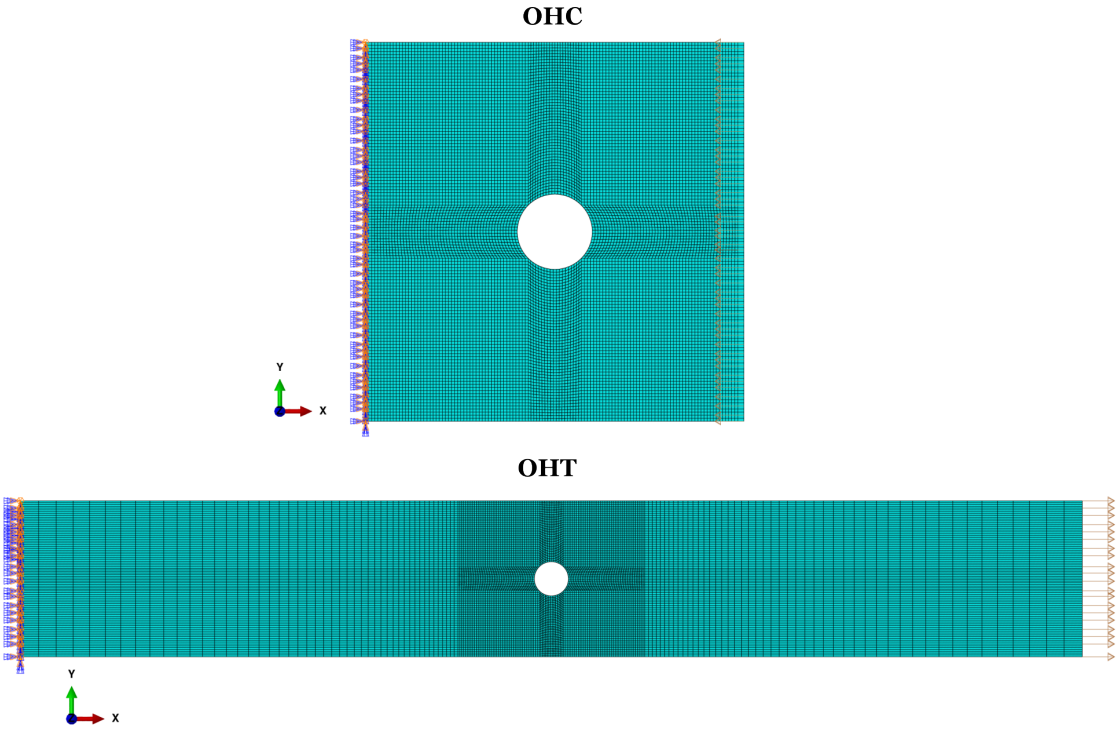


Figure 5.24: Mesh and boundary conditions of OH models, for the case of compression (depicted above) and tension (depicted below).

damage is simulated, is 0.26 mm, which is selected to be slightly lower than the characteristic lengths for regularizing energy dissipation. Furthermore, enhanced hourglass control, distortion control with a length ratio of 0.80 and the conditions for element deletion specified in Eq. 5.29 were used in the elements of this region, following the same modelling approach as in the previous Section. Geometric non-linearity is also considered in the analysis.

Numerical results Fig. 5.25 shows the predictions for open-hole tensile strength, with the proposed finite element modelling, for a 10/80/10 laminate. In particular, the normalized stress-displacement relationships obtained for the 3 material sets are shown and, on the left-hand side, ply damage only is accounted while, the curves on the right-hand side consider also the effect of delamination through cohesive elements. Comparing these numerical results with the experimental data, it can be noted that all the implemented approaches fail in predicting the stress peak before collapse, with a large deviation from the expected OH strength. It can be observed that, when including only intralaminar damage, the first 2 material sets lead to overconservative predictions, with over 30% error, while the third material set over-predicts the OH strength with an error of about 14%. The obtained outcomes with cohesive elements highlight that the effect of delamination results in an apparent improved strength due to friction, especially for the material set 2 and 3. However, both approaches cannot be considered suitable for addressing failure of OH laminates.

Table 5.7: Sets of material properties, normalized on the values of the first set, used for correlation study on OH specimens.

Property	Mat. Set 1 [-]	Mat. Set 2 [-]	Mat. Set 3 [-]
Elastic properties			
E_{1T}	1.0	0.828	0.986
E_{1C}	1.0	1.027	0.982
$E_{2T} = E_{3T}$	1.0	0.964	1.0
$E_{2C} = E_{3C}$	1.0	0.964	1.118
$\nu_{12} = \nu_{13}$	1.0	1.104	1.104
ν_{23}	1.0	1.518	1.518
$G_{12} = G_{13}$	1.0	1.220	1.598
Strength properties			
X_T	1.0	0.981	0.984
X_C	1.0	0.984	0.984
Y_T, Y_{BT}	1.0	1.0	1.0
Y_C, Y_{BC}	1.0	1.0	1.0
S_L	1.0	1.675	1.675
S_T	1.0	1.0	1.0
Fracture properties			
$\mathcal{G}_{1-}$, $\mathcal{G}_{1+}$, f_{GC}, f_{GT}	1.0	1.0	1.0
$\mathcal{G}_{\mathrm{Ic}}$	1.0	1.0	1.0
$\mathcal{G}_{\mathrm{IIc}}$	1.0	0.290	0.290
η, μ	1.0	1.0	1.0
Interlaminar properties			
K	1.0	1.0	1.0
$\tau_1^0 = \tau_2^0 (= S_L)$	1.0	1.675	1.675
$\tau_3^0 (= S_T)$	1.0	1.0	1.0
$\mathcal{G}_{\mathrm{Ic}}$	1.0	1.0	1.0
$\mathcal{G}_{\mathrm{IIc}}$	1.0	0.290	0.290
η	1.0	1.0	1.0

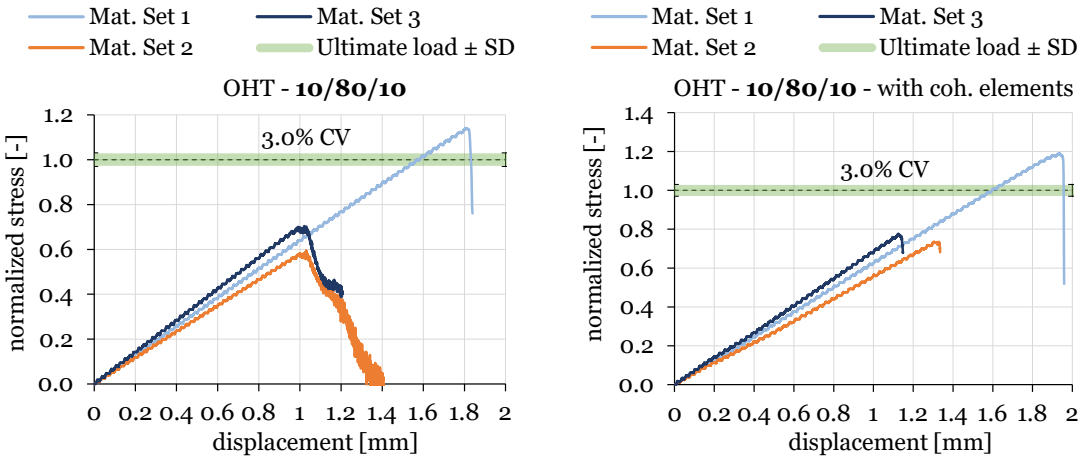


Figure 5.25: Normalized stress-applied displacement curves for 10/80/10 OH laminate under tension, obtained for different sets of material properties.

Moreover, the large over- and under-predictions hint that the numerical results are very sensible to material properties and thus, the latter need a deeper investigation. Indeed, the material was not fully characterized and the defined sets of properties rely on some assumptions. For this reason, this work will also study the effect of two material properties: the transverse Poisson's ratio (ν_{23}) and the pure mode II fracture toughness ($\mathcal{G}_{IIc}$), by including a 4th and 5th set of properties. Both sets are based on the properties of the material set 3, but in set 4, the normalized ν_{23} is equal to one (being the corresponding value in set 1) while, in set 5, only $\mathcal{G}_{IIc}$ was modified, whose normalized value was increased to one.

Normalized results for each of the analyzed OH laminates are presented in Fig. 5.26 for the tension case, while the same study under compressive loading is presented in Fig. 5.27. The obtained results show that material properties have a remarkable influence on the predicted strength of OH laminates under tension, while a less significant effect can be seen under compression. A quantitative comparison between the numerical and experimental results for open-hole tensile and compressive strengths is presented in Fig. 5.28. The standard error related to the experimental test results is also included.

With the aim of selecting the most suitable set of material properties (among the five studied) and modelling strategy (in terms of implementation of cohesive elements), the overall performance of each approach was evaluated based on the accuracy of the obtained predictions. As mentioned before, the first 3 material sets cannot be considered suitable to simulate the OH tension and compression tests. In fact, the first set often over-predicted the OH strength, with a relative error larger than 14% for 3 out of 8 cases, while the sets 2 and 3 lead to overconservative predictions under tension, despite being quite accurate for the cases under compression. Indeed, for the studied material system, the loading condition that resulted critical for simulation is the tensile one.

The study on the effect of ν_{23} and $\mathcal{G}_{IIc}$ highlighted that both variables have a negligible effect on the prediction of the OH compressive strength, while being relevant to correctly address the failure behaviour under tension. Although the modified value of pure mode II fracture toughness

allowed to mitigate the conservatism of the predicted strength, the overall agreement cannot be regarded as satisfactory, especially for the 50/40/10 specimen (relative error of 36%, when including delamination). A good trade-off is achieved reducing the value of ν_{23}, as only amendment from the material set 3, which enabled significantly improved and consistent predictions. For OH tension, a mean error of 5.5% and maximum error of 13% was achieved modelling only ply intralaminar damage, while a mean error of 20% and maximum error of 30% with models with cohesive elements. Then, for OH compression, a mean error of 6.2% and maximum error of 13% was obtained modelling only ply intralaminar damage, while a mean error of 6.7% and maximum error of 8% with models with cohesive elements.

To study the critical failure mechanisms and their propagation, a more detailed analysis is required. This kind of investigation is essential to identify the region where damage initiation is predicted and the corresponding failure mode, as well as the crack growth. In addition, it will allow assessing in detail the effect of delamination and to select the most appropriate modelling strategy. For this scope, the output fields related to the damage progression obtained during the simulations are provided in Figs. 5.29-5.30. They refer to the simulations obtained with the selected material set, which is the one with the adjusted transverse Poisson's ratio ν_{23}. Following the nomenclature used for the previous study: (i) "SDV_D_SCM" is the user-defined damage variable of the SCM for matrix-dominated failure, (ii) "SDV_D1_CDM" is the user-defined damage variable of the CDM for fibre-dominated failure and (iii) "SDEG" is the Abaqus®' internal damage variable for delamination events.

Based on the obtained results, the following observations can be made:

- The tensile strength of 10/80/10 is well predicted using the properties from the material set 3 and tuning the value of ν_{23} according to set 1. The progressive development of damage taking place in this soft OH laminate starts with 45° matrix cracks on the surface, stepping down through the laminate via delamination (e.g., the -45°/90° interface in Fig. 5.30) and further matrix cracks until reaching the -45°/0° interface, at which point final collapse occurs due to fibre failure.

- The predicted failure mechanisms occurring in the quasi-isotropic 25/50/25 OH laminate under tension are the same described for the 10/80/10 laminate, with more extended matrix cracks in the 90° ply before final failure, which in this case is controlled by delamination.

- The failure behaviour of the hard 40/40/20 OH laminate is brittle and it takes place after some initial matrix cracks in the embedded 90° ply, close to the 0° ply block, providing less and less support to the oriented plies that sustain the load. Final collapse is predicted to occur due to delamination and fibre failure.

- The oriented 50/40/10 OH laminate is predicted to fail due to complete delamination of the interfaces close to the blocked 0° ply. This prediction is quite conservative, when compared to experiments, indicating that the interlaminar properties need further investigations. Indeed, the model without cohesive elements predicts very well the load drop, with a relative

error of around 4%. In this model, final failure is brittle and controlled by fibre failure after axial splitting (local damage) that occurs tangentially to the free edge of the hole.

- The values of the predicted notched compressive strengths are in good agreement with the measured failure strengths, for all analyzed OH laminates. Delamination affects the prediction, in all the cases, contributing to lower the load drop, often improving the correlation. It can be observed that, for all the studied OH laminates, final collapse is fibre dominated, which propagates perpendicularly to the applied load, and matrix cracks and delamination develop in the same direction, due to stress redistribution.

It can be summarized that the proposed mesoscale model allowed to perform a detailed analysis of the notched tensile and compressive strength of 4 different OH specimens. The evolution of failure is in agreement with the expected one and a satisfactory prediction of the strengths was obtained, especially for the cases under compression. Despite failure initiation is often matrix- or fibre-dominated, the results show that delamination can be one of the critical failure modes that drive final failure and, therefore, it must be accounted for reliable failure predictions. However, the lower consistency in the predictions of the notched tensile strength with models including cohesive elements indicate that further studies are required to better represent the interlaminar behaviour of the studied material system. Additionally, for soft OH laminates (e.g. 10/80/10), large deformation takes place in the 45° plies and in-plane shear plasticity would be required to be included in the damage mode. This work has been recently done by Zhuang et al. [157], proposing a bi-linear elastoplastic model to represent the non-linear response under longitudinal shear and it will be considered for the further development of the damage model.

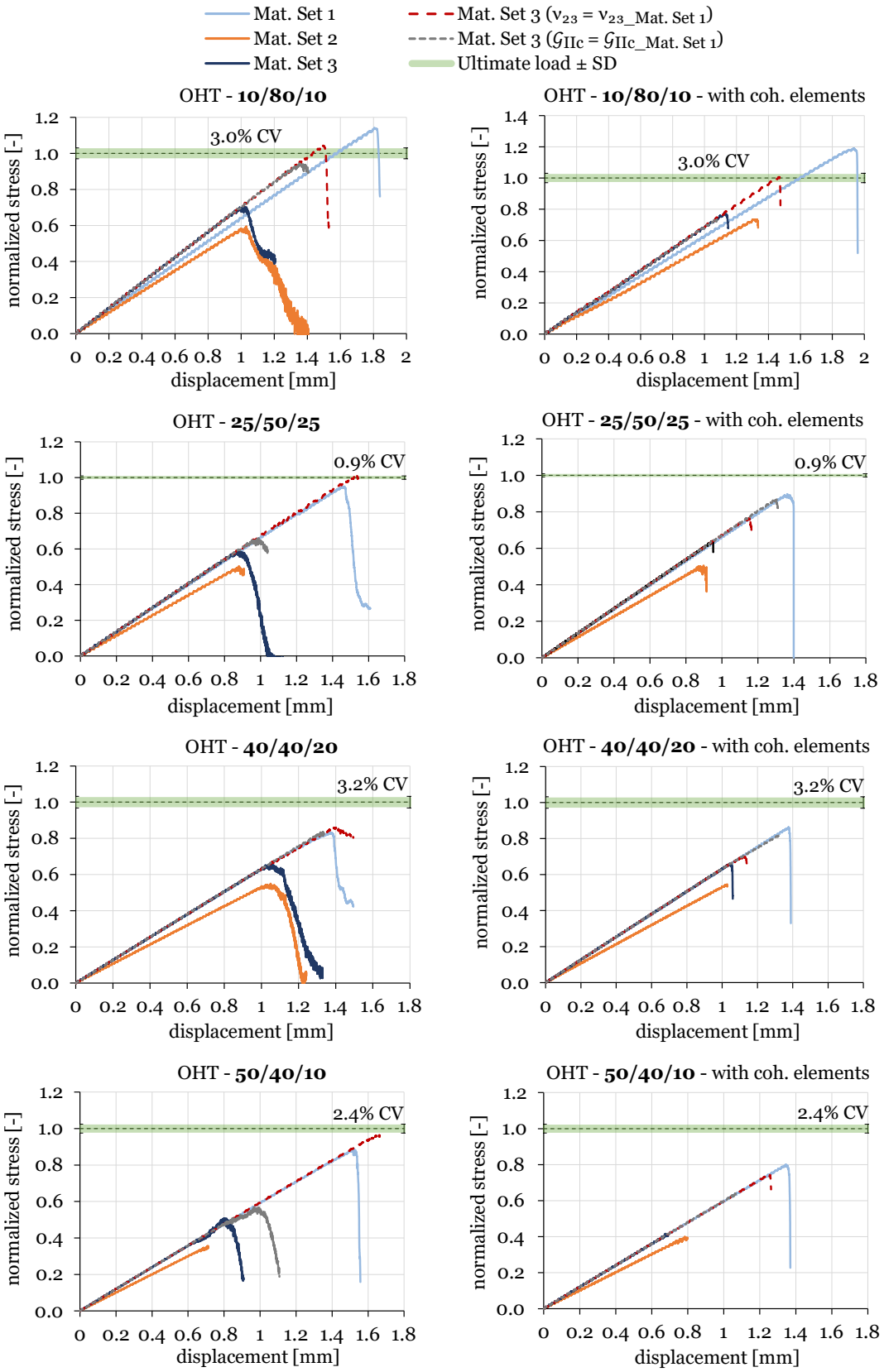


Figure 5.26: Overall correlation between experimental results with coefficient of variation and predictions of OH specimens subjected to tension.

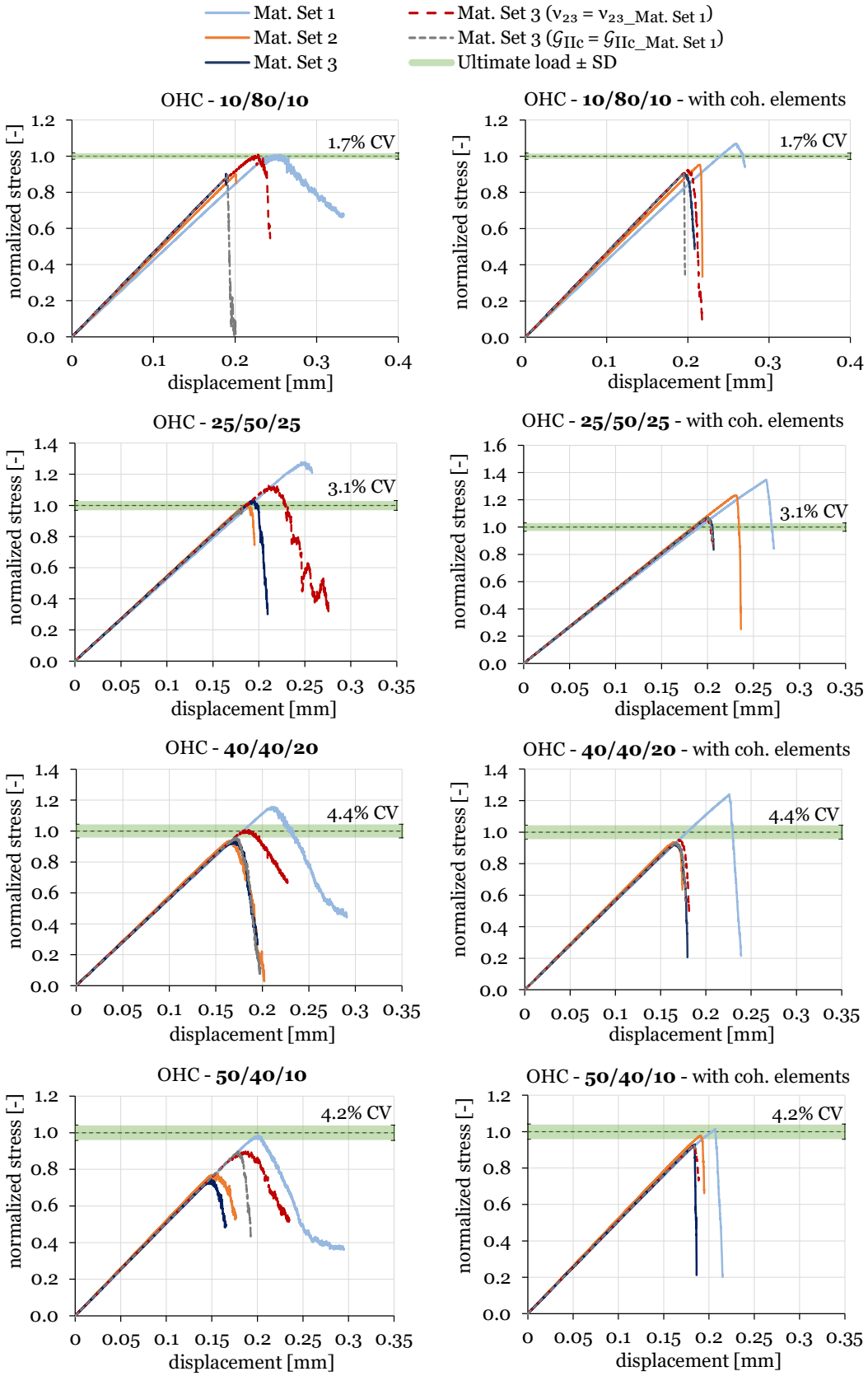


Figure 5.27: Overall correlation between experimental data with coefficient of variation and predictions of OH specimens subjected to compression.

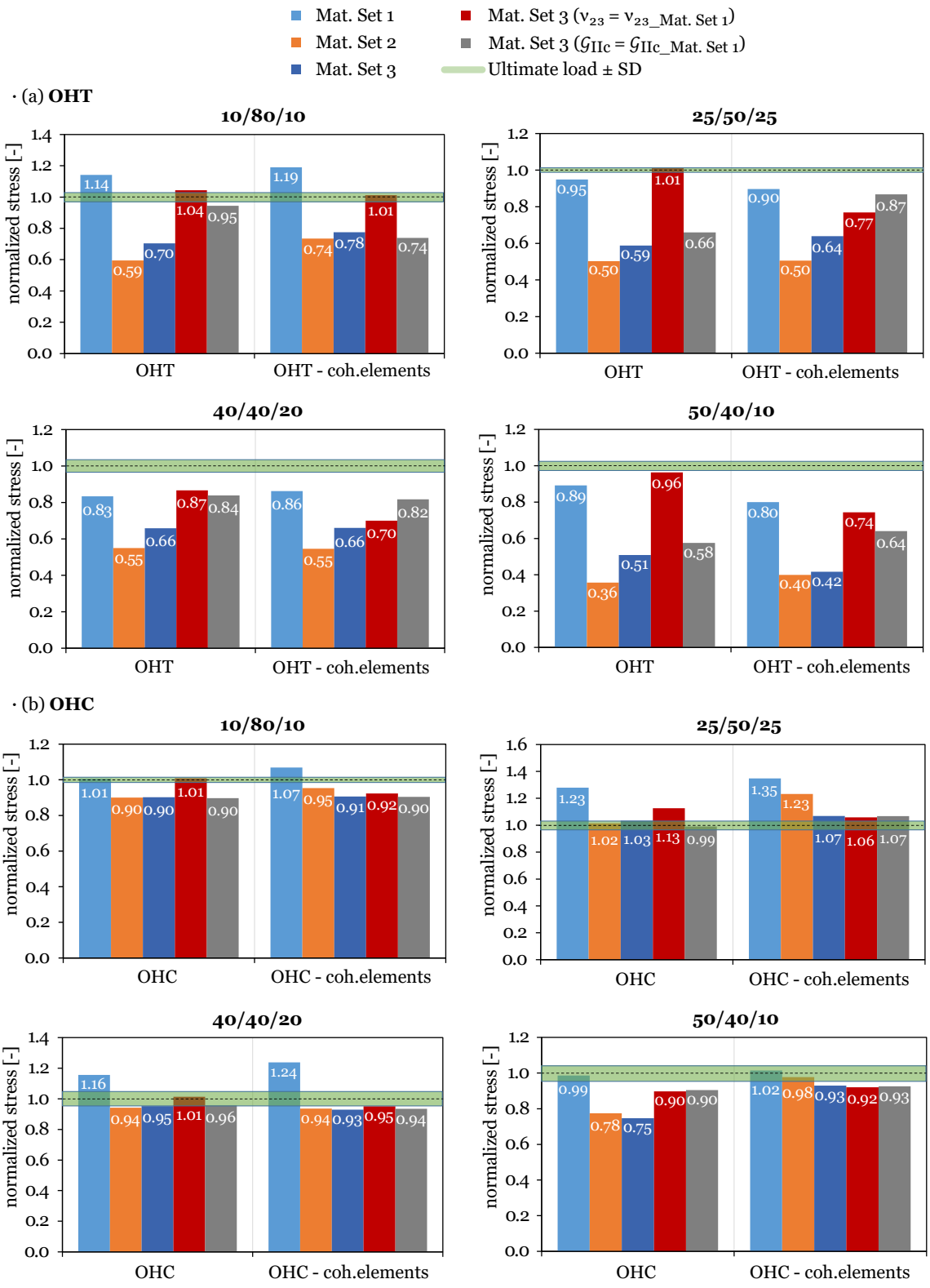


Figure 5.28: Column plots of the obtained numerical results and experiments with standard deviation for OH laminates, under tension in (a) and under compression in (b).

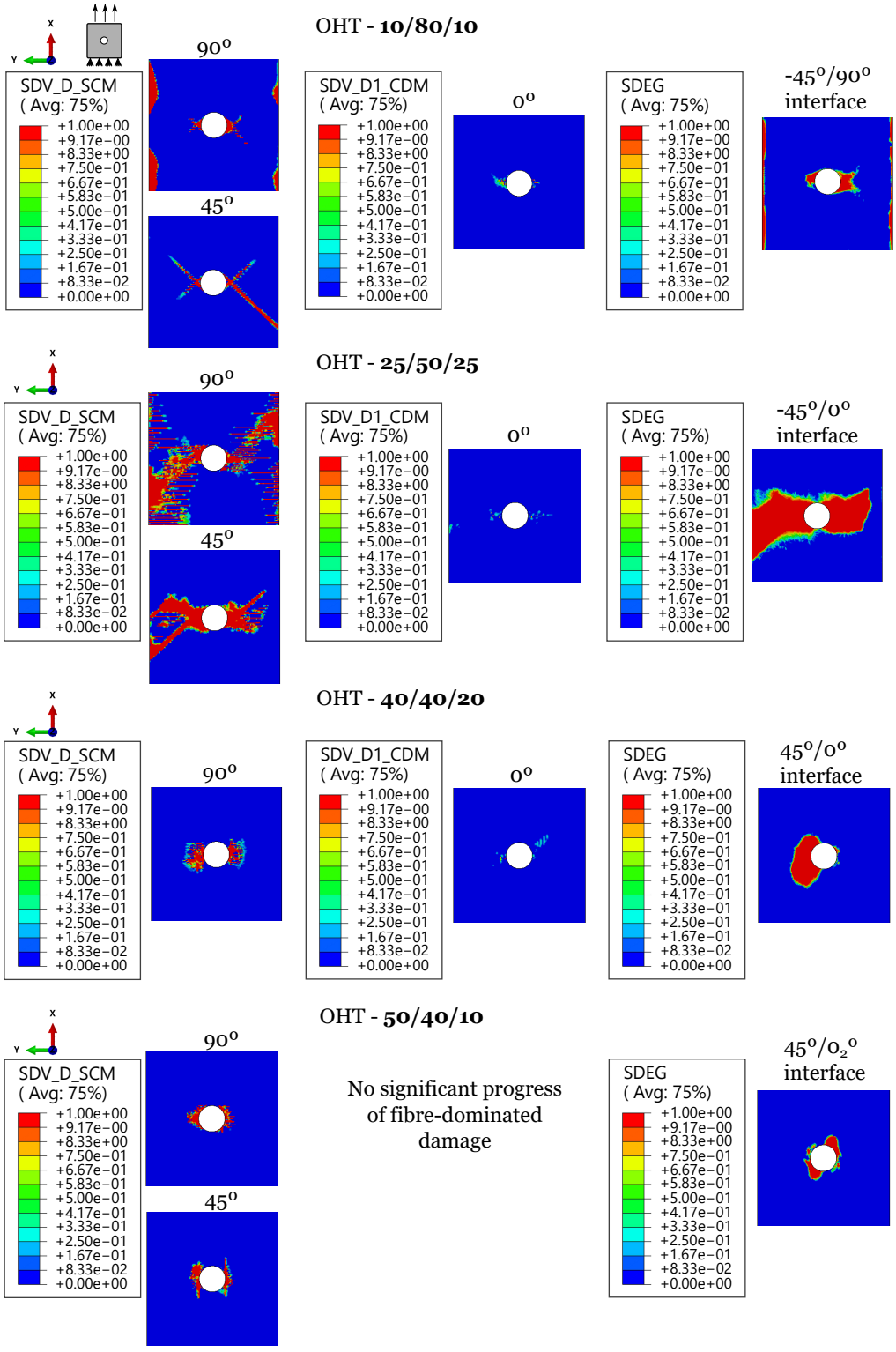


Figure 5.29: Damage progression in OH models subjected to longitudinal tension.

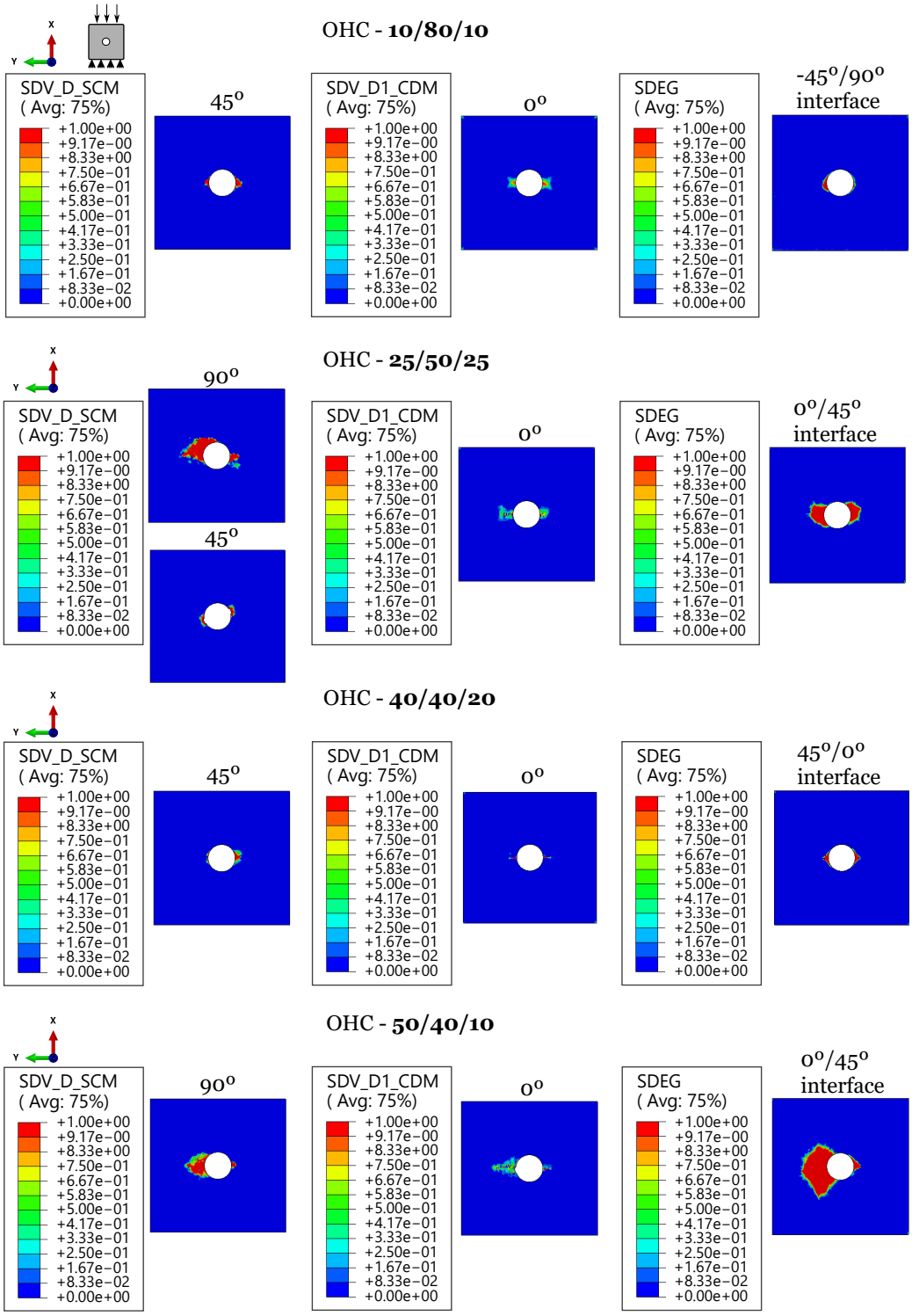


Figure 5.30: Damage progression in OH models subjected to longitudinal compression.

5.3.2 Validation at the structural detail level

Section 5.1 described the analytical framework of the mesoscale damage model, with the proposed developments in the description of fibre-dominated failure to account for the effects of pressure. The motivation behind the proposed modification is to achieve an increased accuracy in the prediction of the extended load-carrying capability of thick multidirectional laminates or structural elements designed to sustain, in their life-cycle, fully 3D stress stresses. By overcoming the limitations in the numerical description of kink band formation and broadening, the developed mesoscale damage model can be applied to perform detailed failure analysis of composite structures, subjected to any complex triaxial stress states.

Accounting for high levels of triaxiality is essential, for instance, for the accurate design of composite mechanically-fastened joints. Indeed, one of the bottleneck in the employment of CFRPs is related to their low bearing and shear capabilities, which are deemed decisive for the strength of bolted joints [158]. For this reason, an efficient and reliable description of the damage behaviour of bolted connections is crucial to enhance the structural performance of airframes.

The consolidated practice in industry, for the design of bolted connections, usually rely on semi-empirical failure models, such as the methods based on characteristic distances, which requires costly and time-consuming experimental tests [131, 159]. Therefore, in recent years, high-fidelity FE models have been proposed as a suitable approach to predict the elastic limit and damage behavior of bolted joints in fibre-reinforced laminates. However, the degree of maturity of the proposed damage models (as described in Section 2.5) and the computational cost of performing detailed failure analysis of large models often prevents its direct application for complex cases, such as bolted joints. This limitation does also apply to the mesoscale damage model proposed in this work, as its current state of development makes it not appealing for design office, due to the high computational cost involved for large-scale applications.

In this context, the integration of tools predicting the accumulation of (interlaminar and intralaminar) damage into efficient global-local FE frameworks is of great interest for the aerospace industry. In fact, one of the research gaps identified in Section 2.7, deals with feeding global models with detailed information on ply damage from local models. This approach, if integrated into a MDO platform, would enable a reliable failure-informed optimization, with an acceptable computational time. Furthermore, in this work, the identification of critical regions for local failure analysis has been addressed in Chapter 4, where "hot-spot" analysis proved to provide reliable indication for a targeted increase of the modelling resolution.

The present Section aims at complementing the validation studies, as presented in this Chapter, by addressing a test case characterized by complex triaxial stress states. Indeed, up to this point, the research work carried out to validate the proposed mesoscale damage model, involved test cases subjected to in-plane loadings and characterized by negligible stresses in the out-of-plane direction. For this reason, herein, the progressive evolution of damage in the bolted connection of a stringer run-out will be tackled using the proposed damage model.

In particular, the idea of this work is to exploit the failure predictions for a stringer run-out

obtained with the "hot-spot" failure analysis, as presented in Section 4.3, to generate a local model and predict the accumulation of damage events using the proposed mesoscale damage model. In this way, it will be possible to check whether: (i) paired failure predictions can be obtained and (ii) the mesoscale damage model can complement the analysis providing useful and meaningful details on the evolution of damage up to ultimate load.

Finite element modelling The "hot-spot" failure analysis of the stringer run-out loaded in tension, as described in Section 4.3, have shown that the onset of intralaminar failure is predicted to occur in the vicinity of the bolts. In particular, the numerical results have identified fibre kinking and matrix cracking as critical failure modes taking place at a similar load level, in several plies of the skin and stringer, due to stress concentration around the hole. Additionally, it was highlighted that the critical failure regions at the bottom surface of the stringer match the ones at the top surface of the skin. Following these results, a local model encompassing the bolted connection was generated as illustrated in Fig. 5.31.

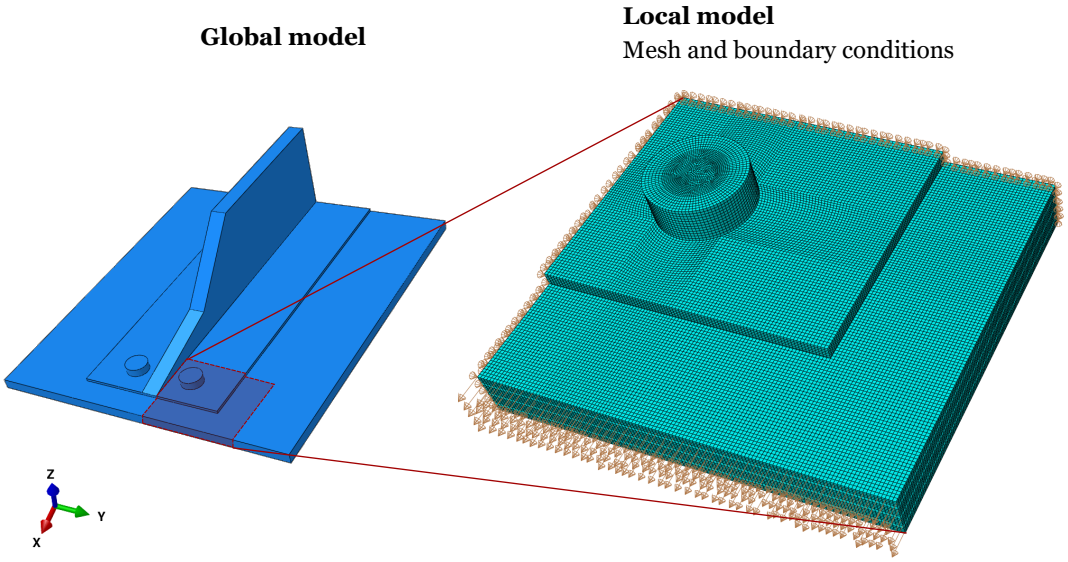


Figure 5.31: Global and local model of a stringer runout, subjected to tensile loading.

The FE model was built in Abaqus/CAE® and simulated using Abaqus/Explicit®. It consists of 2 parts: one representing the metallic bolt and the other one modelling the composite plate, which includes the skin and stiffener of the run-out.

The numerical model for the composite plate is generated using a ply-by-ply discretization, with C3D8R solid elements to simulate the mechanical response of the composite plies and a 0.1 mm layer of COH3D8 cohesive elements to predict the debonding between skin and stiffener. The constitutive response of Abaqus®' cohesive elements is defined using a traction-separation law, as described in Section 2.4.1. The evolution of intralaminar damage is predicted by means of a user-defined material subroutine (VUMAT), which includes the mesoscale damage model proposed in this work.

It should be noted that ply damage is simulated only in the vicinity of the bolt, following the multi-zone strategy shown in Fig. 5.32, while the material response of the side region is kept linear elastic for the entire simulation. The finite element characteristic size and control settings, i.e. enhanced hourglass control and conditions for element deletion, are implemented following Section 5.3.1.1. Failure of the bolt is not included in this numerical analysis.

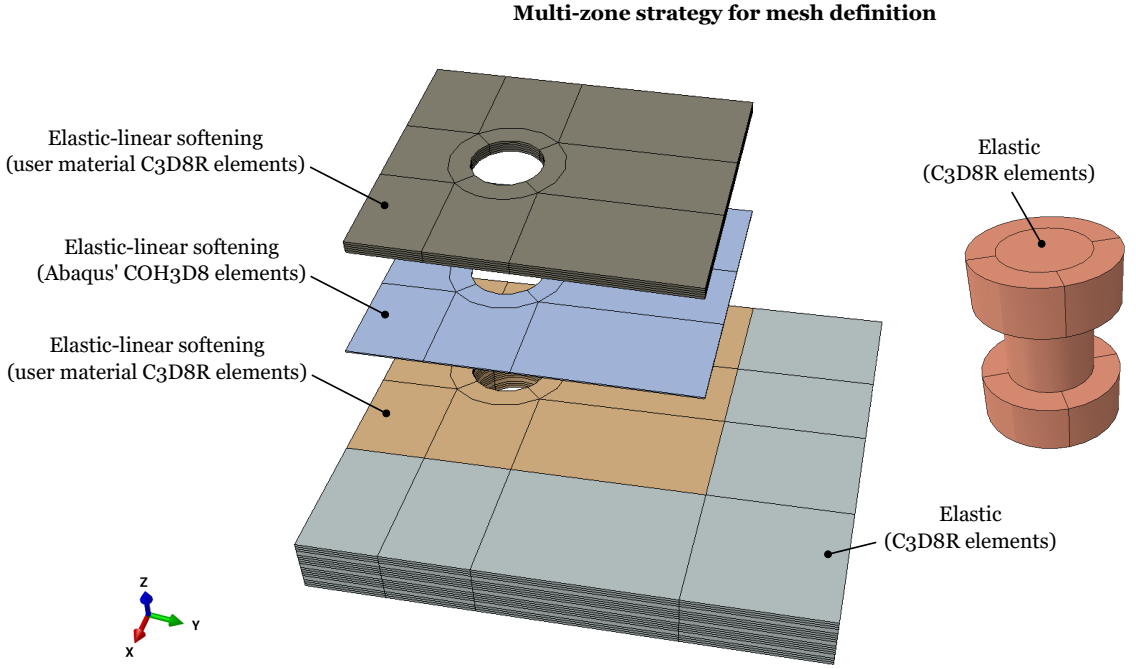


Figure 5.32: Multi-zone modelling strategy for the definition of different mesh and material response.

Skin and stringer are made from IMA/M21E carbon-epoxy UD pre-pregs, while the bolt is made from stainless steel. The material properties used for this study cannot be disclosed as they are protected by intellectual property, as mentioned in Section 4.3. In-situ properties are accounted for this study and calculated as described for the previous validation cases.

The definition of contact between the parts is realized by selecting surface-to-surface contact pairs, as shown in Fig. 5.33. In this case, the surfaces in contact are external, between the bolt head and the plate, and internal, between bolt shank and the plate. For all the selected pairs, the applied contact includes "hard" normal behaviour, to avoid penetration, and frictional tangential behaviour, with friction coefficient $\mu_{\text{m-c}} = 0.2$ between the metallic bolt and the composite plate.

The boundary conditions of this local FE model are applied clamping the lower edge of the plate to the longitudinal and out-of-plane direction, and the side edge to the horizontal direction, as shown in Fig. 5.31. A two step job is set-up to simulate firstly the pre-loading of the bolt and then the tensile load. The pre-loading of the bolt is simulated by decreasing the temperature of the bolt shank, by means of a suitable Smooth step amplitude. The bolt shank is assigned with an orthotropic thermal expansion that is nonzero only in the direction of the bolt shank, global Z, axis (i.e., null thermal expansion in the radial directions, global X and Y axes, see Fig. 5.32). A

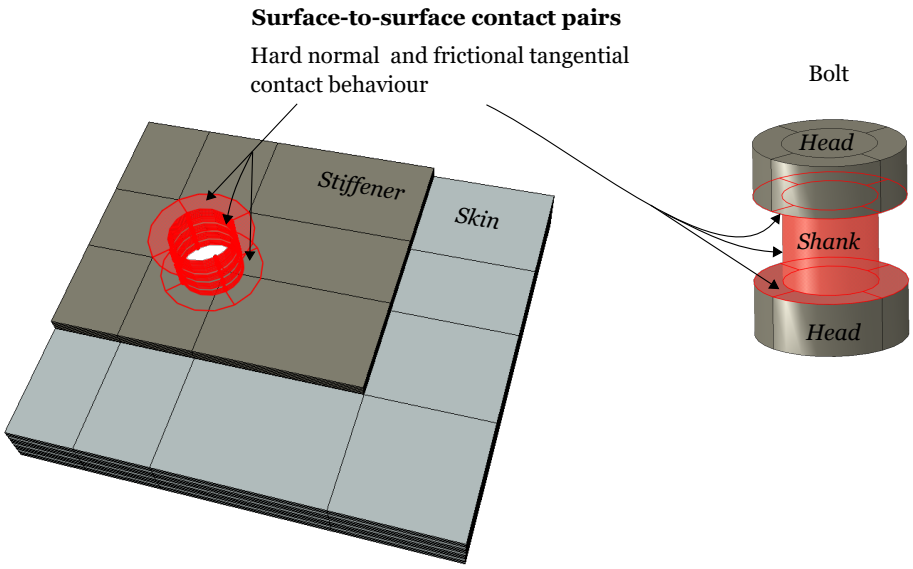


Figure 5.33: Definition of contact behaviour between bolt, skin and stiffener.

calibration procedure is followed in order to apply the clamping load reported from experiments. Then, the introduction of the tensile load on the upper end is also realized using Smooth step amplitude. Furthermore, geometric non-linearity is considered in the analysis, as it is expected to be characterized by local high deformations.

Numerical results To study the effect of the bolt load, different values of pre-loading were included in the analysis. In particular, starting from the value of 1 kN reported in the experiments, a higher and a lower pre-loading of 1.5 and 0.6 kN, respectively, were considered. The obtained numerical results are summarized in Fig. 5.34.

It can be observed that the applied bolt load has a minor influence of the mechanical response of the bolted connection, which is in line with the experimental findings on the stringer runout. In particular, it has no effect on the load level at which the first load drop takes place, also known as "knee point", while it slightly increases the bearing stress before final collapse, only when the level of pre-loading is 1.5 kN.

Fig. 5.34 also shows the predicted evolution of damage for the investigated bolted connection, considering the case of bolt load equal to 1 kN. Following the nomenclature adopted in the previous validation studies, the propagation of fibre damage, matrix cracking and delamination are presented for points "A" and "B", as highlighted in the stress-displacement curve. For this purpose, the damaged elements are superposed on the geometry of the bolted connection by using a visualization option available in Abaqus®. Different colors were selected for highlighting the different degree of damage. Partially-damaged elements are coloured in green, where the damage variable is the range between 0.10 and 0.99, the elements where damage is in its early stage in blue, with a damage variable between 0.001 and 0.10, and the ones severely damaged in red, with a damage variable greater than 0.99.

The obtained results show that the evolution of damage is controlled by delamination growth, which drives the first knee point and the final load drop. It starts from the front side, as the tensile load is only applied to the skin, generating a high interlaminar stress between skin and stiffener. Fibre failure is predicted to initiate in the vicinity of the hole, but its evolution, in terms of severity of damage and extent, is confined and it has a minor effect on the overall mechanical response. Matrix failure events also start in the vicinity of the bolt, in the skin, but with a more significant extension and contributing to a greater number of severely damaged elements.

A detailed plot of the output field at point "A" and "B" of the stress-displacement curve, for the most damaged plies is provided in Fig. 5.35. As expected, matrix cracks progress more in the vicinity of the delaminated area, between skin and stiffener, and therefore, it affects the corresponding 45° plies. It can be noted also that hot-spot failure analysis and mesoscale damage model share the same predictions in terms of critical location for intralaminar failure (as shown in Figs. 4.17-4.19).

The numerical results highlight also an edge effect on damage onset, hinting that the area to be modelled would need to be enlarged for more reliable results away of the bolted connection. Indeed, this detailed analysis has the aim to test the proposed damage model for cases involving triaxial stress states. However, the applied load does not account for the results from a global analysis and, in general, the performed analysis cannot be considered representative of the stringer runout, as stress redistribution after damage is not considered. Therefore, strong assumptions were made and, despite the limitations of the analysis, the results confirm the indications obtained from the "hot-spot" failure analysis for failure initiation and provide a detailed description of damage progression, which is in agreement with the experimental results.

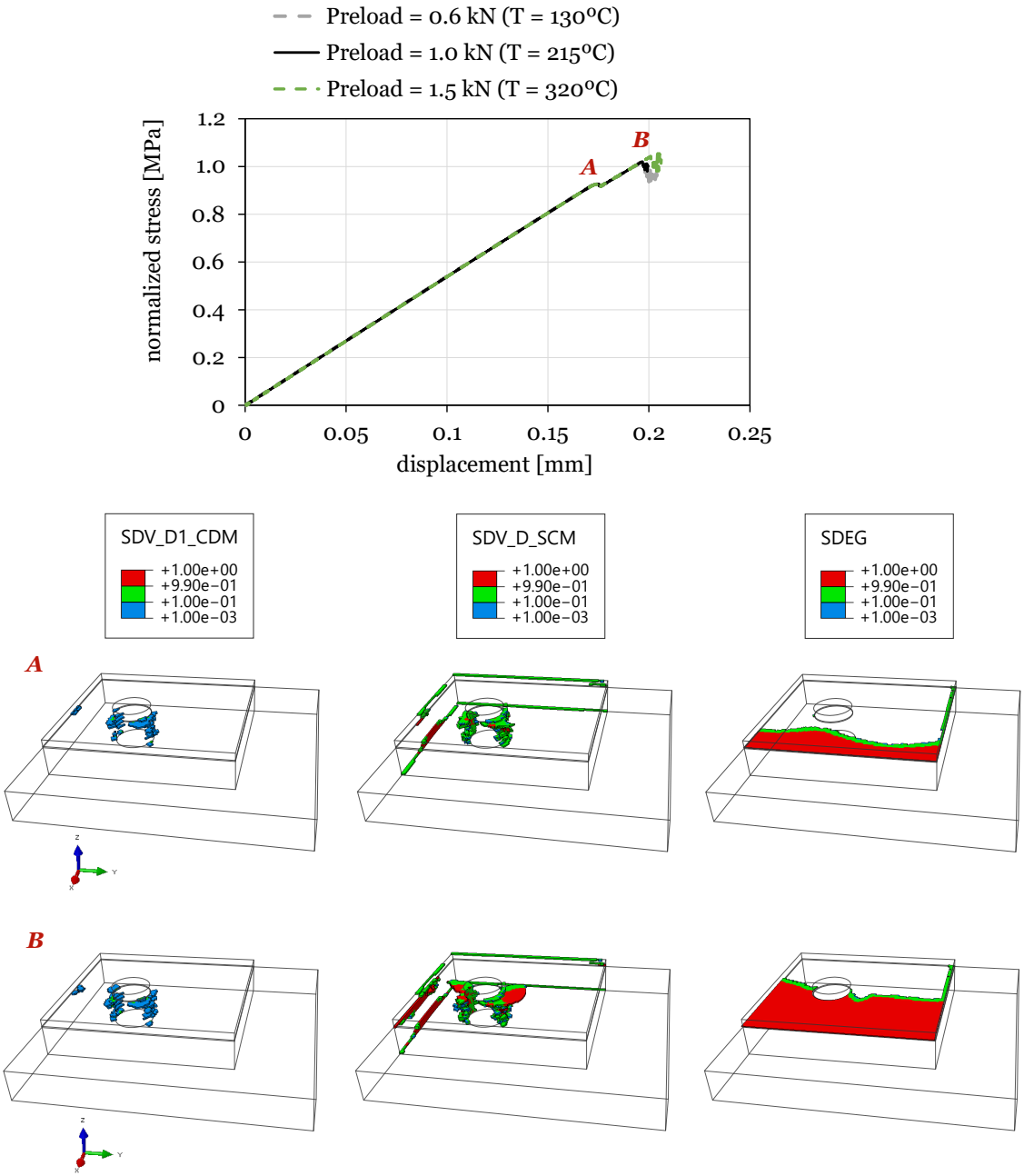


Figure 5.34: Stress-displacement curves, obtained applying different levels of pre-loading, for a bolted connection under tension. Below the evolution of intralaminar damage and delamination is showed for the case of 1 kN clamping load.

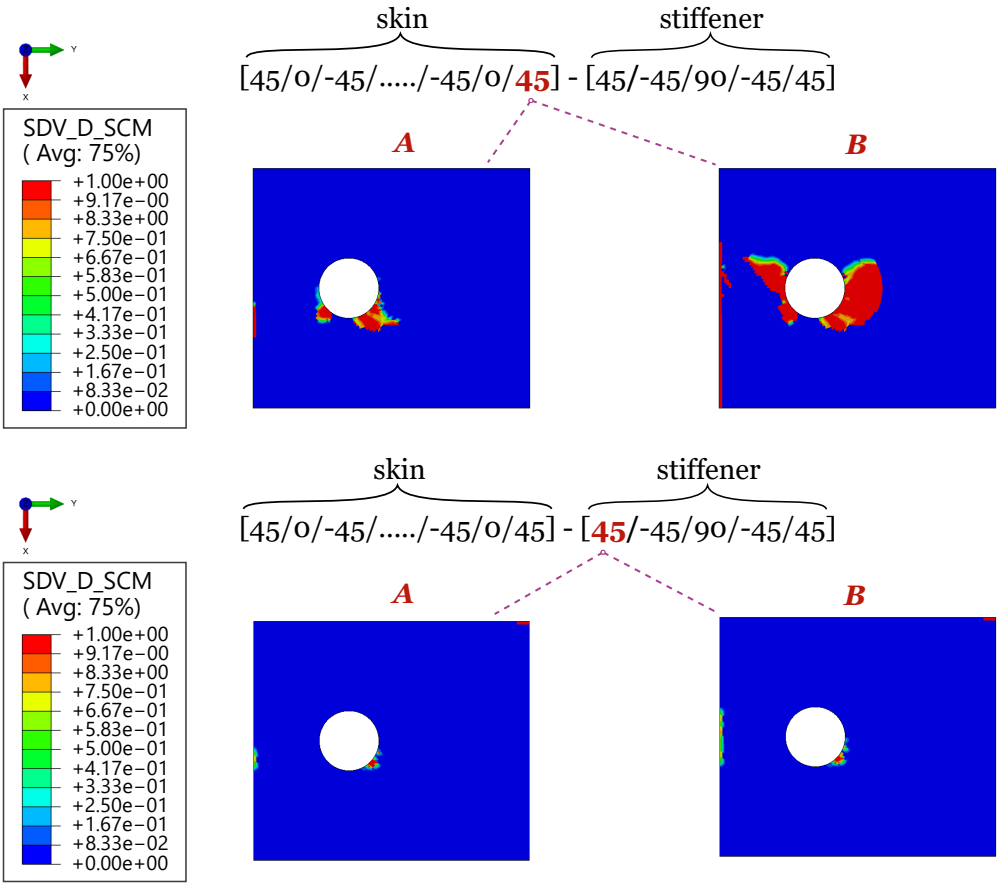


Figure 5.35: Matrix damage evolution in a bolted connection subjected to longitudinal tension.

Part IV

Conclusions

Chapter 6

Conclusion and future work

This chapter presents the conclusions and suggestions of future work. The first section provides a summary of the research topic, the objectives of the work, the implemented methodologies to achieve the goals and the obtained results. The conclusions of the research work are drawn discussing the obtained results, as well as strengths and limitations of the original contributions introduced with this thesis. Finally, the research ideas regarding the future development of the work are described in detail.

6.1 Conclusions

Although research on failure of composite materials has achieved a high level of maturity, describing the underlying failure mechanisms within the constituents of the composite and their effect on the ultimate macroscopic behavior, some challenges remain. In this thesis, the addressed challenge includes mainly: (i) the development of models across different length scales, which are required for the effective design and optimization of aircraft structures, and (ii) the application of those models to structural details relevant for aircraft structures.

In this work, to tackle failure predictions at the laminate level, an extension of a recently introduced concept, called omni strain failure theory, was proposed. An omni strain failure envelope is the minimum envelope obtained by considering failure envelopes for all possible orientations in strain space. The extension of this theory was motivated by the inherent limitations in failure predictions of the original concept, since it was based on the Tsai-Wu criterion. For this reason, the proposed development was based on the 3D invariant-based failure criteria, to generate omni strain envelopes that predict laminate failure under general 3D stress states and identify critical failure modes. This concept allows simple generalization of ply-based criteria to laminate-based criteria, overcoming two important constraints in multidisciplinary design optimization of composite aerostructures: (i) computing time, by establishing laminate failure criteria independently of ply discretization, and (ii) excessive conservatism, by incorporating safe LPF criteria instead of overconservative FPF criteria.

A validation study of the predicting capability of omni LPF envelopes was performed, using experimental results from the first and second WWFE. A good agreement was observed for the 2D cases, where the added value brought by the proposed envelopes consisted mostly in the identification of the critical failure modes, while having a minor effect on the accuracy of the failure predictions. This additional information is particularly useful when analyzing glass-fiber composites. Indeed, their LPF is governed by different failure modes; while LPF of CFRP laminates is always governed by fibre failure.

Then, a triaxial test case was studied to further validate the implemented omni-strain criterion. The obtained results highlighted that the proposed 3D omni LPF surface presented some degree of conservatism, with respect to experimental data on an angle-ply laminate, providing, nevertheless, a safe design space with minimal analysis cost due to its laminate invariant character. However, such degree of conservatism will not be expected in industry-standard CFRP quad laminates, containing [0], [$\pm$45] and [90] plies. Moreover, it is shown that the influence of the out-of-plane stress cannot be neglected to properly capture laminate failure under hydrostatic pressure and to obtain safe LPF predictions under general 3D stress states. So, the described method proves to be a very robust tool, giving reliable and fast failure indications in either 2D or complex 3D stress states. Being a quick tool, it can be used for preliminary design and integrated in multidisciplinary design optimization platforms, meeting the industrial need for computational efficiency, while simplifying the failure analysis and sizing of composite laminates.

This part of the thesis also presents advanced numerical methods to predict failure at the ply and laminate level in a FE framework. Firstly, a set of 3D phenomenological failure theories, known as the 3D invariant-based failure criteria, was implemented in a FE code to perform "hot-spot" ply failure analysis and identify the critical locations for damage onset and the corresponding ply failure modes. Additionally, a simplified failure theory to be applied at the laminate level, called unit circle, was also implemented to perform "hot-spot" laminate failure analysis with recourse to models with an equivalent-single layer discretization. Two test cases were selected for the validation of "hot-spot" failure analysis at two different levels: at the coupon level, open-hole laminates with different layups were tested under quasi-pure bending; at the structural level, a stringer runout loaded in tension was analyzed.

The "hot-spot" identification analysis resulted satisfactorily accurate for the prediction of critical locations for intralaminar failure onset for both test cases, confirming the critical failure modes and the locations prone to damage onset observed in experiments. Furthermore, the proposed "hot-spot" failure analysis strategies are useful preliminary tools that can be used to obtain quick indications about intralaminar failure onset, the corresponding failure modes, without going through complex analysis and numerical problems.

The last part of the present thesis addressed advanced mesoscale failure models for composite materials. In particular, to predict the inelastic deformation up to ultimate failure in detailed models, the 3D invariant-based criteria were coupled with a meso-scale damage model that accounts for the kinematics of matrix crack and kink band formation during damage propagation. The motivation of the proposed material model was to account for the effect of complex 3D stress

states in the prediction of both onset and broadening of longitudinal and transverse failure mechanisms. Indeed, the novelty of the presented work relies on the description of longitudinal failure mechanisms, which was modified to capture the effect of hydrostatic pressure and general 3D stress states. This was done by using the 3D kinking model for the onset of failure, as well as for damage evolution in the longitudinal direction. Therefore, for the first time, the full set of 3D invariant-based failure criteria was implemented for the onset and propagation of intralaminar damage, within a meso-scale damage model.

After presenting the theoretical background of the damage model, an extended verification study at the single element level and coupon level was performed. These studies proved the correct implementation of the model, showing that detailed analysis can be correctly realized, for instance, exploiting the prediction of failure initiation and progression, with the corresponding failure mode and fracture angle. Furthermore, the test made applying different levels of hydrostatic pressure confirmed that the model can capture the expected apparent increase of strength.

Then, a validation study was performed considering experimental data at the coupon level. In particular, the proposed damage model was tested to capture the size effect in quasi-isotropic unnotched coupons under tensile and compressive loading. Two types of scaling were addressed: sublaminate level scaling, being the repetition of the sub-laminate stacking sequence, and ply-level scaling, realized by changing the thickness of each ply block. As an additional test, experimental results on OH laminates under tension and compression was considered. For both studies, the numerical simulation was run with Abaqus/Explicit®. Intralaminar failure onset and propagation was predicted using solid C3D8R elements, delamination was captured using cohesive COH3D8 elements and *in-situ* properties were included by using different material cards according to the position and thickness of the plies.

The validation at the coupon level of the proposed meso-scale damage model was successfully completed. The obtained results were in agreement with the experimental findings, in terms of quantitative predictions (with an acceptable deviation from the mean value) and predicted damage progression before final collapse. In the first study, the developed model was able to capture well the size effect in the unnotched strength and to highlight the importance of delamination in the obtained predictions. Then, the investigation of the notched tensile and compressive strength highlighted that the proposed damage model provides reliable predictions of the progression of failure events. However, the lower consistency in the predictions of the notched tensile strength with models including cohesive elements hinted that further experimental work is needed to better characterize the interlaminar properties of the studied material system.

To complement the validation work, the bolted connection of the stringer runout, analyzed for “hot-spot” failure identification, was addressed. This work exploited the indications from the “hot-spot” failure analysis, to generate a local model encompassing the critical region for failure onset. Furthermore, this test case involves significant 3D stress states, which must be accounted for an accurate prediction of the bearing strength. The obtained results confirmed that delamination governs the failure scenario and that the predictions for intralaminar failure are paired with the ones identified by the “hot-spot” failure method. Furthermore the effect of the applied bolt load

was studied, resulting to have a minor effect on the mechanical response of the bolted connection, as expected.

Although the predicted evolution of failure correlates well with experimental findings, the performed analysis does not account for the local stress field obtained from a global finite element analysis and, thus, it cannot be considered representative of the stringer runout case. However, it proved that the proposed mesoscale is a suitable tool to be integrated into a global-local framework, as it provides useful and reliable details on the evolution of damage up to ultimate load.

6.2 Future work

To exploit the advanced failure models developed in this thesis, their integration in the MDO framework would be of great interest. The proposed extension of omni-strain failure concept could be already of interest for this purpose, being a quick tool generating a reliable design space for first-ply and last-ply failure under general 3D stress states.

Additionally, the proposed "hot-spot" failure analysis strategies could be useful to identify critical regions against failure onset in large global models. Exploiting these indications, a global-local analysis can be performed, increasing the resolution of the failure analysis only where required. Within the same scope, the integration of the proposed mesoscale damage model proved to be a valid option for local detailed failure analyses. In this way, the progression of ply damage can be effectively captured, also under complex 3D stress states.

In spite of the accuracy obtained using the meso-scale damage model, to make it suitable for "design office" application, a further work is required. In particular, the user-material subroutine needs to be reviewed for code optimization, to effectively reduce its computational cost. Furthermore, additional effort is required to improve the formulation of the constitutive law, in order to allow larger element sizes, while preventing the snap-back effect. This development can be done, for instance, by artificially tuning the strengths and correctly dissipating the fracture energy.

As mentioned in Section 5.3.1.2, to capture the large deformation characterizing soft laminates, in-plain shear plasticity needs to be incorporated in the damage model. This type of work was recently done, showing to be crucial for those applications [157]. Finally, additional validation studies can be also performed. For instance, the size effect in flexural strength can be studied and predicted, exploiting the experimental findings available in the literature.

Part V

Appendix

Appendix A

Bisection method

The bisection method is a root-finding technique, used in this work to compute the locus of points defining a certain failure envelope, also known as failure loci. The method states that if a function $f(x)$ is continuous between a and b, and $f(a)$ and $f(b)$ have opposite signs, then there exists at least one root in the interval $[a,b]$. Supposing that $f(a)$ is negative and $f(b)$ is positive, as schematically shown in Fig. A.1, at each iteration [160]:

1. Calculate the midpoint of the interval $x_0 = \dfrac{(a+b)}{2}$.
2. Calculate the function value at the midpoint $f(x_0)$.
3. (a) If $f(x_0)$ is lower than a designed tolerance value $\Delta\varepsilon_{tol}$, the iteration stops and returns x_0.

   (b) Otherwise, if $f(x_0) > \Delta\varepsilon_{tol}$, the root lies between x_0 and a or x_0 and b, depending on whether $f(x_0)$ is positive or negative, respectively.In other words, if $f(x_0)$ is negative (as shown in Fig. A.1), the new interval will be $[b_1 = b,\ a_1 = x_0]$, otherwise the new interval will be $[b_1 = x_0,\ a_1 = a]$. Then return to (1.) and perform new iteration, calculating a new midpoint, until the convergence condition (3.a) is verified.

It is clear that the interval width is reduced by a factor of 0.5 at each step and at the n-th step, the new interval will be $[a_n, b_n]$ of length $|b-a|/2^n$. This enables an assessment of the convergence rate of the method.

For the present application, in order to consider all the possible combinations of applied loading in stress or strain space, it is convenient to search each failure point using a polar coordinate system and, thus, to apply the bisection method for each angular position, coinciding with θ in Fig. A.2. The number of failure loci will coincide with the number of angular increments, by which the stress or strain space is divided. An example of failure envelope, constructed using the bisection method as described before, is shown in Fig. A.2. For each angle (θ), the value of "r", calculated by means of the bisection method, represents the combination of applied strains (ε_{11}, ε_{22}) at which failure occurs. The implementation of this method for the generation of failure envelopes in strain space was realized by means of a Python script.

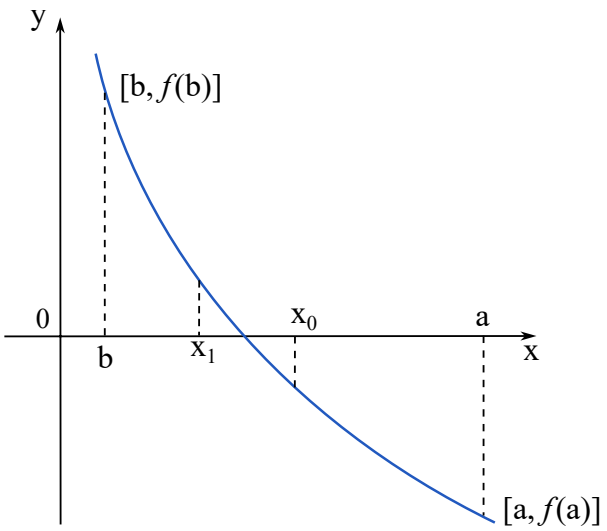


Figure A.1: Graphical representation of the bisection method.

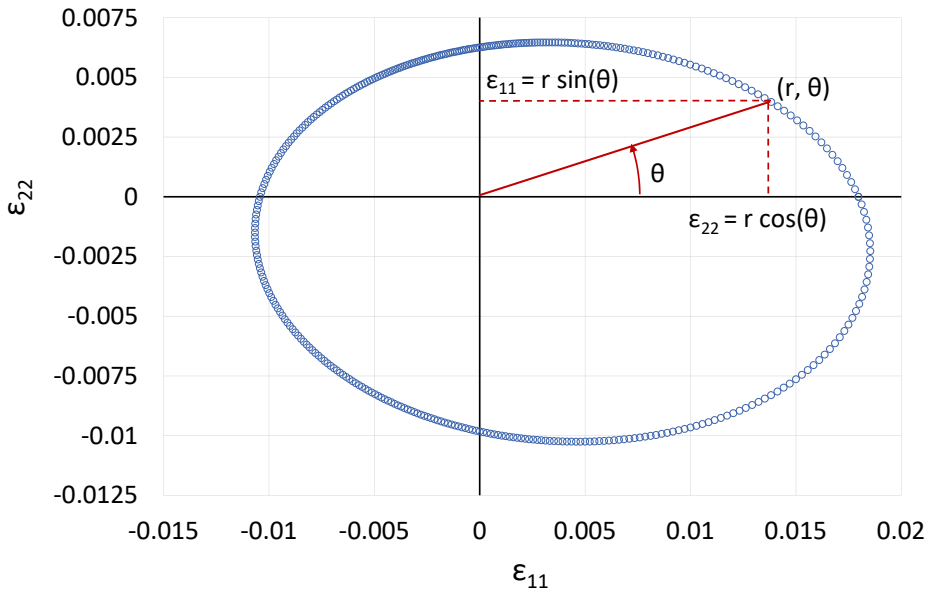


Figure A.2: Example of identification of failure loci in ε_{11} - ε_{22} strain space, with polar coordinates.

Bibliography

[1] M. Darecki. Flightpath 2050. *Flightpath 2050 Europe's Vision for Aviation*, page 28, 2011.

[2] Advisory Council for Aviation Research and Innovation in Europe (ACARE). Strategic Research & Innovation Agenda. Technical Report February, 2017.

[3] J. Shin. NASA Aeronautics: Strategic Implementation Plan. *NASA*, 2015.

[4] NASA. Nasa aeronautics: Strategic implementation plan. 2019 update. Technical report, 2019.

[5] Air Transport Action Group (ATAG). Aviation benefits beyond borders. Technical report, April 2014.

[6] ACARE. Time for change: The need to rethink europe's flightpath 2050. https://www.acare4europe.org/wp-content/uploads/2022/02/Time_for_change_FlightPath_2050.pdf/, 2020. Accessed: 2022-12-10.

[7] Directorate-General for Research European Commission and Unit C.3 — Low Emission Future Industries Innovation, Directorate C — Clean Planet. Fly the green deal, europe's vision for sustainable aviation, report of the advisory council for aviation research and innovation in europe (acare). Technical report, Advisory Council for Aviation Research and Innovation in Europe (ACARE), 2022.

[8] S. Shparberg and B. Lange. Global market forecast 2022. Technical report, Airbus, July 2022.

[9] C.S. Lopes, Z. Gürdal, and P.P. Camanho. Tailoring for strength of composite steered-fibre panels with cutouts. *Composites Part A: Applied Science and Manufacturing*, 41(12):1760–1767, 2010.

[10] G. Schuhmacher, F. Daoud, Ö. Petersson, and M. Wagner. Multidisciplinary Airframe Design Optimisation. *28th International Congress of the Aeronautical Sciences*, pages 1–13, 2012.

[11] F. Daoud, Ö. Petersson, S. Deinert, and P. Bronny. Multidisciplinary airframe design process: Incorporation of steady and unsteady aeroelastic loads. *12th AIAA Aviation Technology, Integration and Operations (ATIO) Conference and 14th AIAA/ISSMO Multidisciplinary Analysis and Optimization Conference*, (September):1–15, 2012.

[12] A. Schumacher and T. Vietor. *Advances in Structural and Multidisciplinary Optimization*. 2018.

[13] Optimacs - a european industrial doctorate training network. https://optimacs.net/. Accessed: 2020-05-10.

[14] G. Corrado, G. Ntourmas, M. Sferza, N. Traiforos, A. Arteiro, L. Brown, D. Chronopoulos, F. Daoud, F. Glock, J. Ninic, E. Ozcan, J. Reinoso, G. Schuhmacher, and T. Turner. Recent progress, challenges and outlook for multidisciplinary structural optimization of aircraft and aerial vehicles. *Progress in Aerospace Sciences*, 135:100861, 2022.

[15] D. Gay, S.V. Hoa, and S.W. Tsai. *Composite materials: Design and applications*. 2014.

[16] A. Puck and W. Schneider. On failure mechanisms and failure criteria of filament-wound glass-fibre/resin composites. *Plastics and Polymers*, 37:33–43, 01 1969.

[17] A. Puck and H. Schürmann. Failure analysis of FRP laminates by means of physically based phenomenological models. *Failure Criteria in Fibre-Reinforced-Polymer Composites*, 3538(96):832–876, 1998.

[18] A. Puck and H. Schürmann. Failure Analysis of FRP Lamninates by Means of Physically Based Phenomenological Models.pdf. *Composites Science and Technology*, 62:1633–1662, 2002.

[19] J. Bai and S.L. Phoenix. Compressive failure model for fiber composites by kink band initiation from obliquely aligned, shear-dislocated fiber breaks. *International Journal of Solids and Structures*, 42(7):2089–2128, 2005.

[20] P. Maimí Vert. *Modelizacion constitutiva y computacional del daño y la fractura de materiales compuestos*. 2007.

[21] M.G.R. Sause. *In Situ Monitoring of Fiber-Reinforced Composites Theory, Basic Concepts, Methods, and Applications*. 2016.

[22] S.C. Garcea, I. Sinclair, S.M. Spearing, and P.J. Withers. Mapping fibre failure in situ in carbon fibre reinforced polymers by fast synchrotron x-ray computed tomography. *Composites Science and Technology*, 149:81–89, 2017.

[23] S.T. Pinho, P. Robinson, and L. Iannucci. Fracture toughness of the tensile and compressive fibre failure modes in laminated composites. *Composites Science and Technology*, 66(13):2069–2079, 2006.

[24] M.J. Laffan, S.T. Pinho, P. Robinson, and L. Iannucci. Measurement of the in situ ply fracture toughness associated with mode I fibre tensile failure in FRP. Part II: Size and lay-up effects. *Composites Science and Technology*, 70(4):614–621, 2010.

[25] J. Lee and C. Soutis. Thickness effect on the compressive strength of T800/924C carbon fibre-epoxy laminates. *Composites Part A: Applied Science and Manufacturing*, 36(2 SPEC. ISS.):213–227, 2005.

[26] Q. Sun, G. Zhou, H. Guo, Z. Meng, Z. Chen, H. Liu, H. Kang, and X. Su. Failure mechanisms of cross-ply carbon fiber reinforced polymer laminates under longitudinal compression with experimental and computational analyses. *Composites Part B: Engineering*, 167:147–160, 2019.

[27] B.W. Rosen. Mechanics of composite strengthening. *Fibre Composite Materials, American Society of Materials, Metals Park, Ohio*, pages 37–75, 1965.

[28] A.S. Argon. Fracture of composites. volume 1 of *Treatise on Materials Science & Technology*, pages 79–114. Elsevier, 1972.

[29] S. Pimenta. Micromechanics of kink-band formation, 2008.

[30] C.G. Dávila, P.P. Camanho, and C.A. Rose. Failure criteria for frp laminates. *Journal of Composite Materials*, 39:323–345, 2005.

[31] S.T. Pinho, L. Iannucci, and P. Robinson. Physically-based failure models and criteria for laminated fibre-reinforced composites with emphasis on fibre kinking: Part i: Development. *Composites Part A: Applied Science and Manufacturing*, 37(1):63–73, 2006.

[32] G. Catalanotti, P.P. Camanho, and A.T. Marques. Three-dimensional failure criteria for fiber-reinforced laminates. *Composite Structures*, 95:63–79, 2013.

[33] P.P. Camanho, A. Arteiro, G. Catalanotti, A.R. Melro, and M. Vogler. Three-dimensional invariant-based failure criteria for transversely isotropic fibre-reinforced composites. In *Numerical Modelling of Failure in Advanced Composite Materials*, pages 111–150. Woodhead Publishing, Cambridge, 2015.

[34] I.M. Daniel and I. Ori. *Engineering Mechanics of Composite Materials, 2nd edition*. Oxfort University press, New York, 2006.

[35] M.J. Hinton, A.S. Kaddour, and P.D. Soden. Predicting failure in fibre composites: Lessons learned from the world-wide failure exercise. *Technical Paper - Society of Manufacturing Engineers. EM*, (EM02-109), 2002.

[36] M.J. Hinton, A.S. Kaddour, and P.D. Soden. *Failure Criteria in Fibre Reinforced Polymer Composites: The World-Wide Failure Exercise*. 2004.

[37] A.S. Kaddour, M.J. Hinton, S. Li, and P.A. Smith. Damage prediction in polymeric composites: Up-date of Part(A) of the Third World-Wide Failure Exercise (WWFE-III). *ICCM International Conferences on Composite Materials*, pages 1–5, 2011.

[38] A.S. Kaddour and M.J. Hinton. *Benchmarking of triaxial failure criteria for composite laminates: Comparison between models of 'Part (A)' of 'WWFE-II'*, volume 46. 2012.

[39] A.S. Kaddour and M.J. Hinton. Maturity of 3D failure criteria for fibre-reinforced composites: Comparison between theories and experiments: Part B of WWFE-II. *Journal of Composite Materials*, 47(6-7):925–966, 2013.

[40] A.S. Kaddour, M.J. Hinton, P.A. Smith, and S. Li. A comparison between the predictive capability of matrix cracking, damage and failure criteria for fibre reinforced composite laminates: Part A of the third world-wide failure exercise. *Journal of Composite Materials*, 47(20-21):2749–2779, 2013.

[41] R.M. Christensen. *A Physically Based Cumulative Damage Formalism*, pages 51–65. Springer Netherlands, Dordrecht, 2009.

[42] R.G. Cuntze. *Comparison between experimental and theoretical results using Cuntze's "failure mode concept" model for composites under triaxial loadings - Part B of the second world-wide failure exercise*, volume 47. 2013.

[43] S.T. Pinho, C.G. Dávila, P.P. Camanho, L. Iannucci, and P. Robinson. Failure models and criteria for frp under in-plane or three-dimensional stress states including shear nonlinearity. *Nasa/Tm-2005-213530*, page 68, 2005.

[44] J. Echaabi, F. Trochu, and R. Gauvin. Review of failure criteria of fibrous composite materials. *Polymer Composites*, 17:786–798, 1996.

[45] F. Paris and K.E. Jackson. A study of failure criteria of fibrous composite materials. Contractor Report (CR) NASA/CR- 2001-210661, George Washington University, Hampton, Virginia, March 2001.

[46] M.N. Nahas. Survey of Failure and Post-Failure Theories of Laminated Fiber-Reinforced Composites. *Journal of Composites Technology and Research*, 8(4):138–153, 1986.

[47] R.M. Jones. *Mechanics of Composite Materials, Second Edition*. 1999.

[48] R. Narayanaswami and H.M. Adelman. Evaluation of the tensor polynomial and hoffman strength theories for composite materials. *Journal of Composite Materials*, 11(4):366–377, 1977.

[49] S.W. Tsai and J.D.D. Melo. An invariant-based theory of composites. *Composites Science and Technology*, 100:237–243, 2014.

[50] G. Corrado, A. Arteiro, A.T. Marques, J. Reinoso, F. Daoud, and F. Glock. An extended invariant approach to laminate failure of fibre-reinforced polymer structures. *The Aeronautical Journal*, 126(1300):1045–1068, 2022.

[51] S.W. Tsai and J.D.D. Melo. A unit circle failure criterion for carbon fiber reinforced polymer composites. *Composites Science and Technology*, 123:71–78, 2016.

[52] C.T. Sun, B.J. Quinn, and J. Tao. Comparative Evaluation of Failure Analysis Methods for Composite Laminates. Technical report, U.S. Department of Transportation, May 1996.

[53] R.F. Gibson. *Principle of Composite Material Mechanics - Fourth Edition*. 2016.

[54] L.J. Hart-Smith. Predictions of the original and truncated maximum-strain failure models for certain fibrous composite laminates. *Composites Science and Technology*, 58(7):1151–1178, 1998.

[55] L.J. Hart-Smith. Predictions of a generalized maximum-shear-stress failure criterion for certain fibrous composite laminates. *Composites Science and Technology*, 58(7):1179–1208, 1998.

[56] L.J. Hart-Smith. Chapter 5.4 - comparison between theories and test data concerning the strength of various fibre-polymer composites. In M.J. Hinton, A.S. Kaddour, and P.D. Soden, editors, *Failure Criteria in Fibre-Reinforced-Polymer Composites*, pages 770–809. Elsevier, Oxford, 2004.

[57] Z. Hashin. Failure criteria for unidirectional fiber composites. *Journal of Applied Mechanics, Transactions ASME*, 47(2):329–334, 1980.

[58] S.E. Yamada and C.T. Sun. Analysis of laminate strength and its distribution. *Journal of Composite Materials*, 12(3):275–284, 1978.

[59] F.K. Chang and K.Y. Chang. A progressive damage model for laminated composites containing stress concentrations. *Journal of Composite Materials*, 21(9):834–855, 1987.

[60] F.K. Chang and K.Y. Chang. Post-failure analysis of bolted composite joints in tension or shear-out mode failure. *Journal of Composite Materials*, 21(9):809–833, 1987.

[61] *LS-Dyna*. Livermore Software Technology Corporation, California, United States, 2003.

[62] R.M. Christensen. Stress based yield/failure criteria for fiber composites. *International Journal of Solids and Structures*, 34(5):529–543, 1997.

[63] A. Puck. *Festigkeitsanalyse von Faser-Matrix-Laminaten, Modelle für die Praxis*. Hanser, 1995.

[64] S.R. Swanson, M.J. Messick, and Z. Tian. Failure of Carbon/Epoxy Lamina Under Combined Stress. *Journal of Composite Materials*, 21(July 1987):619–630, 1986.

[65] P. Maimí, P.P. Camanho, J.A. Mayugo, and C.G. Dávila. A continuum damage model for composite laminates: Part i - constitutive model. *Mechanics of Materials*, 39:897–908, 2007.

[66] P. Maimí, P.P. Camanho, J.A. Mayugo, and C.G. Dávila. A continuum damage model for composite laminates: Part ii - computational implementation and validation. *Mechanics of Materials*, 39:909–919, 2007.

[67] S.T. Pinho, R. Darvizeh, P. Robinson, C. Schuecker, and P.P. Camanho. Material and structural response of polymer-matrix fibre-reinforced composites. *Journal of Composite Materials*, 46(19-20):2313–2341, 2012.

[68] P.P. Camanho, A. Arteiro, A.R. Melro, G. Catalanotti, and M. Vogler. Three-dimensional invariant-based failure criteria for fibre-reinforced composites. *International Journal of Solids and Structures*, 55:92–107, 2015.

[69] M. Vogler, G. Ernst, and R. Rolfes. Invariant based transversely-isotropic material and failure model for fiber-reinforced polymers. *Computers, Materials and Continua*, 16(1):25–49, 2010.

[70] P.P. Camanho and A. Arteiro. *Analysis Models for Polymer Composites Across Different Length Scales*, pages 199–279. Springer International Publishing, 2017.

[71] N. Li, C. Ju, P. Yang, and F. Zhuang. Stress invariant-based failure criteria for predicting matrix failure of transversely isotropic composites: Theoretical assessment and rationalized improvement. *Thin-Walled Structures*, 181:110110, 2022.

[72] A. Riccio, editor. *Damage Growth in Aerospace Composites*. Springer Aerospace, 2015.

[73] J.M. Whitney and R.J. Nuismer. Stress Fracture Criteria for Laminated Composites Containing Stress Concentrations. *Journal of Composite Materials*, 8(July):253–265, 1974.

[74] R.Y. Kim and S.R. Soni. Experimental and Analytical Studies On the Onset of Delamination in Laminated Composites. *Journal of Composite Materials*, 18(1):70–80, 1984.

[75] Ye, L. Role of matrix resin in delamination onset and growth in composite laminates. *Composites Science and Technology*, 33(4):257–277, 1988.

[76] J.C. Brewer and P.A. Lagace. Quadratic Stress Criterion for Initiation of Delamination. *Journal of Composite Materials*, 22(12):1141–1155, 1988.

[77] C.G. Dávila and E.R. Johnson. Analysis of delamination initiation in postbuckled dropped-ply laminates. *AIAA Journal*, 31(4):721–727, 1993.

[78] P.P. Camanho and F.L. Matthews. Delamination onset prediction in mechanically fastened joints in composite laminates. *Journal of Composite Materials*, 33(10):906–927, 1999.

[79] J.P. Hou, N. Petrinic, and C. Ruiz. A delamination criterion for laminated composites under low-velocity impact. *Composites Science and Technology*, 61(14):2069–2074, 2001.

[80] X. Li, S.R. Hallett, and M.R. Wisnom. Predicting the effect of through-thickness compressive stress on delamination using interface elements. *Composites Part A: Applied Science and Manufacturing*, 39(2):218–230, 2008.

[81] E.F. Rybicki and M.F. Kanninen. A finite element calculation of stress intensity factors by a modified crack closure integral. *Engineering Fracture Mechanics*, 9(4):931–938, 1977.

[82] R. Krueger. Virtual crack closure technique: History, approach, and applications. *Applied Mechanics Reviews*, 57(1-6):109–143, 2004.

[83] R. Krueger, P.J. Minguet, and T.K.O. Brien. Implementation of interlaminar fracture mechanics in design: an overview. *International Conference on Composite Materials (ICCM-14)*, 2003.

[84] D. Xie and S.B. Biggers. Progressive crack growth analysis using interface element based on the virtual crack closure technique. *Finite Elements in Analysis and Design*, 42(11):977–984, 2006.

[85] D.S. Dugdale. Yielding of steel sheets containing slits. *Journal of the Mechanics and Physics of Solids*, 8(2):100–104, 1960.

[86] G.I. Barrenblatt. The mathematical theory of equilibrium of cracks in brittle fracture. *Adv. Appl. Mech*, 7:55–129, 1962.

[87] J. Chen, M. Crisfield, A.J. Kinloch, E.P. Busso, F.L. Matthews, and Y. Qiu. Predicting progressive delamination of composite material specimens via interface elements. *Mechanics of Composite Materials and Structures*, 6(4):301–317, 1999.

[88] M. Elices, G.V. Guinea, J. Gómez, and J. Planas. The cohesive zone model: Advantages, limitations and challenges. *Engineering Fracture Mechanics*, 69(2):137–163, 2001.

[89] P.W. Harper and S.R. Hallett. Cohesive zone length in numerical simulations of composite delamination. *Engineering Fracture Mechanics*, 75(16):4774–4792, 2008.

[90] A. Turon, C.G. Dávila, P.P. Camanho, and J. Costa. An engineering solution for mesh size effects in the simulation of delamination using cohesive zone models. *Engineering Fracture Mechanics*, 74(10):1665–1682, 2007.

[91] A. Turon, P.P. Camanho, J. Costa, and J. Renart. Accurate simulation of delamination growth under mixed-mode loading using cohesive elements: Definition of interlaminar strengths and elastic stiffness. *Composite Structures*, 92(8):1857–1864, 2010.

[92] F.P. van der Meer and L.J. Sluys. A numerical investigation into the size effect in the transverse crack tension test for mode ii delamination. *Composites Part A: Applied Science and Manufacturing*, 54:145–152, 2013.

[93] G. Catalanotti, C. Furtado, T. Scalici, G. Pitarresi, F.P. van der Meer, and P.P. Camanho. The effect of through-thickness compressive stress on mode ii interlaminar fracture toughness. *Composite Structures*, 182:153–163, 2017.

[94] *Abaqus 2017 Analysis User's Manual*. Dassault Systèmes Simulia Corp, United States, 2016.

[95] M.L. Benzeggagh and M. Kenane. Measurement of mixed-mode delamination fracture toughness of unidirectional glass/epoxy composites with mized-mode bending apparatus. *Composite Science and Technology*, 56:439–449, 1996.

[96] P. Camanho and C.G. Dávila. Mixed-Mode Decohesion Finite Elements in for the Simulation Composite of Delamination Materials. *Nasa*, TM-2002-21(June):1–37, 2002.

[97] P.P. Camanho, S. Bowron, and F.L. Matthews. Failure mechanisms in bolted CFRP, 1998.

[98] F.L. Matthews and P.P. Camanho. A progressive damage model for mechanically fastened joints in composite laminates. *Journal of Composite Materials*, 33(24):2248–2280, 1999.

[99] C. González and J. LLorca. Mechanical behavior of unidirectional fiber-reinforced polymers under transverse compression: Microscopic mechanisms and modeling. *Composites Science and Technology*, 67(13):2795–2806, 2007.

[100] E. Totry, C. González, and J. LLorca. Failure locus of fiber-reinforced composites under transverse compression and out-of-plane shear. *Composites Science and Technology*, 68(3-4):829–839, 2008.

[101] E. Totry, C. González, and J. LLorca. Prediction of the failure locus of C/PEEK composites under transverse compression and longitudinal shear through computational micromechanics. *Composites Science and Technology*, 68(15-16):3128–3136, 2008.

[102] E. Totry, J.M. Molina-Aldareguía, C. González, and J. LLorca. Effect of fiber, matrix and interface properties on the in-plane shear deformation of carbon-fiber reinforced composites. *Composites Science and Technology*, 70(6):970–980, 2010.

[103] T.J. Vaughan and C.T. McCarthy. A micromechanical study on the effect of intra-ply properties on transverse shear fracture in fibre reinforced composites. *Composites Part A: Applied Science and Manufacturing*, 42(9):1217–1228, 2011.

[104] T.J. Vaughan and C.T. McCarthy. Micromechanical modelling of the transverse damage behaviour in fibre reinforced composites. *Composites Science and Technology*, 71(3):388–396, 2011.

[105] L.P. Canal, C. González, J. Segurado, and J. LLorca. Intraply fracture of fiber-reinforced composites: Microscopic mechanisms and modeling. *Composites Science and Technology*, 72(11):1223–1232, 2012.

[106] A.R. Melro, P.P. Camanho, F.M. Andrade Pires, and S.T. Pinho. Micromechanical analysis of polymer composites reinforced by unidirectional fibres: Part I-Constitutive modelling. *International Journal of Solids and Structures*, 50(11-12):1897–1905, 2013.

[107] A.R. Melro, P.P. Camanho, F.M. Andrade Pires, and S.T. Pinho. Micromechanical analysis of polymer composites reinforced by unidirectional fibres: Part II-Micromechanical analyses. *International Journal of Solids and Structures*, 50(11-12):1906–1915, 2013.

[108] L.M. Kachanov. Time of the rupture process under creep conditions, izy akad. *Nank S.S.R. Otd Tech Nauk*, 8:26–31, 1958.

[109] P.P. Camanho and S.R. Hallett. *Numerical Modelling of Failure in Advanced Composite Materials*. Woodhead Publishing Series in Composites Science and Engineering, 2015.

[110] E. Benvenuti. A regularized XFEM framework for embedded cohesive interfaces. *Computer Methods in Applied Mechanics and Engineering*, 197(49-50):4367–4378, 2008.

[111] C.G. Dávila, C.A. Rose, and E.V. Iarve. *Modeling fracture and complex crack networks in laminated composites*, pages 297–347. 2013.

[112] P. Kanouté, D.P. Boso, J.L. Chaboche, and B. A. Schrefler. Multiscale methods for composites: A review. *Archives of Computational Methods in Engineering*, 16(1):31–75, 2009.

[113] A.C. Orifici, I. Herszberg, and R.S. Thomson. Review of methodologies for composite material modelling incorporating failure. *Composite Structures*, 86:194–210, 2008.

[114] J. Reinoso, A. Blázquez, A. Estefani, F. París, J. Cañas, E. Arévalo, and F. Cruz. Experimental and three-dimensional global-local finite element analysis of a composite component including degradation process at the interfaces. *Composites Part B: Engineering*, 43:1929–1942, 2012.

[115] M. Akterskaia, P.P. Camanho, E. Jansen, A. Arteiro, and R. Rolfes. Progressive delamination analysis through two-way global-local coupling approach preserving energy dissipation for single-mode and mixed-mode loading. *Composite Structures*, 223:110892, 2019.

[116] K.-R.B. Bramsiepe, V.H. Handojo, M.Y. Meddaikar, M. Schulze, and T. Klimmek. Loads and structural optimisation process for composite long range transport aircraft configuration. *2018 Multidisciplinary Analysis and Optimization Conference*, pages 1–20, 2018.

[117] S.T. Ijsselmuiden, M.M. Abdalla, and Z. Gürdal. Implementation of strength-based failure criteria in the lamination parameter design space. *AIAA Journal*, 46:1826–1834, 2008.

[118] A. Arteiro, L.F. Pereira, M.A. Bessa, C. Furtado, and P.P. Camanho. A micro-mechanics perspective to the invariant-based approach to stiffness. *Composites Science and Technology*, 2018.

[119] M.J. Hinton and A.S. Kaddour. Triaxial test results for fibre-reinforced composites: The Second World-Wide Failure Exercise benchmark data. *Journal of Composite Materials*, 47(6-7):653–678, 2013.

[120] H. Thom. A review of the biaxial strength of fibre-reinforced plastics. *Composites Part A: Applied Science and Manufacturing*, 29(8):869–886, 1998.

[121] B. Vermes, S. W. Tsai, A. Riccio, F. Di Caprio, and S. Roy. Application of the tsai's modulus and double-double concepts to the definition of a new affordable design approach for composite laminates. *Composite Structures*, page 113246, 2020.

[122] H. Molker, R. Gutkin, S. Pinho, and L.E. Asp. Hot spot analysis in complex composite material structures. *Composite Structures*, 207:776–786, 2019.

[123] H. Molker, R. Gutkin, and L.E. Asp. Implementation of failure criteria for transverse failure of orthotropic non-crimp fabric composite materials. *Composites Part A*, 92:158–166, 2017.

[124] X. Zou, S. Yan, M. Reza, L. Brown, and A. Jones. An abaqus plugin for efficient damage initiation hotspot identification in large-scale composite structures with repeated features. *Advances in Engineering Software*, 153:102964, 2021.

[125] C.S. Lopes, Z. Gürdal, and P.P. Camanho. Variable-stiffness composite panels: Buckling and first-ply failure improvements over straight-fibre laminates. *Computers & Structures*, 86(9):897–907, 2008. Composites.

[126] F. Laurin, C. Julien, and P. Paulmier. Damage and strength analysis of open-hole laminated plates under tensile, compressive and bending loadings. *ECCM 2016 - Proceeding of the 17th European Conference on Composite Materials*, (June):26–30, 2016.

[127] J.S. Charrier. *Développement de méthodologies dédiées à l'analyse robuste de la tenue de structures composites sous chargements complexes tridimensionnels*. PhD thesis, École Nationale Supérieure d'Arts et Métiers - ENSAM, 2013.

[128] T. Vandellos. *Développement d'une stratégie de modélisation du délaminage dans les composites stratifiés*. PhD thesis, École Doctorale des Sciences Physiques et de l'Ingénieur, l'Université Bordeuax 1, 2011.

[129] M. Hautier. *Analyse des réparations des matériaux composites: mise en oeuvre d'un procédé par infiltration et étude du comportement mécanique*. PhD thesis, Université Paul Sabatier - Toulouse III, 2010.

[130] J. Reinoso, A. Blázquez, L. Távara, F. París, and C. Arellano. Damage tolerance of composite runout panels under tensile loading. *Composites Part B: Engineering*, 96:79–93, 2016.

[131] F. Zhuang, A. Arteiro, C. Furtado, P. Chen, and P.P. Camanho. Mesoscale modelling of damage in single- and double-shear composite bolted joints. *Composite Structures*, 226:111210, 2019.

[132] *Abaqus 2020 Documentation*. Dassault Systèmes Simulia Corp, United States, 2020.

[133] P.P. Camanho, M.A. Bessa, G. Catalanotti, M. Vogler, and R. Rolfes. Modeling the inelastic deformation and fracture of polymer composites-Part II: Smeared crack model. *Mechanics of Materials*, 59:36–49, 2013.

[134] F. Zhuang, P. Chen, A.o Arteiro, and P.P. Camanho. Mesoscale modelling of damage in half-hole pin bearing composite laminate specimens. *Composite Structures*, 214:191–213, 2019.

[135] A. Arteiro. *Structural Mechanics of Thin-Ply Laminated Composites*. PhD thesis, University of Porto, 2016.

[136] A. Turon, P.P. Camanho, J. Costa, and C.G. Dávila. A damage model for the simulation of delamination in advanced composites under variable-mode loading. *Mechanics of Materials*, 38(11):1072–1089, 2006.

[137] Z.P. Bazant and B.H. Oh. Crack Band Theory for fracture of Concrete. 1983.

[138] P.M. Moran, X.H. Liu, and C.F. Shih. Kink band formation and band broadening in fiber composites under compressive loading. *Acta Metallurgica et Materialia*, 43(8):2943–2958, 1995.

[139] C. Furtado, G. Catalanotti, A. Arteiro, P.J. Gray, B.L. Wardle, and P.P. Camanho. Simulation of failure in laminated polymer composites: Building-block validation. *Composite Structures*, 226:111168, 2019.

[140] SAE International. *Polymer Matrix Composites: Materials Usage, Design, and Analysis COMPOSITE MATERIALS HANDBOOK*, volume 3. 2012.

[141] S. Pimenta, R. Gutkin, S.T. Pinho, and P. Robinson. A micromechanical model for kink-band formation: Part I - Experimental study and numerical modelling. *Composites Science and Technology*, 69(7-8):948–955, 2009.

[142] P.P. Camanho, P. Maimí, and C.G. Dávila. Prediction of size effects in notched laminates using continuum damage mechanics. *Composites Science and Technology*, 67(13):2715–2727, 2007.

[143] M.R. Wisnom, B. Khan, and S.R. Hallett. Size effects in unnotched tensile strength of unidirectional and quasi-isotropic carbon/epoxy composites. *Composite Structures*, 84(1):21–28, 2008.

[144] M. Vogler, R. Rolfes, and P.P. Camanho. Modeling the inelastic deformation and fracture of polymer composites-Part I: Plasticity model. *Mechanics of Materials*, 59:50–64, 2013.

[145] H. Koerber, J. Xavier, and P.P. Camanho. High strain rate characterisation of unidirectional carbon-epoxy IM7-8552 in transverse compression and in-plane shear using digital image correlation. *Mechanics of Materials*, 42(11):1004–1019, 2010.

[146] H. Koerber, P. Kuhn, M. Ploeckl, F. Otero, P.W. Gerbaud, R. Rolfes, and P.P. Camanho. Experimental characterization and constitutive modeling of the non-linear stress–strain behavior of unidirectional carbon–epoxy under high strain rate loading. *Advanced Modeling and Simulation in Engineering Sciences*, 5(17):1–24, 2018.

[147] B.G. Green, M.R. Wisnom, and S.R. Hallett. An experimental investigation into the tensile strength scaling of notched composites. *Composites Part A: Applied Science and Manufacturing*, 38(3):867–878, 2007.

[148] J. Lee and C. Soutis. A study on the compressive strength of thick carbon fibre–epoxy laminates. *Composites Science and Technology*, 67(10):2015–2026, 2007.

[149] J. Lee and C. Soutis. Measuring the notched compressive strength of composite laminates: Specimen size effects. *Composites Science and Technology*, 68(12):2359–2366, 2008.

[150] M.R. Wisnom and S.R. Hallett. The role of delamination in strength, failure mechanism and hole size effect in open hole tensile tests on quasi-isotropic laminates. *Composites Part A: Applied Science and Manufacturing*, 40(4):335–342, 2009.

[151] S.R. Hallett, W.G. Jiang, B. Khan, and M.R. Wisnom. Modelling the interaction between matrix cracks and delamination damage in scaled quasi-isotropic specimens. *Composites Science and Technology*, 68(1):80–89, 2008.

[152] S.R. Hallett, B.G. Green, W.G. Jiang, and M.R. Wisnom. An experimental and numerical investigation into the damage mechanisms in notched composites. *Composites Part A: Applied Science and Manufacturing*, 40(5):613–624, 2009.

[153] M.R. Wisnom, S.R. Hallett, and C. Soutis. Scaling effects in notched composites. *Journal of Composite Materials*, 44(2):195–210, 2010.

[154] R. Amacher, J. Cugnoni, J. Botsis, L. Sorensen, W. Smith, and C. Dransfeld. Thin ply composites: Experimental characterization and modeling of size-effects. *Composites Science and Technology*, 101:121–132, 2014.

[155] W. Tan, B.G. Falzon, and M. Price. Predicting the crushing behaviour of composite material using high-fidelity finite element modelling. *International Journal of Crashworthiness*, 20(1):60–77, 2015.

[156] W. Tan and B.G. Falzon. Modelling the crush behaviour of thermoplastic composites. *Composites Science and Technology*, 134:57–71, 2016.

[157] F. Zhuang, A. Arteiro, R.P. Tavares, P.P. Camanho, and P. Chen. Modelling damage in half-hole pin bearing cross-ply and angle-ply composite laminates. *Composite Structures*, 300:116103, 2022.

[158] A. Fink, P.P. Camanho, J.M. Andrés, E. Pfeiffer, and A. Obst. Hybrid cfrp/titanium bolted joints: Performance assessment and application to a spacecraft payload adaptor. *Composites Science and Technology*, 70(2):305–317, 2010.

[159] P.P. Camanho and M. Lambert. A design methodology for mechanically fastened joints in laminated composite materials. *Composites Science and Technology*, 66(15):3004–3020, 2006.

[160] S.S. Sastry. *Introductory methods of numerical analysis*. 2012.